European Union

Ministero dell'Istruzione
dell'Università e della Ricerca

Università degli Studi di
Palermo

TESI DI DOTTORATO

SOLID STATE HYDROGEN STORAGE: A STUDY ON DIFFERENT MATERIALS AND DEVELOPMENT OF AN APPLICATIVE SYSTEM

Supervisore:
Prof. GIACOMO D'ALÌ STAITI

Co-Supervisore:
Prof. GIOVANNI PRINCIPI

Coordinatore del Corso di Dottorato:
Prof. BERNARDO SPAGNOLO

Dottorando:
Eng. BENEDETTO SCHIAVO

SSD: FIS/01

Università degli Studi di Palermo
Dipartimento di Fisica

Corso di DOTTORATO DI RICERCA INTERNAZIONALE
in FISICA APPLICATA - XXIII Ciclo

A Gesù, che è Dio, per la Grazia che ci accompagna ogni giorno.
Ai Miei Cari, ancora una volta e sempre.
A Maria Chiara, sempre di più.

Contents

Abstract..... V

List of abbreviations..... VII

Preface..... 1

Chapter 1 – Hydrogen for the future..... 5

1.1 Introduction..... 5

1.2 Hydrogen as clean fuel and energy carrier..... 7

1.2.1 Main physical properties of hydrogen..... 7

1.2.2 Hydrogen as a fuel..... 8

1.3 Hydrogen production..... 11

1.3.1. Production from fossil fuels..... 11

1.3.2. Production from renewable sources..... 13

1.4 Hydrogen distribution..... 15

Chapter 2 – Methods for hydrogen storage..... 19

2.1 The problem of hydrogen storage..... 19

2.1.1 Compressed hydrogen gas..... 21

2.1.2 Liquid hydrogen..... 22

2.2 Hydrogen sorption..... 22

2.3 Hydrides..... 24

2.3.1 Thermodynamics of hydrogen absorption and hydrides stability..... 25

2.3.2 Kinetics..... 27

2.3.3 Interstitial hydrides..... 28

2.3.4 Promising modified binary hydrides..... 30

2.3.5 Complex hydrides ... 31
2.4 High surface area materials ... 34
2.4.1 Carbon structures ... 35
2.4.2 Organic and inorganic nanotubes ... 37
2.4.3 Zeolites ... 37
2.4.4 Metal-Organic Frameworks (MOFs) ... 37
2.4.5 Organic polymers ... 38
2.5 Other systems for hydrogen storage ... 39
2.5.1 Clathrates ... 39
2.5.2 Ionic liquids ... 39
2.5.3 $NaBH_4$ solutions ... 39
2.5.4 Rechargeable organic liquids ... 40
2.5.5 Chemical hydrides (H_2O-reactive) ... 40

Chapter 3 – Experimental methods and instruments ... 49
3.1 Introduction ... 49
3.2 The ball milling technique ... 49
3.3 Gas sorption analyzer ... 53
3.4 Differential scanning calorimetry (DSC) ... 55
3.5 Coupled volumetric – calorimetric measurements ... 58
3.6 Test Station ... 59
3.7 X-ray powder diffraction (XRPD) ... 60
3.7.1. Crystal lattice geometry ... 60
3.7.2. The *Bragg*'s law ... 61
3.7.3. Used experimental XRPD facilities ... 62
3.7.4. The *Rietveld* method ... 64
3.8 X-ray absorption spectroscopy (XAS) ... 66
3.9 Other experimental techniques ... 70

Chapter 4 – Investigation on the nanostructured $LaNi_5$ alloy ... 73
4.1 Motivation for this study ... 73
4.2 Effect of ball milling on the hydrogen sorption properties of $LaNi_5$ ... 74
4.3 Impurity analysis ... 76
4.4 DSC studies ... 77
4.5 Effect of the annealing on the hydrogen sorption properties ... 79
4.6 XRPD analysis ... 80
4.7 EXAFS measurements ... 82
4.8 Summary ... 89

Chapter 5 – Calcium borohydrides-based reactive hydride composite..... 95
5.1 The system..... 95
5.2 Sample preparation and measurement conditions..... 96
5.3 Results and Discussions..... 97
5.3.1 Effect of milling time on the system CaH_2+MgB_2..... 97
5.3.2 Addition of AlB_2..... 100
5.3.3 Tests with possible catalysts..... 106
5.4 Summary..... 110
Appendix to chapter 5..... 115

Chapter 6 – Hydrogen storage in a polymer-based system..... 117
6.1 Polymeric materials for hydrogen storage..... 117
6.2 Samples description..... 118
6.3 Samples characterization..... 120
6.3.1 XRPD measurements..... 121
6.3.2 Electron microscopy analysis..... 121
6.4 Hydrogenation..... 126
6.5 Summary..... 128

Chapter 7 – Design and building of a solid state hydrogen storage tank..... 133
7.1 The task..... 133
7.2 Preliminary tests..... 134
7.3 Tank design..... 139
7.4 Alloy's preparation..... 141
7.5 Tank building and testing..... 144
7.5.1 Tests with one cylinder..... 145
7.5.2 First rack testing..... 146
7.5.3 Two racks (I+II) configuration testing..... 149

Chapter 8 – Concluding remarks..... 153

Curriculum Vitae..... 157

Acknowledgements..... 161

Abstract

Hydrogen is often proposed as the suitable clean fuel and energy vector for the near future. Before the widespread use of hydrogen and the realization of a hydrogen economy become reality, several issue must be addressed, mainly related to the efficiency and costs of the hydrogen production, delivery and utilization. In particular, safe and efficient hydrogen storage is a key issue. Compressed hydrogen high pressure cylinders and liquid hydrogen cryogenic systems, used today to store hydrogen, need high energy amounts and have severe safety implications.

In this thesis, the results of the research activity on solid state hydrogen storage are reported. Different types of materials have been investigated as potential candidates to store hydrogen. Among hydrides, a study of the ball milling effect on the $LaNi_5$ intermetallic alloy has been carried out; some unexpected results have been obtained and then explained on the basis of the experimental evidences. A composite system based on calcium borohydride (complex hydride) and magnesium hydride (light metal hydride) has been studied starting from ball milling a dehydrogenated form; the effect of milling time, partial substitution of magnesium diboride, and addition of dopants, on the sorption properties of the starting system have been investigated. As a low cost alternative, manganese oxide incorporated in a functionalized polymer has been studied and interesting hydrogen capacity values have been measured at temperatures at which high efficiency polymer electrolyte (PEM) fuel cells are fed with hydrogen. As an applicative system, a hydrogen storage tank for a small car prototype has been designed, built and tested; the final achieved performances of the system are reported and compared with the customer requirements.

List of abbreviations

BCC	Body-Centred Cubic (structure)
BET	Brunauer Emmet Teller (theory)
BPR	Ball to Powder Ratio
CCS	Carbon Capture and Sequestration (or Storage)
CFRP	Carbon Fibres Reinforced Polymers
CNT	Carbon NanoTube
COF	Covalent Organic Frameworks
DFT	Density Functional Theory
DOE	Department Of Energy (of United States of America)
EDX	Energy Dispersive X-ray (spectroscopy)
EMT	Effective Medium Theory
EXAFS	Extended X-Ray Absorption Fine Structure (spectroscopy)
FC	Fuel Cell
FCU	Flow Control Unit
FT	Fourier Transform
GFRP	Glass Fibres Reinforced Polymer
GHG	GreenHouse Gas
GMB	Glass MicroBalloon
GUI	Graphical User Interface
HCP	HyperCrosslinked Polymer

ICE	Internal Combustion Engine
IUPAC	International Union of Pure and Applied Chemistry
LabVIEW	Laboratory Virtual Instrument Engineering Workbench
MAS	Magic Angle Spinning
MOF	Metal-Organic Framework
MS	Mass Spectroscopy
MSRD	Mean Square Relative Displacement
NMR	Nuclear Magnetic Resonance (spectroscopy)
PCI	Pressure Composition Isotherm
PEC	PhotoElectroChemical (cell)
PEEK	Poly Ether Ether Ketone
PEM	Proton Exchange Membranes or Polymeric Electrolyte Membrane
PIM	Polymers of Intrinsic Microporosity
PIXE	Proton-Induced X-Ray Emission (spectroscopy)
PLC	Programmable Logic Controller
RHC	Reactive Hydride Composite
RT	Room Temperature
SEM	Scanning Electron Microscope
SS	Stainless Steel
SMR	Steam Methane Reforming
STP	Standard Temperature and Pressure
TPD	Temperature Programmed Desorption
XRPD	X-Ray Powder Diffraction
UAV	Unmanned Aerial Vehicle
WSS	Weighted Sum of Squares

Preface

Never as today, the need of new and clean energy sources has been felt as necessary at a world scale. Besides the strategic role that the possession of energy assets has on the economical independence of a country, there is today an environmental global question, related to the still increasing use of fossil fuels, which cannot be ignored or deferred anymore.

In this view, clean renewable energy sources (e.g. solar, wind, hydro-, geothermal, tides, waves, etc..) as well as alternative fuels (biodiesel, bioethanol, hydrogen) and energy vector systems (hydrogen, batteries) are being intensively studied in order to achieve suitable alternatives to fossil fuels.

In particular, hydrogen is an interesting potential candidate both as energy vector and clean fuel **[1]**. For this reason, great research efforts as well as private and public funds are addressed to make it a real suitable alternative **[2]**.

The experimental work reported in this thesis would be a contribution in this direction, as it deals with the study of different materials as potential candidates for efficient and safe hydrogen storage, and with the development of a hydrogen tank for applicative purposes. The thesis is organized as follows.

Chapter 1 introduces the issues related to the potential widespread use of hydrogen as efficient energy vector and clean fuel.

Chapter 2 deals with the problem of hydrogen storage and the different classes of materials considered as potential candidates for hydrogen storage in solid state; the theory of hydrogen sorption phenomena in these materials and a brief overview of the state of art are reported.

In **Chapter 3** the main laboratory techniques used during the experimental activity are described. The ball milling process and the related used instruments for sample preparation are introduced. A brief description of the characterization methods, such as differential scanning calorimetry, X-ray powder diffraction and X-ray absorption techniques, as well the *Sievert*'s type manometric/volumetric apparatus for hydrogen sorption evaluation are reported.

In the three subsequent chapters, the results of the experimental investigations on different systems for solid state hydrogen storage are reported and discussed. In particular, **Chapter 4** presents some new unexpected results during an experimental campaign on $LaNi_5$ alloy samples. **Chapter 5** deals with the formation of the reactive hydride composite $Ca(BH_4)_2$+MgH_2 from the ball milled binary system CaH_2+MgB_2 and with the effect of the milling time on its hydrogen sorption properties. Moreover, the effect of magnesium diboride partial or total substitution with aluminum diboride in the initial system, as well as the addition of some doping agents on the sorption properties of the CaH_2+AlB_2 system have been investigated and discussed. In **Chapter 6**, a low cost composite constituted by a polymer-based system with inserted manganese oxide is presented and the results of the hydrogen sorption tests are given. **Chapter 7** reports part of the activity carried out during a research period at the Helmholtz Zentrum Geesthacht (HZG), Germany. The experimental work there has been focused on the development of a hydrogen storage tank for a city car prototype. The results of the preliminary measurements for the hydrogen tank design, the preparation of the hydrogen storage material, as well as the results on the hydrogen tank constructed and tested in various configurations are reported.

Finally, an outlook and the concluding remarks on the work presented in the thesis are given in **Chapter 8**.

[1] A. Züttel, A. Borgshulte, L. Schlapbach, *Hydrogen as a future energy carrier*, Whiley-WCH (2008).

[2] DOE Office of Energy Efficiency and Renewable Energy Hydrogen, *Fuel Cells & Infrastructure Technologies Program Multi- Year Research, Development and Demonstration Plan*, available at: http:// www.eere.energy.gov/hydrogenandfuelcells/mypp.

Chapter 1

Hydrogen for a sustainable future

1.1 Introduction

The continuous growth of world population and the desire-need of the under-developed/developing Countries of reaching the economical and living standards of the industrial ones, creates the relentless increase of greenhouse gases (GHGs) emissions, in particular carbon dioxide (CO_2), in the atmosphere (**figure 1.1**).

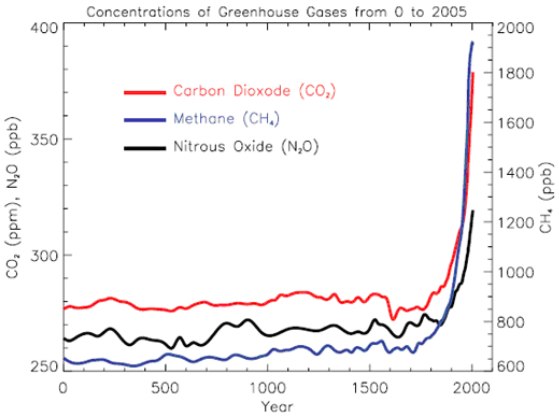

Figure 1.1 *GHGs concentrations in the atmosphere from the year 0 to the year 2000* ***[1.1]***.

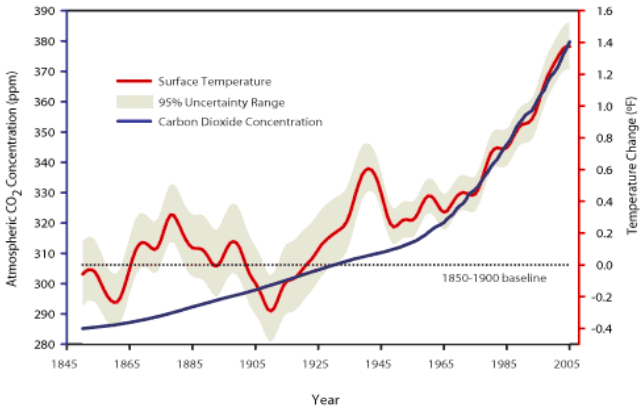

Figure 1.2 *Surface temperature and CO_2 concentration in the atmosphere from 1845 to 2005* ***[1.2]***.

Correspondingly to the industrial development, the concentration of CO_2 raised up during the last two centuries, reaching nowadays values above 380 ppmv (the most recent detection in August 2011 from the Mauna Loa Observatory **[1.3]** in Hawaii is already 390 ppmv!). It is estimated that the 30 % of the CO_2 emissions comes from transportation, thus caused by (only part of a) human activity. The correspondence between the global warming and the CO_2 concentration has been reported since the 19th century by Tyndall and Arrhenius **[1.4]** and has

a clear evidence from the trend of the last decades (**figure 1.2**). Ice cores drawn from Greenland, Antarctica, and tropical mountain glaciers show how throughout Earth's history the climate has varied, sometimes considerably; they also show that in the past large changes in climate have happened very quickly (tens of years), geologically-speaking **[1.5]**. However, past warming does not automatically mean that today's warming is also natural. Recent warming and sensible changes, such as oceans level and acidity rise, glaciers shrinking, extreme season temperatures, have been shown to be due to human industrialization processes. This implies that corrective measures are needed today in order to control the CO_2 emissions. **Figure 1.3** shows a prediction of the global temperature, land temperature and CO_2 concentration for the 21st century, based on the current emissions and just taking into account the possible feedback effect of the CO_2 rise on the ability of seas and forests to absorb and process the carbon dioxide. **[1.6]**.

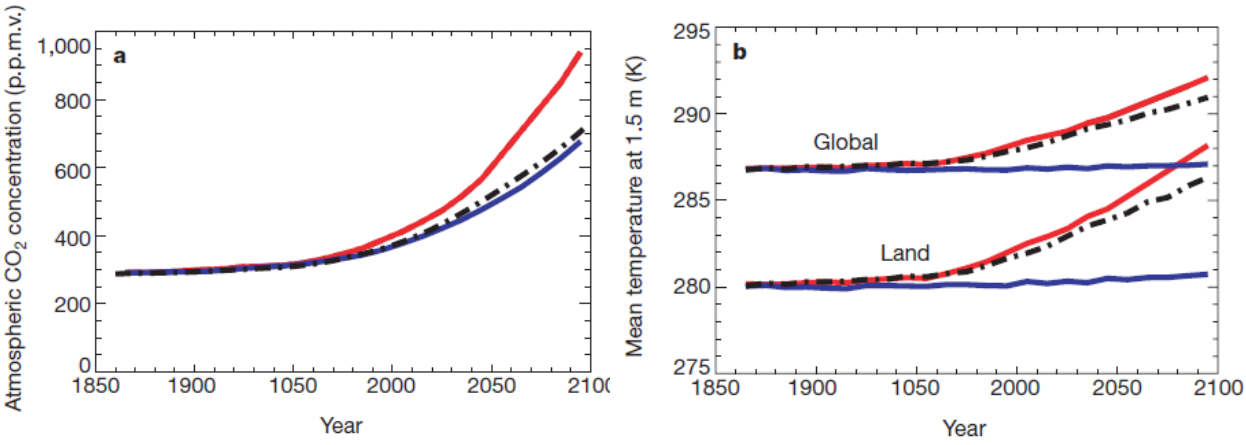

Figure 1.3 *Prediction of CO_2 concentration and global and land temperatures for the 21th century, with three different scenarios: simulation neglecting direct CO_2-induced climate changes (blue line), simulation with fixed (= not affected) vegetation (dot-dashed line), simulation with variable vegetation (red line).*

Actually, a big challenge that the world must face today is to allow the industrial and technological growth without causing environmental imbalances. What is more, together with the environmental question, the limited reserves of fossil fuels force the industrialized Countries to purse technologies of energy production and utilization from alterative and possibly renewable sources. As obvious, the whole question implies economical, political and social choices and consequences that will affect the world population already in the next and middle-term future.

The use of a clean fuel, producible by means of renewable energy sources and with the possibility to be transported and distributed safely and cheaply, would have a huge impact on this issue, creating possibilities of new and optimistic global scenarios. Hydrogen has been claimed to be the suitable substance to replace fossil fuel since the 1970s, and more recently the question of the hydrogen-based economy got a big echo as a new possible perspective for the world's development **[1.7]**. The potentiality of the use hydrogen for a sustainable future is discussed in the next paragraphs.

1.2 Hydrogen as clean fuel and energy carrier

1.2.1 Main physical properties of hydrogen

Hydrogen is the most abundant element in the universe, it is the fuel of the stars and, in particular, of our Sun. It is present in the Earth almost everywhere, in the largest amount bond with oxygen in the water and with carbon in the hydrocarbons, while only traces of hydrogen gas are present in the atmosphere.

Hydrogen does not have colour, flavour or colour and it is not toxic, but it is highly flammable. Its boiling point is -252.8 °C at pressure of 1 bar, thus it is a gas at room temperature. Except for helium, all other gases are solids at the temperature of liquid hydrogen. It is the lightest chemical element, with atomic mass of 1.00794 a.m.u.[(a)]. The hydrogen biatomic molecule (dihydrogen) is the smallest one, with a bond length of about 0.74 Å (just for comparison, the oxygen bi-atomic molecule has a diameter of around 3 Å) and a H-H bond energy of 432 kJ/mol. Other main physical properties of hydrogen are reported in **table 1.1.**

Table 1.1 *Some physical and chemical properties of the elemental and molecular hydrogen substance; where not specified, the reported values refers to IUPAC [(b)] Standard Temperature and Pressure (STP)* conditions **[1.8]**.

Elemental Hydrogen	
Electron configuration	1s1
Electronegativity (Pauling scale)	2.20
Ionization energies	1st: 1312.0 kJ·mol^{-1}
Isotopes	1H 99.985% 2H 0.015% 3H 0.015%

Molecular Hydrogen			
Critical point	-239.96 °C , 13.15 bar	Density at 0 °C, 1 bar	0.08988 g/dm^3
Triple point	-259.35 °C , 0.0704 bar	Liquid density at m.p.	0.070 g/cm^3
Melting point	-259.14 °C	Solid density at m.p.	0.0763 g/cm^3
Boiling point	-252.87 °C	Liquid density at b.p.	0.07099 g·cm^3
Heat of fusion	0.117 kJ·mol^{-1}	Liquid composition	100% Orto
Heat of vaporization	0.904 kJ·mol^{-1}	Gas composition	75% Orto, 25% Para
Molar heat capacity	28.836 J·mol^{-1}·K^{-1}	Crystal structure	hexagonal
Thermal conductivity	0.1805 W·m^{-1}·K^{-1}	Magnetic ordering	diamagnetic

(a) It is the acronym for atomic mass unit, used to indicate mass on an atomic or molecular scale. It is defined as one twelfth of the rest mass of an unbound neutral atom of ^{12}C in its nuclear and electronic ground state and it has a value of 1.660538921(73)×10^{-27} kg.

(b) International Union of Pure and Applied Chemistry (IUPAC), is an international, non-governmental and objective body for advance and use of chemical science for scientific purposes (http://www.iupac.org/).

1.2.2 Hydrogen as a fuel

Hydrogen is highly flammable: in air it burns in the wide range of concentration, 4-75 vol% and detonates in the range 18-59 vol%, even though detonation can occur only in small and confined spaces **[1.9]**. In **table 1.2** a comparison among the physical properties of some fuel is reported. It is evident how the heating value per mass unit of a fuel increases as the hydrogen content increases **[1.10]**; thus hydrogen itself is able to provide the highest combustion energy per mass unit. Hydrogen burns with a flame almost invisible during the daytime with a temperature up to 2045 °C. Although its dangerousness, some features of hydrogen reduce the risks during an accidental fire. Hydrogen is less flammable with respect to gasoline, with a autoignition temperature more than 250 °C higher than that of the gasoline **[1.11]**. Hydrogen gas is fifteen times lighter than air and it diffuses upwards more than five times faster than nitrogen (the nitrogen percentage in the air mixture is around 72%); for these reasons, when hydrogen burns, it is consumed very quickly and with flames always upwards. In addition, the thermal radiation of hydrogen flame has a low wavelength, thus easily absorbable by the atmosphere. Fuels, such as gasoline, diesel, LPG[(c)], natural gas, are heavier than hydrogen and need more time to be dispersed in the air, thus keeping the fire zone close for longer time. It has been experimentally demonstrated how a gasoline-fed car burns for 20-30 min, with respect to 1-2 min for an analogous hydrogen-fed car **[1.12]**: the low thermal radiation of the hydrogen flame reduces the possibility for neighbouring materials to go up in flames, thus reducing fire time and toxic emissions due to combustion.

Table 1.2 *Comparison among some physical properties of hydrogen and some other fuels.*

Fuel	Chemical composition (average)	Heat of combustion ($\Delta H_c°$)		Autoignition temperature at 1 atm [°C]	Flammability limits in air [%]
		Higher Heating Value (HHV)[(d)] [kJ/kg]	Lower Heating Value (LHV)[(d)] [kJ/kg]		
Coal (Anthracite)	C >91.5%, H>3.7%, O>2.5%, S~1.0%, others~1.3%	34.1	33.3	600	N.A.
Diesel	C~86.5%, H~13.2% , S~0.3%	45.9	43.0	210	1-8
Gasoline (n-octane)	$C_{16}H_{18}$	46.7	42.5	206	1-6
Propane	C_2H_6	48.9	45.8	470	2-10
Methane	CH_4	55.5	50.1	537	4-16
Hydrogen	H_2	141.9	120.1	400	4-75

[(c)] LPG is the acronym of Liquefied Petroleum Gas, a flammable gas mixture of light alkanes; its main component is propane (for this reason, sometimes the mixture is indicate as Liquefied Propane Gas) and it is used as a fuel in heating appliances and vehicles.

[(d)] The lower heating value corresponds to the heat provided by the combustion reaction with the produced water in the final state of the reaction (usually vapour); higher heating value is the total heat amount if also the heat obtained by the produced water condensation is considered.

The hydrogen combustion reaction with oxygen is the following:

$$H_2 + \tfrac{1}{2} O_2 \rightarrow H_2O \qquad \Delta H_c^\circ = 286 \text{ kJ/mol}_{H_2} = 141.9 \text{ kJ/kg} \qquad (1.1)$$

where water is the only product, together with heat. There is no production of pollutant substances, such as SO_x, NO_x, thin powders, CO, CO_2, typical of combustion processes with fossil fuels. Even though vapour is a greenhouse gas, it can be definitively considered not as a pollutant, if it is used to gain further energy by its condensation. However, usually a fuel is not burn in oxygen, but in air, which is much easier to provide and directly available in the Earth's atmosphere. In this case the combustion of hydrogen could produce traces of NO_x, due to the presence of nitrogen in the air mixture, if high temperatures are reached during the combustion process. In internal combustion engines (ICEs) or burners, hydrogen chemical energy is converted to thermal energy with the efficiency limitations related to a thermal machine, according to *Carnot*'s principle **[1.13]**. Then, if electrical or mechanical energy has to be produced, the efficiency of the further conversion energy steps should be considered. More energy can be obtained from the hydrogen by using a fuel cell, where the energy content of the fuel is converted directly to electrical energy **[1.14]**. **Figure 1.4** reports a schematic drawing of a hydrogen fuel cell. Two electrodes (anode and cathode) are separated by a membrane, but the presence of an electrolyte allows the migration of H^+ ions from the anode to the cathode. The involved electrochemical reactions are:

anode reaction (oxidation): $$H_2 \rightarrow 2\,H^+ + 2\,e^- \qquad (1.2)$$

cathode reaction (reduction): $$\tfrac{1}{2}\,O_2 + 2e^- + 2\,H^+ \rightarrow H_2O \qquad (1.3)$$

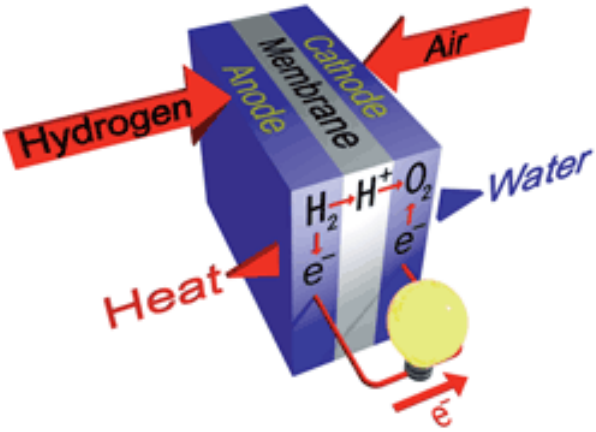

Figure 1.4 *Hydrogen-air fuel cell (image from Fuel Cell Today)*

The anode is the negative electrode, where the hydrogen molecules break and atoms get ionized, supplying electrons to the electrical circuit. At the cathode (positive electrode), the electrons coming from the electrical circuit are used to ionize the oxygen molecules present in the air mixture. The ionized hydrogen and oxygen atoms definitively form water molecules.

The overall cell-reaction is the hydrogen combustion reaction **(1.1)** reported above, which is the sum of the reactions occurring at the two fuel cell electrodes. The electrochemical conversion generates heat, which must be removed in order to keep the process temperature constant.

The electrochemical process is based on the reacting gases ionization. The bond between the two atoms of the hydrogen molecule is quite weak (432 kJ/mol), so that the gas can be easily ionized. Differently from hydrogen, other fuels, such as methane (CH_4) have stronger molecular bond so that part of the electrical potential produced by the fuel cell should be used to ionize the fuel gas (anodic overpotential) **[1.15]**. Some electrode overpotential is actually needed also in the hydrogen fuel cell, but at the cathode in this case, in order to ionize the oxidative oxygen gas, which has a stronger molecular bond than hydrogen. For this purpose noble metals (Pt in particular) based alloys and non-noble metals (other transition metals) oxides can be used as electrocataysts **[1.16]**. Although batteries and fuel cells have the same working principle, as both convert the chemical potential of some species in electrical power, fuel cells can run theoretically continuously if the fuel and the oxidative (i.e. combustive) agent are fed. Differently, the batteries duration is bound to the availability of the internal reacting species (i.e. the chemical charge), which consumes during the energy production up to depletion.

Fuel cells are used in assembled configurations called “stacks” **[1.17]**, where the cells are set in series by means of bipolar plates for the flow of gases (**figure 1.5**); for larger power supply systems, different stacks are assembled to form “modules”. With this modular configuration fuel cells systems can supply power in wide ranges with low efficiency variation.

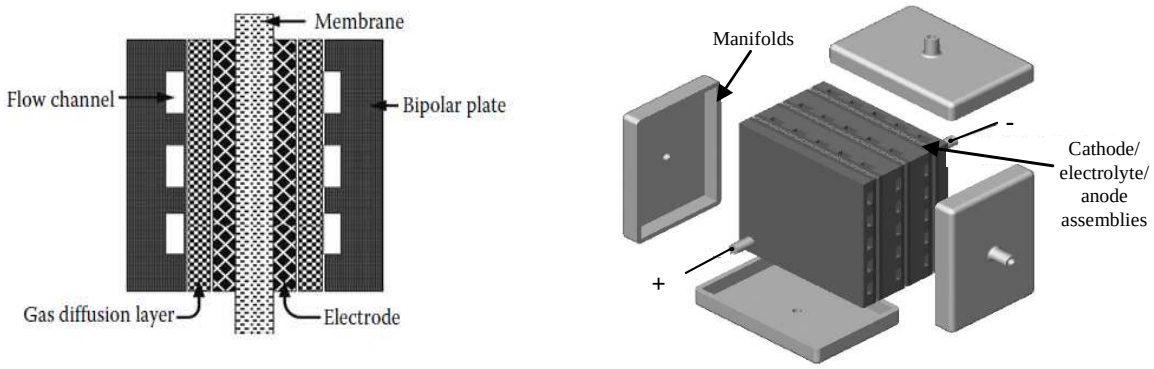

Figure 1.5 *Schematic drawings of a fuel cell cross-section with bipolar plates (left) and a fuel cells stack (right).*

The internal combustion engine of a car fed by fossil fuels converts about 20% of the fuel energy into used power; instead, typically, fuel cell power generation systems today in operation achieve 40% to 50% fuel-to-electricity efficiency. In combination with a turbine, fuel cell electrical efficiencies can exceed 60% and when cogeneration is used, fuel utilization can reach 85%. Different types of fuel cells are used, depending on the application, each type presenting advantages and drawbacks: on **table 1.3**, a schematic comparison among the most used types of fuel cells is shown **[1.18]**.

Even though the fuel cell technology is already at a mature stage for application, improvements, such as durability, reliability, material cost reduction (e.g. for the electrodes catalysts), efficiency, are still needed in order to increase the appetite for the hydrogen use as a fuel alternative to the fossil ones.

Table 1.3 *Comparison among the most used types of fuel cells* ***[1.18]***.

Type of Fuel Cell (FC) →	*Proton Exchange Membrane (PEMFC)*	*Direct Methanol (DMFC)*	*Alkaline (AFC)*	*Phosphoric Acid (PAFC)*	*Molten Carbonate (MCFC)*	*Solid Oxide (SOFC)*
temperature	50-100 ℃	50-100 ℃	60-120 ℃	150-220℃	600-700 ℃	650-1000℃
electrolyte	polymeric (poly-perflurosulfonic acid) membrane	polymeric (poly-perflurosulfonic acid) membrane	potassium hydroxide	phosphoric acid	potassium, sodium and lithium carbonate	doped zirconium oxide
electrical efficiency	53-58 % (transportation) 25-35 % (stationary)	20-25 %	60 %	32-38%	45-47 %	34-43 %
system output	< 1kW - 250 kW	< 1.5 kW	10 kW - 100 kW	50 kW - 1 MW	< 1kW - 1 MW	5 kW - 3 MW
applications	• back-up power • portable power • transportation • small distributed generation	• consumer goods (laptops, mobile phones, etc...)	• space • military	• industrial cogeneration • distributed generation	• industrial cogeneration • large distributed generation	• industrial cogeneration • large distributed generation
advantages	• Solid electrolyte reduces corrosion & electrolyte management problems • Low temperature • Quick start-up	• High energy storage • No reforming needed • Easy storage and transport	• High efficiency • Cathode reaction faster in alkaline electrolyte	• Higher overall efficiency with cogeneration • Increased tolerance to impurities in hydrogen	• High efficiency • Fuel flexibility • Can use a variety of catalysts • Suitable for cogeneration	• High efficiency • Fuel flexibility • Can use a variety of catalysts • Solid electrolyte reduces electrolyte management problems • Suitable for cogeneration
drawbacks	• Requires expensive catalysts • High sensitivity to fuel impurities • Waste heat at low temperature not suitable for cogeneration	• Low power output	• Expensive removal of CO_2 from fuel and air streams required to protect the electrolyte	• Requires expensive platinum catalysts • Low current and power • Large size/weight	• High temperature speeds corrosion and breakdown of cell components • Complex electrolyte management • Slow start-up	• High temperature enhances corrosion and breakdown of cell components • Slow start-up • Brittleness of ceramic electrolyte with thermal cycling

1.3 Hydrogen production

As already mentioned, hydrogen is abundant almost everywhere in the Earth, but bond to other elements; thus its potentiality in being used as a clean alternative fuel is strictly connected to the possibility to make it available as pure substance. In the following two subsections the main methods used today to produce hydrogen are briefly discussed.

1.3.1 Production from fossil fuels

The world hydrogen production is about 500 billions Nm^3 per year **[1.19]**; one third of this amount is produced as a by-product of industrial processes, such as hydrocarbons cracking or

chlorine-soda process. The main part of hydrogen is obtained from fossil sources through processes which produce the so-called "Syngas" (= synthesis gas), i.e. a mixture of carbon monoxide and hydrogen, fundamental intermediate for the industrial synthesis of important chemical commodities, such as ammonia and methanol. From the carbon monoxide of the syngas further hydrogen can be produced by the exothermic "water gas shift reaction":

$$CO + H_2O \rightarrow CO_2 + H_2 \qquad \Delta H° = -41 \text{ kJ/mol} \qquad (1.4)$$

The processes used for the production of the syngas, as a preliminary step for the final hydrogen production, are reported below **[1.20]**.

1) *Natural gas Steam Reforming or Methane Steam Reforming (SMR)*. With this method, half of the world hydrogen production and more than the 90% in U.S. is provided. The reaction to produce the syngas is:

$$CH_4 + H_2O \rightarrow \underbrace{CO + 3\,H_2}_{\text{Syngas}} \qquad \Delta H° = -192 \text{ kJ/mol} \qquad (1.5)$$

Methane (natural gas) reacts with vapour on a Ni catalyst at temperature of 700-800 °C. Even though the reaction is favoured by the low pressure (four moles of gases are produced from two moles of reacting gases), usually a pressure of 20-25 bar is used, both for this and the following water gas shift reaction. This is because both syngas mixture and hydrogen are more marketable as compressed gas. An excess of vapour is usually employed in order to prevent the side reaction of methane with some coke, formed during the process. If hydrocarbons heavier than methane are feed to the process, an adiabatic "prereformer" is used as previous stage reactor, to convert the heavier hydrocarbons to CH_4, CO, CO_2 and H_2, thus increasing the overall process efficiency, even with a larger variety of loads. The water gas shift reaction is then conducted at 130 °C.

2) *Hydrocarbons partial oxidation*. With this process hydrogen can be obtained from light hydrocarbons (e.g. methane or LGP mixture) and from heavier ones (e.g. heating oil) as well. The general reaction for the syngas production is:

$$C_nH_m + n/2\ O_2 \rightarrow \underbrace{n\,CO + m/2\,H_2}_{\text{Syngas}} \qquad \Delta H < 0 \qquad (1.6)$$

The partial oxidation is performed with air or, even better, oxygen. Catalyzed process occurs at 800 °C and atmospheric pressure; if no catalyst is used, temperature of 1200-1500 °C and pressure of 20-30 bar are needed. The water gas shift reaction completes the carbon oxidation, producing about 70% of the hydrogen of the overall process.

3) *Coal gasification*. The carbon contained in coal reacts with water in endothermic way; but also partial or full coal carbon oxidation in air or oxygen is performed in order to use the heat of the two exothermic reactions **(1.8)** and **(1.9)** for the whole process:

$$C + ½\ H_2O \rightarrow \underbrace{CO + H_2}_{\text{Syngas}} \qquad \Delta H° = -111 \text{ kJ/mol} \qquad (1.7)$$

$$\begin{cases} C + \frac{1}{2} O_2 \rightarrow CO & \Delta H° = -111 \text{ kJ/mol} \quad (1.8) \\ C + O_2 \rightarrow CO_2 & \Delta H° = -394 \text{ kJ/mol} \quad (1.9) \end{cases}$$

Further hydrogen is then obtained through the water gas shift reaction performed at 400-500 °C using iron and chrome catalysts.

As shown, the hydrogen production methods from fossil fuels give the greenhouses gases CO and CO_2 as co- or by-product, due to the presence of carbon in the initial load, as well as other pollutants, due to the high temperature of the processes and depending on the presence of sulfur in the initial load. Thus, from the environmental point of view, the production of hydrogen by these methods seems not to be an advantage. However, the huge amount of carbon mono- and di-oxide could be reduced as final emissions to the atmosphere, by performing carbon capture sequestration (CCS) inside particular ecosystems **[1.21]** or geological formations, especially the same wells from which the fossil fuels are extracted **[1.22]**. In this way, the use of hydrogen, even produced by fossil sources, could be an advantage if compared to the direct use of fossil fuels for transportation.

1.3.2 Production from renewable sources

Hydrogen can be produce in a sustainable way from water and biomass.

Biomass is renewable, abundant and easy to use. Over the life cycle, net CO_2 emission is nearly zero due to the photosynthesis of green plants **[1.23]**. The hydrogen production processes from biomass can be divided in two general categories: thermochemical and biological processes. The thermochemical processes are:

- combustion;
- pyrolysis;
- liquefaction;
- gasification;
- ethanol reforming;

while the biological processes include:

- direct biophotolysis;
- indirect biophotolysis;
- biological water-gas shift reaction;
- photo-fermentation;
- dark-fermentation.

All these processes still need research efforts and tests, even though at different levels, to become viable methods at the industrial scale. However, the availability of the different starting substances makes these processes very interesting; in particular, biological dark fermentation is a promising hydrogen production method for the commercial use in the future, while thermochemical pyrolysis and gasification are economically viable and will become competitive with the conventional natural gas reforming method.

Hydrogen can be obtained from water with different methods, among which the electrolysis is the easiest and economically convenient **[1.24]**. With this process the water molecule are divided in hydrogen and oxygen gases by mean of electricity, according to the electrochemical reaction:

$$H_2O + \text{electricity} \rightarrow H_2 + \tfrac{1}{2} O_2 \qquad (1.10)$$

As it can be noticed, this reaction is exactly the opposite of the hydrogen combustion **(1.1)**, occurring in the fuel cell, producing electricity. Thus, if the hydrogen obtained from water electrolysis is used in the fuel cells, again water is obtained and the "hydrogen cycle" is performed by using electricity. This cycle occurs in a sustainable way if the electricity needed for the electrolysis is obtained from renewable energy sources, such as solar (photovoltaic and thermodynamic), wind, waves, tides. However the cycle will become economically convenient once the cost of the energy production from renewable sources will decrease reaching a competitive level **[1.25]**. It must be underlined that the use of hydrogen as energy vector can give a fundamental contribution for the exploitation of these natural sources to produce electricity, due to their fickleness in both time and intensity. Some of the energy produced and not used can be chemically stored in hydrogen, which would return it in periods when the energy demand is higher than the energy production rate.

Besides electrolysis, other less efficient water-splitting methods can be used to produce hydrogen. Thermolysis is a water breaking processes using high temperatures, viz. 800-1000 °C for water dissociation; in order to reach this temperature, various energy sources are adopted, above all solar thermal energy. Water can be dissociated to produce hydrogen also by photoconversion, where solar energy is exploited in semiconductors, catalysts and membranes based systems to split the water molecule into hydrogen and oxygen **[1.26]**.

Combinations of the cited methods for hydrogen production from water are also used. For example, in thermochemical water splitting, the high temperatures of thermolysis can be reduced if catalysts and other reactive intermediates are used for the occurring chemical reactions to produce hydrogen from water **[1.27]**. Photoconversion can also be used to produce the electricity for the water electrolysis: in this case, a photoelectrochemical cell (PEC) is used **[1.28]**.

Power coming from nuclear plants can be used to feed electrolysis or thermolysis; the used fuel in this case is still a fossil type one, and, as it is known, its use has critical environmental (nuclear waste management) and safety (accidents in power plants) implications. At this regards, it must be considered that recently (2011) important countries of the European Union, such as Germany and Italy, decided not to proceed anymore with further investments on nuclear power generation and decreed the dismantling of the already existing plants.

1.4 Hydrogen distribution

Once produced and before being used, hydrogen must be delivered and distributed. As reported above (**table 1.2**), hydrogen has the highest heating value per mass unit among fuels; however the energy content in hydrogen is lower than other fuels, if compared per volumetric unit, because of the low density of gas and liquid hydrogen (**table 1.1**). This determinates higher costs for hydrogen transportation, compared to other gaseous fuels. Today pipelines are present only close to the places where hydrogen is produced or used. In US about 2000 km of hydrogen pipelines are already installed, which is a minimum amount if compared to the about 2 million of km of the natural gas national network **[1.29]**. There are technological aspects and problems that must be considered for the use of long pipelines for hydrogen delivery, such as: hydrogen potential embrittlement[(e)] in the base steel and in the welds used for pipelines construction, the costs of the hydrogen compression stations, the prevention of hydrogen leakage from pipelines and other containment materials. The building of wide reliable and suitable pipelines is strictly connected to the development of a hydrogen-based economy and needs huge initial investments **[1.30]**.

Hydrogen can also be compressed and liquefied in order to increase its density. However both the methods require not negligible energies to reach the desired conditions, i.e. pressure up to hundreds of bar or cryogenic temperatures (T_{eb} = -253 °C at 1 bar). Anyway, these are preferred options for long distances hydrogen delivery, if pipelines are absent. In particular, liquefied hydrogen is preferred for its higher density and transportation is performed in super-insulated cryogenic tank trucks or barges.

The approach of a more distributed production seems to be a more convenient alternative to big hydrogen production plants and long distance hydrogen delivery: in this way, hydrogen would be produced close to the end use places. However, centralized production assures lower production costs, due to the greater economies of scales. The comparison of the two alternatives and mixed scenarios of central/distributed hydrogen production are being considered to address the potential investments. In all the cases, there is always a big issue, which must be considered in order to assure continuous hydrogen availability for the users: the possibility to store the produced hydrogen (**figure 1.6**). The stored fuel would be available in stationary applications (houses, industries, refuelling stations, etc...) during demand peaks, and would be the tanks content for the hydrogen fed vehicles. This issue, which constitutes the topics of this thesis, is discussed in the next chapter.

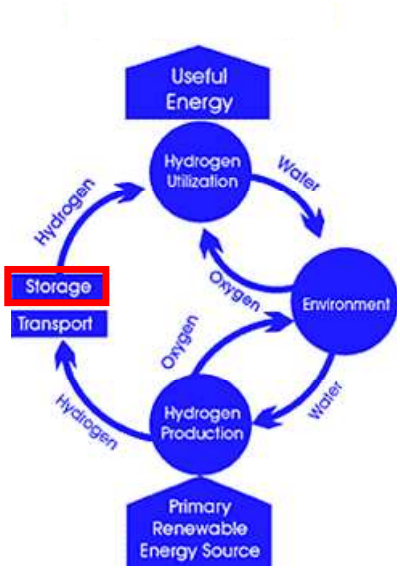

Figure 1.6 *The hydrogen use cycle **[1.31]**: in red frame the hydrogen storage, a fundamental step for the development of a hydrogen-based economy.*

(e) Hydrogen embrittlement consists in the hydrogen absorption inside the steel, causing loss of ductility and change of the material to brittle, with the exposure to cracks and thus sealing failure.

[1.1] P. Forster, V. Ramaswamy, P. Artaxo, T. Berntsen, R. Betts, D.W. Fahey, J. Haywood, J. Lean, D.C. Lowe, G. Myhre, J. Nganga, R. Prinn, G. Raga, M. Schulz and R. Van Dorland, *Changes in Atmospheric Constituents and in Radiative Forcing – In: - Climate Change 2007: The Physical Science Basis. Contribution of Working Group I to the Fourth Assessment Report of the Intergovernmental Panel on Climate Change* [Solomon, S., D. Qin, M. Manning, Z. Chen, M. Marquis, K.B. Averyt, M. Tignor and H.L. Miller (eds.)]. Cambridge University Press, Cambridge, United Kingdom and New York, NY, USA (2007).

[1.2] Center for Climate and Energy Solutions (C2ES): *Atmospheric Carbon Dioxide & Global Surface Temperature Trends*, available at: http://www.c2es.org/facts-figures/trends/co2-temp

[1.3] http://www.esrl.noaa.gov/gmd/obop/mlo/

[1.4] J. Upperbrink, *Arrhenius and Global Warming*, Science 272, 5265 (1996) 1122.

[1.5] National Research Council (NRC), *Surface Temperature Reconstructions For the Last 2,000 Years*, National Academy Press, Washington, DC (2006).

[1.6] P.M. Cox, R.A. Betts, C.D. Jones, S.A. Spall, I.J. Totterdell, *Acceleration of global warming due to carbon-cycle feedbacks in a coupled climate model*, Nature 408 (2000) 184-187.

[1.7] J. Rifkin, *The Hydrogen Economy: The creation of the Worldwide Energy Web and the Redistribution of Power on Earth*, Tarcher /Putnam (2002).

[1.8] A.D. McNaught, A. Wilkinson, *IUPAC Compendium of Chemical Terminology – 2nd Edition*, IUPAC (2006).

[1.9] *Initial Guidance for Using Hydrogen in Confined Spaces – Results from Inshyde*, "HYSAFE" Project - Deliverable D113 (2009).

[1.10] U. Bossel, *Well-to-wheel Studies, Heating Values, and the Energy Conservation Principle*, European Fuel Cells Forum (2003).

[1.11] S. McAllister, J.-Y. Chen, A.C. Fernandez-Pello, *Fundamentals of Combustion Processes*, Springer (2011).

[1.12] M.R. Swain, *Fuel Leak Simulation*, Proceedings of the 2001 DOE Hydrogen Program Review, NREL/CP-570-30535, pag. 679.

[1.13] T. Bose, P. Malbrunot, *Hydrogen: facing the energy challenges of the 21st century*, John Libbey Eurotext (2007).

[1.14] L. Carrette, K.A. Friedrich, U. Stimming, *Fuel Cells – Fundamentals and Applications*, Fuel Cells, 1 (2001) 5–39.

[1.15] N.M. Sammes, *Fuel cell technology: reaching towards commercialization*, Springer (2006).

[1.16] B. Viswanathan, C. Venkateswara Rao, U.V. Varadaraju, *On the search for non-noble metal based electrodes for oxygen reduction reaction*, Photo/Electrochemistry & Photobiology in the Environment, Energy and Fuel (2006), 43-101.

[1.17] V.S. Bagotsky, *Fuel Cells: Problems and Solutions*, John Wiley and Sons (2009).

[1.18] U.S. Departement of Energy Fuel Cells Technologies Program, *Comparison of Fuel Cell Technologies*, (2008).

[1.19] F. Mueller-Langer, E. Tzimas, M.Kaltschmitt, S. Peteves, *Techno-economic assessment of hydrogen production processes for the hydrogen economy for the short and medium term*, Int. J. Hydrogen Energy 32 (2007) 3797-3810.

[1.20] Y. Yürüm, *Hydrogen Energy System: Production and Utilization of Hydrogen and Future Aspects*, Kluwer Academic Publishers, in cooperation with NATO Scientific Affairs Division (1994).

[1.21] L. Olsson, J. Ardö, *Soil Carbon Sequestration in Degraded and Semiarid Agro-ecosystems – Perils and Potentials*, Ambio 31, 6 (2002) 471-477.

[1.22] H. Yang, Z. Xu. M. Fan, R. Gupta, R.B. Slimane, A.E. Bland, I. Wright, *Progress in carbon dioxide separation and capture: A review*, J. Environ. Sci. 20, 1 (2008) 14-27.

[1.23] M. Ni, D.Y.C. Leung, M.K.H. Leung, K.Sumathy, *An overview of hydrogen production from biomass*, Fuel Process. Technol. 87 (2006) 461-472.

[1.24] S.A. Grigoriev, V.I. Porembsky, V.N. Fateev, *Pure hydrogen production by PEM electrolysis for hydrogen energy*, Int. J. Hydrogen Energy (2006) 171-175.

[1.25] J. Turner, G. Svendrup, M.K. Mann, P.-C. Maness, B. Kroposki, M. Ghirardi, R.J. Evans, D. Blake, *Renewable hydrogen production*, Int. J. Hydrogen res. 32 (2008) 379-407.

[1.26] J.R. McKone, E.L. Warren, M.J. Bierman, S.W. Boettcher, B.S. Brunschwig, N.S. Lewis, H.B. Gray, *Evaluation of Pt, Ni, and Ni-Mo electrocatalysts for hydrogen evolution on crystalline Si electrodes*, Energy Environ. Sci., 2011, 4 (2011) 3573-3583.

[1.27] A. Steinfeld, *Solar hydrogen production via a two-step water-splitting thermochemical cycle based on Zn/ZnO redox reactions*, Int. J. Hydrogen Energy 27, 6 (2022) 611-619.

[1.28] O.K. Varghese, C.A. Grimes, *Appropriate strategies for determining the photoconversion efficiency of water photoelectrolysis cells: A review with examples using titania nanotube array photoanodes*, Sol. Energy Mater. Sol. Cells 92, 4 (2008) 374-384.

[1.29] U.S. Departement of Energy Fuel Cells Technologies Program, *Hydrogen Delivery,* (2010).

[1.30] G. Birgisson Esq., W. Lavarco Eqs., *An effective regulatory regime for transportation of hydrogen,* Int. J. Hydrogen Energy 29 (2004) 771-780.

[1.31] *Hydrogen Fuel Cells Car Now* http://www.hydrogencarsnow.com/hydrogen-atoms.htm.

Chapter 2

Methods for hydrogen storage

2.1 The problem of hydrogen storage

The possibility to store hydrogen in efficient and safe way would give a huge boost to the development of the hydrogen economy and would in fact lead to a clean revolution in transportation. Today hydrogen is stored mainly as compressed gas in high pressure containers or liquid hydrogen in cryogenic vessels. Both methods require high energy for compression and liquefaction, respectively, and present safety issues, due to the high pressure in the first case and to the high hydrogen volatility and flammability in the second one. Research is still focused on the improvement of the safety and the efficiency of these systems in order to allow spread applications. However, compressed and/or liquefied hydrogen systems have inherently limited efficiency and storage energy density, and for this reason, alternative methods are needed for suitable hydrogen storage systems. In the last decade increasing research efforts as well as public and private investments are being employed for the study of different systems as potential hydrogen storage candidates. The Department Of Energy (DOE) of United States of America periodically fixes the targets for suitable hydrogen storage systems, on the basis of the research progress. These targets refer to a driving range of 400-500 km for a light duty vehicle, for which 4-5 kg of hydrogen are needed to feed a PEM fuel cells powertrain onboard. In **table 2.1** the last official DOE's targets (2007) as well as the revised values after the 2011 interim update **[2.1]** are reported.

Table 2.1 *Technical system targets for onboard hydrogen storage for light duty vehicles.*

Storage Parameter	Units	2007 targets			2011 targets	
		2010	2015	Ultimate	2017	Ultimate
Energy Density						
System Gravimetric Capacity	kWh/kg	1,5	1,8	2,5	1,8	2,5
	kgH_2/kg	0,045	0,055	0,075	0,055	0,075
	wt%	4,5%	5,5%	7,5%	5,5%	7,5%
System Volumetric Capacity	kWh/L	0,9	1,3	2,3	1,3	2,3
	kgH_2/L	0,028	0,040	0,070	0,040	0,070
Durability/Operability						
Operating ambient temperature (stable performances)	°C	-30/50	-40/60	-40/60	-40/60	-40/60
Min/Max deliver temperature	°C	-40/85	-40/85	-40/85	-40/85	-40/85
Operational cycle life	cycles	1000	1500	1500	1500	1500
Min delivery pressure from storage system (FC = Fuel Cell, ICE = internal combustion engine)	bar (abs)	5 FC / 35 ICE	5 FC / 35 ICE	3 FC / 35 ICE	5 FC / 35 ICE	3 FC / 35 ICE
Max delivery pressure from storage system (FC = Fuel Cell, ICE = internal combustion engine)	bar (abs)	12 FC	12 FC	12 FC	12 FC / 35 ICE	12 FC / 35 ICE
Charging/Discharging Rates						
System fill time (5 kgH_2)	min	4,2	3,3	2,5	3,3	2,5
	kgH_2/min	1,2	1,5	2,0	1,5	2,0
Minimum flow rate	(g/s)/kW	0,02	0,02	0,02	0,02	0,02
Start time to full flow (20 °C)	s	5	5	5	5	5
Start time to full flow (-20 °C)	s	15	15	15	15	15
Transient response (at operating temp.) 10% - 90% and 90% - 0%	s	0,75	0,75	0,75	0,75	0,75

On the chart of **figure 2.1**, several different studied systems for hydrogen storage are located, referring to their gravimetric and volumetric capacities, and the areas corresponding to the last official 2007 DOE's targets for 2010 and 2015 are indicated.

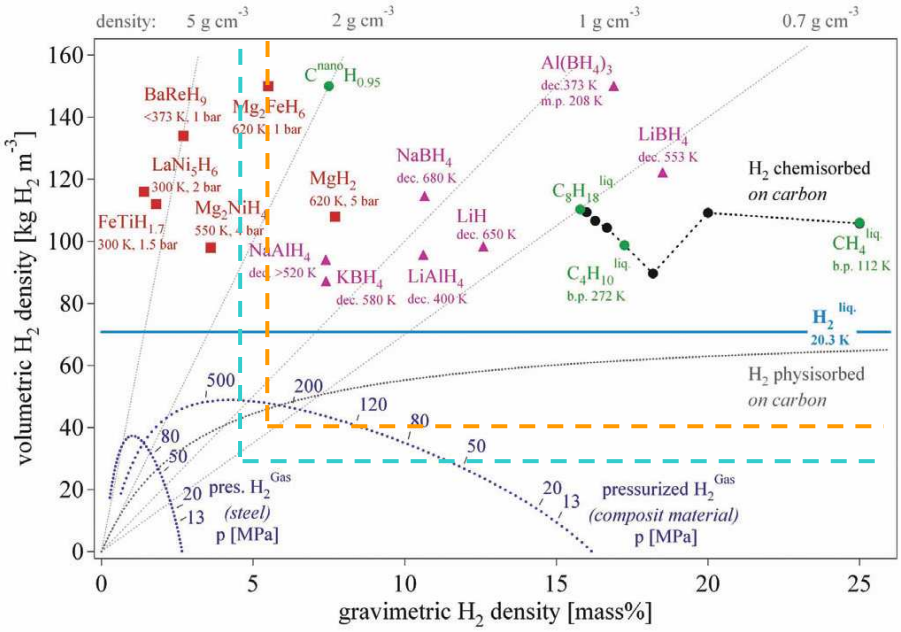

Figure 2.1 *Hydrogen storage densities for various systems. Source: Schlapbach and Züttel, Nature, 2001[2.2].*

As evident, there are several materials largely fulfil both gravimetric and volumetric capacity requirements, however for these materials some disadvantages should be overcome to make them a suitable solution, the serious one being the working temperature. Actually, there is still not any system able to reach all the desired targets, especially for vehicular application.

In the following sections both technologies mostly used today for hydrogen storage (compressed and liquid hydrogen), as well as the candidate systems and methods investigated as safer and more efficient alternatives, are presented.

2.1.1 Compressed hydrogen gas

Pressure vessels are used to store high pressure compressed hydrogen up to 800 bar, depending on the limits of authorization by the specific Country's law. The vessel body can be constituted by single metals or alloys (steel, aluminum, titanium) or lighter materials composites, e.g. glass fibres reinforced polymers (GFRPs) or carbon fibres reinforced polymers (CFRPs) surrounding a metal or plastic liner **[2.3]**. In any case, higher pressure containers need thicker walls so that an increase in volumetric hydrogen capacity corresponds to a lower gravimetric hydrogen density in the system. Moreover, at high density the volumetric behaviour of the hydrogen gas is far from the ideal gas and a doubling of the pressure corresponds to an increase of only 40-50% of the hydrogen amount. This determines, for each material, a maximum pressure value after which also the volumetric hydrogen density of the system decreases (**figure 2.1**). There are also examples of hybrid high pressure vessels partially filled with hydrogen storage materials, in order to increase the volumetric hydrogen density, despite a reduction of gravimetric hydrogen percentage **[2.4]**. Usually, high pressure vessels are constituted by cylinders, because this shape is the best compromise between volume occupancy and technical building reasons; however cylinders do not optimize the space inside a car, and this must be also take into account for the placement onboard.

Pressurized hydrogen can also be stored in glass (silica) microballoons (GMBs). The small (typically, up to 500 µm diameter) spheres are filled with hydrogen at high pressure (350-700 bar) and high temperature (> 300 °C) by permeation in high pressure vessels. Then they are cooled (residual hydrogen pressure inside is typically 200 bar) and transferred to a vessel, which will host them inside the car. The release of hydrogen from the sphere is then driven by the temperature increase. In this way, inherently safe low pressure hydrogen tank can be used with a demonstrated hydrogen capacity of 5.4 wt%. However these methods have specific drawbacks, such as: a) the need to recharge the spheres in separated high pressure and high temperature vessels, b) the slow lost of hydrogen from the microspheres occurring at room temperatures, c) the difficult management of hydrogen release-response at the needed temperatures, higher than 300 °C, also not compatible with PEM fuel cells, d) the breakage of spheres material, occurring after different charging/discharging cycles. Researchers are engaged in improving the spheres constituent material in order to reduce drawbacks and wall thickness **[2.5]**.

2.1.2 Liquid hydrogen

Hydrogen can be liquefied at -252 °C (21 K) at ambient pressure, and in any case, no liquid hydrogen is present above the critical temperature of -240 °C (33 K). This implies that, for safety reason, liquid hydrogen can be stored only in open containers: if refrigerating and insulating fail, the pressure in a close storage system could increase up to 10^4 bar at room temperature. For the liquefied hydrogen the gravimetric and volumetric densities are 100 wt% and 70 kgH_2/m^3, respectively (see **figure 2.1**); however, if all the cryogenic system is considered, typically the values decrease respectively to 7.5 wt% and 33 kgH_2/m^3, which are still interesting values for a hydrogen storage system. The big problem of this technology is the energetic efficiency. Liquid hydrogen is produced mainly by Joule-Thompson effect on pre-cooled hydrogen: differently from other gases, hydrogen warms upon expansion at room temperature, and its inversion temperature, under which cooling expansion occurs, is just -71 °C (202 K). In general, an energy lost of 30-40 % occurs during liquid hydrogen production. Hydrogen boil-off losses, as a result of heat leak from the cryogenic tank, must be also considered. These losses are function of size, shape (in particular surface-to-volume ratio) and thermal insulation of the container, with values up to 0.4 % of the stored liquid per day. The high energy amount needed to liquefy hydrogen, together with the boil-off losses limit the use of liquid hydrogen vessels to application where the fuel is consumed in short time and costs are not a primary issue (space, military). However, from the infrastructural point of view studies are in progress, comparing the energy loss connected with the use of liquid hydrogen with the advantages to easily transport it in reduced volumes also for long distances.

As applicative examples, Toyota **[2.6]** and Honda **[2.7]** produced cars with fuel cells fed by compressed hydrogen tanks. Liquid hydrogen tanks have been used for cars model by BMW **[2.8]**, city buses by Mercedes-Benz, while AeroVironment developed and tested the first Unmanned Aerial Vehicle (UAV). Companies such as Boeing, Lange Aviation, and the German Aerospace Center are testing liquid hydrogen tanks for manned and unmanned airplane. There are also examples of trucks fuelled by hydrogen in pressurized cryogenic vessel prototype, where hydrogen can be stored both in liquid or gaseous form **[2.9]**. In any case, the perplexity of people toward the safety of compressed and/or liquefied hydrogen tank is also a factor that should be taken into account in the view of vehicles equipping.

2.2 Hydrogen sorption

When a gas substance interacts with the surface of a condensed (i.e. liquid or solid) phase, a phenomenon of *physisorption* or *chemisorption* occurs. In the case of *physisorption*, weak intermolecular Van der Waals forces (deriving from fluctuation of charge distributions and responsible for the non-ideal behaviour of gases and for the vapours condensation) cause binding of the gas on the condensed material surface. In *chemisorption*, the involved forces are valence forces, analogous to those responsible for the formations of chemical compounds.

Both physisorption and chemisorption mechanisms can be represented by a one-dimensional diagram of potential energy vs the distance from the interacting surface (Lennard-Jones potential **[2.10]**), as reported in **figure 2.2**. Hydrogen can interact with the surface in molecular form or already as atoms before reaching the gas-condensed phase interface: the curves of the two cases are separated by the hydrogen molecule dissociation energy E_D (218 kJ/molH). Atomic hydrogen approaches and interacts with the surface up to a minimum energy value, corresponding to the overall chemisorption energy E_C (≈ -50 kJ/molH). Instead, in case of physorption, the interaction of molecular hydrogen with the surface is less intense and the system stabilizes with a physisorption energy, indicated with E_P. For hydrogen molecule, an increase of the potential energy is needed to come closer to the interacting surface; further approach can cause a change in the interaction and determine hydrogen dissociation after a certain potential energy barrier (intersection with the chemisorption curve). In this case, the hydrogen dissociation can be energetically favourable if the intersection is below the zero reference energy and the overall energy for the dissociation of hydrogen is E_{NA}; on the contrary, if the intersection is above the zero reference energy level, the overall energy E_A is required for the dissociation process.

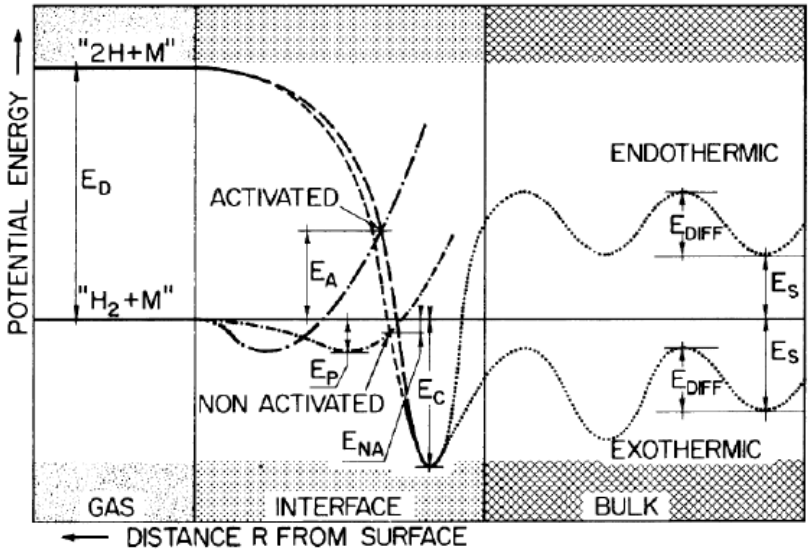

Figure 2.2 *One-dimensional Lennard-Jones potential curves for physisorption* (dashed line), *chemisorption (dotted-dashed line) and absorption (dotted line) mechanisms* ***[2.11]***.

When the process is limited to physisorption, once a monolayer of gas is deposited on the surface, the further approaching gas interacts with the first deposited layer. Thus, the energy for the deposition of the second and the further layers corresponds to the sublimation or vaporization heat of the gas substance and, consequently, at temperatures higher than the boiling point only a single layer can be deposited. Clearly, the amount of deposited gas in the first layer increases as the surface area increases; additionally, the energy of the physisorption process is enhanced by the presence of small size pores, due to the overlap of the attractive forces of the opposite walls on the gas substance. For this reason, materials with both high surface area and small pores size are preferred and synthesized. However, the estimation of

actual surface area and pore size becomes more difficult for very high surface area materials with pores of nanometric dimensions. The reliability of the measurements becomes highly dependent on the dimension of the molecule of the used probe gas and on the used methods, such as Langmuir isotherms **[2.12]** or Brunauer Emmett and Teller (BET) theory **[2.13]**.

Up to now, the interaction of the gas with the surface has been described. A further and more common distinction is done between the terms adsorption and absorption, adopted for a gas interacting with a condensed surface. The *adsorption* process is the enrichment of one or more components in the interfacial layer, so that the phenomenon is limited to the surface of the condensed material. On the contrary, *absorption* occurs when the overall phenomenon involves also the bulk of the condensed material. The general term *sorption* is used when neither adsorption or absorption phenomenon is specified; similarly the suffix –ate (*sorbate*) refers to the taken-up substance (i.e. the gas), while –ent (*sorbent*) refers to the sorbing substance (i.e. the condensed material). Ultimately, adsorption and absorption refer to the location of the sorbed species with respect o the sorbent, i.e. surface or bulk, respectively. Still referring to **figure 2.2**, after the chemisorption occurred and the minimum energy after hydrogen dissociation is reached, the system can evolve with the diffusion of atomic hydrogen from the stable superficial chemisorption sites into the bulk absorption sites: the overall feature of the process can be either endothermic or exothermic (the latter being the common case). The energy of the absorption sites is $\pm E_S$, and the net stabilization energy is E_{DIFF}.

Evidently, the exposed model describes an ideal case of a gas interacting with a clean surface, e.g. metal. In general, the real case is more variegated, for example with presence of oxides on the surface, which limits the interaction at interface and the diffusion of the atomic hydrogen inside the bulk material.

A particular method sometimes used to enhance the interaction between the hydrogen gas and a high specific area material used to store hydrogen is the *hydrogen spillover*. With this method, the high surface area material is used as a substrate and receives hydrogen, which has already interacted at the gas-solid interface with another material (e.g. a metal), put on the top of the substrate. The hydrogen transfer from the islands to the substrate is ensured by *linking bridges* between the substrate and the active material.

2.3 Hydrides

After chemisorption on the surface, the hydrogen atoms can jump to the undersurface layers and start diffusing inside the material's (typically a metal) bulk. In this case, absorption occurs and a new material forms, the *hydride*. Depending on the type of the created bond with hydrogen, the compound is classified as *ionic*, *metallic* (or *metal*), or *covalent hydride*. Metal hydrides are also-called interstitial hydrides, as the hydrogen occupies interstitial sites of the crystal lattice. For metal hydrides, the *pressure composition isotherm* (*PCI*) curves describe the hydride formation process (**figure 2.3)**. PCIs are thermodynamic curves, where each point

corresponds to the final concentration of hydrogen inside the material at a certain pressure and for the selected temperature. The region on the left side of the bell-shaped profile describes the state of a solid solution (α-phase) with hydrogen dissolved inside the metal, up to a limit H/M ratio usually less than 0.1 and with a corresponding expansion of the metal lattice of 2-3 Å per hydrogen atom **[2.14]**. For concentrations higher than 0.1 H/M the hydride phase (β-phase) starts nucleating and growing. If the increase of the hydride phase occurs at constant pressure, the region of the isotherm "inside the bell" shows a flat plateau. Once the hydride phase is completely formed, the material shows its usable maximum hydrogen capacity: after this value, a further increase in hydrogen concentration needs a strong increase of the pressure. The plateau region becomes shorter as the temperature of the isotherm increases, up to a final value T_c, above which α-phase and β-phase are not distinguishable anymore.

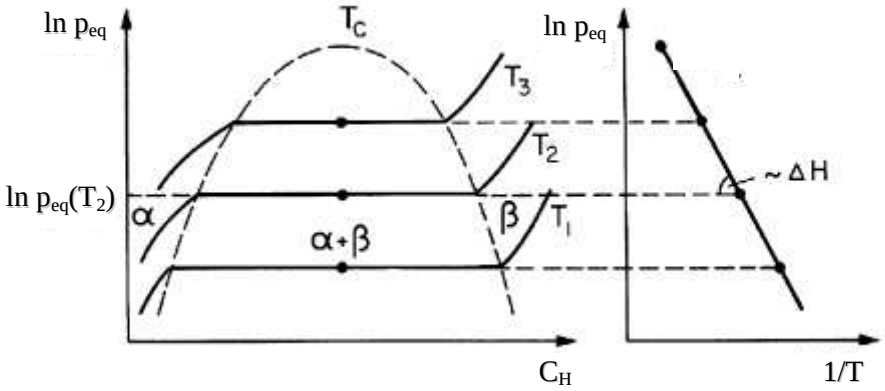

Figure 2.3 *Pressure Composition Isotherms (PCI) curves (left) and Van't Hoff plot (right) for the hydride formation* ***[2.15]****.*

2.3.1 Thermodynamics of hydrogen absorption and hydrides stability

The equilibrium between the solid solution α-phase and the hydride β-phase in presence of hydrogen gas pressure is given by the equality of the *Gibbs*' free energy to zero:

$$\Delta G = \Delta G^0 - RT\ln\frac{p_{eq}}{p^0_{eq}} = \Delta H^0 - T\Delta S^0 - RT\ln\frac{p_{eq}}{p^0_{eq}} = 0 \qquad (2.1)$$

$$\Rightarrow \quad \ln\frac{p_{eq}}{p^0_{eq}} = \frac{\Delta H^0}{RT} - \frac{\Delta S^0}{R} \qquad \textit{Van't Hoff} \text{ equation} \qquad (2.2)$$

The *Van't Hoff* equation represents a straight line in the coordinates 1/T and $\ln(p_{eq}/p^0_{eq})$, where ΔH°/R is the slope and -ΔS°/R is the intersection with y-axes. Thus, if PCI curves at different temperatures are acquired and equilibrium pressures measured, it is possible to obtain the *Van't Hoff* plot and hence calculate the hydride formation standard enthalpy (ΔH°) and standard entropy (ΔS°). As a first approximation, for an absorption process in which the initial hydrogen gas is included as atoms in the bulk of a solid phase, the standard entropy can be assumed equal to the opposite of the standard entropy of the hydrogen gas formation: $\Delta S° \approx - S°_{H_2} = -130$ J/K·molH_2. Considering reaction **(2.2)**, this implies that, to reach an equilibrium pressure of 1 bar at 300 K, the standard formation enthalpy ΔH° should be -39.2 kJ/molH_2. The heat exchange in reversible way during a physical/chemical process is given

by $\Delta Q = T \Delta S$; this implies that in a hydrogen absorption process the heat is released by the system to the environment, i.e. the process is exothermic. Reversely, hydrogen release from the hydride is an endothermic process and usually heat must be supplied to the system; this is not necessary if hydrogen release spontaneously occurs at room temperature and the environment itself can supply the needed heat. This is possible depending on the difference at room temperature between the hydride equilibrium pressure and the current pressure of the environment where hydrogen must be released (driving force). According to equation **(2.2)**, this difference depends mainly on the process enthalpy, i.e. on the stability of the hydride with respect to the dehydrogenated system. For the materials investigated as hydrogen storage candidates, typical reference parameters for their comparison are the equilibrium pressure at room temperature (25 °C) or, dually, the temperature corresponding to an equilibrium pressure of 1 bar, both depending on the absorption/desorption reaction enthalpy.

Some general rules of thumb can be considered for the hydrides stability, on the basis of the research results collected up to now.

In general, transition elements with electronegativity in the range 1.35-1.82 (Allen-Rochow scale **[2.16]**) do not form stable interstitial hydrides. Exceptions are vanadium (1.45), chromium (1.56), molybdenum (1.30), technetium (1.36). Referring to the crystal lattice, the stability of a hydrogen atom inside an interstitial site can be assumed as the weighted average of the stabilities of the corresponding binary hydrides of the neighbouring atoms.

The enthalpy of formation of binary ionic and metal hydrides can be calculated according to different computing models. Simpler methods, such as semiempirical models based on the rigid electronic band theory **[2.17]**, the Born-Haber calculations (more indicated for ionic-type hydrides), or the *Miedema*'s model (more suitable for metal hydrides) are attractive because of the little computation effort needed; however the level of their accuracy is limited and they usually tends to overestimate the reaction enthalpy. According to the *Miedema*'s model, the more stable the intermetallic compound is, the less stable the corresponding hydride is, and viceversa **[2.18]**. *Miedema*'s model has also been extended for the estimation of reaction enthalpy in ternary hydrides **[2.19]**. Other more complex computational approaches, such as Effective Medium Theory (EMT) and Density Functional Theory (DFT) as well as *ab initio* calculations are used in order to develop more accurate description models.

For covalent complex hydrides, such as tetrahydroborates (borohydrides) and tetrahydroalanates (alanates), the stability is found to increase linearly with the Pauling electronegativity of the cation element **[2.20]**.

In recent years the concept of hydride *destabilization* has been introduced by Vajo and Olson **[2.21]**. The idea is schematically described in **figure 2.4**. The high reaction enthalpy of a generic desorption process from hydride AH_2 toward the dehydrogenated phase A and H_2 gas can be reduced if another species B is introduced into the system, in a way that the AB_X compound forms, more stable than A. In these conditions, the system cycles between AH_2 and AB_X with a lower enthalpy reaction. Thus the introduction of the B component destabilizes the hydride with respect to the previous desorption process which forms A. The reduction of

the reaction enthalpy corresponds to a lower temperature for absorption/desorption equilibrium pressure of 1 bar, according to *Van't Hoff* equation **(2.2)**.

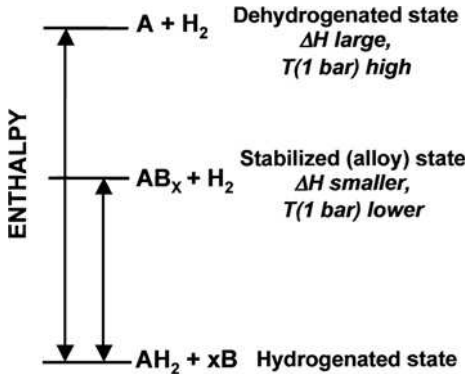

Figure 2.4 *The destabilization of a hydride (AH_2), due to the introduction of a different phase (B)* ***[2.21]***.

Following this idea, the Reactive Hydride Composite (RHC) approach was invented in 2004 independently by two different groups **[2.22]** **[2.23]**. According to this approach, two (or more) dehydrogenated compounds react during hydrogenation, forming one, two or more hydrides. The cycling process occurs with reaction enthalpies lower than those of the systems with the single hydrides.

Nanoscaling of the hydrides can also bring to a decrease in desorption energy. The high surface area available at nanoscale gives strong influence to interface energy contributions, such as surface tension, molar volume and excess surface energy, which can shift the equilibrium of the correspondent macroscopic system toward dehydrogenated species **[2.24]**. *Nanoconfinement* of hydrides can be achieved by using light materials nanoscaffolds, such as carbon aerogel, graphite, activated carbon, carbon fibers, silica. The main problems related to the use of these scaffolds are the additional weight with the consequent reduction of the overall hydrogen capacity of the systems, and the difficulties in maintaining the nanoconfinement after many hydrogen absorption/desorption cycles (durability of the nanostructure).

2.3.2 Kinetics

The kinetic of hydrogen absorption/desorption is related to different steps constituting the overall process, e.g. hydrogen molecular splitting or recombining and species mobility at the interacting surface, diffusion of hydrogen atoms and other species inside the bulk, phases nucleation and growth, etc… Each of these stages can strongly affect the whole process, and sometimes create high energy barrier for the process to proceed. This implies that, even though the thermodynamic is favourable, the process can be kinetically blocked. This fact can be sometimes misunderstood, and thermodynamic limitation can be erroneously attributed to the system. Actually, it can also happen that the thermodynamics of an absorption process can remain totally hidden if high temperatures are used in order to overcome the slow kinetics. In fact, according to the PCI curves, equilibrium pressure increases with increasing temperatures, and with the use of high temperature, the system can pass from a kinetic block to a thermodynamic one. For example, before the work of Bogdanović and Schwickardi **[2.25]** on

the effect of Ti-doping on hydrogen absorption properties of sodium alanate, few results on the thermodynamic of this system were obtained, due to the slow kinetics of the process and the difficulties to reach thermodynamic equilibrium conditions.

In general, the kinetics of an absorption process can be enhanced in different ways, besides with temperature. As in the just mentioned sample, catalysts addition can provide active sites for hydrogen dissociation at the gas/material interface and create diffusion paths from the surface to the bulk. For hydrogen storage by physorption, the catalyst is the active material supplying hydrogen to the high surface area material used as substrate (hydrogen spillover).

Grain boundaries constitute defects of the crystalline structure of the materials, where an intimate contact between different orientations on the same phase or between different phases can create enhanced diffusion paths for the hydrogen atoms.

Nanostructuring increases the surface area to volume ratio, thus increasing the active surface and shortening the diffusion path inside the bulk. Both alloying of hydrogen storage material with catalysts as well as generation of defects and particle size reduction can be achieved by the high energy ball milling technique, described in the next chapter, as materials preparation method.

Similar effects of mechanical milling, as regards particle size reduction and defects creation, can be determined also by hydrogen absorption/desorption cycling. The diffusion of hydrogen inside the material creates lattice expansion and cracks formation, generating also new clean surfaces. This effect is indicated as *decrepitation* and can be used as an alternative to mechanical milling, as discussed in **chapter 7**.

In the following subsections and in the next sections a brief overview on the main solid state hydrogen storage materials is given, on the basis of the state of art recently reported by Darren **[2.26]**.

2.3.3 Interstitial hydrides

The study of metallic hydrides began nearly 150 years ago, with the discovery of the hydrogen-absorbing properties of palladium by Thomas Graham **[2.27]**. Work beginning in the 1960s resulted in the later commercialisation of Nickel-Metal Hydride (Ni-MH) batteries, in which the negative electrode material forms an intermetallic hydride. For mobile storage applications, the gravimetric capacity of many interstitial hydrides is relatively low, but some of these compounds show remarkable and practical hydrogen absorption and desorption characteristics.

Intermetallic compounds are typically constituted by two metallic components, A and B, which tend to form AH_x and BH_y stable and an unstable hydrides, respectively. The resultant intermetallic hydride $A_mB_nH_z$, where m and n are integers and z is a real number, will then tend to have an enthalpy of formation, ΔH_{AB} intermediate between ΔH_A and ΔH_B. Varying the ratio n/m, ΔH_{AB} can be shifted in either direction. Generally, the components A and B can be fully or partially substituted by other elements of relatively similar size or chemistry. Families of intermetallic compounds forming hydrides are AB_5, A_2B_7, AB_3, AB_2, AB and A_2B compounds **[2.28]**. Some intermetallics, principally Mg-based compounds such as Mg_2Ni and

Mg_2Cu, form stoichiometric hydride complexes upon hydrogenation and can therefore be categorised as complex transition metal hydrides rather than interstitial intermetallic hydrides. Furthermore, there are interesting cases, such as the intermetallic compound $LaMg_2Ni$, that forms a mixed hybrid hydride ($LaMg_2NiH_7$), consisting of NiH_4 tetrahedra and interstitial H-ions.

AB_5 compounds. The archetypal of this group of intermetallic compounds forming hydrides is the $LaNi_5$ alloy. This substance has an enthalpy of formation of -15.7 kJ/molH and an enthalpy of decomposition of 15.1 kJ/molH **[2.29]** and shows a reversible gravimetric capacity around 1.3 wt% **[2.28]**. $LaNi_5$ and some other binary AB_5 compounds, such as $CaNi_5$, can be subjected to significant disproportionation and therefore lose their reversible capacity during hydrogen cycling. However, these compounds can be modified via partial substitution to reduce the disproportionation. The most effective substituent for this purpose for $LaNi_5$ is Sn, with a composition of $LaNi_{5-x}Sn_x$, where $x \approx 0.2$ **[2.30]**. For economic reasons, mischmetal (Mm), a naturally occurring mixture of rare earths, can be substituted to La as the A component. A elements are usually one or more of the lanthanides, or Ca, or Y and Zr, while the nature of the B elements is more various, such as Co, Al, Mn, Fe, Cu, Sn, Si and Ti, as either full or partial replacing components **[2.28]** **[2.31]**. More than 470 records for AB_5 compounds are currently listed in the Sandia National Laboratories (US) Metal Hydride Properties database **[2.32]**. It can be seen clearly that the gravimetric storage capacity of these materials is substantially lower than the current US DOE target for mobile hydrogen storage applications. However, the AB_5-based intermetallics show some remarkable cycling properties including excellent resistance to gaseous impurity contamination, good long term cycling stability and a high volumetric storage density, and they are therefore prime examples of practically effective reversible hydrogen storage materials.

AB_2 compounds. The A elements are typically from group 4 (Ti, Zr, Hf) or lanthanides (La, Ce, Pr, and so on), whereas the B element can be a transition or non-transition metal, with a preference for V, Cr, Mn and Fe. The Sandia database **[2.32]** currently includes more than 620 records for AB_2 compounds. Like the AB_5 compounds, they can show a range of hydriding properties depending on the elemental composition. A $Ti_{0.98}Zr_{0.02}Cr_{0.05}V_{0.43}Fe_{0.09}Mn_{1.5}$ alloy has been used as hydrogen fuel tank in a fleet of Daimler vans and automobiles **[2.33]**. This is an example of how AB_2- type alloys, along with the AB_5-based compounds, form conventional interstitial metallic hydrides that work well in real applications, by satisfying many of the required performance criteria.

AB Compounds. In comparison to the number of different AB_2 and AB_5 compositions reported in the literature, the number of AB compounds of interest for hydrogen storage is fairly limited and less than 250 records are currently listed in the Sandia database **[2.32]**. The most interesting compound of this class is TiFe, with a maximum hydrogen storage capacity of 1.86 wt% and a reversible value of 1.5 wt% **[2.28]**. It has an ordered Body-Centered Cubic (BCC) structure, and shows two distinct plateaus in its hydrogen absorption isotherm. Partial substitution of Fe with Mn and Ni can be used to modify the hydrogen absorption behaviour, by lowering the pressure of the first ambient temperature isotherm plateau, and therefore

stabilizing the hydride with respect to pure TiFe. With respect to AB_5 compounds, for AB_2 alloy the activation is more difficult and the sensitivity to gaseous impurities is significantly higher.

Solid solution alloys can be obtained by dissolving one or more hydrogen-absorbing metallic elements in another one, which shows interesting hydrogen storage properties too. Unlike the intermetallics compounds described above, these materials do not necessarily have stoichiometric or near-stoichiometric compositions. They can be formed from a number of host solvents, including Pd, Ti, Zr and V; thermodynamic data for many solid solution alloy hydride compositions have been given by Fukai **[2.34]**. Pd-based alloys suffer from low gravimetric capacities and the high cost of palladium, while Ti and Zr-based solid solutions tend to be too stable. Vanadium-based alloys have been found to possess favourable absorption properties, but vanadium is prohibitively expensive. The use of lower cost alloys, such as ferrovanadium, has shown to be an alternative and so Fe containing V-based solid solution alloys have been tested **[2.28]**. For example, Ti–V–Fe ($Ti_{43.5}V_{49.0}Fe_{7.5}$) and Ti–V–Cr–Mn alloys can approach 4 wt% of hydrogen capacities **[2.35]**, but they need elevated temperatures in the range 520–745 K to absorb/release hydrogen. The pressure-composition isotherms for these materials show two plateaus, of which only the higher pressure plateau can be considered for hydrogen storage applications. Therefore, in a practical pressure range, the reversible capacity is significantly lower than the maximum capacity quoted above at around 2.5 wt%. Solid solution alloys containing the so-called Laves-phase and BCC phases, such as Ti–V–Mn, Ti–V–Cr and Ti–V–Cr– Mn compounds, with different compositional variations can be found in literature **[2.36]**.

2.3.4 Promising modified binary hydrides

Among binary alkaline or alkaline-earth metal hydrides (usually ionic hydrides), the partially covalent magnesium hydride, MgH_2, is the one with the best hydrogen storage properties. Actually, MgH_2 has attracted by far the most attention as a potential storage material. Along with it, there are two other important binary hydrides that should also be mentioned: the covalent hydride AlH_3 and the metallic hydrides PdH_x.

Aluminum hydride, AlH_3 is of interest for hydrogen storage due to its high gravimetric storage capacity of 10.1 wt% **[2.37]**. However, it is effectively non-reversible, within a realistic hydrogen pressure range for a practical storage unit and therefore requires offboard regeneration, which is an unfavourable process both economically and energetically speaking **[2.38]**. AlH_3 is an example of a kinetically stabilized hydrogen storage material **[2.39]**, as it has high equilibrium hydrogen pressures at ambient temperature but in these conditions does not desorb appreciable amounts of hydrogen due to kinetic limitations.

Palladium hydrides, PdH_x. As mentioned above, palladium was the first transition metal element to be studied as hydrogen absorbing material **[2.28]**. It is actually poorly practical as a storage material because of its relatively high operating temperature and low gravimetric capacity, as well as its high cost. However, it holds some interest because of the results obtained on the nanoscale material **[2.40]** **[2.41]**. The results show interesting differences in

hydrogen absorption behaviour of the nanoscaled palladium compared to the bulk material and, for this reason, research is being actively pursued on.

Magnesium hydride, MgH_2. It is an attractive potential storage material because of its gravimetric capacity of 7.66 wt%. However, in addition to its high thermodynamic stability ($\Delta H \approx$ -75 kJ/molH_2), the kinetics of hydride formation and decomposition for the bulk material is too slow for practical purposes **[2.42]**. However, the kinetics has been improved significantly using mechanical milling both with and without catalytic additives, although the temperatures required for hydrogen desorption in these systems are still too high for practical applications. The most successful catalyst found to date appears to be Nb_2O_5 **[2.43]**. The reasons for the enhanced absorption and desorption rates are not yet understood and some authors suggest that additives induce further MgH_2 particles or grains size reduction during the milling process, rather than act catalytically **[2.44]**. Alternative methods of producing nanoscale magnesium have been reported, e.g. electrochemical synthesis **[2.45]**. In addition to the kinetic enhancement, there are some theoretical evidences that a reduced particle size can alter the thermodynamics of Mg-based systems. Ab-initio and density functional theory (DFT) calculations, reported by Wagemans et al. **[2.46]**, demonstrate that there may be some potential for nanoscale magnesium hydride to provide hydrogen storage capabilities in a practical temperature range, although further work in this area is needed.

2.3.5 Complex hydrides

In complex hydrides atomic hydrogen is bound covalently to a light element, forming a complex anion (i.e. $[AlH_4]^-$, $[NH]^{2-}$, $[NH_2]^-$, $[BH_4]^-$) that is ionically connected to a metallic cation. Hydrogen is then released by decomposition of the host material into two or more components.

Alanates. The most representative compound for this group of complex hydrides is sodium alanate, $NaAlH_4$. The decomposition process of this compound involves the following two steps:

$$3\ NaAlH_4 \rightarrow Na_3AlH_6 + 2\ Al + 3\ H_2 \qquad 3.73\ wt\% \qquad (2.3)$$

$$Na_3AlH_6 \rightarrow 3\ NaH + Al + \frac{3}{2}\ H_2 \qquad 5.93\ wt\% \qquad (2.4)$$

The reactions **(2.3)** and **(2.4)** occur approximately at 215 °C (488 K) and 250 °C (523 K), respectively. The overall amount of hydrogen released in the two steps is 7.5 wt%, referring to the initial $NaAlH_4$ compound. The further step of NaH dehydrogenation occurs above 425 °C (698 K), temperature too high for practical hydrogen storage purposes. According to the two steps above, two plateaus appears in the PCI curve at 210 °C, at 154 bar and 210 bar of hydrogen pressure, respectively **[2.47]**. As already mentioned, the work of Bogdanović and Schwickardi **[2.48]** constituted a breakthrough for the consideration of sodium alanate and for complex hydrides in general, as hydrogen storage candidates, as the addition of $TiCl_3$ on this system showed remarkable effect on the reversibility and the kinetics of the hydrogenation process. Subsequently, the doping method has been improved **[2.49]** and other chlorides have been identified as effective catalysts, such as $ScCl_3$, $CeCl_3$ and $PrCl_3$ **[2.50]**. With these

improvements, Ti-doped $NaAlH_4$ readily desorbs hydrogen at temperatures around 120 °C (373 K) and can be rehydrogenated at 170°C (443 K) at 150 bar of hydrogen pressure **[2.51]**. Other alanates are being studied for hydrogen storage, including $LiAlH_4$, $KAlH_4$, $Mg(AlH_4)_2$ and $Ca(AlH_4)_2$, with theoretical gravimetric hydrogen capacities reported in **table 2.2**.

Table 2.2 *Key properties of the main interesting alanates.*

Alanate	Theoretical capacity [H_2 wt%]	Desorption temperature [°C]
$LiAlH_4$	10.6	190
$NaAlH_4$	7.5	120
$KAlH_4$	5.7	300
$Mg(AlH_4)_2$	9.3	140
$Ca(AlH_4)_2$	7.8	> 230

Other mixed Al-coordinated compounds with alkali and alkali-earth metals have been reported in literature as potential candidates for solid state hydrogen storage. Examples are: Na_2LiAlH_6, K_2NaAlH_6, K_2LiAlH_6 and $LiMg(AlH_4)_3$ **[2.37]** **[2.52]** and others, with lower hydrogen capacities, such as Mg–Li–Al–H **[2.53]**, Mg–Ca–Al–H, Li–Ca–Al–H and Na–Ca–Al–H **[2.54]** composites, and Mg–Na–Al–H, Mg–K–Al–H and Ca–K–Al–H compounds **[2.55]**. In general, a better understanding of the Ti-doping role, still not completely clear, will hopefully guide to the improvements of hydrogen storage properties of these promising materials.

Nitrides, amides, imides. The Li–N–H system as a candidate for hydrogen storage was first investigated by Chen et al. **[2.56]**. Upon hydrogenation, the lithium nitride Li_3N forms lithium imide (Li_2NH), lithium amide ($LiNH_2$) and lithium nitride hydride (Li_4NH), but only the first two hydrogenated compounds take part to the reversible hydrogenation process. The dehydrogenation reactions are the following:

$$LiNH_2 + 2\,LiH \leftrightarrow Li_2NH + LiH + H_2 \qquad 5.19\ wt\% \qquad (2.5)$$

$$Li_2NH + LiH + H_2 \rightarrow Li_3N + 2\,H_2 \qquad 5.47\ wt\% \qquad (2.6)$$

The overall amount of hydrogen released in the two steps is 10.4 wt%, referring to the initial system $LiNH_2$ + 2 LiH. However, dehydrogenation of the imide requires high vacuum and temperatures above 600 K **[2.56]**, which are unsuitable conditions for applications. Differently, $TiCl_3$-catalyzed reaction between the amide and the amide is reversible under more moderate conditions, i.e. T_{des} = 150 -250 °C, p_{abs} = 30 bar **[2.57]** **[2.58]**, with a reversible capacity of 5.19 wt%. A number of other similar materials have been studied as hydrogen storage media, including the ternary $Mg(NH_2)_2$, $RbNH_2$, $CsNH_2$ compounds and Ca–N–H system, and the quaternary and higher systems Li–Ca–N–H, Li–Al–N–H, Na–Mg–N–H, Na–Ca–N–H, Mg–Ca–N–H and Li–Mg–Ca–N–H **[2.59]**. In general, together with high hydrogenation and dehydrogenation temperatures, other common drawbacks for Li–N–H systems are air or moisture sensitivity and the evolution of ammonia during the

dehydrogenation reaction **[2.60]**, the latter causing degradation of samples during long term cycling and poisoning for PEM fuel cell membranes **[2.61]**.

Borohydrides and ammonia borane. Complex hydrides with the highest gravimetric hydrogen capacities belong to this group. Lithium borohydride, $LiBH_4$, contains 18.5 wt% of hydrogen, and releases it through one of the following two reactions **[2.62]**:

$$LiBH_4 \leftrightarrow Li + B + 2\,H_2 \qquad 18.51\ wt\% \qquad (2.7)$$

$$LiBH_4 \leftrightarrow LiH + B + \frac{3}{2}\,H_2 \qquad 13.88\ wt\% \qquad (2.7')$$

However, the decomposition temperature is too high for practical purposes. According to Orimo et al. **[2.59]**, $LiBH_4$ releases three of its four hydrogen atoms upon melting at 280 °C (553 K), with an enthalpy of decomposition of -88.7 kJ/molH_2. LiH is very stable and its dehydrogenation occurs only above 727 °C (1000 K). Nevertheless, the dehydrogenation reaction of $LiBH_4$ is a reversible process, although rehydrogenation requires elevated pressures and temperatures of 350 bar at 600 °C (873 K) and 200 bar at 690 °C (963 K). Other interesting and studied alkali and alkaline-earth metals borohydrides are $NaBH_4$, KBH_4, $Mg(BH_4)_2$ and $Ca(BH_4)_2$, whose gravimetric hydrogen capacities are listed in **table 2.3**.

Table 2.3 *Key properties of the main interesting borohydrides.*

Borohydrides	Theoretical capacity [H_2 wt%]	Desorption temperature [°C]
$LiBH_4$	18.5	280
$NaBH_4$	10.6	350
KBH_4	7.4	125
$Mg(BH_4)_2$	14.9	320
$Ca(BH_4)_2$	11.6	260

However, full hydrogenation cannot be reversibly achieved at practical temperatures. Moreover, similarly to imide and amides, borohydrides are moisture sensitive and can desorb borane, which, even at trace levels, would cause storage capacity loss during cycling and fuel cell damage. According to the reactive hydride composites strategy, mentioned in **subsection 2.3.1**, destabilization of complex hydrides via mixing with other compounds has been attempted, in particular concerning $LiBH_4$with additives such as hydrides (MgH_2), magnesium salts (MgF_2, MgS_2 and $MgSe_2$), elemental metals (Al), alloys, oxides (TiO_2) and carbon. For complex hydrides in general, this approach is being intensely considered.

Along with the cited borohydrides another class of boron-complexes is the one of ammonia borane-based compounds NH_xBH_x, being x an integer from 1 to 4. These materials are sometimes indicated as *thermal hydrides* **[2.63]**. For these compounds, as x decreases from 4 to 1, the theoretical hydrogen storage densities goes from 6.1 to 7.2 wt%, and the temperature of decomposition toward the corresponding lighter borane (x-1) goes from less that 25 °C to more than 500 °C. For example, for x = 4 is:

$$NH_4BH_4 \rightarrow NH_3BH_3 + H_2 \qquad 6.13\ wt\% \qquad (2.8)$$

with a decomposition temperature lower than 25 °C. The problems for ammonia boranes are the irreversibility of the desorption reactions (offboard regeneration is needed), the high hydrogen decomposition temperatures as x increases, and, of course, the presence of borane together with H_2 gas as decomposition products, which would cause PEM fuel cells poisoning.

Complex transition metal hydrides. These are mainly complexes of magnesium with transition metals, e.g. Mg_2FeH_6, Mg_2NiH_4, Mg_3MnH_7, and Mg_2CoH_5 **[2.65]**. For hydrogen storage applications, this class of compounds suffers from the same problems as the other complex hydrides described above, namely the high absorption and desorption temperatures. Mg_2NiH_4 is probably the material in this group more studied so far as a candidate for hydrogen storage. It has a gravimetric hydrogen capacity of 3.6 wt%, an enthalpy of formation of -32.3 kJ/molH and requires temperatures above 247 °C (520) K for hydrogen desorption, and still higher temperatures for absorption. The found reduction of desorption temperatures by ball milling corresponds to a reduction of the storage capacity to 1.6 wt% **[2.66]**.

Figure 2.5 reports the *Van't Hoff* plots of some of the species cited in this section, belonging to intermetallic and complex hydrides. A rough comparison of their relative thermodynamic stability can be made by comparing the slope of the lines, which represent the hydriding process enthalpy, according to reaction **(2.2)**.

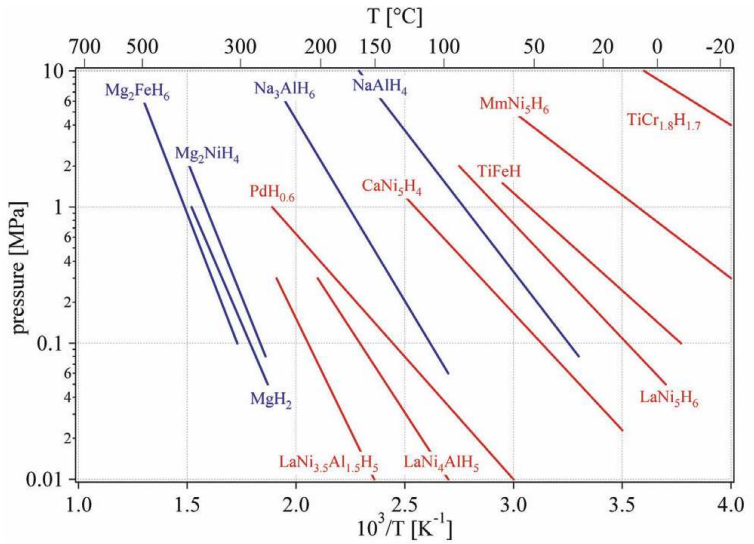

Figure 2.5 *Van't Hoff plots of some intermetallic and complex hydrides* ***[2.2]***.

2.4 High surface area materials

Differently from the hydrides previously presented, which store atomic hydrogen inside their crystal lattice, the materials reported in this section host molecular hydrogen on their surface by adsorption. Thus, for this material, the surface area extent and the amount and size of the pores are the key features. According to the current IUPAC classification scheme **[2.63]**, pores can be divided by size into three categories: *micropores*, of dimensions below 2 nm, *mesopores*, between 2 and 50 nm, and *macropores*, greater than 50 nm. The porous materials

being considered for physisorbed molecular hydrogen storage are predominantly microporous. They can also be classified as ultramicroporous, with pore dimensions less than 0.7 nm, close to the size of a single hydrogen molecule. At these length scales the adsorption potentials of the opposing pore walls overlap, which significantly increases the density of the adsorbed hydrogen, compared to the gas phase, at any given temperature and pressure. In general, for adsorption process of a gas on a solid surface, the amount of the adsorbate is a function of the partial pressure in the gas bulk phase. The measurement of the amount of gas adsorbed over a range of partial pressures at constant temperature gives an adsorption isotherm. Many different types of isotherms have been observed in the literature, but a general qualitative classification by IUPAC indicates six main types of adsorption isotherms, as reported in **figure 2.6**.

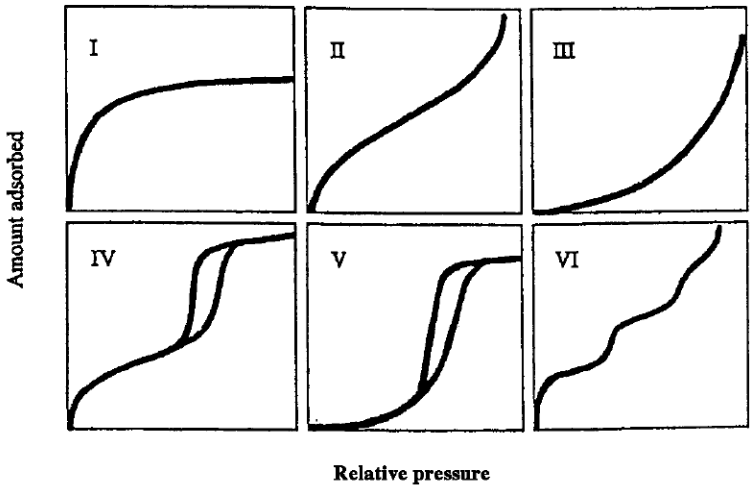

Figure 2.6 *The IUPAC classification for adsorption isotherms* ***[2.63]***.

Hydrogen adsorption by microporous materials invariably gives type I (described by Langmuir) isotherms. In general, the kinetics of hydrogen adsorption by microporous materials are very rapid, which is practically advantageous for hydrogen storage, but low temperatures are required to achieve significant capacities at useful storage pressures. Low temperature storage requires cooling, which inevitably adds to the weight of a storage unit and diminishes the energetic efficiency of the systems. The hydrogen adsorption capacity of microporous materials synthesized and studied up to now is too low for practical use. In particular, the low volumetric hydrogen density should not be neglected, even for future possible system with satisfying gravimetric hydrogen capacity. In order to develop suitable systems, the aim is to enhance the interaction of hydrogen with the constituting materials.

2.4.1 Carbon structures

Different types of microporous carbon structures have attracted interest for hydrogen storage, including *activated carbons*, *carbon nanotubes* and *carbon nanofibres* and, more recently, *templated carbons*. Carbon has a low molar mass, it is chemically stable, it can be synthesised in a number of different forms, and produced in large amounts with relatively low costs.

Activated carbon. It is a porous form of carbon that can be synthesised via both chemical and physical activation methods. Depending on the method and the raw material, the resultant carbon will have a specific, although not necessarily clearly defined, pore structure with a wide size distribution. This is in contrast to the crystalline adsorbents, such as the zeolites or Metal-Organic Frameworks (MOFs), which have a well defined pore size and pore geometry. Carbons are also challenging to be characterised accurately, as demonstrated by the variability in the results of a recent interlaboratory study **[2.67]**. As a reference value, gravimetric storage capacities of 5.5 wt% at 77 K has been recently founded by Yürüm et al. **[2.68]**. In addition to the experimental characterisation difficulties, modelling work on these materials is significantly limited by the lack of knowledge regarding their microstructure, which is difficult to be characterised, due to the fact that activated carbons are X-ray and neutron amorphous.

Carbon nanotubes (CNTs). These are cylindrical nanostructures formed from rolls of graphene. They can have diameters of 0.7 nm up to several nanometres and form single and multi-walled (i.e. concentric) tubes that form close-packed bundles. In a work of 1997 **[2.69]**, potential room temperature storage capacities of 5–10 wt% was reported, a value derived from a rather optimistic extrapolation of thermal desorption data. Measured on a sample consisting of an estimated 0.1–0.2 wt% of nanotubes (the remainder of the sample was uncharacterised soot). The high temperature desorption peak claimed to indicate the ambient temperature storage capabilities of the nanotube sample was later shown by Hirscher et al. **[2.70]** to be due to metal nanoparticles deposited during an ultrasonic purification process. Although modelling work has predicted the possibility of relatively high storage capacities in nanotube structures, the reported values are no greater than those for activated carbons and it therefore appears that they offer no significant advantage over other forms of carbon, which can be considerably easier to synthesise in large quantities.

Carbon nanofibres. They consist of graphene layers, stacked together in various orientations with respect to the axis of the fibre, including parallel and perpendicular, as well as intermediately angled (so-called *herringbone*) configurations. In a work of 1998 **[2.71]**, incredibly high hydrogen capacities for carbon nanofibres of up to 67 wt% were claimed. This hydrogen density corresponds to an H/C atomic ratio of around 24, indicating that the measured capacities were significantly overestimated. Subsequent studies of both nanotubes and nanofibres produced a wide range of values, none of which substantiated these initial claims, and an interesting controversy developed **[2.72]**. Although this issue has not yet been resolved completely, carbon nanotubes and carbon nanofibres, as well as other carbon nanostructures, such as fullerenes and carbon nanohorns seem not to be resolutive for the problem of hydrogen storage.

Templated carbons. These are a form of microporous or mesoporous carbon, typically synthesised by introducing a carbon precursor, such as sucrose or acetonitrile, into the pores of an inorganic template. Carbonisation and the subsequent removal of the template results in a pore structure, that is relatively well defined compared to activated carbon. There have been a number of studies on these materials with the largest capacity reported to date being 6.9

wt% for a zeolite-templated carbon at 77 K and 20 bar **[2.73]**. Unlike activated carbons, these materials show evidence of microstructural ordering at X-ray diffraction measurements.

2.4.2 Organic and inorganic nanotubes

Along with carbon, many other organic and inorganic materials are used to synthesize nanotubes, such as: boron nitride (BN), titanium sulfide (TiS_2), molybdenum sulfide (MoS_2), titanium oxide (TiO_2), tungsten carbide (WC), silicon and silicon carbide (SC). In general, the hydrogen sorption properties of some of these materials appear very interesting, e.g. hydrogen capacity of 4.2 wt% has been reported for collapsed BN nanotubes at 10 MPa and ambient temperature **[2.74]**. Moreover, the ability of some multiwalled nanotubes to intercalate other species **[2.75]** provides a possible proposed mechanism that could allow significant amounts of hydrogen to be stored at practical temperatures. However, the suitability of these nanostructured materials for a large scale application, such as automotive transportation, remains an open question.

2.4.3 Zeolites

Zeolites are microporous aluminosilicates formed from AlO_4 and SiO_4 tetrahedra. They have a range of practical applications that exploit their ion exchange, molecular sieving and catalytic properties. The term zeolite is often used to describe also compounds with similar structures, that are formed by elements other than Al and Si, including P, Ga, Ge, B and Be, but these materials are also known as *zeotypes*. These materials form a variety of different structures, all with crystalline nature, which gives them uniform cavities and channels in the microporous regime, with high specific surface areas and large pore volumes. Nevertheless, the hydrogen storage capacities reported in the literature have, to date, been fairly low. Vitillo et al. **[2.76]** tabulated a number of the experimentally determined hydrogen uptakes, with the highest reported value of 1.81 wt% at 77 K or above. More recently, a hydrogen storage value of 2.55 wt% has been reported for Na-X at 77 K and 40 bar **[2.77]**. Theoretical calculations an simulations indicate possible hydrogen storage capacities around 4.6 wt%, which are still low with comparison to the challenging US DOE storage system targets. Similarly to carbons, zeolites can be easily produced at industrial scale. Moreover, among microporous adsorbent material, zeolites have some significant practical advantages. They possess high thermal stability in comparison to metal-organic frameworks and organic polymers. Their crystalline nature allows easy characterisation and they have a well defined and understood pore size in comparison with activated carbon. For this reason, they are considered as model systems for the further investigation of the interaction of hydrogen with microporous materials.

2.4.4 Metal-Organic Frameworks (MOFs)

Metal-Organic Frameworks (MOFs) are crystalline inorganic-organic hybrid solids consisting of metal ions or clusters linked by organic bridges. The archetypal MOF is Zn4O(bdc), where bdc stands for 1,4-benzenedicarboxylate, which is commonly known as either MOF-5 or IRMOF-1. This material consists of zincoxide clusters joined by benzene

linkers. The acronyms used to indicate the MOFs do not follow any particular pattern but tend to refer to either the material type or the researchers' institution. Hundreds of different MOFs have been studied for their hydrogen adsorption properties. Tabulated data compiled by Thomas **[2.78]** indicate maximum hydrogen uptakes at 77 K in the range 1.0-7.5 wt%, however, usually, values are close to 1-1.5 wt% when measurements conditions approach ambient temperature and pressure. An interesting feature of MOFs is the presence of *exposed metals* in the pores, which could enhance the hydrogen-surface interaction and thus catalyse the hydrogen uptake. This aspect offers the promise of developing MOFs with much improved storage properties. Another interesting aspect is the so-called *framework flexibility*, for which MOFs can give hysteresis, unusual for the physisorption process, with hydrogen release pressures higher than adsorption ones. MOFs hold greater promise as potential storage media than zeolites, as the reported gravimetric capacities are significantly higher and the unique features, such as structural flexibility and exposed metal sites, give them more potential for future development. However, these materials tend to be less robust than zeolites and microporous carbons, because they exhibit lower thermal stability. Nevertheless, their commercialisation is already underway, principally by *BASF* who market a series of framework materials under the trade name *Basolite*^{TM}, demonstrating that practical application and use of these materials on an industrial scale is clearly feasible.

2.4.5 Organic polymers

There are three main classes of microporous organic polymers that have emerged recently as potential candidates for adsorptive hydrogen storage: *polymers of intrinsic microporosity* (PIMs), *hypercrosslinked polymers* (HCPs) and *covalent organic frameworks* (COFs) **[2.79]**. Similarly to MOFs and zeolites, COFs are crystalline, whereas PIMs and HCPs, similarly to activated carbon, have a disordered structure and cannot be characterised by X-ray and neutron diffraction. PIMs are rigid and contorted macromolecules, unable to pack space efficiently, thus forming a microporous network with high BET surface areas in the range 500–1100 m^2/g **[2.80]**. HCPs derive a similarly high degree of microporosity, and hence high BET surface areas, from a high density of crosslinks, the covalent chemical bonds that occur between macromolecules in polymeric materials **[2.81]**. COFs are instead crystalline networks, formed exclusively from the light elements H, B, C, O and Si, which are linked by strong covalent bonds **[2.82]**. A rough comparison among the three types of organic polymers, indicates, at 77 K and pressure in the region of 90-150 bar, a hydrogen capacities around 3 wt% for PIMs and HCPs, whereas for COFs values 2.5 times higher have been measured and impressive values up to 18.9 wt% have been obtained by simulations **[2.82]**.

In addition to PIMs, HCPs and COFs, the hydrogen adsorption behaviour of a number of other organic polymers have been reported in the literature. Early results, indicating high hydrogen uptake by HCL-treated conducting polymers, polyaniline and polypyrrole, were not successfully reproduced by other researchers **[2.83]**. Although the uptakes of the investigated polymers are not outstanding so far, these systems are attractive as potential storage media due to the light elements from which they are formed, and the easiness in synthesising. One

disadvantage in comparison to other microporous media is their relatively low thermal stability, which means that care must be taken not to induce thermal decomposition during the degassing process.

2.5 Other systems for hydrogen storage

Other systems are being investigated as alternative candidates for hydrogen storage purpose; however, with comparison to the results already obtained for hydrides and the high surface materials cited above, investigation on these systems is in general at a still earlier stage. Here below these further alternatives **[2.63]** are briefly presented.

2.5.1 Clathrates

These are inclusion compounds or cage structures formed in hydrogen-bonded networks of water. They have long been known due to their occurrence in natural gas and oil pipelines. The guest molecules can include species such as methane, nitrogen, carbon dioxide and argon, as well hydrogen. Although pure hydrogen clathrate hydrates are stable only at high pressures or low temperatures, a recent work has shown that they can be stabilized under near-ambient conditions, by using an organic promoter such as tetrahydrofuran (THF) **[2.84]**. There are three clathrate hydrate structures, namely sI, sII and sH, and the latter two have been studied for their hydrogen storage properties. A potential hydrogen storage capacity of 1 wt% for sII-type clathrates has been confirmed after a first indication of 4 wt%. **[2.85]**. Recently, hydrogen storage in the sH-type phase has been proposed, with estimated capacities in the region of 1.4 wt% **[2.86]**.

2.5.2 Ionic liquids

These liquids are composed of cations and anions and melt at or below 100 °C (373 K) **[2.87]**. Their negligible vapour pressure makes them environmentally friendly with respect to the volatile organic solvents used in many industrial and chemical processes. Stracke et al. **[2.88]** recently reported the potential of imidazolium ionic liquids for hydrogen storage, with a volumetric hydrogen capacity of up to 30 g L^{-1}. However, the dehydrogenation temperature of the Pd/C-catalysed material was in the region 230 to 300 °C (503 to 573 K) and the hydrogenation time was approximately 100 hours. These performances are not encouraging, but refers to only one of more than a million simple ionic liquids, and many more binary and ternary ones **[2.87]**.

2.5.3 $NaBH_4$ solutions

$NaBH_4$ aqueous solutions can be used as a liquid hydrogen storage medium. The catalytic hydrolysis reaction is:

$$NaBH_{4\ (l)} + 2\ H_2O_{\ (l)} \rightarrow 4\ H_{2\ (g)} + NaBO_{2\ (s)} \qquad 10.92\ wt\% \qquad (2.9)$$

The main advantage with using $NaBH_4$ solutions is that they allows safe and controllable onboard generation of H_2. The main disadvantage is that the reaction product $NaBO_2$ must be regenerated back to $NaBH_4$ offboard. Although the use of $NaBH_4$ solutions in vehicles may be prohibitive due to high regeneration costs (should be reduced from present 50 USD/kg to < 1 USD/kg **[2.63]**), there do exist few commercial companies (Millennium Cell - USA and MERIT - Japan) that promote this technology, usable for portable and stationary applications.

2.5.4 Rechargeable organic liquids

Some organic liquids can also be used to indirectly store hydrogen in liquid form. Once the hydrogen is released, they must be regenerated offboard. One example of a rechargeable organic liquid process is the dehydrogenation of methylcyclohexane (C_7H_{14}) to toluene (C_7H_8):

$$C_7H_{14\ (l)} \rightarrow C_7H_{8\ (l)} + 3\ H_{2\ (g)} \qquad 6.16\ wt\% \qquad (2.10)$$

The ideal reaction **(2.10)** yields a gravimetric and volumetric H_2 energy storage density of 6.2 wt.% and 43 kg H_2/m^3, respectively. As for the methylcicloexane, typically the organic liquids involved in these processes are hazardous materials, as they react with oxidants in explosive ways. This means that it is necessary to perform detailed safety and toxicity studies in the view of applications.

2.5.5 Chemical hydrides (H_2O-reactive)

Alkaline and alkaline earth metals can react by hydrolysis, producing hydrogen and hydroxides. In this case, the term chemical hydride is used. These systems can be handled in a semi-liquid form, such as mineral oil slurry. In this form, hydrides can be pumped and safely handled. Controlled injection of H_2O during vehicle operation is used to generate H_2 via hydrolysis reactions. The liberation of H_2 is exothermic and does not require waste heat from the vehicle power source. The overview of the hydrolysis reactions for the most common chemical hydrides is provided in **table 2.4** and shows that the theoretical potential storage density is around 5-8 wt.%. In practical systems, one approach for NaH is to encapsulate small spheres in polymeric shells. In general, MgH_2 probably offers the best combination of H_2-yield and cost. The key R&D question to be faced is the cost of regenerating the material. Actually, this is an energy intensive process, and it is doubtful that cost can be reduced to vehicle targets.

Table 2.4 *Hydrolysis reactions and theoretical hydrogen storage densities for the main chemical hydrides.*

Hydrolysis reaction	**Theoretical H_2 capacity [wt%]**
$LiH + H_2O \rightarrow H_2 + LiOH$	7.8
$NaH + H_2O \rightarrow H_2 + NaOH$	4.8
$MgH_2 + 2\ H_2O \rightarrow 2\ H_2 + Mg(OH)_2$	6.5
$CaH_2 + 2\ H_2O \rightarrow 2\ H_2 + Ca(OH)_2$	5.2

[2.1] U.S. Department of Energy, *Fuel Cell Technologies Program Multi-Year Research, Development and Demonstration Plan - Hydrogen Storage, 2011 Interim Update*, (2011) http://www1.eere.energy.gov/hydrogenandfuelcells/mypp/pdfs/storage.pdf.

[2.2] A.Züttel, *Materials for hydrogen storage*, Mater. Today 6, 9 (2003) 24-33.

[2.3] D.Mori, K. Hirose, *Recent challenges of hydrogen storage technologies for fuel cell vehicles*, Int. J. Hydrogen Energy 34 (2009) 45569-4574.

[2.4] N. Takeichi, H. Senoh, T. Yokota, H. Tsuruta, K. Hamada, H.T. Takeshita, H. Tanaka, T. Kiyobayashi, T. Takano, N. Kuriyama, *"Hybrid hydrogen storage vessel", a novel high-pressure hydrogen storage vessel combined with hydrogen storage material*, Int. J. Hydrogen Energy 28 (2003) 1121-1129.

[2.5] D.K. Kohli, R.K. Khardekar, R.Singh, P.K. Gupta, *Glass micro-container based hydrogen storage scheme*, Int. J. Hydrogen Energy 33 (2008) 417-422.

[2.6] L.D. Burns, J.B. McCormick, C.E. Borroni-Bird, *Hydrogen fuel-cell cars could be the catalyst for a clearer tomorrow*, Scientific American, October (2000) 65-73.

[2.7] C.Davis, B. Edelstein, B. Evenson, A. Brecher, D. Cox, *Hydrogen Fuel Cell Vehicle Study – A report Prepared for the Panel on Public Affairs (POPA), American Physical Society* (2003).

[2.8] T. Wallner, H. Lohse-Bush, S. Gurski, M. Duoba, W. Thiel, D. Martin, T. Korn, *Fuel economy and emissions evaluation of BMW Hydrogen 7 Mono-Fuel demonstration vehicles*, Int. J. Hydrogen Energy 33 (2008) 7607-7618.

[2.9] S.M. Aceves, G.D. Berry, J. Martinez-Frias, F. Espinosa-Loza, *Vehicular storage of hydrogen in insulated pressure vessels*, Int. J. Hydrogen Energy 31 (2006) 2274-2283.

[2.10] J.E. Lennard-Jones, *Processes of adsorption and diffusion on solid surfaces*, Trans. Faraday Soc. 28 (1932) 333-359.

[2.11] K.J. Gross, K. Russel, Carrington, *Recommended Best Practices for the Characterization of Storage Properties of Hydrogen Storage Materials*, DOE Hydrogen Program - National Renewable Energy Laboratory Contract No. 147388 (2011).

[2.12] I. Langmuir, *The constitution and fundamental properties of solids and liquids. part i. solids,*J. Am. Chem. Soc. 38 (1916) 2221-95.

[2.13] S. Brunauer, P.H. Emmett, E. Teller, *Adsorption of Gases in Multimolecular Layers*, J. Am. Chem. Soc. 60, 2 (1938) 309-319.

[2.14] Y. Fukai, *Site occupancy and phase stability of some metal hydrides.* Z. Phys. Chem. 164 (1989) 165–174.

[2.15] Ch. Lexcellent, G. Gondor, *Analysis of hydride formation for hydrogen storage: Pressure-composition isotherm curves modelling*, Intermetallics 15(2007) 934-944.

[2.16] A.L. Allred, E.G. Rochow, *A scale of electronegativity based on electrostatic force*, J. Inorg. Nucl. Chem. 5, 4 (1958) 264-268.

[2.17] R. Griessen, A. Driessen, *Heat of formation and band structure of binary and ternary metal hydrides*, Phys. Rev. B 30, 8 (1988) 4372-4381.

[2.18] A.R. Miedema, *The electronegativity parameter for transition metals: Heat of formation and charge transfer in alloys*, J. Less-Common Met. 32, 1 (1973) 117-136.

[2.19] J.F. Herbst, *On extending Miedema's model to predict hydrogen content in binary and ternary hydrides*, J. Alloys Compd 337, 1-2 (2002) 99-107.

[2.20] Y. Nakamori, K. Miwa, A. Ninomiya, H. Li, N. Ohba, S.-I. Towata, A. Züttel, S.-I. Orimo, *Correlation between thermodynamical stabilities of metal borohydrides and cation electronegatives: first-principles calculations and experiments*, Phys. Rev. B 74 (2006) 045126.

[2.21] J.J. Vajo, G. Olsen, *Hydrogen in destabilized chemical systems*, Scr. Mater. 56 (2007) 829-834.

[2.22] G. Barkhordarian, T. Klassen, R. Bormann, Patent pending, Int. Pub. No.: WO 2006/063627 A1 (priority date 2004).

[2.23] J.J. Vajo, F.O. Mertens, S. Skeith, M.P. Balogh. Patent pending, Int. Pub. No: WO 2005/097671 A2, (priority date 2004).

[2.24] M. Fichtner, *Properties of nanoscale metal hydrides*, Nanotechnology 20 (2009) 204009.

[2.25] B. Bodganović, M. Schwickardi, *Ti-doped alkali metal aluminium hydrides as potential novel reversible hydrogen storage materials*, J. Alloys Compd. 253-254 (1997) 1-9.

[2.26] D.P. Broom, *Hydrogen Storage Materials: The Characterisation of Their Storage Properties*, Springer (2008).

[2.27] T. Graham, *On the absorption and dialytic separation of gases by colloid septa*, Philos. Trans. R. Soc. Lond. 156 (1866) 399–439.

[2.28] G. Sandrock, *A panoramic overview of hydrogen storage alloys from a gas reaction point of view*, J Alloy Compd 293–295 (1999) 877–888.

[2.29] S. Luo, J.D. Clewley, T.B. Flanagan, R.C. Bowman Jr., L.A. Wade, *Further studies of the isotherms of $LaNi_{5-x}Sn_x$-H for x = 0–0.5*, J. Alloys Compd. 267 (1998) 171–181.

[2.30] R.C. Bowman Jr., C.H. Luo, C.C. Ahn, C.K. Witham, B. Fultz, *The effect of tin on the degradation of $LaNi_{5-y}Sn_y$ metal hydrides during thermal cycling*, J. Alloys Compd. 217 (1995)185–192.

[2.31] D. Chandra, J.J. Reilly, R. Chellappa, *Metal hydrides for vehicular applications: the state of the art*, JOM 58, 2 (2006) 26–32.

[2.32] G. Sandrock, G. Thomas, *The IEA/DOE/SNL on-line hydride databases*, Appl. Phys. A 72 (2001) 153–155.

[2.33] J. Töpler, K. Feucht, *Results of a test fleet with metal hydride motor cars*, Z. Phys. Chem. (NF) 164 (1989) 1451–1461.

[2.34] Y. Fukai, *The metal-hydrogen system: basic bulk properties*, Springer (2005).

[2.35] B. Sakintuna, F. Lamari-Darkrim, M. Hirscher, *Metal hydride materials for solid hydrogen storage: a review*, Int. J. Hydrogen Energy 32 (2007) 1121–1140.

[2.36] E. Akiba, M. Okada, *Metallic hydrides III: body-centered-cubic solid-solution alloys*, MRS Bull. 27, 9 (2002) 699–703.

[2.37] B.C. Hauback, *Structures of aluminium-based light weight hydrides*, Z. Kristallogr. 223 (2008) 636–648.

[2.38] J. Graetz, *New approaches to hydrogen storage*, Chem. Soc. Rev. 38 (2009)73–82.

[2.39] J. Graetz, J.J. Reilly, *Kinetically stabilized hydrogen storage materials*, Scr. Mater. 56 (2007) 835–839.

[2.40] T. Kuji, Y. Matsumura, H. Uchida, T. Aizawa, *Hydrogen absorption of nanocrystalline palladium*, J. Alloys Compd. 330–332 (2002) 718–722.

[2.41] M. Yamauchi, H. Kobayashi, H. Kitagawa, *Hydrogen storage mediated by Pd and Pt nanoparticles*, ChemPhysChem 10 (2009) 2566–2576.

[2.42] R.L. Corey, T.M. Ivancic, D.T. Shane, E.A. Carl, R.C. Bowman Jr., J.M. Bellosta von Colbe, M. Dornheim, R. Bormann, J. Huot, R. Zidan , A.C. Stowe, M.S. Conradi, *Hydrogen motion in magnesium hydride by NMR*, J. Phys. Chem. C 112 (2008) 19784–19790.

[2.43] G. Barkhordarian, T. Klassen, R. Bormann, Catalytic *mechanism of transition-metal compounds on Mg hydrogen sorption reaction*, J. Phys. Chem. 110 (2006) 11020–11024.

[2.44] K.-F. Aguey-Zinsou, J.-R. Ares Fernandez, T. Klassen, R. Bormann, *Effect of Nb_2O_5 on MgH_2 properties during mechanical milling*, Int. J. Hydrogen Energy 32 (2007) 2400–2407.

[2.45] K.-F. Aguey-Zinsou, J.-R. Ares-Fernández, *Synthesis of colloidal magnesium: a near room temperature store for hydrogen*, Chem. Mater. 20 (2008) 376–378.

[2.46] R.W.P. Wagemans, J.H. van Lenthe, P.E. de Jongh, A.J. van Dillen, K.P. de Jong KP, *Hydrogen storage in magnesium clusters: quantum chemical study*. J. Am. Chem. Soc. 127 (2005)16675–16680.

[2.47] T.N. Dymova, Y.M. Dergachev, V.A. Sokolov, N.a. Grechanaya, *Dissociation pressure of $NaAlH_4$ and Na_3AlH_6*, Dokl. Nauk. SSSR 225 (1975) 591-592.

[2.48] B. Bogdanović, M. Schwickardi, *Ti-doped alkali metal aluminium hydrides as potential novel reversible hydrogen storage materials*, J. Alloys Compd. 253–254 (1997) 1–9.

[2.49] C.M. Jensen, R. Zidan, N. Mariels, A. Hee, C. Hagen, *Advanced titanium doping of sodium aluminium hydride: segue to a practical hydrogen storage material?*, Int. J. Hydrogen Energy 24 (1999) 461–465.

[2.50] B. Bogdanović, M. Felderhoff, A. Pommerin, F. Schüth, N. Spielkamp, *Advanced hydrogen-storage materials based on Sc-, Ce-, and Pr-doped $NaAlH_4$*, Adv. Mater. 18 (2006) 1198–1201.

[2.51] C.M. Jensen, K.J. Gross, *Development of catalytically enhanced sodium aluminium hydride as a hydrogen-storage material*, Appl. Phys. A 72 (2001) 213–219.

[2.52] J. Graetz, Y. Lee, J.J. Reilly, S. Park, T. Vogt, *Structures and thermodynamics of the mixed alkali alanates*, Phys. Rev. B 71 (2005) 184115.

[2.53] A. Léon, O. Zabara, S. Sartori, N. Eigen, M. Dornheim, T. Klassen, J. Muller, B. Hauback, M. Fichtner, *Investigation of (Mg, Al, Li, H)-based hydride and alanate mixtures produced by reactive ball milling*, J. Alloys Compd. 476 (2009) 425–428.

[2.54] S. Sartori, A. Léon, O. Zabara, J. Muller, M. Fichtner, B.C. Hauback, *Studies of mixed hydrides based on Mg and Ca by reactive ball milling*, J. Alloys Compd. 476 (2009) 639–643.

[2.55] S. Sartori, X. Qi, N. Eigen, J. Muller, T. Klassen, M. Dornheim, B.C. Hauback, *A search for new Mg- and K-containing alanates for hydrogen storage*, Int. J. Hydrogen Energy 34 (2009) 4582–4586.

[2.56] P. Chen, Z. Xiong, J. Luo, J. Lin, K.L. Tan, *Interaction of hydrogen with metal nitrides and imides*, Nature 420 (2002) 302–304.

[2.57] B. Sakintuna, F. Lamari-Darkrim, M. Hirscher, *Metal hydrides materials for solid hydrogen storage: A review*, Int. J. Hydrogen Energy 32 (2007) 1121-1140.

[2.58] D.H. Gregory, *Lithium nitrides, imides and amides as lightweight, reversible hydrogen Stores*, J. Mater. Chem. 18 (2008) 2321–2330.

[2.59] S. Orimo, Y. Nakamori, J.R. Eliseo, A. Züttel, C.M. Jensen, *Complex hydrides for hydrogen storage. Chem. Rev.* 107 (2007) 4111–4132.

[2.60] S. Hino, T. Ichikawa, N. Ogita, M. Udagawa, H. Fujii, *Quantitative estimation of NH_3 partial pressure in H_2 desorbed from the Li-N-H system by Raman spectroscopy*, Chem. Commun. (2005) 3038-3040.

[2.61] F.A. Uribe, S. Gottesfeld, T.A. Zawodzinski Jr., *Effect of ammonia as potential fuel impurity on proton exchange membrane fuel cell performance*. J. Electrochem. Soc. 149, 3 (2002) A293–A296.

[2.62] A. Züttel, S. Rentsch, P. Fischer, P. Wenger, P. Sudan Mauron, C. Emmenegger, *Hydrogen storage properties of $LiBH_4$*, J. Alloys Compd. 356–357 (2003) 515–520.

[2.63] T. Riis, G. Sandrock, Ø. Ulleberg, P.J.S. Vie, *Hydrogen storage R&D: priorities and gaps*, International Energy Agency (IEA) - Hydrogen Implementing Agreement (HIA) Hydrogen Coordinating Group (HCG) Storage paper (2005).

[2.64] G.H. Findenegg, *Fundamentals of Adsorption*, Engineering Foundation, New York (1984) 207-218.

[2.65] K. Yvon, *Hydrogen in novel solid-state metal hydrides*, Z. Kristallogr. 218 (2003) 108–116.

[2.66] S. Orimo, H. Fujii, *Materials science of Mg-Ni-based new hydrides*, Appl. Phys. A 72 (2001) 167–186.

[2.67] C. Zlotea, P. Moretto, T. Steriotis, *A Round Robin characterisation of the hydrogen sorption properties of a carbon based material*, Int. J. Hydrogen Energy 34, 7 (2009) 3044–3057.

[2.68] Y. Yürüm, A. Taralp, T.N. Veziroglu, *Storage of hydrogen in nanostructured carbonmaterials*, Int. J. Hydrogen Energy 34 (2009) 3784–3798.

[2.69] A.C. Dillon, K.M. Jones, T.A. Bekkedahl, C.H. Kiang, D.S. Bethune, M.J. Heben, *Storage of hydrogen in single-walled carbon nanotubes*, Nature 386 (1997) 377–379.

[2.70] M. Hirscher, M. Becher, M. Haluska, U. Dettlaff-Weglikowska, A. Quintel, G.S. Duesberg, Y.-M. Choi, P. Downes, M. Hulman, S. Roth, I. Stepanek, P. Bernier, *Hydrogen storage in sonicated carbon materials*, Appl. Phys. A 72 (2001) 129–132.

[2.71] A. Chambers, C. Park, R.T.K. Baker, N.M. Rodriguez, *Hydrogen storage in graphite nanofibers*, J. Phys. Chem. B 102, 22 (1998) 4253–4256.

[2.72] F. Lamari Darkrim, P. Malbrunot, G.P. Tartaglia, *Review of hydrogen storage by adsorption in carbon nanotubes*, Int. J. Hydrogen Energy 27 (2002) 193–202.

[2.73] Z. Yang, Y. Xia, R. Mokaya, *Enhanced hydrogen storage capacity of high surface area zeolite-like carbon materials*, J. Am. Chem. Soc. 129 (2007) 1673–1679.

[2.74] C. Tang, Y. Bando, X. Ding, S. Qi, D. Golberg, *Catalyzed collapse and enhanced hydrogen storage of BN nanotubes*, J. Am. Chem. Soc. 124, 49 (2002) 14550–14551.

[2.75] C.N.R. Rao, M. Nath, *Inorganic nanotubes*, Dalton Trans (2003) 1-24.

[2.76] J.G. Vitillo, G. Ricchiardi, G. Spoto, A. Zecchina, *Theoretical maximal storage of hydrogen in zeolitic frameworks*, Phys. Chem. Chem. Phys. 7 (2005) 3948–3954.

[2.77] X. Du, E. Wu, *Physisorption of hydrogen in A, X and ZSM-5 types of zeolites at moderately high pressures*, Chin. J. Chem. Phys. 19, 5 (2006) 457–462.

[2.78] K.M. Thomas, *Adsorption and desorption of hydrogen on metal-organic framework materials for storage applications: comparison with other nanoporous materials*, Dalton Trans 9 (2009) 1487–1505.

[2.79] P. Makowski, A. Thomas, P. Kuhn, F. Goettmann, *Organic materials for hydrogen storage applications: from physisorption on organic solids to chemisorption in organic molecules*, Energy Environ. Sci. 2 (2009) 480–490.

[2.80] N.B. McKeown, P.M. Budd, *Polymers of intrinsic microporosity (PIMs): organic materials for membrane separations, heterogeneous catalysis and hydrogen storage*, Chem. Soc. Rev. 35 (2006) 675–683.

[2.81] C.D. Wood, B. Tan, A. Trewin, H. Niu, D. Bradshaw, M.J. Rosseinsky, Y.Z. Khimyak, N.L. Campbell, R. Kirk, E. Stöckel, A.I. Cooper, *Hydrogen storage in microporous hypercrosslinked organic polymer* networks, Chem. Mater. 19 (2007) 2034–2048.

[2.82] S.S. Han, H. Furukawa, O.M. Yaghi, W.A. Goddard, *Covalent organic frameworks as exceptional hydrogen storage materials*, J. Am. Chem. Soc. 130 (2008) 11580–11581.

[2.83] B. Panella, L. Kossykh, U. Dettlaff-Weglikowska, M. Hirscher, G. Zerbi, S. Roth, *Volumetric measurement of hydrogen storage in HCL-treated polyaniline and polypyrrole*, Synth. Met. 151 (2005) 208–210.

[2.84] V.V. Struzhkin, B. Militzer, W.L. Mao, H.K. Mao, R.J. Hemley, Hydrogen storage in molecular clathrates, Chem. Rev. 107 (2007) 4133–4151.

[2.85] N.L. Papadimitriou, I.N. Tsimpanogiannis, A.T. Papaioannou, A.K. Stubos, *Evaluation of the hydrogen-storage capacity of pure H_2 and binary H_2-THF hydrates with Monte Carlo simulations*, J. Phys. Chem. C 112 (2008) 10294–10302.

[2.86] A.R.C. Duarte, A. Shariati, L.J. Rovetto, C.J. Peters, *Water cavities of sH clathrate hydrate stabilized by molecular hydrogen: phase equilibrium measurements*, J. Phys. Chem. B 112, 7 (2008) 1888–1889.

[2.87] N.V. Plechkova, K.R. Seddon, *Applications of ionic liquids in the chemical industry*, Chem. Soc. Rev. 37 (2008) 123–150.

[2.88] M.P. Stracke, G. Ebeling, R. Cataluña, J. Dupont, *Hydrogen-storage materials based on imidazolium ionic liquids*, Energy Fuels 21 (2007) 1695–1698.

Chapter 3

Experimental methods and instruments

3.1 Introduction

The main experimental techniques used during the experimental activity are reported in this chapter. The next section describes the ball milling technique, used to prepare the samples belonging to all the systems discussed in all the following chapters, except for the polymer-based ones (**chapter 6**). Subsequently, an overview of the methods and instruments for the evaluation of the hydrogen sorption properties of the materials is given (gas sorption analyzer and coupled volumetric-calorimetric measurements) in **sections 3.3** and **3.5**. In between (**section 3.4**) a brief description of differential scanning calorimetry (DSC) technique is reported. **Section 3.6** gives an outline of the system used for the design and test of a hydrogen storage tank. In the subsequent sections, some elements of background theory on the methods used for the structural investigations are given. Additional information on the used techniques and experimental conditions are reported in the following chapters, along with the discussion on the experimental results.

3.2 The ball milling technique

This method is used to grind materials for different purposes and applications, such as new materials, minerals, building materials, metallurgy **[3.1]**, ceramics **[3.2]**, fire proof materials, as well as medicine **[3.3]**, agricultural chemicals, food **[3.4]**, health products. The material to be ground is inserted inside the milling vial together with the milling media, which usually are

balls, beads, shots, or less commonly, rods or segments. The mill motor and driving components produce the vial motion, which causes crashes between the milling media (balls) and the material to be ground inside the vial. The most pursued purpose of the ball milling is the reduction of particle size of the ground material together with the uniform mixing. However other processes, like wet (if some solvent is present inside the vial) or dry synthesis, or mechanical alloying[(a)], can occur due to the high energy collisions, that the material particles undergo whenever they are in between a ball and the vial's walls, or two balls **[3.5]**.

Depending on the movement that the milling vial is subject to, there are different type of mill, each type with specific features and producing particular effects on the grounded material. Shakers and vibrator mills are also indicated as high efficiency mills, due to the finer pulverization they assure if compared to other types of mill at the same power consumption conditions **[3.6]**. Planetary mills use rotation to generate the movement of the material and the grinding media inside the milling vial. As the name indicates, in addition to rotation around the vial axis, a revolution motion occurs, but in the opposite direction (**figure 3.1**).

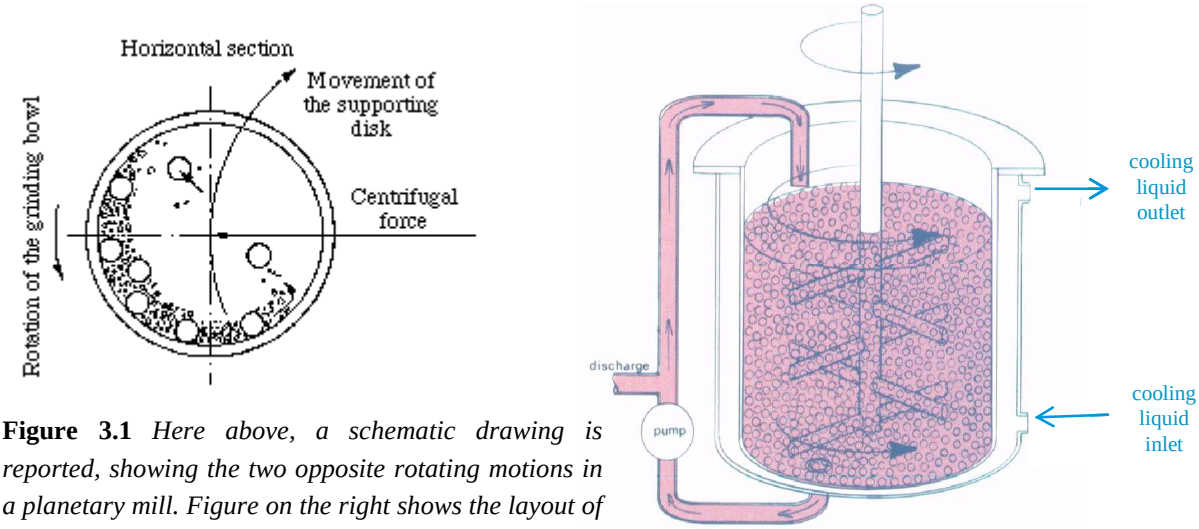

Figure 3.1 *Here above, a schematic drawing is reported, showing the two opposite rotating motions in a planetary mill. Figure on the right shows the layout of an attritor mill, also suitable for wet synthesis.*

For this kind of mill, a key factor to be taken into account is the so-called "critical speed", indicated as the speed after which the grinding media start rotating with the same angular speed and direction of the milling vial, thus strongly reducing the energy of the collisions. Higher temperatures can be achieved inside the rotation-type mills, compared to the vibrating-type ones **[3.7]**, and this fact has some implication in the management of the milling operation and conditions. For example, high temperatures can occur even at the minimum rotation speed needed to crush down the material, and as a result the powder can sinter and adhere to the inner milling vial walls; because of this fact, depending on the material and the operative conditions, hard blocks can stuck to walls can be produced, rather than loose powder. An example of this phenomenon is reported and discussed in **chapter 7**.

The presence of the impeller and the balls creates a combination of forces, such as compression, moment, shear. For this reason, also the attritor type mill is indicated as a high efficiency milling equipment. Shearing action is present in the attritor mill as the balls spin with different verse during their random movement; this feature, which is less intense in other types of milling equipment, generates efficient grinding and creates more spherical particles **[3.8]**. The attritor mill is versatile both for dry and wet grinding (usually batch) processes.

With high energy ball milling non-equilibrium processes (e.g. mechanical alloying) can occur, allowing the formation of metastable phases, which cannot be synthesized by conventional methods **[3.9]**. This advantage can be exploited also for the synthesis of hydrogenated phases of materials, such as hydrides for hydrogen storage. In fact, the milling process can be performed with a hydrogen atmosphere inside the milling vial, thus making the hydrogen participating as a reactant, as well as the material to be ground, in the so-called "reactive milling" process. In this regard, temperatures achievable due to the milling process together with the exothermic effect of the hydrogen absorption reaction must be taken into account in order to avoid overpressure inside the milling chamber. The temperature raising can be contrasted by using external coolant, refrigeration systems, or more easily, by alternating milling and pause intervals, rather than perform one single milling run. According to the property of materials, dry grinding or wet grinding can be adopted, as well as continuous or interval grinding.

Another big advantage of the ball milling is the possibility to scale it up easily to the industrial level, especially for the vibrating-type equipment. In general, ball milling is a batch process, where the milling chamber is filled with the milling media and the material to be ground, and then closed before starting the process; after the process, the ground material is discharged and separated from the milling media. Nevertheless, there are also examples of industrial ball milling process, that use a continue open-circuit layout, feeding from one side the material and discharging the final product from the other end, already classified and separated from the grinding media **[3.10]**.

By setting the parameters of the ball milling process, it is possible to tailor a material for the required application. For example, the particle size of products can be changed by adjusting different parameters, i.e. feeding amount, type and grade of grinding media, amplitude and frequency of vibration or speed of rotation. In industrial processes the mill can also be connected with classifiers in series to gain products with even narrow particle size distribution, while the retained particles can be brought back for a further milling stage.

Due to the high energy collisions and the consequent stress on the materials, the potential risk of material contamination from milling media or vial should always be considered. In order to minimized this effect, especially for applications where material purity is a key factor, special resistant and few contaminative material, such as high manganese content steel, stainless steel, aluminium oxide, zirconium oxide, quartz, tungsten carbide, silicon nitride, can be adopted.

In the course of the experimental work reported in this thesis, different types of mills have been used. For all the milling procedures adopted, the material constituting the used milling

vials is hardened steel, while stainless steel balls of 10 mm diameter have been used as milling media (**figure 3.2**). The used ball to powder ratio (BPR) is always 10, that is a value in the range (10-20) commonly used to guarantee a sufficient number of collisions per time unit. In order to avoid the heating of the sample during the milling process, for all the grinders, an alternate sequence of milling/pause runs has been adopted, each step (milling or pause) lasting15-20 min. Here below the models of the used ball milling equipment are described.

The *Spex 8000N* shaker mill (**figure 3.3**) has been used to prepare samples of the CaH_2-MgB_2-AlB_2 composites for the study reported in **chapter 5**. It is an efficient, compact laboratory mill, with a single milling vial for materials processing up to 10-15 g, depending on the material density. The 5 cm amplitude and 1200 Hz motion creates an intense shaking and allows the efficient milling.

Figure 3.2 *Hardened steel milling vials and 10 mm Ø stainless steel balls used as milling media.*

Figure 3.3 *Shaker mill SPEX8000N. On the left side the vial's allocation is visible.*

A planetary miller *Pulverisette 6* (*P6*) by *Fritsch* has been used to prepare the $LaNi_5$ samples for the study reported in **chapter 4**: a rotation speed of 240 rpm (the maximum rotation speed for this equipment is 650 rpm) has been used to grind the material in a 225 ml stainless steel vial.

A bigger planetary mill of the same series from Fritsch, i.e. the *Pulverisette 5* (*P5*), has been used for the milling tests of the intermetallic alloy *HydralloyC5*®, reported in **chapter 7**. The mill is able to host four milling vials of 225 ml each, thus potentially reducing by four times the time needed to process the material with the previous mono-vial equipment. However, for this mill the maximum rotation speed is lower, i.e. 400 rpm. The two described planetary mills described are reported in **figure 3.4**.

Figure 3.4. *Pulverisette series planetary mills: on the left picture, the P6 with one single vial; on the right picture, the P5 able to host up to four vials.*

Both the used planetary mills are equipped with a programmable logic controller (PLC) to set rotation speed and milling/pause cycling times as well. For the adopted shaker mill a PLC modulus has been implemented and a remote control has been configured to manage the milling/pause intervals.

3.3 Gas sorption analyzer

The investigation of the hydrogen sorption properties of the materials has been carried out using the automatic *Sievert*'s type equipment *PCTPro2000* by *Setaram*. The *Sievert*'s method is based on the use of calibrated volumes to evaluate the absorbed or desorbed (i.e. released) amount of a gas in or from a solid material **[3.11]**. The known volumes of the sample holder and of the process gas reservoir are put in communication each other when the test starts. By measuring the temperature and the pressure of the system, the amount of the gas phase can be calculated using an appropriate equation of state. The decrease or the increase of the gas amount from the initial value is respectively interpreted as an absorption or a desorption of the gas substance.

As an alternative to the manometric-volumetric methods used in the *Sievert*'s type apparatus, other instruments use flowmeters to evaluate the amount of the hydrogen flown from the gas reservoir to the sample holder (in case of absorption) or contrariwise (in case of desorption). By measuring the temperature and pressure of the sample holder, the hydrogen in the gas phase is calculated and then the absorbed or desorbed hydrogen amount is obtained by difference with that totally flown. The advantage of this method with respect to the *Sievert*'s one, based on calibrated volumes, is the possibility to keep the pressure of the sample holder strictly constant throughout the sorption test. However, flowmeters are in general critical components as regards the measurement reliability, as they are suitable for a specific flowrate range. In fact, it must be taken into account that, in order to charge fast the sample holder with hydrogen (to reach the desired pressure), a high flow is needed; on the contrary, in order to follow the sorption test up to saturation, even a little flow of hydrogen should be detected and correctly measured.

With the *Sievert*'s type apparatus, both kinetics and thermodynamic measurements can be performed, even though for the latter a system with automated procedures is quite essential, as it is discussed below.

Figure 3.5 shows the main window of the *PCT-Pro2000* graphical user interface (GUI), developed in *LabVIEW* environment. A schematic drawing of the equipment's layout is shown. The sample holder (autoclave) can be put in communication with modular volumes, which act as gas reservoirs. The supplied gas are hydrogen, as process gas for the sorption tests, and helium, as utility gas for purging or volume calibration operations; besides, nitrogen is used to activate the pneumatic valves, indicated by numbers (green-coloured when open). Vent line allows the pressure discharge, while through the vacuum line the system can be evacuated. The limit pressure for the instrument is theoretically 200 bar (full scale of the

pressure reducer), even though a limit value of 170 bar is suggested, especially for experiment at high temperatures. A programmable temperature controller is used to manage the temperature of the sample holder up to 400 °C, while another controller keeps the reservoir volumes at around 30 °C. Special sample holders are also available for measurements in cryogenic conditions.

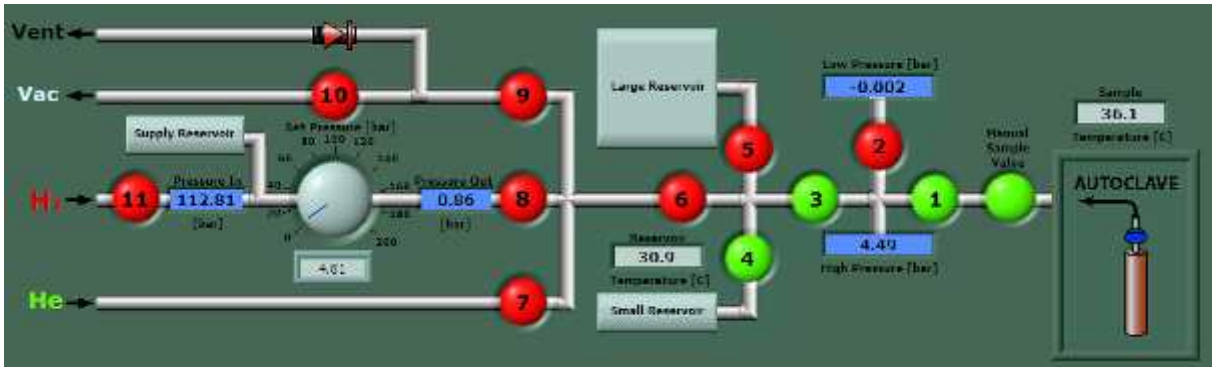

Figure 3.5 *Snapshot of the LabVIEW user interface main window of the PCT-Pro2000 instrument.*

Single kinetic absorption or desorption curves are obtained by setting different pressure values in the selected gas reservoir and the sample holder, initially isolated. Once the two volumes have been put in communication each other, the sorption process starts and proceeds up to the final equilibrium situation (i.e. saturation, in case of absorption). Kinetic curves at different temperatures can be used to evaluate the absorption/desorption rate constant and the activation energy. In **chapters 4-7**, which deal with the experimental results, kinetic curves for different systems are reported.

Thermodynamic information can also be derived by recording the Pressure-Composition Isotherms (PCIs). These pressure-composition (quasi-) equilibrium curves are obtained performing a sequence of kinetic measurements, increasing step by step the system pressure, at the same temperature (isothermal conditions): each point of the PCI is the final hydrogen concentration of a kinetic curve obtained at a certain pressure. PCI measurements take usually a long time, and the slower the system kinetics is at the used temperature, the longer is the time needed for the measurement. Thus, to perform PCI measurements in reasonable time, a programmable automatic apparatus is essential, also considering that the system pressure should be changed at each kinetic step. During the experimental work, PCI curves have been obtained for the $LaNi_5$ system and results are reported and discussed in **chapter 4**.

Cycling measurements can also be performed automatically with the *PCT-Pro2000*. Cycle-kinetics option allows measuring a sequence of alternated absorption /desorption curves with settable different conditions for both two kind of test. This is a very useful tool in order to investigate important properties of the material for hydrogen storage, for example: a) the material activation period before reaching the maximum sorption performances; b) the durability of the material, i.e. the ability to keep the performances after n sorption cycles. The cycling configuration has been used to investigate the properties of the intermetallic alloy used for the applicative system described in **chapter 7**.

Figure 3.6 shows an example of a test settings window of the *PCT-Pro2000* equipment's graphical user interface, in particular the one used for cycle-kinetics measurements: in addition to the general inputs of the experiment (name and sample information), the gas reservoir volume and pressure, as well as the duration time are settable both for absorption and desorption processes. Other tools allow the optimization of the saved data points during the tests (asymptotic) or the skip to the following step once an acceptable equilibrium is reached (equilibrium test) as well as in-line data correction due to temperature changes. All the calculations for the *PCT-Pro2000* are made by *HyData* software.

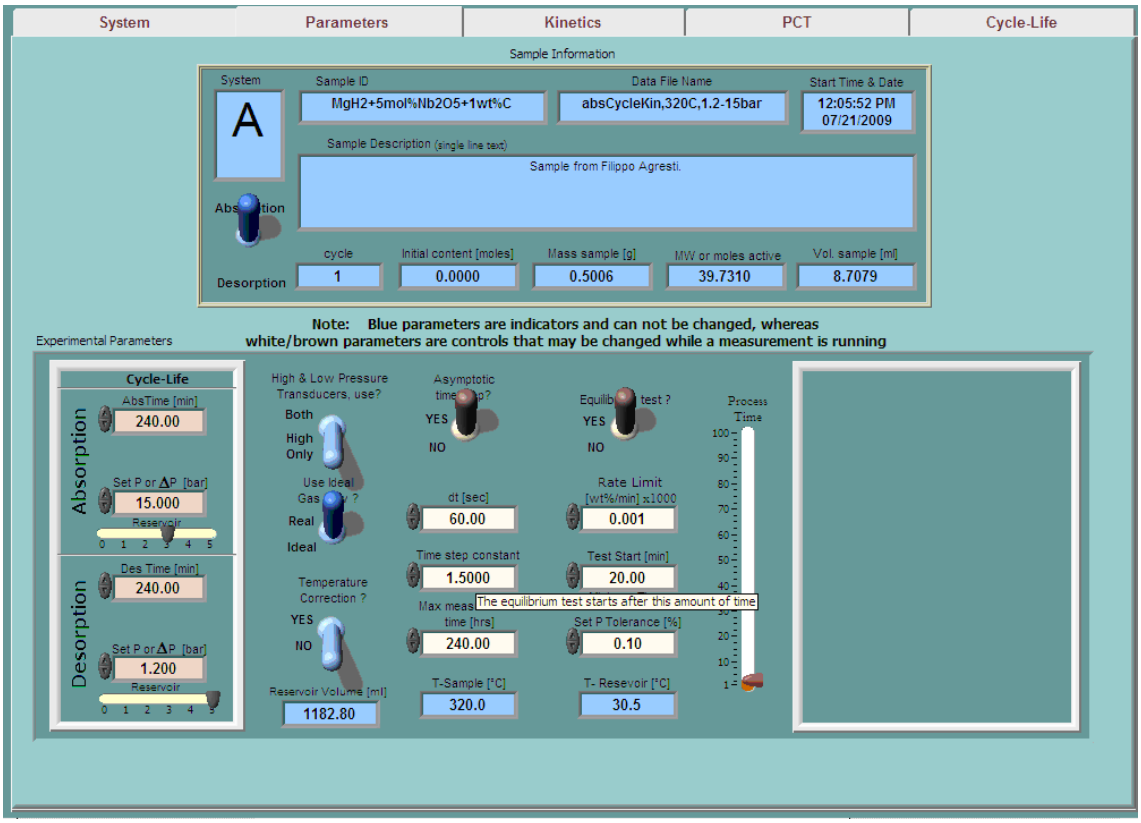

Figure 3.6 *Parameters setting window for a cycle-kinetics measurement.*

3.4 Differential scanning calorimetry (DSC)

A number of processes occurring inside physical/chemical systems are connected to heat exchange and thermal effects. In general, the aim of the *calorimetry* is the evaluation of the amount of heat, Q, acquired or released by the studied system, when it changes temperature (i.e. heating or cooling) or it is involved in transformations, such as chemical reactions or phase transitions. By measuring both temperature and exchanged heat in isobaric conditions, it is possible to evaluate properties, such as specific heat capacity, latent heat, reaction enthalpies **[3.12]**. In a DSC equipment, the temperatures of the sample under investigation and of a reference system are kept almost equal each other, while performing a temperature program (i.e. a sequence of temperature controlled stages, such as, heating, isothermal, or

cooling), and collecting the data at regular intervals (*scanning* mode). Usually, the DSC instrument are designed to work with small amounts of samples (up to 100 mg), and this is the case for the DSC instruments used during the experimental work reported on this thesis. **Figure 3.7** schematically describes the oven zone of the *DSC-1* (*Mettler Toledo*) instrument, used for the measurements on $LaNi_5$ samples, whose results are reported in **chapter 4**. Two pans are located in the two indicated housing: the material to be studied is inserted inside the sample pan, while the other pan hosts the reference. The oven heating is uniformly assured and controlled by the use of a set of resistances, schematically indicated in the figure as "central resistance". The temperatures of the sample (T_S) and of the reference (T_R) are measured during the scan by two thermocouples, respectively. On the basis of the difference between T_S and T_R, an electro-thermal device supplies the additional heat in order to make T_S and T_R coincide. This additional heat is supplied by Joule effect with a filament (resistance, R) close to the sample or the reference pan. From the intensity of the electric current, $i(t)$, on the filament, the additional power, $P(t)$, is calculated as:

$$P(t) = i^2(t) \cdot R = \frac{dQ}{dt} \tag{3.1}$$

which is then equal to the heat flux. For test performed in isobaric conditions, this amount is also equal to the enthalpy flux, which is the signal in a typical DSC measurement curve.

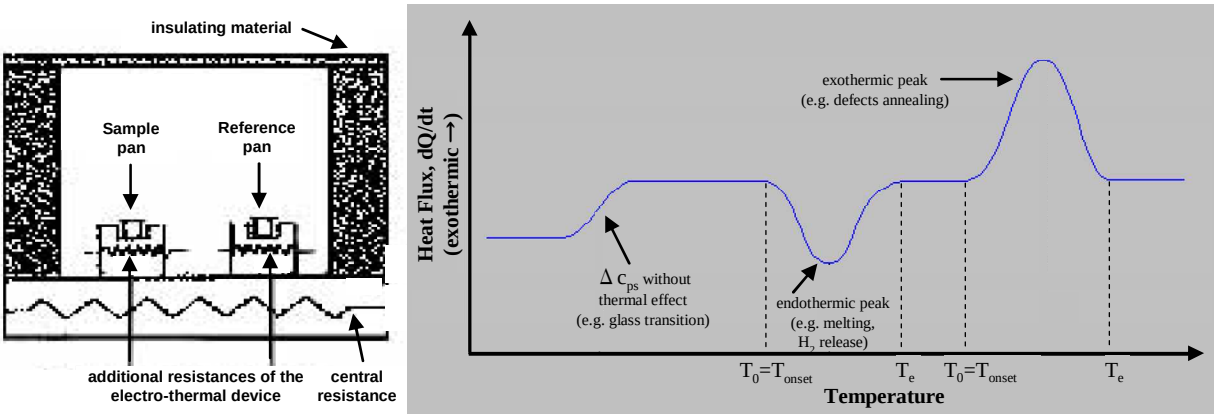

Figure 3.7 *The scheme on the left represents the section of a typical DSC instrument oven, with the sample and the reference housing and heating devices (resistance). The graph on the right reports the main (ideal) features of a DSC curve (see the text for the explanation).*

As explained above, the sample and reference temperatures are kept equal each other by using local heating resistances. For systems in which only heating occurs, at the considered range temperatures, the signal reported on a DSC curve is actually the difference between the heat flux on the sample and the reference:

$$\Delta\left(\frac{dQ}{dt}\right) = \left(\frac{dQ}{dt}\right)_S - \left(\frac{dQ}{dt}\right)_R = \left(\frac{dT}{dt}\right) \times \left[\left(\frac{dQ}{dT}\right)_S - \left(\frac{dQ}{dT}\right)_R\right] = \beta \times \left[m_s c_{p,s} - m_r c_{p,r}\right] \tag{3.2}$$

In the last expression on the right, β is the heating rate, and m and c are the masses and the specific heat capacities of the sample and the reference, respectively (in isobaric conditions).

In order to evaluate the specific heat of the sample, once the heating rate and the sample mass are known, the reference contribution

$$\left(\frac{dQ}{dt}\right)_{baseline} = \beta\, m_r c_{p,r} \tag{3.3}$$

must be subtracted. This contribution can be evaluated with an analogous measurement with the same reference, but in which the sample pan is empty; the corresponding obtained curve is called *baseline*. In the experiment performed during the reported experimental work, no reference sample was used, i.e. the reference pan has been kept empty. In this case, the baseline has essentially no contribution, as it can be verified by an experiment with two identical empty pans (in fact, the baseline depends on intrinsic properties of the system, such as thermal isolation or temperature controller dynamics, and on the amount of the gas replaced by the sample inside the pan).

If the sample undergo to other processes, besides heating, such as phase transition, defects annealing or chemical reactions, there would be other contributions to the total enthalpy flux, each of them being generally indicated as:

$$\left(\frac{dQ}{dt}\right) = \Delta_p H \times m_S \times \frac{d\alpha}{dt} = \beta\left(\Delta_p H \times m_S \times \frac{d\alpha}{dT}\right) \tag{3.4}$$

where α is the process progress fraction and $d\alpha/dt$ is the process progress rate. Once the onset temperature (**figure 3.7**) is reached, the process starts with a small rate, then it accelerates up to a maximum rate, and finally it ends again with a small rate. For this reason, the single process is represented by a peak. In a DSC plot, the correspondence of the acquired heat (endothermic process) with the sign of the y-axis must be specified. In **figure 3.7**, the y-axis orientation indicates released heat, i.e. an exothermic feature. Endothermic features can indicate processes such as melting, vaporization or, in case of hydrogen storage materials, hydrogen release, as well as decomposition in general (see **chapter 5**). The annealing of the material surface and bulk, are indicated by exothermic features, due to the release of the energy excess present in unordered systems with respect to the corresponding ordered structures. It is to note from equation **(3.4)** that the specific enthalpy of a process can be evaluated by integrating the corresponding peak, once the heating rate and the sample mass are known. This is the principle on which the hydrogen release enthalpies are calculated for the hydrogen storage systems discussed in **chapter 5**, by a coupled manometric-calorimetric measurements method, which is also described in the next section.

In order to reduce or eliminate the possibility of degradation for the oxygen- and moisture-sensitive materials studied for hydrogen storage, sealed sample holders or pans have been used for both the two calorimeters used during the experiments: *DSC-1* (*Mettler-Toledo*) for simple calorimetric measurements (**chapter 4**) and *Sensys* DSC instrument (*Setaram*) for coupled manometric-calorimetric measurements (**chapter 5**). In both cases, the sample holders and pans have been filled with the sample and sealed inside an argon filled glove-box.

3.5 Coupled calorimetric – volumetric measurements

As reported in **chapter 2**, the enthalpy of the absorption/desorption processes can be obtained by fitting the different plateau pressures at different temperatures with the *Van't Hoff* plot. Each plateau pressure can be obtained by performing a PCI measurement at a certain temperature. As discussed above, for systems with slow sorption kinetics PCI curves are not easy to be obtained for systems with slow kinetics and the measurements take in general a very long time (days or weeks).

An alternative and much faster method to evaluate the enthalpy of the hydrogen sorption reaction is based on a single absorption/desorption run in a coupled manometric-calorimetric system, where both absorbed/desorbed hydrogen amount and the thermal effects are evaluated. During the experimental activity reported in this thesis, these tests have been performed by coupling the *Sievert*'s type gas sorption analyzer *PCT-Pro2000* with a *Sensys* DSC instrument (by *Setaram*). As procedure for both hydrogen absorption and release processes, a temperature programmed experiment is performed: the pressure of the experiment is set at the beginning, then the sample is heated from an initial temperature up to a final one, at a selected heating rate. In this way, temperature programmed absorption (TPA) or desorption (TPD) experiments can be performed on a sample. The amount of the gas absorbed or released by the sample during the temperature programmed experiment is evaluated by the manometric instrument as it happens for a simple kinetic measurement, while the calorimeter provides the heat flow profile with the increasing temperature. The integration of the calorimetric peak corresponding to the absorption (exothermic) or desorption (endothermic) reaction gives the full enthalpy of the process; this value, normalized to the measured absorbed or desorbed hydrogen amount gives the enthalpy per mass unit. The cell of the high pressure calorimeter is connected to the manometric instrument by a stretch of 1/8" stainless steel tube with internal volume around 6 ml; in this way the pressure increase due to the sample heating is negligible for the correct absorbed/desorbed amount evaluation **[3.13]**. As an example, the diagram obtained by coupled measurement for a full absorption/desorption cycle on a Mg-based system is reported in **figure 3.8**: it is noticeable how the enthalpy values obtained in the two sorption processes are very similar **[3.14]**.

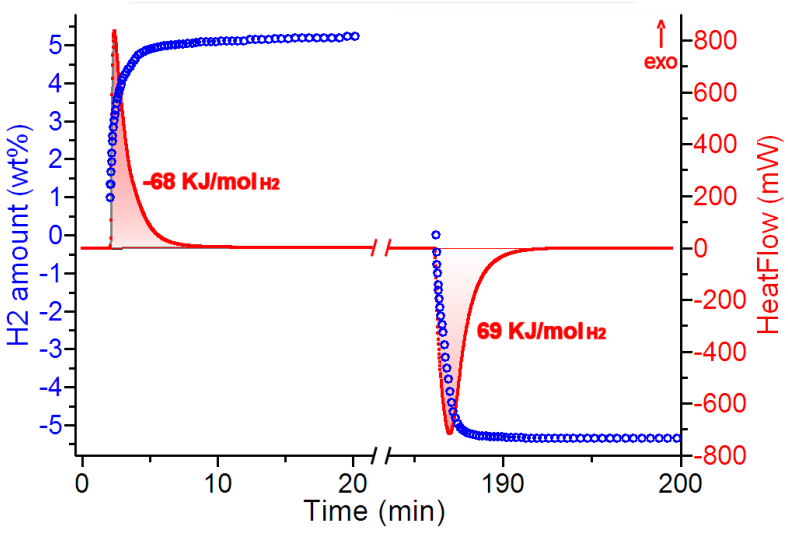

Figure 3.8 *Coupled manometric-calorimetric measurement for a hydrogen sorption cycle: the blue curves represent the absorbed/desorbed hydrogen amount during the temperature programmed runs; the red lines are the corresponding calorimetric profiles.*

3.6 Test Station

In **chapter 7** the design and the development of an hydrogen storage tank for a vehicular application is presented. During the experimental work on this issue, a homemade tank test system, developed at *Helmoltz Zentrum Geesthacht (HZG)* – Germany, has been used. All the preliminary tests on the hydrogen storage material used for the tank, as well as the test of the tank with the different adopted configurations, have been performed with this system, which is hereafter indicated as "Test Station" (see **figure 3.9** for a schematic layout). The hydrogen storage tank can be connected to the system and tested up to a limit pressure of 100 bar. Two feeding lines of hydrogen and helium are present, as process and flushing gas, respectively. A big volume is installed in the discharge line to decrease the system pressure during hydrogen discharge: this allows hydrogen to come out from the vent line into the environment (inside a cupboard) only at reduced pressures. Eight pneumatic valves (FV) are manually controlled by the user through a graphical user interface (GUI) and are used to set the desired test mode (absorption, desorption, volume calibration, purging). Two flow controller units (FCUs), operating respectively in the range 0.1-10 Nl/min and 10-200 Nl/min, are used to regulate the gas flux. The smaller inner diameter adopted for the stainless steel lines (6mm) is large enough to create negligible pressure drop through the flow path. There is no pressure reducer in the system, but only a pressure transducer (PT-1) to measure the current pressure value; the pressure inside the tank is controlled only by regulating the gas flowrate. One thermocouple gives the temperature of the gas inside the lines, while up to five thermocouples can be used to measure the tank temperature (in **figure 3.9** only one of five, the TT-2, is indicated).

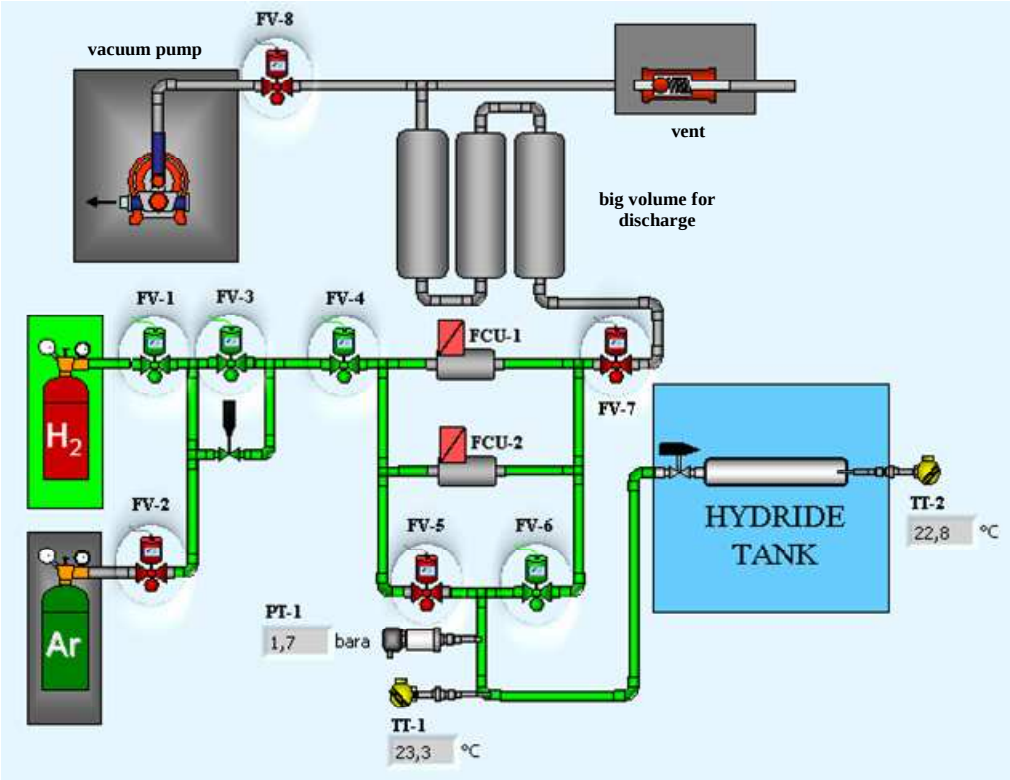

Figure 3.9 *Snapshot of a Graphic User Interface (GUI) window, showing a schematic layout of the Test Station.*

All the calculation and data recording are performed by a home-developed software in *LabVIEW* environment. The software provides safety blocks, which prevent the opening of the valves in a selective way, in order to avoid risks due to incorrect procedures adopted by the user. Additional technical details on the Test Station are reported in reference **[3.15]**.

The issue concerning the drawbacks for systems using flowmeters for the evaluation of hydrogen sorption properties of materials has been already mentioned in **section 3.3**. Together with this aspect, the implication of the Test Station layout for the simulation of the tank operative conditions for vehicular application is discussed in **chapter 7**.

3.7 X-ray powder diffraction (XRPD)

This non-destructive technique has been adopted for the investigation of the crystal structure of the studied samples. In 1912, the German physicist Max von Laue found that the diffraction of X-rays can be used to get information on the crystal structure of materials. A crystal is constituted by unit cells, regularly repeated in the three dimensions. The atoms constituting the material are arranged in fixed position on the cells. The material striking X-rays are scattered by the atoms and only under certain condition, diffraction occurs.

3.7.1 Crystal lattice geometry

Referring to **figure 3.10**, the vectors ***a***, ***b***, ***c*** identify the unit cell of a crystal in the three dimensions, as well as the direction of the crystallographic axes. The corresponding Greek (α, β, γ) and capital letters (*A*, *B*, *C*) indicate, respectively, the corresponding angles and faces, opposite to the vectors. The three parameters *a*, *b*, *c*, are called lattice (or cell) constants (or parameters) and describe the cell size, as well as the distance of two adjoining cells.

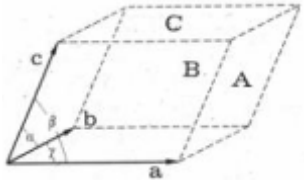

Figure 3.10 *Example of unit cell.*

In 1845, *A. Bravais* identified seven primary types of unit cells for the crystalline systems, on the basis on their possible symmetries (cubic, tetragonal, orthorhombic, monoclinic, triclinic, trigonal, and hexagonal). Actually, the possible presence of other atomic position centred on the lattice faces or inside, determines the extension of the possible different lattice structures to fourteen possible *Bravais* lattices **[3.16]**, shown in **figure 3.11**. Three nodes of the lattice identify a crystal plane (**figure 3.12**). If a plane cross the three crystallographic axes in the three nodes of the lattice $\{m_1, 0, 0\}$, $\{0, m_2, 0\}$, $\{0, 0, m_3\}$, the three index $\{m_1, m_2, m_3\}$ give the crystal plane orientation. However, rather than m_1, m_2 and m_3, their reciprocal numbers $h=1/m_1$, $k=1/m_2$, $l=1/m_3$, are commonly used to identify the orientation of a plane.

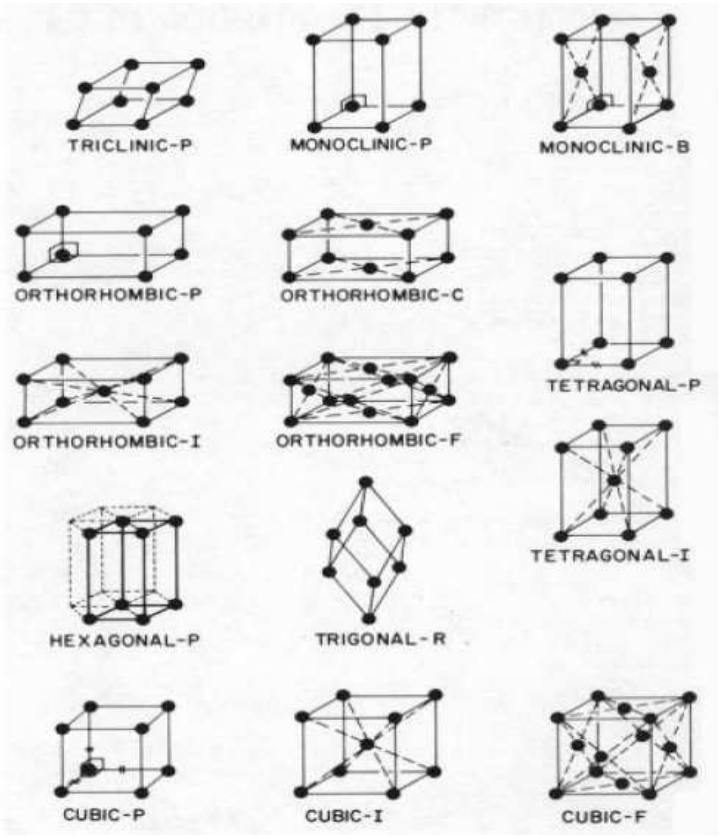

Figure 3.11 *The fourteen Bravais lattices*

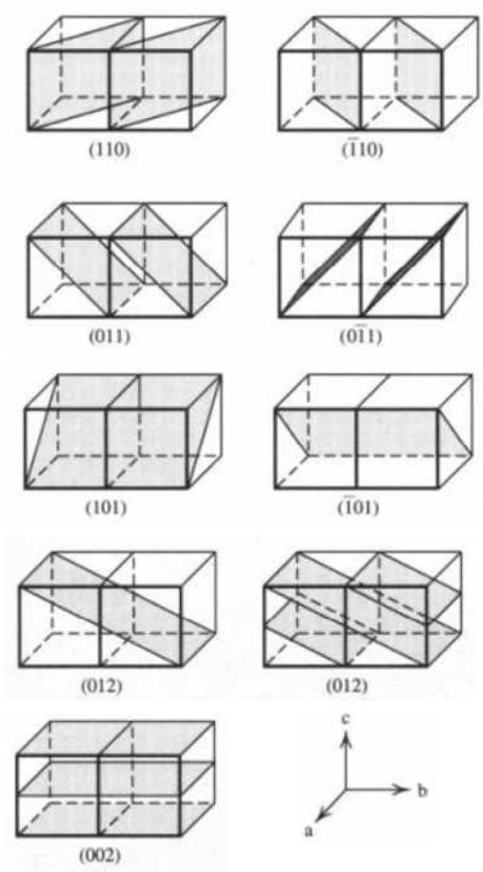

Figure 3.12 *Orientations of crystallographic planes.*

The indices *h*, *k*, *l* are called *Miller* indices, are integers and inversely proportional to the intersection of the crystal plane with the crystallographic axes. Thus, for example, if $m_1=\infty$, i.e. the crystal plane is parallel to the ***a*** vector, the corresponding *Miller* index is $h=0$. In **figure 3.12**, different families of parallel crystal planes are shown, together with their corresponding orientations. According to a spread convention, the negative values of the Miller indices are marked with a line above the numbers.

On the basis of the different type of *Bravais* lattice, symmetry axes and related perpendicular planes, 230 space groups have been identified for crystals, and are indicated referring to the *Hermann-Maguin* notation. All the information on the space groups is contained in the *International Table for Crystallography*.

3.7.2 The *Bragg*'s law

Referring to **figure 3.13**, atoms A and B occupy two respective sites on two parallel crystal planes, situated at distance *d*. The two wavelets 1 and 2 of the X-ray beam are scattered by atoms A and B, respectively, producing reflected wavelets, among which, the ones indicated by 1' and 2', forming with the atoms planes the same angle θ as the incident beam.

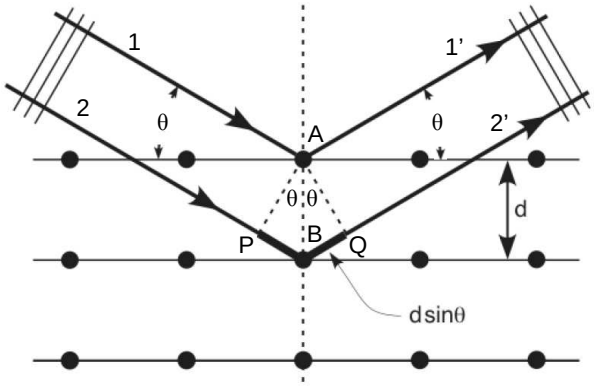

Figure 3.13 *The Bragg formulation of the X-ray diffraction.*

The diffraction occurs when the reflected wavelets give constructive interference each other, i.e. when they are in phase. This occurs when the difference path between the two wavelets before and after the incidence, viz. PB+BQ, is a multiple of the beam wavelength λ. This condition can be written as follows:

$$n\lambda = 2d\sin\theta \qquad \Rightarrow \qquad d = \frac{n\lambda}{2\sin\theta} \geq \frac{n\lambda}{2} \tag{3.5}$$

which is the *Bragg*'s law and it is valid for any set of parallel crystal planes. As the diffraction described above is extended to the three dimensions of the real space, the three integer *Miller* indices, *h*, *k*, *l*, are used to describe the orientation of the different diffraction planes, which are also-called *reflections* (i.e. orientation of the reflection planes).

3.7.3 Used experimental XRPD facilities

Laboratory X-ray diffraction set-up, using a Cu Kα source, and synchrotron light have been used to perform XRPD experiments during the experimental activity reported in this thesis.

Laboratory set-up has been adopted for the XRPD measurements for the systems reported in **chapters 4** ($LaNi_5$ system), **5** ($Ca\text{-}MgB_2\text{-}AlB_2$ system) and **6** (SP-MnO system). For each used instrument, a *Bragg-Brentano* geometry and a Cu Kα radiation source have been used. **Figure 3.14** reports the schematization and a set-up of such a type of apparatus.

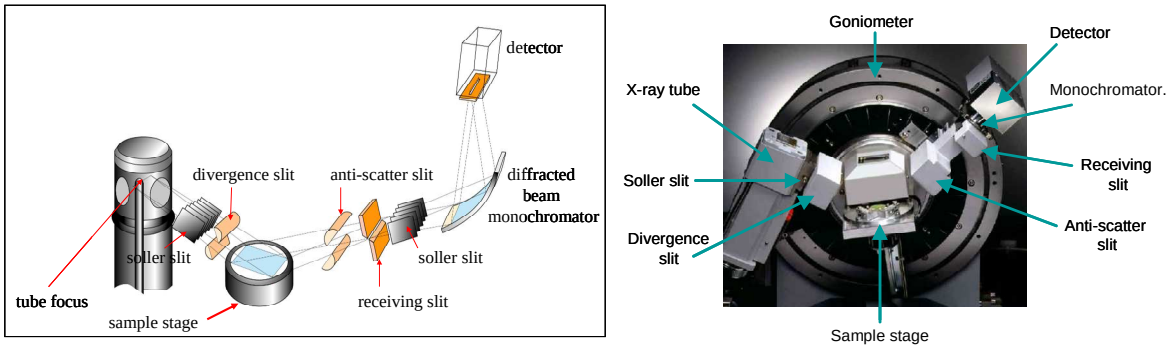

Figure 3.14 *Left: schematization of the optical components and of the light path in Bragg-Brentano diffractometer. Right: an example of a diffractometer set-up.*

The X-rays are emitted by the Cu Kα radiation source; the beam is then collimated by using *Soller* and *divergence* slits, which minimize respectively the side and axial divergences of the beam. The collimated beam strikes the sample at an incident angle θ. The diffracted radiation is then acquired by the detector, after being collimated by analogous slits used for the primary beam. Monochromators are used for both the primary and the diffracted beam. In order to arrange the primary and the diffracted beam at the same angle with respect to the sample, the detector rotates with a speed, which is the double of the sample's one, referring to the primary beam direction. As the sample covers a macro-area in the sample stage, the instrument layout manages the *parafocusing effect* in order to converge and focus the diffracted beam toward the receiving slits and then to the detector. Thus, the source and the detector are located at the same distance from the axis of the sample plane and the sample must be as flat as possible and placed on the axis of the goniometer.

X-ray powder diffraction measurements have also been performed at the *Elettra* synchrotron facility (Trieste, Italy), as reported in **chapter 5** for the CaH_2+AlB_2 system. The synchrotron radiation (SR) used for the study of condensed matter and surfaces, is emitted by high energy charged particles (usually electrons, while protons in the protosynchrotrons) running with a curve path (and thus accelerated) inside the synchrotron ring. The energy of the emitted beam is a function of the particle mass and speed, and of the curvature radius **[3.17]**. At *MCX1* beam line of the *Elettra* facility, the XRPD experiments have been performed with a wavelength of 0.827 Å (the energy of the emitting electrons of the central ring is 2.0-2.4 GeV). Compared with the laboratory X-ray diffraction set-ups, the synchrotron radiation has better features, such has high level of brilliance [(a)], collimation and polarization. Moreover, the high intensity [(b)] of the beam allows much more reliable data collection with better resolutions in a short time. The *Debye-Scherrer* geometry used in the SR-XRPD set-up is reported in **figure 3.15**.

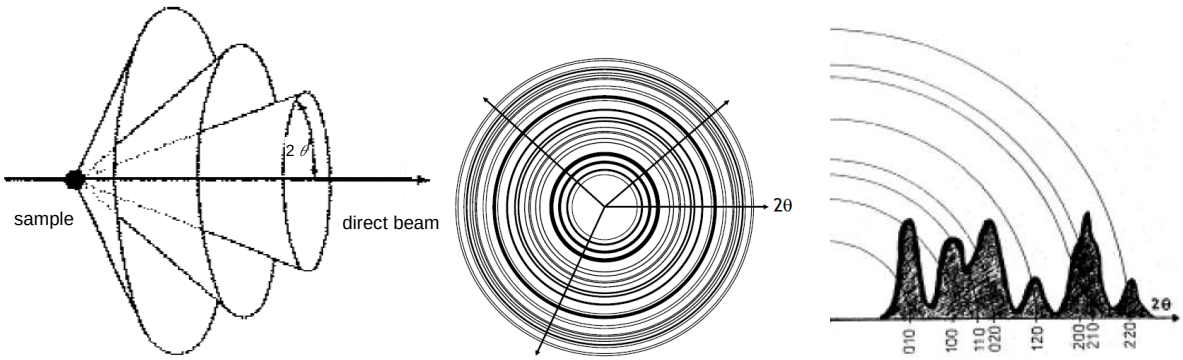

Figure 3.15 *Debye-Scherrer geometry: the cones (left), produced by the diffraction of the beam in the differently oriented crystallites are acquired as rings (centre) by the detector, placed perpendicularly to the primary beam. The figure shows an ideal rings pattern, i.e. with a good statistics of the orientations. The conventional diffraction pattern in the 2θ dimension can be obtained by integrating the rings pattern along the radius coordinate, r.*

(b) The *brilliance* is the amount of energy coming from a unitary solid angle and passing through the surface unit in the unitary time: thus, it is indicated as power for the surface and solid angle unit.

(c) The *intensity* is the amount of energy coming from the whole solid angle and passing through the surface unit in the unitary time: thus, it is defined as power for the surface unit.

When the beam strikes a polycrystalline sample, the radiation is diffracted according to the different orientations of the crystallites. The diffraction cones in the figure represent the node of the reciprocal lattice of the material crystallites. The diffracted radiation is then collected by the detector, placed in a plane perpendicular to the direct beam direction, resulting in the typical diffraction concentric rings (**figure 3.15**, centre). Generally, not all the orientations are statistically well distributed, so that some rings could be not well defined or reliable: in this case, the rotation of the sample (usually) around an axis perpendicular to the direct beam direction can improve the orientation statistics. The diffraction patterns with the reflections intensity versus the 2θ angle can be obtained by integrating part of or the full "cake" (**figure 3.15**, right side) along the radius coordinate, *r*. Programs, e.g. *FIT2D*, are suitable for this purpose. As mentioned, the synchrotron light allows acquiring diffraction patterns in short time and, due to the *Debye-Scherrer* geometry, in all the selected 2θ range. This means that the evolution of the crystal phases of a changing sample can be followed by consecutive acquisitions. At the *MCX1* beam line of the *Elettra* facility, the high flux (1011 photons/s) synchrotron radiation allows periodical acquisitions on the investigated samples. Pressure resistant quartz capillaries have been charged with hydrogenated powder inside an argon filled glove box, and then sealed, in order to avoid contact with air. The diffraction patterns have been acquired while performing a temperature program, in order to cause hydrogen desorption from the material. The results of the data analysis are reported in **chapter 6**.

3.7.4 The *Rietveld* method

The X-ray diffraction patterns of the investigated samples have been analyzed by using a *Rietveld* method-based program, in order to obtain qualitative and quantitative information on the samples crystal structure. The *Rietveld* method was developed since 1969 to refine crystal and magnetic structures, starting from neutron powder diffraction patterns recorded at a fixed wavelength **[3.18]**. Subsequently, the method was successfully adopted for the qualitative and quantitative analysis of both neutron and X-ray powder diffraction patterns, obtained at fixed scattering angle, as well as at fixed wavelength **[3.19]**. The method considers the structural and microstructural parameters of the crystal phases present inside the measured sample. Starting from input information and data supplied by the user, iterative procedures are used in order to refine the structure of each single crystal phase (cell parameters, atomic positions and *Debye-Waller* factors). The method aims at minimizing the residual function *weighted sum of squares (WSS)*:

$$WSS = \sum_i w_i \left(I_i^{\exp} - I_i^{calc} \right)^2 \qquad \text{where:} \qquad w_i = \frac{1}{I^{\exp}} \tag{3.6}$$

by fitting the entire profile of the diffraction pattern to a calculated profile. The method considers the profile intensities obtained at each 2θ angle from the measured powder diffraction pattern, and it is not based on integrated single or overlapping intensities of the diffraction diagram.

Thus, I_i^{exp} and I_i^{calc} indicate the experimental and calculated intensities, while w_i represents the contribution of each intensity to the whole spectrum. The single intensity at each 2θ position is calculated as:

$$I_i^{calc} = S_F \sum_{j=1}^{N_{phases}} \frac{f_j}{V_j^2} \sum_{k=1}^{N_{peaks}} L_k \left|F_{k,j}\right|^2 S_j \left(2\theta_i - 2\theta_{k,j}\right) P_{k,j} A_j + bkg_i \qquad (3.7)$$

in which the contribution of each single phase and, for each phase, the peaks contributions are considered. The *phase scale factor* S_j depends on the beam intensity S_F, the phase volume fraction f_j and the phase cell volume V_j, according to:

$$S_i = S_F \frac{f_j}{V_j^2} \qquad (3.8)$$

L_k is the *Lorentz polarization factor* and depends on the instrument set-up parameters, such as geometry, monochromator (angle α), detector and sample positioning (angle 2θ). For a *Bragg-Brentano* instrument is:

$$L_p = \frac{1 + P\cos^2\left(2\theta\right)}{2\left(1+P\right)\sin^2\theta\cos\theta} \qquad \text{where:} \qquad P = \cos^2\left(2\alpha\right) \qquad (3.9)$$

$F_{k,j}$ is a *generalized structure factor*, which takes into accounts different parameters, in particular: the *multiplicity* m_k of the k peak reflections (i.e. the number of symmetry-equivalent reflections contributing to the single observed peak) with the Miller indices (h ,k ,l), the *Debye-Waller temperature factor* B_n and the *atomic scattering factor* f_n, according to the following equation:

$$\left|F_{k,j}\right|^2 = m_k \left| \sum_{n=1}^{N} f_n e^{-B_n \frac{\sin^2\theta}{\lambda^2}} \left(e^{2\pi i\left(hx_n + ky_n + lx_n\right)} \right) \right|^2 \qquad (3.10)$$

where N is the number of atoms, x_n, y_n, z_n are the coordinates of the single atom and λ is the wavelength X-ray beam.

Coming back to equation **(3.7)**, the term $S(2\theta_i\text{-}2\theta_{k,j})$ is the *profile shape function*, representative of the line broadening, i.e. the shape of the peaks (e.g. half width at half or full maximum).

Pk is the *preferred orientation function* (indicating the texture degree) and *Aj* is the *phase absorption factor*, proportional to the inverse of the *linear absorption coefficient* μ of the sample ($A_j=1/2\mu$).

Finally, the value of the instrument *background* function is expressed by:

$$bkg_i = \sum_{n=0}^{N_b} a_n \left(2\theta_i\right)^n \qquad \text{where:} \quad \begin{cases} a_n = \textit{polynomial coefficients} \\ N_b = \textit{polynomial degree} \end{cases} \qquad (3.11)$$

In order to obtain a good refinement of a diffraction pattern, the more are the available starting information, the better is the obtained fit. Effectively, the initial fit obtained just with

the input data should not be much different from the final one, in order to reach calculation convergence with few iterations and changing as less parameters as possible. Different parameters can be used to indicate the goodness of the fit, even though their value depends also on the experimental apparatus and the measured spectrum. Together with the cited *WSS*, which should be minimized as much as possible, but for which no reference value can be indicated, the R_{wp} *factor* is more significant for the evaluation of the quality of the obtained fit:

$$WSS = \sum_i w_i \left(I_i^{\exp} - I_i^{calc} \right)^2 \qquad \text{where:} \quad w_i = \frac{1}{I^{\exp}} \qquad R_{wp} = \sqrt{\frac{\sum_i \left[w_i \left(I_i^{\exp} - I_i^{calc} \right) \right]^2}{\sum_i \left[w_i I_i^{\exp} \right]^2}} \tag{3.12}$$

The R*wp* value does not depend on the absolute value of the intensities, but the background and the number of the peaks have effect on it. In particular, the higher is the background and the less is the number of the peaks, the higher is the possibility to obtain a good fit. As a rough reference, R*wp* value minor than 0.1 can be considered as an indication of a god fit for a medium complex phase, while for a complex phase (e.g. monoclinic or triclinic) values minor than 0.15 are acceptable values. Of course, for systems with many different phases and peaks in the corresponding diffraction pattern, the reference maximum value for a good refinement increases.

Different *Rietveld* programs have been developed and are available free. *MAUD* (Material Analysis Using Diffraction) program has been used for the quantitative and qualitative analysis of the XRPD spectra, reported in **chapters 4** and **5**. This program was developed in late 90' **[3.20]** and from there onwards, new improved versions have been released, taking into account more parameters. The *MAUD* program is indicated as good for quantitative phase analysis, size-strain and texture. A graphical user interface allows the insertion of the initial instrument and phase information. As a good procedure for the refinement of a diffraction pattern, a first manual adjustment of some parameters, such as cell parameters, intensities and background, is suggested. Then, a sequence of automatic refining procedures is available. In this way, iterations can be performed by adjusting, at each step groups of parameters regarding background, phases, microstructure, crystal structure, texture and strain, respectively. Together with the final fit, the values of the considered parameters, e.g. phase fractions and crystallite sizes, are reported as results of the calculation.

3.8 X-ray absorption spectroscopy (XAS)

This technique is based on the measurement of the X-ray absorption coefficient of the atoms, as a function of the striking radiation energy. The absorption coefficient μ mostly decreases as

the radiation energy *E* increases (i.e. the X-ray become more penetrating), except for some specific energy values, for which the radiation is strongly absorbed by the material and μ sharply raise-up. The absorption peaks are due to the radiation-matter interaction by photoelectric effect: in a single event, an atom is excited by a striking photon and releases an electron of an inner atomic orbital (e.g. 1s). The energy excess not absorbed by the atom is transferred to the photoelectron, which scatters with the atoms around the origin-atom. The quantum interference of the electron wavefunction, due to the scattering (the electron interferes with itself), generates the XAS signal.

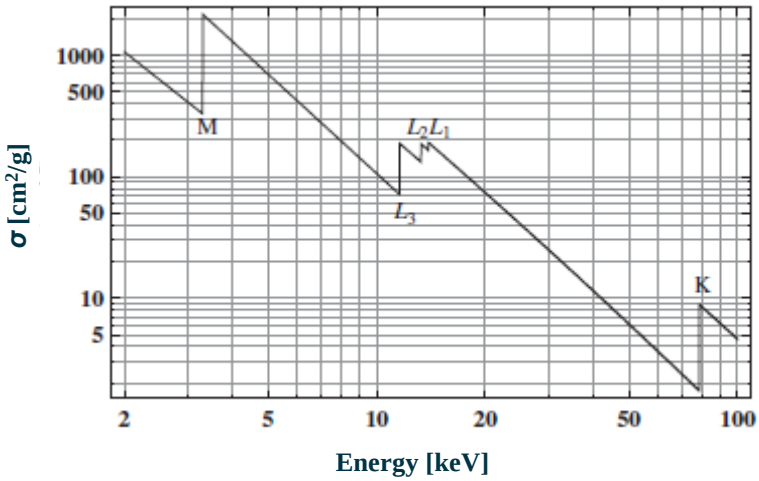

Figure 3.16 *Semi-empirical trend of the X-ray absorption vs. the striking beam energy for a platinum (Z=78) atom. In this log-log graph the absorption is expressed in terms of cross section σ, which is proportional to the absorption coefficient μ (=$\sigma \cdot n_b$, where n_b is the volume density of target particles). The graph shows the absorption edges corresponding to the emission of the photoelectrons from different atomic orbitals: K ($1s_{1/2}$), L_1 ($2s_{1/2}$), L_2 ($2p_{1/2}$), L_3 ($2p_{3/2}$) and M_1 ($3s_{1/2}$).*

As shown on the **figure 3.16**, the higher energy absorption edge (K) for platinum is around 80 keV, falling in the "hard" X-rays region, while the low energy edge M_1 is around 3.3 keV, situated in the "soft" X-rays range. Different regions of the X-ray absorption spectrum can be investigated in order to obtain different information on a material, even though a strong part of the information corresponds to the edge, and thus constitutes a small part of the whole signal. According to this, XAS investigations require the use of a radiation with high brilliance, variable a large range of energy, but also with a fine tuning (the X-ray beam should have an energy bandwidth of few eV or less, in order to resolve the spectra). This can be found at synchrotron facilities, while rather poor is the possibility to perform experiment in small laboratory set-ups. Different acronyms indicate experiments performed on the different region of the absorption spectrum, respectively. XANES (X-ray absorption Near-Edge Spectroscopy) measurements are performed typically before the edge and up 60-100 eV above the edge, while EXAFS (Extended X-ray Absorption Fine Structure) measurements are extended to the limit of the absorption spectrum. In general, as the space region of the sample investigated by XAS concerns an atom (type) and its surroundings, this technique gives information on the local structure of the sample and can be considered as ideal complement to the X-ray diffraction technique for the study of crystalline materials. By performing EXAFS

experiments, information such as coordination numbers, interatomic distances and local disorder, can be obtained, while XANES is useful for getting information of oxidation numbers and geometry.

3.8.1 The EXAFS technique

As mentioned above, the photoelectron liberated by the striking photon propagates due to the energy excess not absorbed by the central atom. The propagation occurs as a spherical wave, which can be back scattered by the near-neighbouring atoms and thus interfere with itself. This quantum interference is, in fact, one of the effects related to the emission of a core electron (e.g. the electron can also be transferred to another bond level), but it is the main phenomenon that leads the experimental region of EXAFS. The amplitude and phase of the scattered photoelectron depends on its mass and energy and on the type and position of the surrounding atoms. In general, by varying the energy of the beam, and thus of the excited photoelectron, the quantum interference can be alternatively constructive or destructive, thus producing an oscillating signal. The EXAFS signal, $\chi(k)$, is evaluated in the wavevectors domain as a sum of contributions corresponding to a certain number of scattering events. **Figure 3.17** shows the EXAFS signal for two of the possible paths of the photoelectron in a MnO sample **[3.21]**.

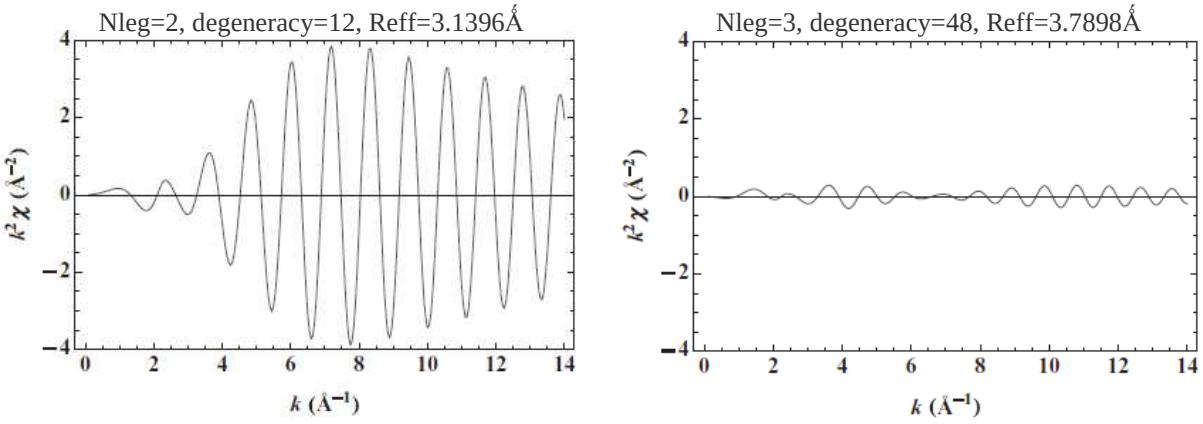

Figure 3.17 *EXAFS signals corresponding to two of the possible paths for the photoelectron in a MnO sample. The "legs" number (Nleg) indicates the number of the consecutive scattering events until the photoelectron comes back to the central absorbing atom. The degeneracy is the number of possible identical paths of the same type for the system, and their contributions are taken into account in the showed signal. Reff is the effective maximum distance from the central atom, achieved with the path. The path is calculated with an ab initio method–based program, FEFF 8.4. The signal is multiply by k^2 to emphasize the oscillatory behaviour.*

Above the edge and in the fine structure region, multiple scattering can be considered, as the method converges, while this is not sure for measurements at lower energies. The total absorption coefficient $\mu(E)$ can be considered as the absorption coefficient of the single (central) atom, $\mu_0(E)$, corrected by a term proportional to the EXAFS signal and taking into account the contributions of the photoelectron scattering by the near neighbouring atoms, i.e. $\mu=\mu_0(1+\chi)$ or $\chi=(\mu-\mu_0)/\mu_0$. *Stern*, *Sayers* and *Lytle* **[3.22]** **[3.23]** proposed the following

simple and extremely useful equation for χ, which is by now indicated as the standard EXAFS equation:

$$\chi(k) = -S_0^2 \sum_i \frac{3\cos^2\theta_i}{kr_i^2} \left| f_i(k) \right| e^{-\frac{2r_i}{\lambda_e}} \sin(2kr_i + 2\delta_1(k) + \arg(f_i(k))$$
$$with \qquad k = \sqrt{\frac{2m_e}{\hbar^2}(E - E_0)} \tag{3.13}$$

where the contributions of the scattering atoms at relative position $\vec{r}_i$ from the central atoms are summed. In the expressions above, m_e is the (rest) mass the electron liberated from the central atom, E_0 is the energy of the edge, θ_i is the angle between the X-ray polarization vector ($\hat{\varepsilon}$) and $\vec{r}_i$, $|f_i(k)|$ and $arg(f_i(k))$ are the modulus and the phase of the complex electron scattering amplitude for each atom. Moreover, the term δ_1 take into account the phase shift due to the effect on the phase of waves with specific angular momentum l when they scatter from a spherical potential (*muffin-tin* potential), while S_0^2 and the photoelectron mean free path λ_e account for losses of coherence due to multielectron excitations. It is to note that the factor $1/r^2$ accounts for the photoelectron intensity decrease (1/r) from the central atom to the near scattering atom and the other way back. Equation **(3.13)** contains some approximations, the strongest one being the neglecting of multiple scattering. This approximation is not suggested particularly when the absorbing atom and the scatterers are collinear. The contributions from multiple scattering oscillate more rapidly the longer the path length, thus they can be confused with single scattering with a farer atom, among the neighbouring ones. Some expressions have been proposed for χ, taking into account the multiple scattering **[3.24]**. In an EXAFS experiment, an average over many sites of the sample is performed. Depending on the position, the results may vary, due to thermal and quantum zero point motions, but also for heterogeneity and disorder of the sample. The lifetime of the core hole, created by the energy absorption by the central atom and the liberation of the photoelectron, has a lifetime approximately 10^3 times shorter than periods of the interatomic vibrations, thus the variations cited above will affect the single EXAFS measurement. The motion due the temperature gives an oscillatory contribution to the phase factor, while the disorder provides a Gaussian damping factor, called *Debye-Waller factor* (as the analogous for XRD), due to the overlapping of signals with different frequency, corresponding to different path lengths. For randomly oriented polycrystalline or solution sample an isotropic average over angles must be performed. In this case, the contributions from atoms of the same atomic number and at similar distances from the absorbing central atom may not be resolvable from each other, and atoms must be conceptually grouped together into “coordination shells”, thus modifying equation (A4.1) to the following one:

$$\chi(k) = -\sum_j \frac{N_j}{kR_j^2} \left| f_j(k) \right| e^{\frac{-2R_j}{\lambda_e(k)}} e^{-2k^2\sigma_j^2} \sin(2kR_j + 2\delta_1(k) + \arg(f_j(k)) \tag{3.14}$$

where N_j is the number of atoms in the j^{th} coordination shell, and the *Debye-Waller factor* σ_j^2 is the mean square variation of distances from R_j for the atoms in the j^{th} coordination shell.

This last quantity is also indicated as mean square relative displacement (MSRD) and, as it is explained above, it gives an indication of the disorder in the local crystal structure of the measured material.

XAS spectra can be acquired in transmission or fluorescence mode. The former is the most straightforward, in which the striking radiation and the one transmitted by the sample are measured. The latter is used when the sample is too diluted or absorbs too much: in this case, the fluorescence radiation, due to the absorbing atom disexcitation is measured. Another method, similar to fluorescence mode, is the electron yield mode, where, during relaxation, electrons emitted form the surface of the sample are considered, rather than the photons of the fluorescence radiation.

3.9 Other experimental techniques

The techniques described in the previous sections have been primarily used for the experimental activity reported in this thesis. In addition, some experimental results showed in the next chapters refer to other experimental methods. In this regard, a brief introduction for each technique is given in the related chapter before reporting and commenting the results.

[3.1] H.J. Fecht, E. Hellstern, Z. Fu, W.L. Johnson, *Nanocrystalline metals prepared by high-energy ball milling*, Metall. Mater. Trans. A 21, 9 (1990) 2333-2337.

[3.2] I.H. Arita, V.M. Castano, D.S. Wilkinson, *Synthesis and processing of hydroxyapatite ceramic tapes with controlled porosity*, J. Mater. Sci. - Mater. Med. 6, 1 (1995) 19-23.

[3.3] R. Singh, J. W. J. Lillard, *Nanoparticle-based targeted drug delivery*, Exp. Mol. Pathol. 86, 3 (2009) 215-223.

[3.4] A. Sorrentino, G. Gorrasi, V. Vittoria, *Potential perspectives of bio-nanocomposites for food packaging applications*, Trends Food Sci. Technol. 18, 2 (2007), 84-95.

[3.5] C. Suryanarayana, *Mechanical alloying and milling*, Prog. Mater. Sci. 46 (2001) 1–184.

[3.6] L. Takacs, V. Šepelak, *Quantitative comparison of the efficiency of mechanochemical reactors*, J. Mater. Sci. 39 (2004) 5487-5489.

[3.7] L. Takacs and J.S. McHenry, *Temperature of the milling balls in shaker and planetary mills*, J. Mater. Sci. 41 (2006) 5246-5249.

[3.8] R. E. Shilling, M. Yang, *Attritor grinding mills and new developments*, Journal of Coatings Technology, September 1 (2000).

[3.9] G.J. Fan, M.X. Quan, Z.Q. Hu, *Metastable phases formation induced by mechanical alloying*, J. Mater. Sci. 30, 19 (1995) 4847-4851.

[3.10] S. Morrell, Y.T. Man, *Using modelling and simulation for the design of full scale ball mill circuits*, Miner. Eng. 10, 12 (1997) 1311-1327.

[3.11] B. Bandyopadhway, A. Ghoshray, N. Chatterjee, *Development of a sievert's type gas doping apparatus*, Bull. Mater. Sci. 9, 4 (1987) 305-308.

[3.12] G.W.H. Höhne, W.F. Hemminger, H.J. *Flammersheim, Differential Scanning Calorimetry – 2nd Ed.*, Springer-Verlag Berlin Heildelberg (2003).

[3.13] A.A. Levchenko, G. Etherington, K.Gross, *Simultaneous calorimetric and gas sorption measurements provide vital information for developing future hydrogen storage materials*, International Gas & Instrumentation, May/June 2009.

[3.14] C. Milanese, A. Girella, S. Garroni, G. Bruni, V. Berbenni, P. Matteazzi, A. Marini, *Effect of C (graphite) doping on the H_2 sorption performances of the Mg-Ni storage system*, Int. J. Hydrogen Energy 35,3 (2010), 1285-1295.

[3.15] G.A. Lozano Martinez, *Development of Hydrogen Storage Systems using Sodium Alanate - PhD Thesis*, Helmholtz-Zentrum Geesthacht (HZG), Zentrum für Material- und Küstenforschung (2010).

[3.16] C. Kittel, *Introduction to Solid State Physics, 8^{th} edition*, John Wiley (2005).

[3.17] H. Wiedemann, *Synchrotron Radiation, 1^{st} edition*, Springer (2002).

[3.18] H.M. Rietveld, *A profile refinement method for nuclear and magnetic structures*, J. Appl.Cryst. 2 (1969) 65-71.

[3.19] A. Albinati, B.T.M. Willis, *The Rietveld method in neutron and X-ray powder diffraction*, J. Appl. Cryst. 15 (1982) 361-374.

[3.20] L. Lutterotti, H. Wenk, S. Matthies, *MAUD (Material Analysis Using Diffraction): a user friendly Java program for Rietveld Texture Analysis and more*, Proceedings of the Twelfth International Conference on Textures of Materials (ICOTOM-12): NRC Research Press (1999) 1599-1604.

[3.21] G. Bunker, *Introduction to XAFS: A Pratical guide to X-ray Absorption Fine Structure Spectroscopy*, Cambridge University Press (2010).

[3.22] D.E. Sayers, E.A. Stern, F.W. Lytle, *New technique for investigating noncrystalline structures: Fourier analysis of the extended x-ray absorption fine structure*, Phys. Rev. Lett., 27, 8 (1971) 1204–1207.

[3.23] E.A. Stern, *Theory of the extended x-ray-absorption fine structure*, Phys. Rev. B 10, 8 (1974) 3027–3037.

[3.24] T. Fujikawa, *Basic features of the short-range-order multiple scattering XANES theory*, J. Phys. Soc. Jpn., 62, 6 (1993) 2155–2165.

Chapter 4

Investigation on the nanostructured $LaNi_5$ alloy

4.1 Motivation for this study

The intermetallic $LaNi_5$ alloy is one of the most studied solid-state hydrogen storage materials – a preferred choice for the prototype systems using hydrogen fuel. For this material hydrogen absorption and release process can be performed at room temperature and not high pressure (e.g. equilibrium $LaNi_5/LaNi_5H_6$ plateau pressure is 2 bar at 298 K) **[4.1]**.

As a well known material, it appeared as an ideal standard to be used in order to test the *Sievert*'s type equipment and other experimental devices, used for the evaluation of hydrogen sorption properties of the materials, at the ITA – Institute for Advanced Technology – laboratory, where most of the experimental work reported in this thesis has been carried out. Within this context, an experimental campaign on $LaNi_5$ compound has been performed in order to set-up the instrumentation, but interestingly, during this time, some unexpected and remarkable information on such a material have been obtained. It was found that unlike some other potential hydrogen storage materials, that show faster hydrogen absorption-desorption kinetics upon nanostructuring, the long-time ball milling of the bulk $LaNi_5$ has an adverse effect on the hydrogen sorption reactions **[4.2]**.

In this chapter, the study carried out on nanostructured $LaNi_5$ powders is presented. Different experimental techniques, such as volumetric-manometric measurements, differential scanning calorimetry (DSC), X-ray powder diffraction (XRPD), together with X-ray absorption fine structure spectroscopy (EXAFS), have been used to investigate different $LaNi_5$ samples. A brief description of the volumetric-manometric measurements, DSC, XRPD

and EXAFS are given in **sections 3.3**, **3.4**, **3.7** and **3.8**, respectively. Further details on these techniques can be obtained from the cited references therein.

4.2 Effect of ball milling time on the hydrogen sorption properties of $LaNi_5$

Hydrogen storage grade $LaNi_5$ purchased by Sigma-Aldrich was used for the present study. Ball milling of this materials was carried out in a *FRITSCH* planetary mill (*Pulverisette 6*), using a hardened steel vial and stainless steel balls, at a speed of 240 rotations-per-minute with a ball to powder ratio of about 10. Milling was carried out in cycles of 20 minutes milling and 20 minutes pause to avoid the heating of the powders during the milling process. Different samples were prepared by milling for different times, i.e. 2, 5, 10, 15, 20 and 100 h.

Figure 4.1 shows the PCI absorption curves (Re-hydrogenation) at 35 °C for one as received and three ball milled (2, 20 and 100 h) $LaNi_5$ samples. Pressure Composition Isotherms (PCIs) curves of the ball milled samples are quite different compared to the PCI of the as-received sample.

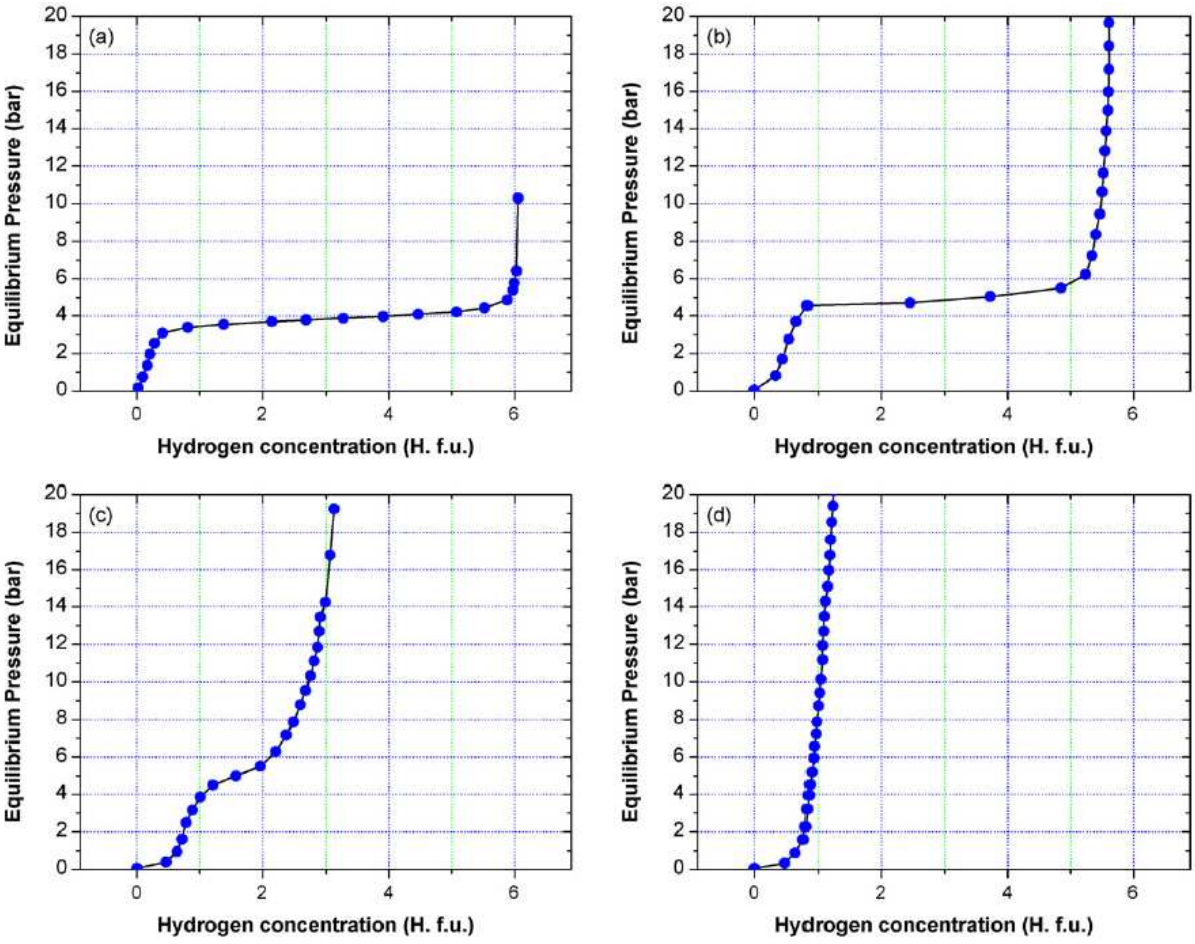

Figure 4.1 *Re-hydrogenation PCI curves at 35 °C for (a) as-received, (b) 2 h milled, (c) 20 h milled and (d) 100 h milled $LaNi_5$ samples.*

As shown in **figure 4.1**, at pressures below 20 bar, the maximum hydrogen storage capacity of $LaNi_5$ decreases gradually by increasing the milling time. There is also a noticeable increase in the plateau pressure for the 2 h and the 20 h milled samples. For the 100 h milled sample, there is almost no plateau region in the PCI curve.

The X-ray diffraction (XRD) studies of Jurczyk et al. show that such a pressure–composition behaviour is due to amorphised $LaNi_5$ particles **[4.3]**. According to what reported in this cited work, the amorphous phase does not contribute to the hydride phase formation, and this causes a decrease in the hydrogen storage capacity with increase in the amorphisation.

Ball milling is a non-equilibrium process **[4.4]**, and thus, by using it, there are chances for the creation of some phases, which are otherwise difficult to form. The reduction in the storage capacity observed in the ball milled samples could be due to either the formation of a non-absorbing amorphous phase **[4.3]**, or other effects that ball milling process generates on the material's lattice. The cause, as it will be explained below, looks like the latter.

Although the results shown in **figure 4.1** suggest that the hydrogen storage capacity decreases by increasing the ball milling time, an independent kinetic measurement with a high starting pressure (around 100 bar), reported in **figure 4.2**, showed that the 100 h milled sample absorbs hydrogen up to the expected maximum capacity, but with slow absorption kinetics, if compared to the as-received sample.

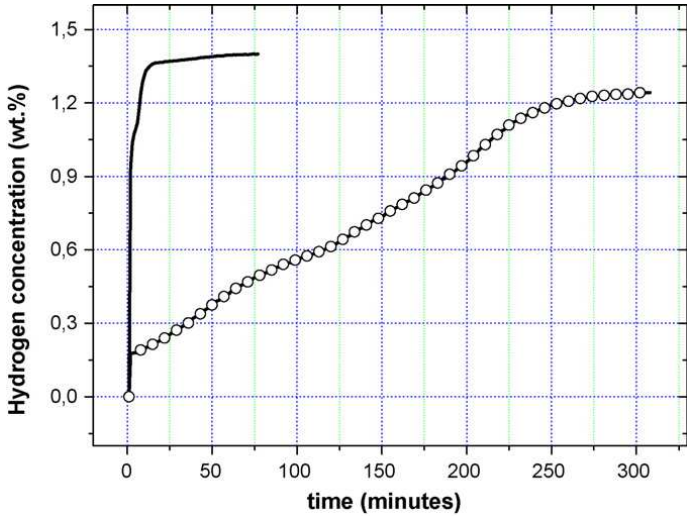

Figure 4.2 *Absorption kinetics for 100h ball milled sample (open circles) at 35 °C and 100 bar of hydrogen pressure. The corresponding curve for the as-received $LaNi_5$ is also reported for comparison (continuous line).*

Under identical conditions with an applied pressure of 20 bar, the 100 h milled sample hardly absorbs any hydrogen, as it is also evident from the PCI curve shown in **figure 4.1 (d)**. These results support the idea that there is not any non-absorbing phase, but rather the presence of an effect that hinders the hydrogen uptake at the same pressure at which as received $LaNi_5$ sample achieves the full hydrogen capacity. In absence of this hindering effect, one would have expected the ball-milled $LaNi_5$ powder to be a better hydrogen storage

media with faster kinetics, if compared with the un-milled material. However, possibly due to the formation of an anomalous state that is very resistant to hydrogen absorption at low pressures, the ball-milled $LaNi_5$ powders show rather poor hydrogen storage properties compared to the un-milled samples. X-ray diffraction and X-ray absorption measurements, performed on the $LaNi_5$ samples, gave some elements for the interpretation of the ball milling effect **[4.5] [4.6]**, which determines the resistance to the hydrogen sorption properties. The results are presented and discussed in **sections 4.6** and **4.7**.

It is interesting to note that some of the earlier studies **[4.7] [4.8]** showed an improvement in the kinetics of the ball milled $LaNi_5$ samples, where the milling times were significantly lower than in the present case. As shown in one of such similar study **[4.9]**, such short ball milling time only leads to particle size reduction up to few micrometers. Scanning electron microscopy studies on the cycled samples show that after a couple of absorption–desorption cycles, average particle size of $LaNi_5$ get reduced and become of the order of few micrometers **[4.10]**. Thus, ball milling for times lower than 1 h, essentially leads to somewhat similar effects as that of the hydrogen absorption–desorption cycling; actually, that effect is known as “decrepitation” of the material **[4.11]**. Thus, short-time ball milling can lead to an improvement in the kinetics of $LaNi_5$ samples compared to un-activated powders.

A careful look at the data presented in **figure 4.1** reveals that for the milled samples there is a significant absorption at very low pressures (initial part of the PCIs), whereas for the un-milled sample [**figure 4.1(a)**], there is almost no absorption until the applied pressure reaches a value close to the plateau pressure. As mentioned earlier, milling causes defects creation and particles size reduction. The hydrogen intake observed for the milled samples at very low pressures is mostly due to the hydrogen adsorption at the defect-states in the surface. If only the low pressure hydrogen sorption processes are considered, the ball milled samples have clearly higher performances. Annealing can lead to the removal of such surface defect-states, and hence the hydrogen intake observed at low pressures for the milled samples are not expected for the ball-milled-and-annealed samples. Indeed this is found to be true for annealed samples, as will be discussed later together with other effects of such a thermal treatment on the sorption properties of $LaNi_5$ samples.

4.3 Impurity analysis

Although ball milling is very effective for the nanostructuring of the powdered samples, there are chances of incorporation of very small amounts of impurities, coming from the erosion of the milling media. Such an effect was seen in an earlier study involving $LaNi_{4.2}Al_{0.8}$ samples prepared by mechanical-alloying **[4.12]**, where Auger electron spectroscopy is used to study the effect of the surface contamination due to the ball milling process. In this cited work, the system showed similar hydrogenation results as the present case and the authors attributed it to the presence of the Fe impurities in the ground powders.

In the present case, also one may expect a slight contamination in the ball milled samples, the amount of impurities increasing with the increase of the milling time. Besides, the effect of such impurities would be more prominent towards smaller size particle, especially in the nanometre regime, and hence the highest time milled sample is supposed to have the largest contamination. Proton induced X-ray emission (PIXE) using 3 MeV H^+ ions is a powerful quantitative technique for the impurity analysis **[4.13]**. It is based on the analysis of the X-rays generated by the relaxation of an atom previously struck by a proton beam. Electrons of inner shells of the target atom can be expulsed when protons strike. X-rays are emitted by the expulsed electrons, while they return to the original shells. The type of the emitted X-rays is strictly related to the nature of the target atom. Thus, PIXE provides an elemental analysis of the sample. The probability of X-ray production from the sample depends on the total number of incident protons, as well as on the protons energy. The greater is the protons flux, the greater is the probability for X-ray production. If quantitative analysis is to be ensured, then both of these factors must be accurately known. The information that PIXE technique provides is in the range of few micrometres and hence the results do not get affected by surface process, like segregation of impurities **[4.14]**. PIXE results from the milled samples indicated that no heavy elements impurities like Fe are present above the ppm-levels (the detection limit of PIXE) in the long-time ball milled samples. The iron presence was checked by comparing the PIXE spectra of the milled samples with a standard sample containing 10 ppm of Fe. These results clearly indicate that Fe contamination, whether present, cannot induce prominent effects in the present ball-milled samples. Thus, it is most probable that the long time ball milling induces the creation of some anomalous state in $LaNi_5$, causing resistance to the hydrogen absorption.

4.4 DSC studies

Upon several absorption-desorption cycles the bulk $LaNi_5$ is found to contain particles with a reduced grain size together with many defects and dislocations **[4.15]**. DSC is one of the effective methods to study the annealing-behaviour of lattice defects in $LaNi_5$, because an excess energy of lattice defects can be detected directly as exothermic features in the heating run of DSC **[4.16]**.

Figure 4.3 shows the DSC curves of both an as-received sample and a well activated $LaNi_5$ (a sample which underwent several absorption-desorption cycles) powders. There is hardly any feature in the DSC plot of the as received sample (solid line). In contrast, for the activated $LaNi_5$ sample (open circles), the DSC curve shows an enhanced heat flow signal from 200 °C onwards. Under this condition, in order to see the annealing effects more clearly, an isotherm of 500 °C for 10 min has been added at the end of the first run, before performing the subsequent scan. The curve after this annealing at 500 °C (filled circles) is more similar to that of the as-received sample, a result in agreement with the results reported by Nakamura et

al **[4.16]**. **Figure 4.4** shows the results of the first, second and third DSC runs on a 10 h milled sample. The three curves have been obtained with the same procedure as above, with an isothermal segment in between. Unlike the as-received sample, the 10 h milled sample showed an enhanced heat flow in the DSC curves. Second and third DSC runs on the 10 h milled samples show similar annealing behaviour as that of the cycled sample. These results clearly show that the ball milling introduce defects in the $LaNi_5$ lattice in addition to the particle size reduction.

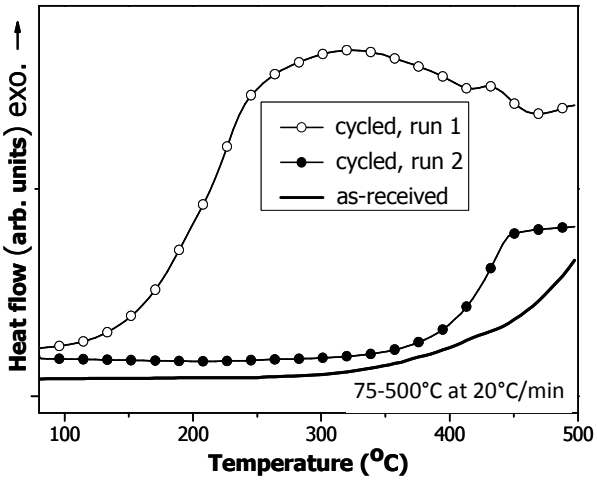

Figure 4.3 *DSC plots for as received (solid line) and cycled (circles) $LaNi_5$ samples. Open circles represent the first run, while filled circles represent the second run (performed after an isotherm at 500 °C for 10 minutes).*

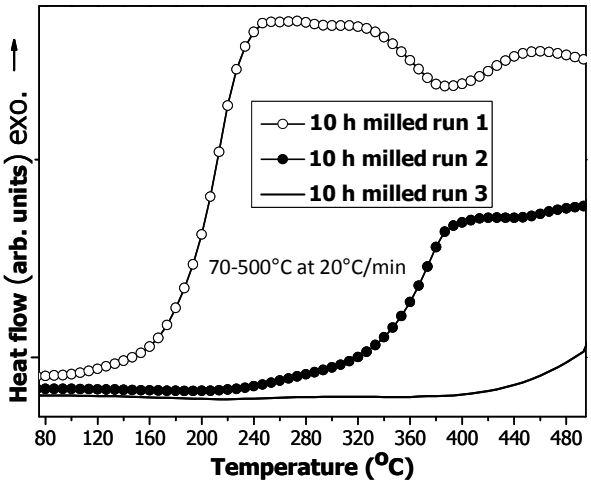

Figure 4.4 *DSC plots for 10 h milled $LaNi_5$ sample for first (open circles), second (filled circles) and third (solid line) DSC runs.*

Figure 4.5 shows the results of the DSC measurements on samples ball-milled for different times. For clarity, the results are presented in three frames with identical y-scale. In each frame, the profile of the as-received (and not cycled) sample is also included for comparison (solid line). In all samples one can observe the effect of defects similar to that of the cycled sample (see **figure 4.3**). In addition, the heat flow is found to increase with increasing the milling time indicating an increase in the defects density.

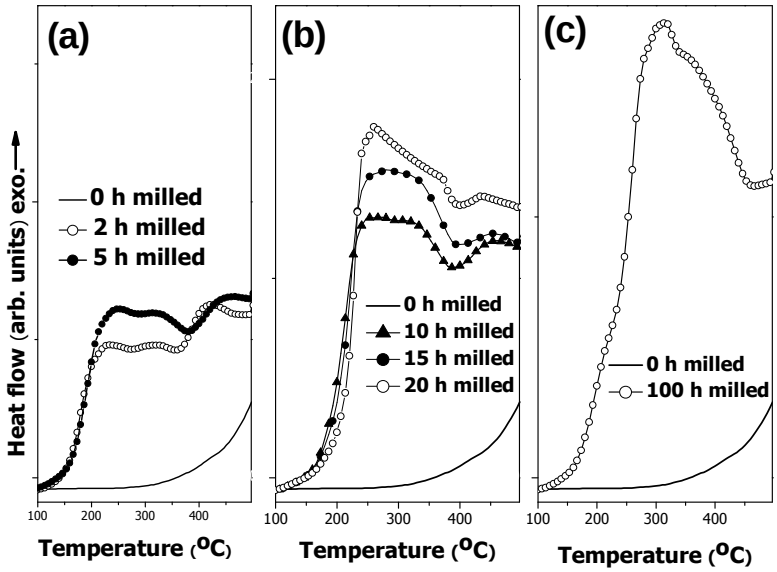

Figure 4.5 *DSC plots for ball milled samples. Results are presented in three frames for clarity. Legends indicate the ball milling time. Y-scale is identical for the three frames. In all the frames, the profile corresponding to the as-received sample (0 h milled) is also included for comparison.*

4.5 Effect of the annealing on the hydrogen sorption properties

The 20h and 100 h ball-milled samples were further studied after an annealing under high vacuum at 730 °C for 1 h. The re-hydrogenation PCI curves (i.e. second PCI run, after activation) at 35 °C of the ball milled and annealed samples are shown in **figure 4.6**.

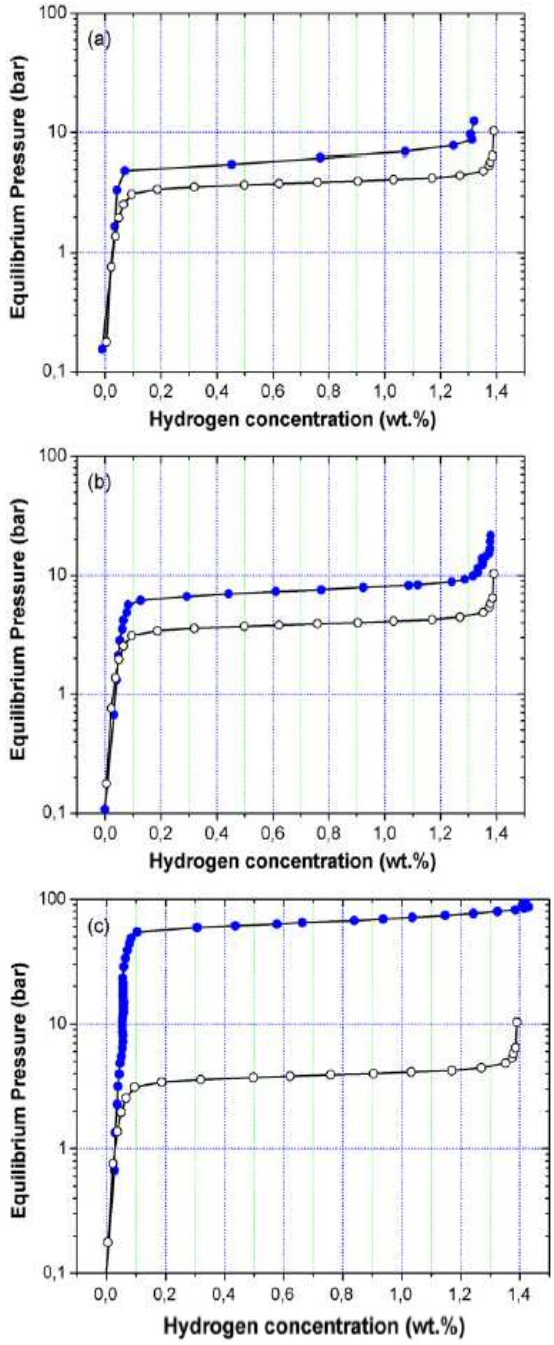

Figure 4.6 *Re-hydrogenation PCI curves at 35 °C for milled-and-annealed $LaNi_5$ samples (solid circles): (a) 2 h, (b) 20 h and (c) 100 h. In all the cases, the re-hydrogenation curve corresponding to the as-received sample before annealing (open circles) is also included for comparison.*

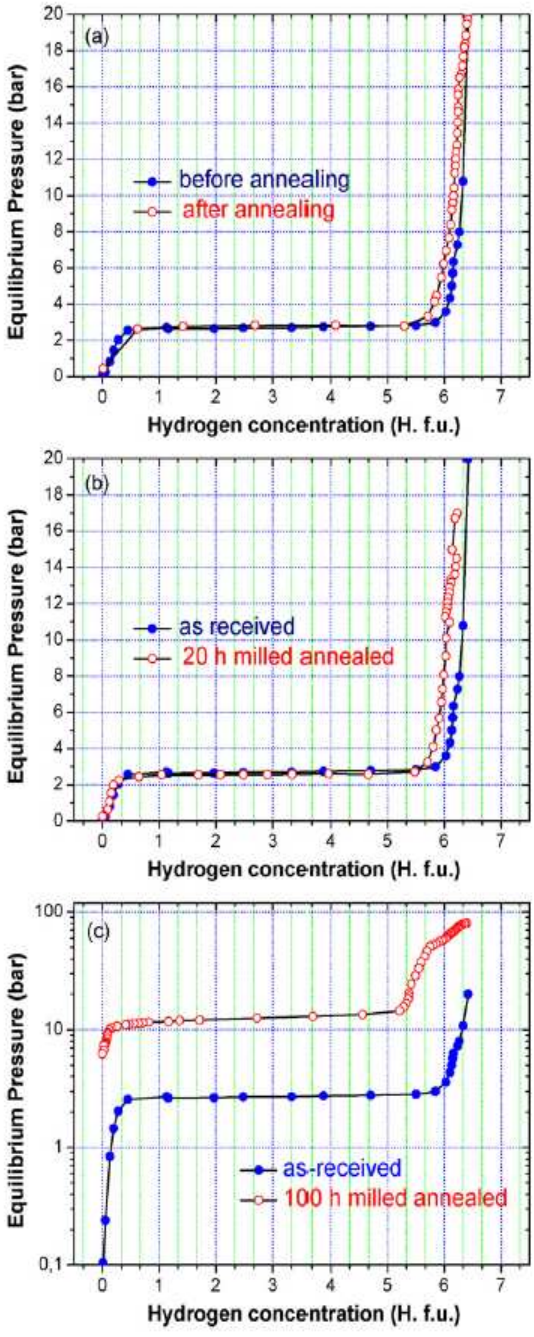

Figure 4.7 *Dehydrogenation PCI curves at 35 °C for the annealed $LaNi_5$ samples (open circles): (a) as-received, (b) 20 h milled and (c) 100 h milled. In all the cases, the dehydrogenation curves corresponding to the as-received sample before annealing (solid circles) is also included for comparison.*

For comparison, the re-hydrogenation data corresponding to the as-received sample is also included in the figure. This comparison shows that there is a clear increase in the plateau pressure of the ball milled and annealed samples. The plateau pressure is found to increase by increasing the milling time. A comparison between **figures 4.1** and **4.6** clearly shows the difference in the low-pressure–absorption behaviour of the as milled and the milled-and-annealed samples (initial parts of the PCI curves). As mentioned earlier, for the annealed samples there is almost no absorption at very low pressures. This is due to the absence of the surface defects that were causing adsorption in the case of the milled samples. The maximum absorption capacity of the ball-milled samples after annealing is almost identical to that of the as-received sample; however, there is a difference in the plateau pressure. This change is maximum for the 100 h milled-and-annealed sample. The dehydrogenation PCI curves of the ball-milled-and-annealed samples at 35 °C are shown in **figure 4.7**. As expected, the dehydrogenation PCI curves of the as-received sample after annealing have exactly the same behaviour as that of the sample before annealing [graph (a)]. Interestingly, there is also a good overlap between the dehydrogenation PCI curve of the 20 h milled-and-annealed sample and that of the as-received sample [graph (b)]. However, in case of the 100 h milled-and-annealed sample, there is a significant increase in the dehydrogenation plateau as compared to the as-received sample. It is interesting to recall that in the as milled case, the 100 h milled sample did not show any plateau in the re-hydrogenation process (below 20 bar).

To investigate more deeply the cause of the poor absorption properties of the long time ball milled samples, XRPD and EXAFS studies have been carried out. Below the details and results about these measurements are reported.

4.6 XRPD analysis

These measurements were carried out using a custom-made laboratory XRPD set-up with Cu K-α radiation. *Rietveld* method refinements of the diffraction data were carried out in order to obtain the structural parameters. A brief description of the *Rietveld* refinement method as well on the XRPD is described in **section 3.7** of this thesis. The refinements of the XRPD spectra have been performed using the free software package *MAUD* **[4.17]** based on the *Rietveld* refining method. **Figure 4.8** presents the XRPD pattern corresponding to the bulk (i.e. not milled) $LaNi_5$ sample. The curve calculated as a fit of the experimental pattern is also reported, as well as the different reflections identified from the refinement. From the difference spectrum reported, it is clear that the assumed crystal structure gives an excellent descriptions of the experimental data. A schematics diagram of the $LaNi_5$ unit-cell used for the refinement is shown in the inset of the figure. The excellent agreement between the experimental and the calculated curve implies that the structural model used for the refinement is in fact the long-range structure of the system. The structural model of the $LaNi_5$ is well established from the earlier studies **[4.18]** **[4.19]** **[4.20]** **[4.21]** **[4.22]** **[4.23]** and

belongs to the hexagonal $CaCu_5$-type with P6/mmm symmetry. The refinement results (reflections, atomic positions and thermal factors, lattice parameters, etc) obtained in the present case are consistent with these earlier reports and some of them are listed in **table 4.1**.

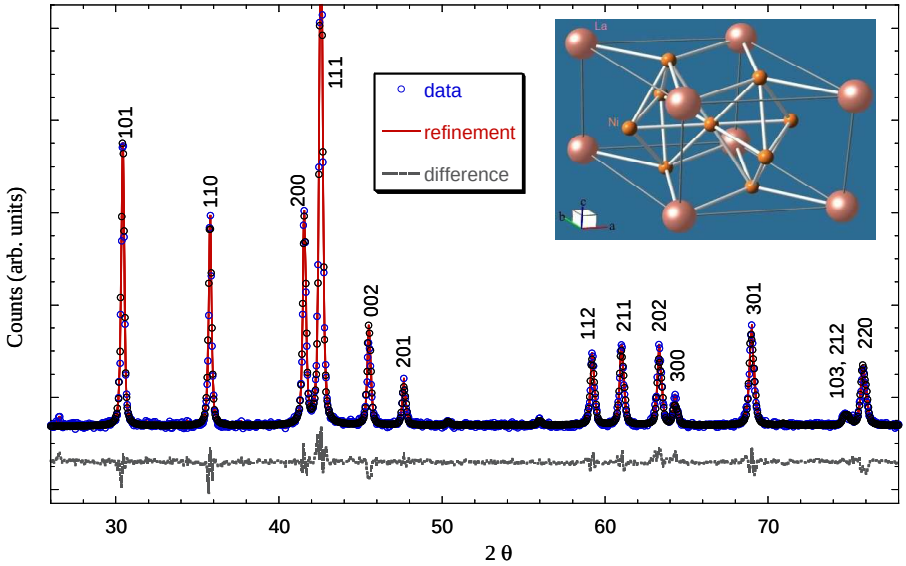

Figure 4.8 *XRPD pattern (blue open circles) obtained for $LaNi_5$ bulk (i.e. not milled) sample. The fitting (red) and the difference (grey) curves and the identified reflections (black numbers) are reported, as obtained from the Rietveld refinement performed with the MAUD software. The inset shows the $CaCu_5$-type cell of $LaNi_5$, where the larger spheres represent the La atoms.*

Once established the structure of the bulk $LaNi_5$, the structure of the 20 h and 100 h milled samples is now discussed. The XRPD patterns corresponding to these three samples are shown in **figure 4.9**. The 20 and 100 h milled samples have all the diffraction peaks as the bulk sample, however, the peaks intensities are found to be progressively damped and peaks are become broadened with the increasing milling time. Such features in the XRPD profiles are typical of the nanoparticles. The fitting (solid) curves, obtained with the refinement of the experimental patterns (open circles) are also included in the figure.

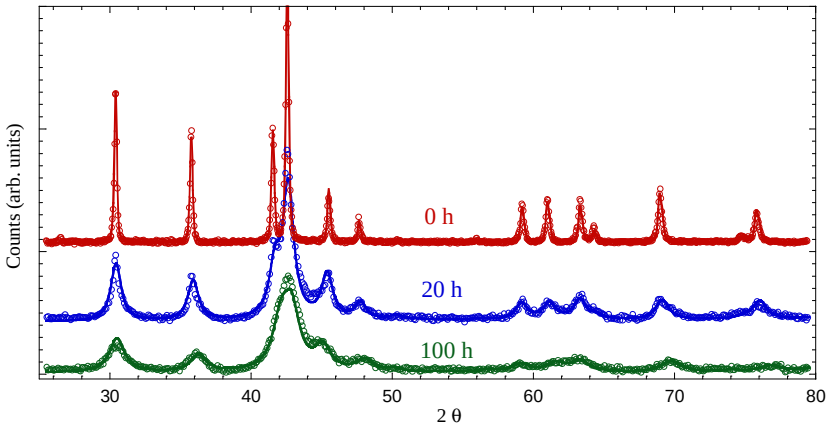

Figure 4.9 *Comparison among XRPD patterns of the bulk (red), 20h milled (blue) and 100h milled (green) samples. The curves calculated by Rietveld refinement of the experimental patterns (open circles) are included as solid lines. With increasing milling time, diffraction peaks are getting broader with reduced intensity, indicating nanostructuring.*

The refinements for the 20 h and 100 h milled samples were carried out using the same $LaNi_5$ structural model as that given above. A summary of the refinement results, obtained by using the *MAUD* software package **[4.24]** and including the estimated crystallite sizes for the 20 and 100 h milled samples, are given in **table 4.1**. Although the milled samples are found to have identical crystal structure as the bulk, the corresponding lattice parameters result slightly different: in particular the lattice parameters *a* and *b* are found to become progressively lower with increasing milling time.

Table 4.1 *Results of the Rietveld refinements performed on the experimental XRPD spectra.*

Sample	*Rwp*(%)	*a*=*b* (Å)	*c* (Å)	Crystallite size (nm)
bulk	1.45	5.0160(4)	3.9836(3)	–
20 h	4.9	5.0106(6)	4.001(8)	12.3(±3)
100 h	20	4.975(3)	4.036(4)	8.3(±5)

$LaNi_5$ space group P6/mmm $\alpha=\beta=90$, $\gamma=120$. La (site1a) x 0.0, y 0.0, z 0.0; Ni (site 2c) x 1/3, y 2/3, z 0.0; Ni (site 3g) x 1/2, y 0.0, z 1/2.

As known, the reduction of particle size up to nanometer range can increase the kinetics, but can also cause a favourable change in the thermodynamics of the hydrogen sorption, lowering the reactions energetics, decreasing the hydrogen release temperature, and improving the system reversibility **[4.25]**. This is because of the coexistence of different conditions at nanoscale, enhancing the material reactivity, such as the increase of the surface to volume ratio (and thus also an higher contribution of physisorption), the increase on the number of absorption sites, and the lower binding energy in small metallic cluster, also due to a lower coordination effect on the surfaces. Moreover, as a consequence of the higher surface area and the surface effects, the catalysts action is enhanced **[4.26]**. However, in order to cause such a modification of thermodynamics, particles size should be reduced up to 1-2 nm, and this can be obtained by using light scaffolds with high surface area, e.g. carbon based nanomaterials **[4.27] [4.28] [4.29]**. In this case, surface energies and material properties of the materials at nanoscale offer the opportunity to tune the energetics of hydrogen adsorption. However, in the case of our nanostructured $LaNi_5$ samples, even the crystallite sizes are bigger than those that should be achieve, in order to have a favourable change on system thermodynamics. In addition, the ball milling process, while reducing the crystallite size, seems also to cause the material to be more resistant to hydrogen absorption and release. For this reason, further investigations have been performed in order to clarify the causes.

4.7 EXAFS measurements

XRPD is a long-range structural probe and gives information on the average crystal structure of the system. In many cases, to gain more understanding, local structural probes are

quite useful. EXAFS is a powerful local structural techniques providing site selected local structural information. As a recent example, EXAFS measurements on the superconducting $FeSe_{1-x}Te_x$ have provided evidence for the nanoscale chemical phase separation, which were not seen by the average structural probes **[4.30]**. To deeper investigate the ball milling effect, responsible of the poor absorption properties of the long time ball milled $LaNi_5$ samples, X-ray absorption studies have been carried out at XAFS beamline of the *Elettra* synchrotron radiation facility, in Trieste (Italy). La L_3-edge and Ni K-edge X-ray absorption measurements have been performed on $LaNi_5$ samples. The temperature of the measurements was 90 K for the former and 80 and 300 K for the latter type of measurement; three ionization chambers mounted in series were used for simultaneous measurements on the sample and a reference. As mentioned earlier, a brief description of the EXAFS techniques is reported in **section 3.8** of this thesis.

Figure 4.10 shows EXAFS oscillations (multiplied by k^3) extracted from room temperature Ni K-edge extended X-ray absorption spectra, measured on the $LaNi_5$ powders with variable ball milling time. The EXAFS amplitude decreases with increasing milling time. The decrease is substantial for the 20 h milled powders compared to the bulk (i.e. as prepared), while the changes from 20 to 100 h are not so significant. Incidentally, such a damping is known to occur in several systems when the bulk is nanostructured. For example, Au, Cu, Ni and Te nanoparticles **[4.31] [4.32] [4.33] [4.34]**, nanocrystalline Fe prepared by ball milling **[4.35]**, substrate-free Pd nanoparticles prepared by evaporation **[4.36]** and Ge **[4.37]** and Pt **[4.38]** nanoclusters synthesized by ion implantation are found to show a systematic damping of the EXAFS oscillations compared to the bulk.

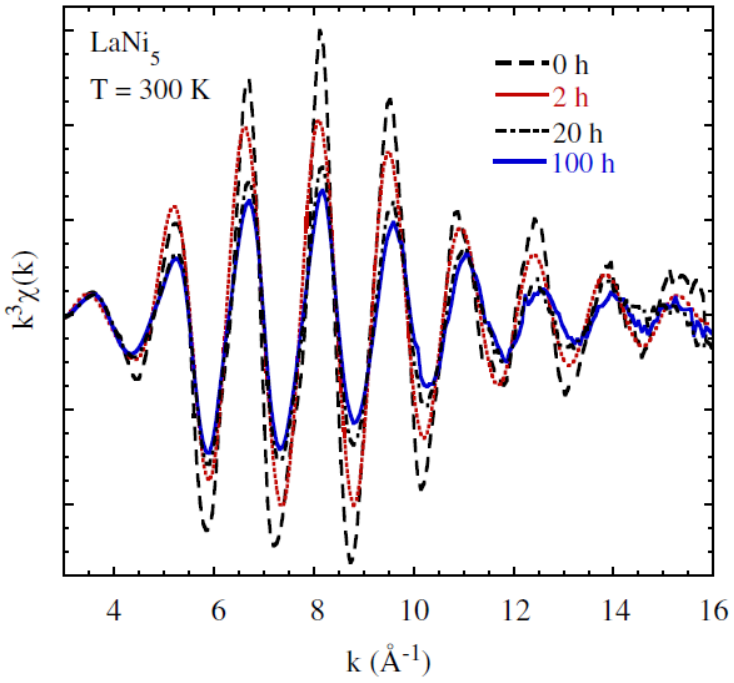

Figure 4.10 *EXAFS oscillations (multiplied by k3) extracted from room temperature Ni K-edge extended X-ray absorption spectra of $LaNi_5$ with different ball milling times. Legends indicate milling times, where 0 h correspond to the unmilled (bulk) sample. With increasing milling time the EXAFS oscillations are getting damped, indicating nanostructuring and an enhanced atomic disorder (as explained below).*

As in the XRPD case, first the analysis of the bulk sample was performed, in order to extract the quantitative local structural information. Later the same analysis procedure was

applied to milled samples. **Figure 4.11** shows the *Fourier* transform (FT) magnitude corresponding to the EXAFS oscillations of the bulk sample, revealing the real space information. FTs were performed in the *k* range 2.9-17 $Å^{-1}$.

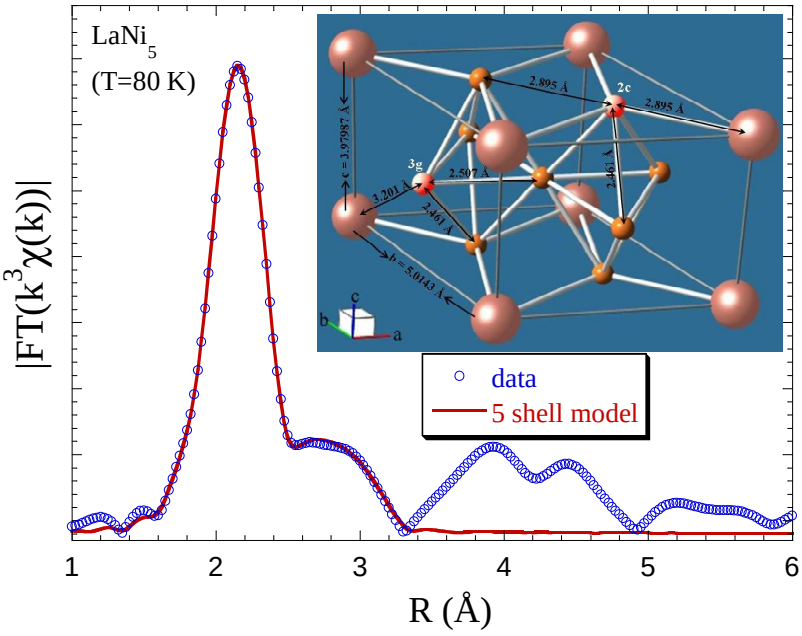

Figure 4.11 *Fourier Transforms (FT) of the EXAFS oscillations (multiplied by k3), extracted from temperature Ni K-edge extended X-ray absorption of the bulk $LaNi_5$ sample, and showing the real space information. The main peak corresponds to the contributions of the three Ni-Ni and Ni-La single scatterings, for the two types of Ni central atoms (Ni 3g and Ni 2c, highlighted in red in the inset). The fitting curve (red) obtained with a five coordination shells model shows a good overlap with the experimental data (blue) in the main peak region.*

In order to obtain quantitative information, the EXAFS oscillations have been modelled by using a standard procedure **[4.39]**, according to which one starts considering the average structure of the compound. From the average structural data inferred from the XRPD, two distinct Ni sites can be identified in the crystal structure. These sites are highlighted in red in the structural model given in the inset of **figure 4.11**. Different near-neighbour arrangements for the two Ni sites make the Ni K-edge EXAFS measurements somewhat complicated. The structural configuration of $LaNi_5$ gives rise to three Ni–Ni near neighbours distances (~2.46, ~2.5, and ~2.85 Å) and two Ni–La near-neighbour distances (~2.9, and ~3.2 Å). For a proper treatment of the Ni K-edge EXAFS data of $LaNi_5$, it is important to consider the presence of the two distinct Ni sites mentioned above. From the Ni 3g site, the first three types of near neighbours are four Ni atoms at ~2.46, four at ~2.51 Å and four La atoms at ~3.2 Å, whereas from the Ni 2c site, the first three types of near neighbours are six Ni atoms at ~2.46 Å, two Ni atoms at ~2.85 Å, and two La atoms at ~2.89 Å. As the EXAFS signal from the two Ni sites cannot be distinguished, we have adopted a method of weighted average from the two Ni site contributions to model the data **[4.5]**. It is to be recalled that the earlier EXAFS studies on this system have over looked this fact and assumed only an average Ni–Ni distance for the analysis of the EXAFS data **[4.40] [4.41] [4.42]**. The main peak in the FT (in **figure 4.11** between 1.3 and 3.4 Å) is due to the Ni–Ni and Ni–La single scatterings. This corresponds to the above discussed three near neighbour contributions from both the two Ni sites. To obtain quantitative information, the EXAFS signal has been modelled using the *WinXAS* program **[4.43]** with calculated phase and amplitude functions from the *FEFF7* program **[4.44]**. According to the description of the EXAFS technique, reported in **section 3.8**, the EXAFS

amplitudes depend on several factors and can be represented by the following general equation:

$$\chi(k) = \sum_i \frac{N_i S_0^2}{kR_i^2} \left| f_i(k, R_i) \right| e^{\frac{-2R_i}{\lambda_e(k)}} e^{-2k^2\sigma_i^2} \sin\left[2kR_i + 2\delta_i(k)\right] \qquad (4.1)$$

where N_i is the number of neighbouring atoms at distance R_i, S_0^2 is the passive electrons reduction factor, $F_i(k,R_i)$ is the backscattering amplitude, λ is the photoelectron mean free path and σ is the correlated *Debye-Waller* factor (DWF), measuring the mean square relative displacements (MSRDs) of the photo-absorber-backscatter pair. Apart from these, the photoelectron energy origin E_0 and the phase shifts details should be known. It has been used a conventional procedure to analyze the EXAFS signal **[4.45]** with five coordination shells (three Ni-Ni and two Ni-La distances). Except for the radial distances R_i and the corresponding DWFs, all other parameters were kept fixed in the least squares fit. The co-ordination numbers were fixed to the weighted average of the same from the two Ni sites. The passive electron reduction factor S_0^2 was kept to 1. The E_0 was fixed to -8.9 eV. The number of independent data points N_{ind} was 18 for the present analysis. The five shells fit described above is also included in the FTs as solid red line. To verify the quality of such a modelling, one can look into the filtered EXAFS oscillations corresponding to the modelled r-space, and the related fitting curve, reported in **figure 4.12**. There is an excellent agreement between the model data and the experiments, indicating that the used model **[4.5]** gives an excellent description of the local structure around Ni.

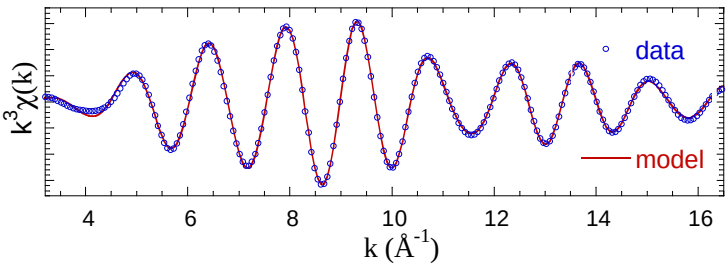

Figure 4.12 *Comparison between the experimental data (blue) and the model (red) for Ni K-edge extended X-ray absorption oscillations (multiplied by k3) for the bulk $LaNi_5$ sample.*

We have applied the same model to the milled samples. It is found that such a modeling gives a good description of the milled samples as well, as shown in **figure 4.13**.

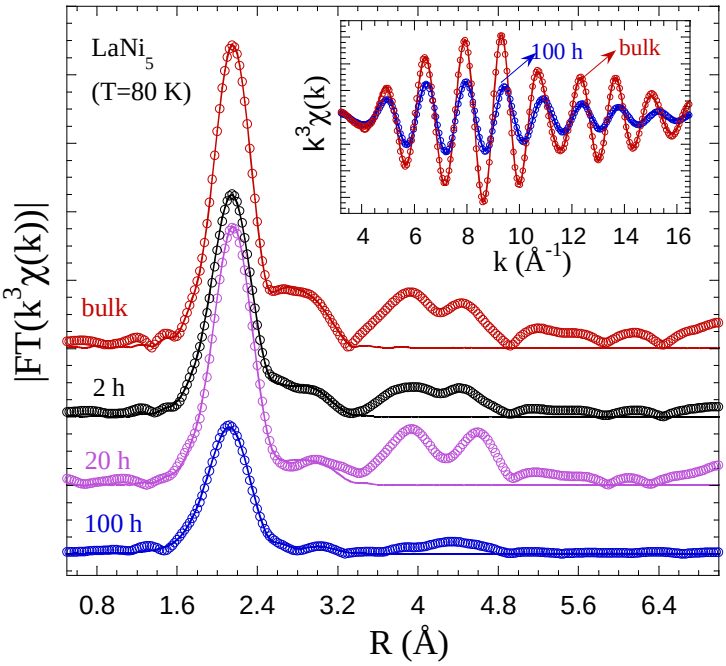

Figure 4.13 *Fourier Transforms (FTs) of the EXAFS oscillations (multiplied by k3), extracted from temperature Ni K-edge extended X-ray absorption of the $LaNi_5$ samples. The figure reports both the experimental data (open circles) and the fitting curves (solid lines) for the bulk sample and the samples ball-milled for different times. The used model shows a good agreement with the experimental data in the region of the main peak, related to the Ni-Ni and Ni-La near-neighbours single scattering contributions.*

The near neighbours bond lengths and the mean square relative displacement of the bond pairs obtained from the model above are given in table below.

Table 4.2 *Near-neighbour distances and mean square relative displacements (MSRDs), resulting from the quantitative analysis of Ni k-edge extended XAS data, performed with the WinXAS program* ***[4.43]*** *with calculated phase and amplitude parameters using FEFF7 program* ***[4.44]****.*

Milling time [h]	distance Ni-Ni$_{(1)}$ [Å]	σ^2 Ni-Ni$_{(1)}$ [Å^2]	distance Ni-Ni$_{(2)}$ [Å]	σ^2 Ni-Ni$_{(2)}$ [Å^2]	distance Ni-Ni$_{(3)}$ [Å]	σ^2 Ni-Ni$_{(3)}$ [Å^2]	distance Ni-La$_{(1)}$ [Å]	σ^2 Ni-La$_{(1)}$ [Å^2]	distance Ni-La$_{(2)}$ [Å]	σ^2 Ni-La$_{(2)}$ [Å^2]
0	2,4600 ±002	0,0039	2,5900 ±002	0,0084	2,8000 ±002	0,0047	2,9300 ±002	0,0056	3,1904 ±002	0,0046
2	2,4600 ±002	0,0049	2,5802 ±002	0,0085	2,8000 ±002	0,0063	2,9300 ±002	0,0064	3,1804 ±002	0,0067
20	2,4600 ±004	0,0049	2,5765 ±004	0,0090	2,7578 ±004	0,0065	2,9300 ±004	0,0080	3,1900 ±004	0,0080
100	2,4600 ±006	0,0078	2,6445 ±006	0,0124	2,7247 ±006	0,0132	2,9300 ±006	0,0081	3,1076 ±006	0,0100

Unlike the Ni sites, local atomic configuration from the La site surroundings is simpler, due to the presence of a single crystallographic site of the La atoms in the unit-cell. Thus, La L_3-EXAFS can be used to obtain complementary local structural information. In this case, the *k*-range available is limited (only up to 9.8 Å^{-1}), due to the occurrence of the Ni K-edge absorption. Although limited, this k-range is sufficient to obtain the near-neighbour bond lengths and corresponding MSRDs around the La atom **[4.6]**. *Fourier* transforms (FTs) of the EXAFS oscillations extracted from the La L_3-edge extended X-ray absorption spectra, measured at 90 K on the $LaNi_5$ powders with variable ball milling time are shown in **figure 4.14**.

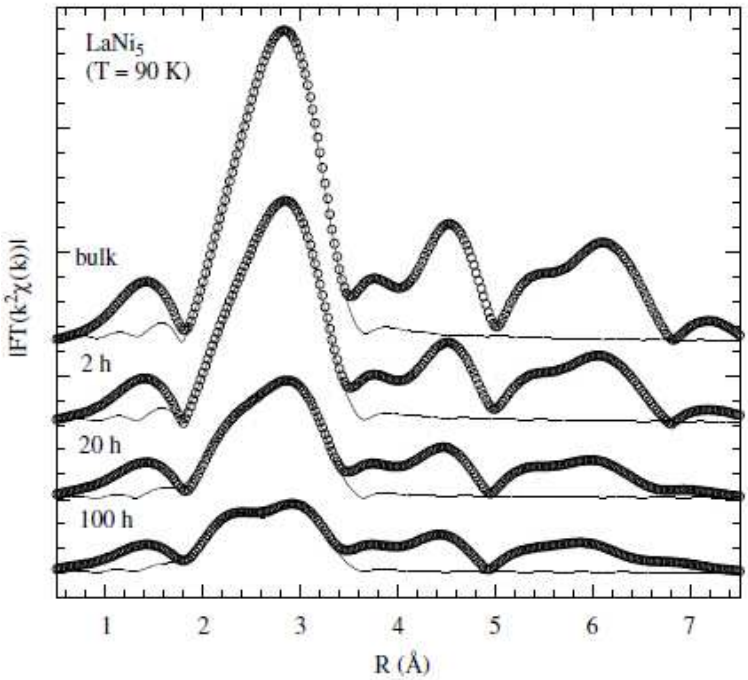

Figure 4.14 *Fourier transforms (FTs) of the La L_3-edge EXAFS oscillations showing partial atomic distribution around the La atom. FTs are performed between k_{min} = 2.5 Å^{-1} and k_{max} = 9.8 Å^{-1} using a Gaussian window. A model fit with two shells representing the two La–Ni near neighbours (solid line) is also included.*

Indeed, a large damping of the signal is clearly seen in the FT amplitude for all the atomic pairs, revealing an overall decrease of the interdistances by increasing milling time. It is to be underlined that this kind of a large damping was also seen in the Ni K-edge EXAFS results shown earlier. Similar to the Ni K-edge case, the average structure of $LaNi_5$ has been used as the input also in this case. In the crystal unit cell, La atoms occupy the 1a site, whereas Ni atoms have two different positions, viz. 3g and 2c. The unit cell of $LaNi_5$ contains 1 La atom, 3 Ni atoms at 3g sites and 2 Ni atoms at 2c sites. In this structural configuration, considering La as a central atom, there are six Ni atoms at a distance ~ 2.89 Å (2c sites) and 12 Ni atoms at a distance ~ 3.2 Å (3g sites). To analyze the EXAFS signal, a standard procedure has been adopted. For the La L_3-edge measurements a two shells fitting has been used (solid lines in **figure 4.14**), where the two shells radii correspond to the distances between the two types of Ni atoms from the central La one, respectively. The near neighbour distances and the corresponding MSRDs obtained from the La L_3-edge EXAFS spectra analysis are presented in **figure 4.15**. While the first La–Ni distance (corresponding to the six Ni atoms at the 2c sites) is found to show negligible changes with milling time, the second La–Ni distance (corresponding to the 12 Ni atoms at the 3g sites) is found to decrease with milling time. However, the MSRDs corresponding to both the distances are found to increase by increasing milling time, indicating increased atomic disorder due to milling. These results are consistent with the information derived from the Ni K-edge EXAFS spectra analysis.

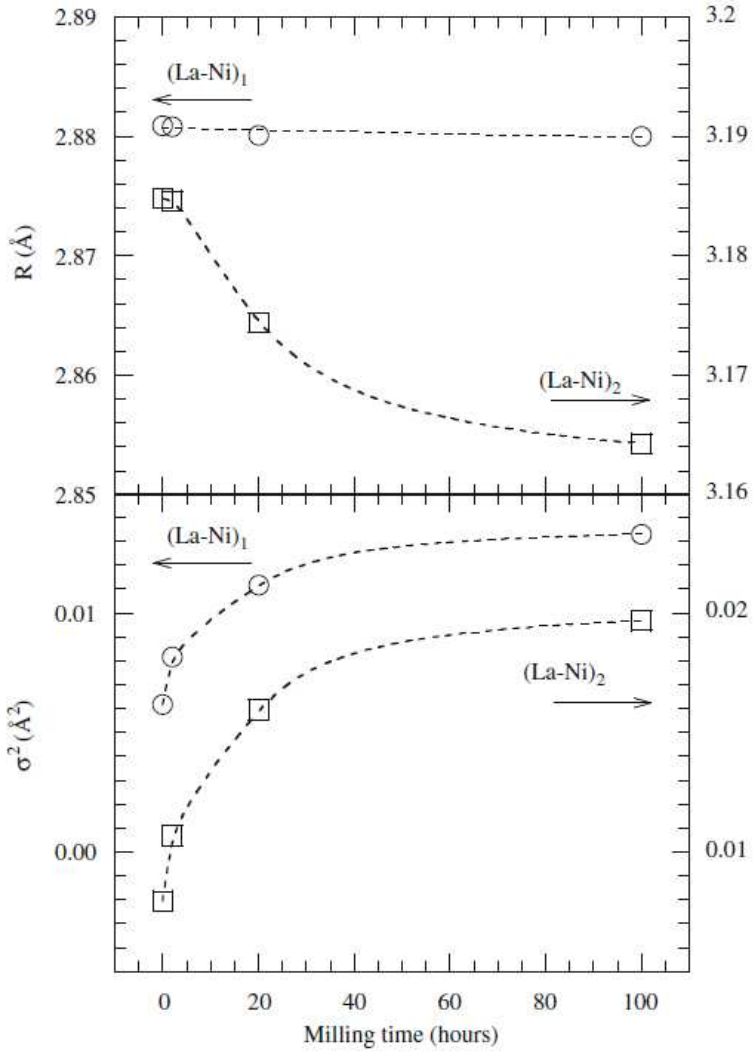

Figure 4.15 *The near-neighbour La - Ni distances (upper graph) and the corresponding mean square relative displacements (lower graph) obtained from the two shells EXAFS fit, as a function of the milling time. While the first distance remains constant (open circles), the second distance is found to decrease with milling time (open squares). However, MSRDs corresponding to both the distances are found to increase with increasing milling time, indicating increased atomic disorder. Dotted lines are only a guide to eyes.*

As well as for the ball milling, also the effect of samples annealing (already shown for the PCI measurements) can be explained referring to EXAFS results. **Figure 4.16** shows the FTs of the La L_3-edge EXAFS data for the 20 and 100 h milled-and-annealed samples, along with the data from the bulk sample. For the 20 h milled powders, annealing seems to restore the near neighbour distances to the bulk value. There is also a substantial improvement in the atomic order, as evidenced by the enhancement in the magnitude of the FTs after annealing, which closely follows the pattern of the bulk. On the other hand, for the 100 h milled sample, the high temperature annealing seems to be insufficient to restore the interatomic distances and the atomic order. In this case, a somewhat significant enhancement in the intensity of the peak corresponding to the first two set of near-neighbours (**figure 4.16**) may appear to indicate an enhanced atomic ordering. However, a careful analysis reveals that this enhancement in peak intensity is not symmetric for the two sets of near-neighbours, unlike in the 20 h case. As discussed earlier, long time ball milling results in substantial disordering in the system, and high temperature annealing of such a disordered system can possibly bring random ordering, causing a small fraction of the original Ni sites to be occupied by La. Such a random local ordering can cause enhancement in the FT intensity of the annealed sample due to the larger atomic scattering factor of the heavier element La compared to the lighter element Ni. The absence of the enhancement in FT magnitudes corresponding to the further shells (other peaks) supports the above conjecture.

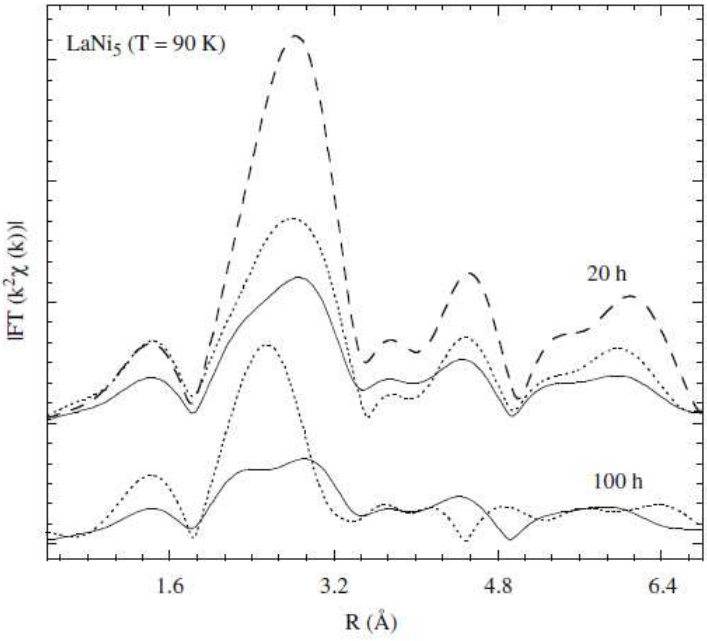

Figure 4.16 *Fourier transforms (FTs) of the La L_3-edge EXAFS oscillations measured before (solid line) and after (dotted line) the high temperature annealing. The atomic order seems to be substantially restored for the 20 h ball-milled sample after annealing, while the 100 h ball-milled sample seems to retain large disorder even after annealing. The FT of the bulk sample is also shown for comparison (dashed line).*

Referring to the hydrogen sorption curves, shown in the first part of this chapter, it is found that the capacity decreases gradually with the increasing ball milling time. However, capacity

can be regained by the high temperature annealing. After annealing, the equilibrium plateau pressure, where the continuous conversion of the α phase to the β phase (hydride) occurs, is found to be highest for the 100 h ball milled samples. Results from La L_3-edge and Ni K edge EXAFS clearly indicate that there is a decrease in the near-neighbour distances and an increase in the corresponding MSRDs for the nanoparticles of $LaNi_5$ produced by long-time ball milling of the bulk. High temperature annealing is found to result in only some random local ordering in the system, thus incapable of restoring the global atomic order in nanostructured $LaNi_5$. This increased atomic disorder in the nanostructured phase may be one of the main reasons behind the enhanced resistance towards the hydrogenation reaction of the long time ball milled $LaNi_5$.

4.8 Summary

In this chapter, a study of the influence of ball milling process on the hydrogen sorption properties of $LaNi_5$ is provided. The obtained PCI curves show a decrease in the absorption properties of the material at pressure below 20 bar, as the milling time increases, while a kinetic measurement at higher pressure revealed that the total capacity is anyway achieved also for long time (100 h) milled sample. DSC measurements indicate how ball milling creates defects on the material, in an increasing way as the ball milling time increase. This is also confirmed by the larger absorption at very low pressure, i.e. below 1 bar, showed by in the PCI curves. The effect of an annealing treatment is revealed from both the PCI and DSC curves, which show a regain of the features of the material as those before the ball milling treatment. The calorimetric profiles indicate a defects annealing, which is confirmed by the lost of hydrogen absorbed amount in the rehydrogenation PCI curves at pressure below 1 bar, for milled and annealed samples. In addition, after the annealing, both the rehydrogenation and dehydrogenation PCI curves show a regain in the total hydrogen capacity at pressure below 20 bar. However, in any case, the annealing treatment results less effective for long time milled (100 h) samples.

In order to deeper explore the reason of the reduced hydrogen uptake in the milled sample and the effect of the annealing, investigation on the average (i.e. long range) and local crystal structure of the material have been performed by XRPD and EXAFS studies, respectively. A *Rietveld* method-based qualitative and quantitative analysis, performed on XRPD spectra of the ball milled samples, showed a strong agreement between the $LaNi_5$ crystal structure as known by literature and the model used to fit the experimental data. The experimental patterns of the milled samples indicate nanostructuring of the material, and the quantitative analysis shows a decrease of the cell parameters and crystallites size, as the milling time increases. However, this does not cause an improvement on hydrogen sorption properties, but rather the ball milling reduces hydrogen sorption properties, as it has been found from PCI measurements. Ni K-edge and La L_3-edge extended X-ray absorption measurements have

been performed at the *Elettra* (Trieste, Italy) synchrotron facility. By these investigations, a reasonable motivation of the reduced hydrogen absorption properties for the ball milled samples has been proposed. Once the good agreement of the model used to fit the EXAFS data has been verified, a quantitative analysis has been performed on the absorption spectra of the $LaNi_5$ ball milled samples. Results show that, as the milling time increases, the near-neighbours distances decrease, according to the cell parameters reduction revealed by the refinements of XRPD patterns. Moreover, the mean square relative displacements of the bond lengths increase, thus revealing disorder in the local crystal structure of the milled samples. The reduction of the interatomic distances and the presence of local structural disorder are created by milling process and may cause an energy barrier to the absorption uptake on the material. Fourier transforms of the EXAFS oscillations of the milled and annealed samples confirm that annealing is useful for bringing back the system toward the conditions of the original unmilled one, even though this does not occurs for long time (100 h) milled samples. Finally, long range (XRPD) and short range investigations on the crystal structure of the $LaNi_5$ samples corroborate the results found with PCI and DSC measurements and provided a reasonable motivation of the effect of the ball milling time and of a possible subsequent annealing treatment.

[4.1] G. Liang, J. Huot, R. Schultz, *Hydrogen storage properties of the mechanically alloyed $LaNi_5$-based materials*, J. Alloys Compd. 320 (2001) 133-139.

[4.2] B. Joseph, B. Schiavo, *Effects on ball-milling on the hydrogen sorption properties of $LaNi_5$*, J. Alloys Compd. 480 (2009) 912-916.

[4.3] M. Jurczyk, M. Nowak, E. Jankowska, J. Jakubowicz, *Structure and electrochemical properties of the mechanically alloyed $La(Ni,M)_5$*, J. Alloys Compd. 339 (2002) 339–343.

[4.4] C. Suryanarayana, *Mechanical alloying and milling*, Prog. Mater. Sci. 46 (2001) 1–184.

[4.5] B. Joseph, A. Iadecola, B. Schiavo, A. Cognigni, L. Olivi, G. D'Alì Staiti, N.L. Saini, *Local structure of ball milled $LaNi_5$ hydrogen storage material by Ni K-edge EXAFS*, J. Solid State Chem. 183 (2010) 1550-1554.

[4.6] B. Joseph, A. Iadecola, B. Schiavo, A. Cognigni, L. Olivi, G. D'Alì Staiti, N.L. Saini, *Large atomic disorder in nanostructured $LaNi_5$ alloys: A La L_3-edge exdended X-ray absorption fine structure study*, J. Phys. Chem. Solids 71 (2010) 1069-1072.

[4.7] L. Zaluski, A. Zaluska, P. Tessier, J.O. Strom-Olsen, R. Schulz, *Catalytic effect of Pd on hydrogen absorption in mechanically alloyed Mg_2Ni, $LaNi_5$ and FeTi*, J. Alloys Compd. 217 (1995) 295–300.

[4.8] H. Aoyagi, K. Aoki, T. Masumoto, *Effect of ball milling on hydrogen absorption properties of FeTi, Mg_2Ni and $LaNi_5$*, J. Alloys Compd. 231 (1995) 804–809.

[4.9] S. Corré, M. Bououdina, N. Kuriyama, D. Fruchart, G. Adachi, *Effects of mechanical grinding on the hydrogen storage and electrochemical properties of $LaNi_5$*, J. Alloys Compd. 292 (1999) 166–173.

[4.10] H. Inui, T. Yamamoto,M. Hirota, M. Yamaguchi, *Lattice defects induced during hydrogen absorption-desorption cycles and their effects on P-C characteristic in some intermetallic compounds*, J. Alloys Compd. 330–332 (2002) 117–124.

[4.11] Kianvash, I.R. Harris, *Hydrogen decrepitation as a method of powder preparation of a 2:17-type, Sm(Co, Cu, Fe, Zr)8.92 magnetic alloy*, J. Mater. Sci. 20, 2 (1985) 682-688.

[4.12] L. Smardz, K. Smardz, M. Jurczyk, J. Jakubowicz, *Surface analysis of polycrystalline and nanocrystalline $LaNi_5$-type alloys*, J. Alloys Compd. 313 (2000) 192–200.

[4.13] S. Mathew, B. Satpati, B. Joseph, B.N. Dev, R. Nirmala R, S.K. Malik, R. Kesavamoorthy, *Magnetism in C_{60} films induced by proton irradiation*, Phy. Rev. B 75 (2007) 075426 (5 pages).

[4.14] H.C. Siegmann, L. Schlapbach, C.R. Brundle, *Self-restoring of the active surface in the hydrogen sponge $LaNi_5$*, Phys. Rev. Lett. 40, 14 (1978) 972-975.

[4.15] G.-H. Kim, S.-G. Lee, K.-Y. Lee, C.-H. Chun, J.-Y. Lee, *Observation of the defects induced by hydrogen absorption and desorption in $LaNi_5$*, Acta Metall. Mater. 43, 6 (1995) 2233-2240.

[4.16] R. Nakamura, K. Asano, K. Yoshimi, Y. Iijima, *Thermal analysis of lattice defects in $LaNi_5$*, J. Alloys Compd. 413, 1-2 (2006) 211-213.

[4.17] L. Lutterotti, S. Matthies, H. Wenk, *MAUD: a friendly Java program for material analysis using diffraction***,** CPD Newsletter 21 (1999) 14-15.

[4.18] Y. Nakamura, K. Oguro, I. Uehara, E. Akiba, *X-ray diffraction peak broadening and degradation in $LaNi_5$-based alloys*, Int. J. Hydrogen Energy 25 (2000) 531-537.

[4.19] A. Percheron-Gugan, C. Lartigue, J.C. Achard, P. Germi, F. Tasset, *Neutron and X-ray diffraction profile analyses and structure of $LaNi_5$, $LaNi_{5-x}Al_x$ and $LaNi_{5-x}Mn_x$ intermetallics and their hydrides (deuterides)*, J. Less-Common Met. 74 (1980) 1-12.

[4.20] P. Thompson, J.J. Reilly, L.M. Corliss, J.M. Hastings, R. Hempelmann, *The crystal structure of $LaNi_5D_7$*, J. Phys. F: Met. Phys. 16 (1986) 675.

[4.21] K. Tatsumi, I. Tanaka, H. Inui, K. Tanaka, M. Yamaguchi, H. Adachi, *Atomic structures and energetics of $LaNi_5$-H solid solution an*d hydrides, Phys. Rev. B 64 (2001) 184105.

[4.22] Y. Yu, H. Han, Y. Zhao, W. Xue, T. Gao, *First-principles calculation of the dynamical and thermodynamic properties of $LaNi_5$*, Solid State Commun. 148, 1-2 (2008) 1-5.

[4.23] Y. Nakamura, K. Oguro, I. Uehara, E. Akiba, *X-ray diffraction peak broadening and degradation in $LaNi_5$-based alloys*, Int. J. Hydrogen Energy 25, 6 (2000) 531-537.

[4.24] L. Lutterotti, *Maud version 2.0: Materials Analysis Using Diffraction* (2005) http://www.ing.unitn.it/~maud/

[4.25] W.P. Wagemans, J.H. van Lenthe, P.E. de Jongh, A. Jos van Dillen, K.P. de Jong, *Hydrogen Storage in magnesium Clusters: Quantum Chemical Study*, J. Am. Chem. Soc. 127 (2005) 16675-16680.

[4.26] J. Vajo, F. Pinkerton, N. Stetson, *Nanoscale phenomena in hydrogen storage*, Nanotechnology 20 (2009) 200201.

[4.27] C. Wu, H.-M. Cheng, Effects *of carbon of hydrogen storage performances of hydrides*, J. Mater. Chem. 20 (2010) 5390-5400.

[4.28] A.F. Gross, C.C. Ahn, S.L. Van Atta, P. Liu, J. Vajo, *Fabrication and hydrogen sorption behaviour of nanoparticulate MgH_2 incorporated in a porous carbon host*, Nanotechnology 20 (2009) 204005.

[4.29] P. Adelhelm, P.E. de Jongh, *The impact of carbon materials on the hydrogen storage properties of light metal hydrides*, J. Mater. Chem. 21 (2011) 2417-2427.

[4.30] B. Joseph, A. Iadecola, A. Puri, L. Simonelli, Y. Mizuguchi, Y. Takano, N.L. Saini, *Evidence of local structural inhomogeneity in $FeSe_{1-x}Te_x$ from extended X-ray absorption fine sructure*, Phys. Rev. B 82 (2010) 020502(R).

[4.31] Balerna, E. Bernieri, P. Picozzi, A. Reale, S. Santucci, E. Burattini, S. Mobilio, *Extended x-ray-absorption fine-structure and near-edge-structure studies on evaporated small clusters of Au*, Phys. Rev. B 31 (1985) 5058-5065.

[4.32] T. Comaschi, A. Balerna, S. Mobilio, *Temperature dependence of the structural paramiters of gold nanoparticles investigated with EXAFS*, Phys. Rev. B 77 (2008) 075432.

[4.33] G. Apai, J.F. Hamilton, J. Stohr, A. Thompson, *Extended X-ray-Absorption Fine Structure of Small Cu and Ni Custers: Binding-Energy and Bond-Length Changes with Cluster Size*, Phys. Rev. Lett. 43 (1979) 165-169.

[4.34] H. Ikemoto, T. Miyanaga, *Extended X-Ray Absorption Fine Structure Study of Local Structure and Atomic Correlations of Tellurium Nanoparticles*, Phys. Rev. Lett. 99 (2007) 165503.

[4.35] Di Cicco, M. Berrettoni, S. Stizza, E. Bonetti, G. Cocco, *Microstructural defects in nanocrystline iron probed by x-ray-absortpion spectroscopy*, Phys. Rev. B 50 (1994) 12386.

[4.36] L. Chih-Ming, H. Tsu-Lien, H. Yen-Heng, W. Kung-Te, T. Mau-Tsu, L. Chih-Hao, C.T. Chen, Y.Y. Chen, *Size-dependent lattice structure of palladium studied by x-ray absorption spectroscopy*, Phys. Rev. B 75 (2007) 125426.

[4.37] L.L. Araujo, R. Giulian, D.J. Sprouster, C.S. Schnohr, D.J. Llewellyn, P. Kluth, D.J. Cookson, G.J. Foran, M.C. Ridgway, *Size-dependent characterization of embedded Ge nanocrystals: Stuctral and thermal properties*, Phys. Rev. B 78 (2008) 094112.

[4.38] R. Giulian, L.L. Araujo, P. Kluth, D.J. Sprouster, C.S. Schnohr, G.J. Foran, M.C. Ridgway, *Temperature-dependent EXAFS analysis of embedded Pt nanocrystal*, J. Phys.: Condens. Matter 21 (2009) 155302.

[4.39] D.C. Koningsberger, B.L. Mojet, G.E. Van Dorsen, D.E. Ramaker, *XAFS spectroscopy; fundamenal principles and data analysis*, Top. Catal. 10 (2000) 143-155.

[4.40] M. Matsuura, K. Asada, K. Konno, M. Sakurai, *EXAFS Debye-Waller factors of La and Ni in $LaNi_5$*, J. Alloys Compd. 390, 1-2 (2002) 31-34.

[4.41] O. Palumbo, C. Castellano, A. Paolone, F. Cordero, R. Cantelli, Y. Nakamura, E. Akiba, *EXAFS study of $LaNi_5$ and $LaNi_{4.5}Al_{0.5}$*, J. Alloys Compd. 433, 1-2 (2007) 33-36.

[4.42] H. Sakaguchi, T. Suenobu, K. Moriuchi, M. Yamagami, T. Yamaguchi, G. Adachi, *The local structure around atoms in a hydrogenated amorphous LaNi5.0 film studied by neutron diffraction*, J. Alloys Compd. 221, 1-2 (1995) 212-217.

[4.43] T. Ressler, *WinSAS: a Program for X-ray Absorption Spectroscopy Data Analysis under MS-Windows*, J. Synch. Radiat. 5 (1998) 118-122.

[4.44] S.I. Zabinsky, J.J. Rehr, A.Ankudinov, R.C. Alberts, M.J. Eller, *Multiple-scattering calculations of x-ray absorption spectra*, Phys. Rev. B 52 (1995) 2995.

[4.45] R. Prints, D. Koningsberger (Eds.), *X-ray Absorption: Principles, Applications, Techniques of EXAFS, SEXAFS, XANES*, Wiley, New York, 1988.

Chapter 5

Calcium borohydride-based reactive hydride composites

5.1 The system

Complex hydrides are being intensely studied as promising hydrogen storage materials because of their high theoretical hydrogen capacity **[5.1].** Among them, the borohydrides, substances containing the anion $[BH_4]^-$ coordinated by ionic bonds to one or more cations, have the highest theoretical hydrogen capacities, with the maximum represented by the $LiBH_4$ (18.4 wt%) and $Be[BH_4]_2$ (20.7 wt%, but the use of this material would be more problematic because of the beryllium powders' toxicity). For this kind of materials high working temperatures and slow sorption kinetics are the main drawbacks and research efforts are focused on the reduction of these hurdles. For this purpose, one route is the addition of substances, like catalysts and destabilizing agents, such as transition metal oxides and halides and other hydrides, in the so-called reactive hydride composites (RHCs) strategy (see **subsection 2.3.1**), where two or more hydrides are mixed and used together to obtain a composed system with better performances if compared to the single species. Another route is the nanoconfinement of the hydrides themselves into scaffolds, to maintain their size at the nanometric scale during cycling. All these solutions should improve the system working conditions despite an acceptable reduction of the hydrogen capacity.

Together with complex hydrides, other light metal hydrides **[5.2]**, such as MgH_2 and AlH_3 have been proposed and are still studied for hydrogen storage because of their high theoretical hydrogen capacity, but high working temperatures are still a drawback.

Calcium borohydride has been attracted much attention in the last years: it has been shown to release about 9.0 wt % of hydrogen when heated up to 550 °C **[5.3]**. Magnesium hydride

MgH_2 is a light alkaline-earth metal hydride, it releases more than 7 wt% of hydrogen at 300 °C and is probably the most studied metal hydride, also investigated for possible practical applications **[5.4] [5.5] [5.6]**. It has been shown that, according to the reactive hydride composites (RHCs) strategy **[5.7] [5.8]**, the system $Ca(BH_4)_2$+MgH_2 shows interesting properties if compared to the single species, and for this reason we decided to focused on it. The influence of milling time on the formation of this hydrogenated system starting from calcium hydride CaH_2 and magnesium boride MgB_2 has been studied. Later on the effect of the addition of aluminum boride AlB_2 on the kinetics and thermodynamics of the hydrogen sorption processes has been investigated.

5.2 Sample preparation and measurement conditions

All the samples were ball milled in a *Spex8000M* shaker mixer/mill for different milling times (from 2 min to 900 min), using 15 min milling and 15 min pause steps to avoid sample heating inside the hardened steel milling vial. All the powders have been handled inside an Ar filled glove box (*MBraun*) with moisture and oxygen level kept below 1 ppm.

Amounts of powder ranging from 0.45 to 0.65 g were introduced in the automatic manometric *Sievert*'s type gas reaction analyzer, *PCTPro-2000* by *Setaram*. A brief description on this experimental apparatus and technique is reported in **section 3.3**. Concerning the hydrogen absorption tests, the samples were charged with an initial pressure of 120 bar, then a temperature ramp from room temperature to 360 °C was performed at 5 °C/min rate, followed by an isothermal step (lasting 1400 min or 3000 min) at 360 °C. Isothermal dehydrogenation runs were performed on the absorbed samples at 390 °C under static vacuum. For the coupled manometric – calorimetric measurements, 50 mg of the samples hydrogenated in the manometric apparatus were loaded in the high pressure cell of the *Sensys* apparatus under Ar atmosphere inside the glove box; then the powders were subjected to a thermal programmed desorption (TPD) measurement performed by heating from room temperature to 580 °C at 2 °C/min. Some elements on differential scanning calorimetry (DSC), the opportunity of using the coupled manometric-calorimetric measurements and the TPD measurement technique are described in **sections 3.4** and **3.5** of the thesis. X-ray powder diffraction (XRPD) measurements have been performed using a *Bruker* D8 Advance diffractometer with Bragg-Brentano geometry and Cu Kα radiation. *Rietveld* refinements on the XRPD profiles have been performed using the software *MAUD* **[5.9]**. More information on the XRPD technique, as well as on the *Rietveld* Refinement method, is reported in **sections 3.7** and the references therein.

5.3 Results and Discussions

5.3.1 Effect of milling time on the system CaH_2+MgB_2 system

Calcium borohydride and magnesium hydride can be obtained from calcium hydride and magnesium boride **[5.10]** according to the reaction:

$$CaH_2 + MgB_2 + 4\,H_2 \rightarrow Ca(BH_4)_2 + MgH_2 \quad \text{theoretical } H_2 \text{ content} = 8.39 \text{ wt\%} \quad (5.1)$$

Before performing hydrogenation, different samples of CaH_2+MgB_2 where milled for with different milling time, viz. 2, 90, 450 and 900 min. **Figure 5.1** shows the XRPD pattern obtained for the 90 min milled sample. The results of the *Rietveld* refinement on the experimental data showed that milling does not lead to the formation of any new phase. Additional results of the refinement are reported in the appendix to this chapter. Also for the samples milled for 2 min and 450 min, XRPD spectra were acquired and refined.

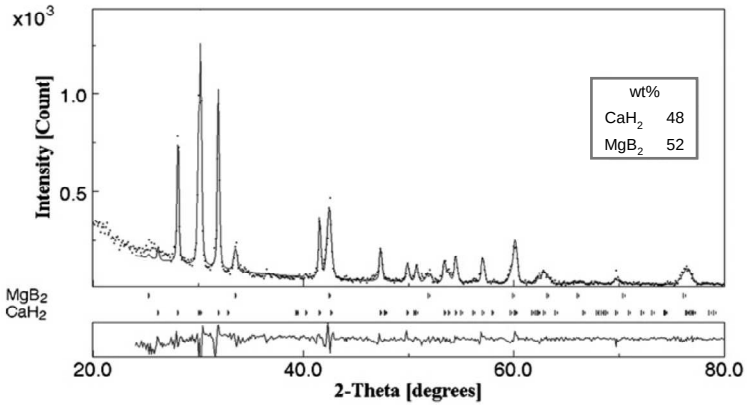

Figure 5.1 *XRPD patterns for CaH_2+MgB_2 after milling for 90 min. The fitting curve (solid line) and the distribution of the phases (inset), as results of the Rietveld refinement, are also reported.*

Table 5.1 (shown later) reports a comparison of the crystallite sizes for the different samples, as obtained from the spectra refinements. As expected, the crystallite sizes decrease as the milling time increase, due to the high energy grinding (**section 3.2**). For each milled sample, an hydrogenation test was performed in a *Sievert*'s type apparatus at 360 °C and 120 bar of initial hydrogen pressure. In **figure 5.2** the initial part of the obtained kinetic curves (up to 200 min) is reported. The effect of milling process on the material is evident, as the kinetics improves as the milling time increases.

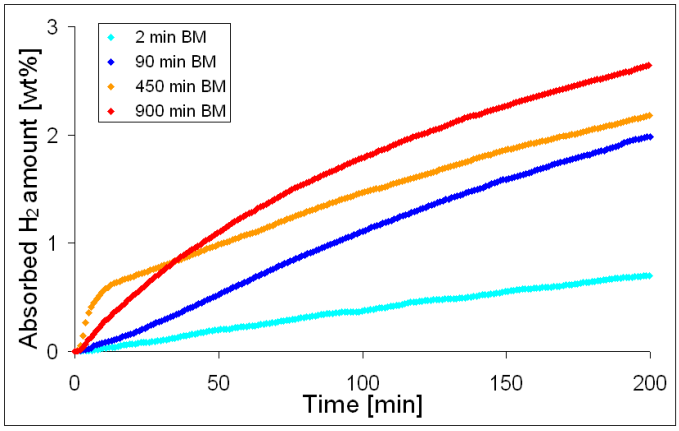

Figure 5.2 *Effect of milling time on the absorption kinetics (first 200 min) for CaH_2+MgB_2 milled samples. Absorption was performed at 360°C and starting hydrogen pressure = 120 bar. The crystallite size reduction improves the hydrogenation kinetics as milling time increases. The 450 min milled sample shows the fastest kinetics in the initial part of the charging procedure.*

It is worth noting that, curiously, the sample milled for 450 min shows the best kinetics just at the beginning, getting worse with respect to the 900 min milled sample after 0.5 h. After the first 200 min, the hydrogen absorption proceeds very slowly. For the 90 min milled sample, a long time measurement was performed and saturation was reached at a hydrogen capacity of 6.6 wt% (after 8000 min, i.e. 5.5 days). Referring to reaction 5.1, the saturation value indicates that, at the used conditions, the system does not reach full absorption, and it shows very slow kinetics. The XRPD pattern of the CaH_2+MgB_2 90 min milled sample after hydrogenation for 3000 min (with achieved hydrogen capacity of 5.7 wt%) is reported in **figure 5.3**. The *Rietveld* analysis reveals a strong presence of the intermediate phase $Ca_4Mg_3H_{14}$ **[5.10]**, together with the desired borohydride, magnesium hydride and small amounts of still unreacted initial compounds, thus confirming that full absorption did not occur. The inset shows the distribution of the revealed crystal phases, as obtained from the refinement. Additional refinement data are reported in the appendix to the chapter.

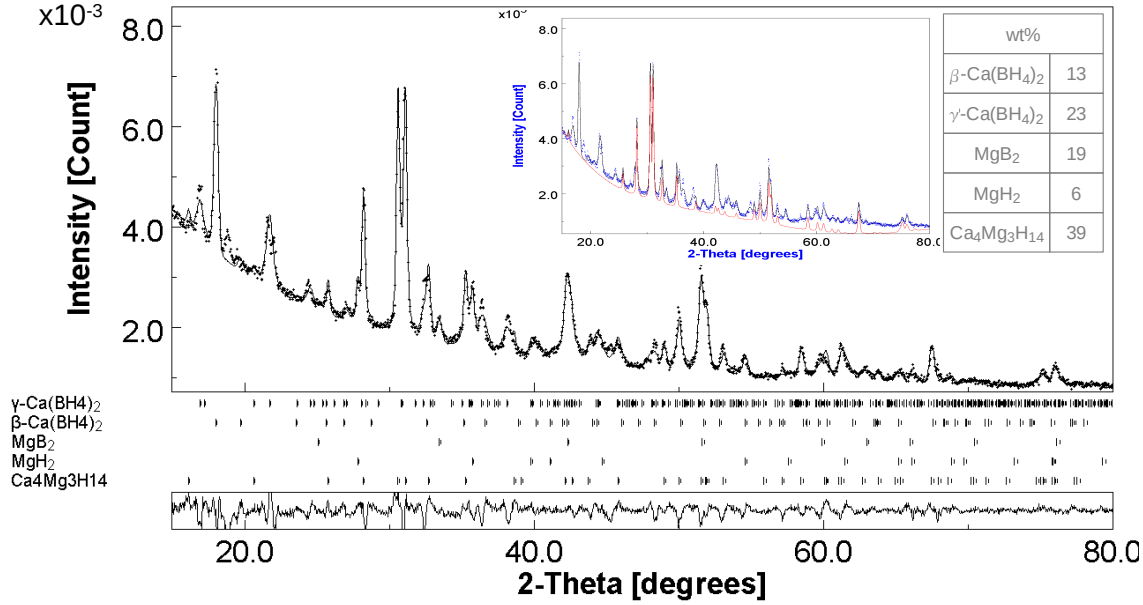

Figure 5.3 *XRPD pattern for the CaH_2+MgB_2 90 min milled sample after hydrogenation for 3000 min at 360°C and initial hydrogen pressure of 120 bar. The Rietveld analysis shows a strong presence of the intermediate hydrogenated phase $Ca_4Mg_3H_{14}$ (39 wt%), together with the desired hydrated products $Ca(BH_4)_2$ and MgH_2 and some still unreacted MgB_2. The insets show calculated weight content of the detected constituent phases and the calculated partial XRD profile (in red) for the $Ca_4Mg_3H_{14}$ phase.*

Once the absence of full absorption was ascertain, the desorption kinetics and the reversibility of the system were investigated. A desorption run at 390 °C under static vacuum showed the release of the full amount of the previously absorbed hydrogen. The desorption kinetics is found to be much faster than the poor absorption one. **Figure 5.4** (left) shows the absorption and the desorption curves recorded for the 90 min milled sample, which takes 3600 min to reach 6.0 wt % of hydrogen content, and fully desorbs in 2400 min at 390 °C, with 90 % of the hydrogen content released in the first 300 min.

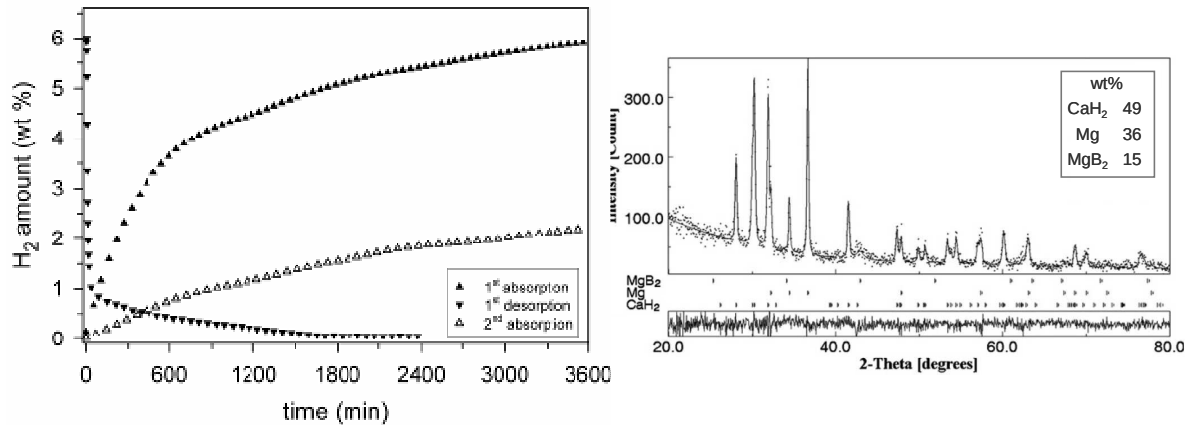

Figure 5.4 *Left. Sorption kinetics (T = 360°C) comparison for the CaH_2+MgB_2 90 min milled sample: desorption is faster than absorption (90% of the total absorbed amount is released in 300 min). Re-hydrogenation (2nd absorption) curve is also shown, indicating that the system is not fully reversible.*
Right. XRPD pattern for CaH_2+MgB_2 milled for 90 min, hydrogenated and subsequently desorbed. The fitting curve (solid line) and the distribution of the phases (inset), as results of the Rietveld refinement, are also reported.

The fact that the system fully desorbs was also confirmed by the *Rietveld* analysis performed on the XRPD spectrum of the same sample after desorption (**figure 5.4**, right): there is not presence of any hydrogenated phases, except for the starting compound CaH_2. However, unbound magnesium is also present in addition to the starting boride, thus suggesting the presence of some amorphous boron phase, not detected by diffraction, and indicating a not full reversibility of the system. The second hydrogenation run for the 90 min milled sample after full desorption is also reported in **Figure 5.4** (left). As it can be seen, the re-hydrogenated system shows a lower capacity than in the first absorption, indicating that full reversibility is not achieved.

Coupled manometric-calorimetric measurements (see **section 3.5**) were performed on the samples ball-milled for different times after the first hydrogenation run. As an example, the results for the 90 min milled sample are shown in **figure 5.5**, where, both calorimetric signal and the corresponding hydrogen released amount are reported. The curve where obtained by heating the sample with a heating ramp of 2 °C/min.

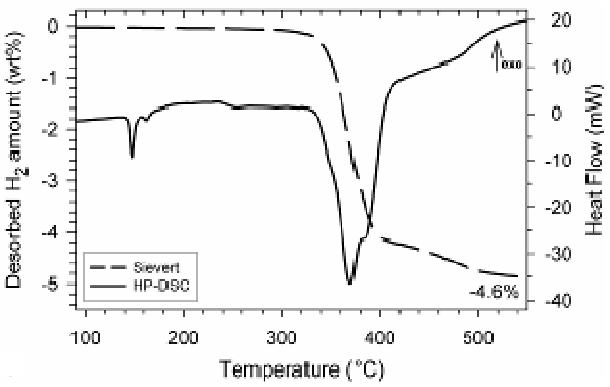

Figure 5.5 *Temperature programmed desorption (TPD) measurements performed by the coupled manometric (Sieverts') – calorimetric (DSC) system. The figure shows the desorption profiles for CaH_2+MgB_2 90 min milled samples after a first absorption at 360°C and 120 bar.*

Table 5.1 summarizes the effects of ball milling on the hydrogen sorption properties of the CaH_2+MgB_2 system. The fifth column reports the amount of hydrogen released by the four samples after a first hydrogenation for 1400 min at the conditions previously described. As clearly visible, the hydrogen and then desorbed amount increases as the milling time increases, thus confirming that the storage capacity improves with the mechanical treatment.

Table 5.1 *Results obtained by XRPD, manometric and coupled manometric-calorimetric measurements on CaH_2+MgB_2 milled samples. Milling time has a clear effect on powder size, hydrogen capacity and release onset temperature. Crystallites sizes (with estimation error of 5%) for CaH2 and MgB2 have been obtained as a result of Rietveld analysis performed on the patterns by the software MAUD [5.9].*

sample	Goodness of the *Rieveld* refinements [R_{wp}%]	crystallites size for the as milled samples [Å]		H_2 desorbed amount after hydrogenation for 1400 min [wt%]	hydrogen release onset [°C]	ΔH double-peak [kJ/molH_2]
		CaH_2	MgB_2			
(CaH_2 + MgB_2) as milled for 2 min	17.8	1261	876	3.2	348	49.0
(CaH_2 + MgB_2) as milled for 90 min	14.2	230	356	4.6	346	49.7
(CaH_2 + MgB_2) as milled for 450 min	13.2	157	282	4.9	338	49.5
(CaH_2 + MgB_2) as milled for 900 min	-	-	-	5.8	336	50.7

Concerning the calorimetric profile, according to what reported in recent studies **[5.3][5.10]**, the first main peak starting at around 130 °C can be attributed to the transition of $Ca(BH_2)_4$ from the α-phase (stable at room temperature) to the β-phase. In the range 150-190 °C other small endothermic features are present, probably indicating other structural changes of the borohydride (γ-phase) or loss of coordination water **[5.11]**.

In the region between 340 °C and 440 °C a double peak indicates the hydrogen release from the borohydride phase, forming the intermediate mixed hydrogenated phase $Ca_4Mg_3H_{14}$, in addition to CaH_2, Mg, B and H_2 (peak on the left). Then, CaH_2, Mg, B and H_2 form from this mixed phase (peak on the right). In our experiments, differently from the cited work **[5.10]**, there is rather an overlap of these two peaks even if we used the same heating rate, i.e. 2.0 °C/min. It must be noted that no clean peak, corresponding to the hydrogen release from MgH_2 appears, as this compound releases hydrogen in a range inside the double peak region **[5.11]**. In **table 5.1** the double peak onset temperature and the desorption enthalpy are reported: the latter remains quite constant (± 2 kJ/mol error), thus suggesting that there is no remarkable difference in the chemical nature of the phases present in the samples, while the former confirms a better behaviour of the samples milled for longer time.

5.3.2 Addition of AlB_2

In order to improve the sorption performance of the system, in particular its reversibility, the addition of aluminum boride has been tested. Aluminum and magnesium form mixed borides **[5.12]**, which can be prepared by high energy ball milling **[5.13]**. The investigation on

the effect of AlB_2 on the studied system is justified by the fact that AlB_2 and MgB_2, having the same layered crystal structure, present a lower decomposition temperature (920 °C and 800 °C, respectively) **[5.14]** compared to either boron or other metal borides. This indicates a lower lattice energy (absolute value) and thus a lower inertness. It has been supposed that the compatibility between Al and Mg could in principle facilitate the formation of borides, rather than unbound boron, during the hydrogen release processes; this could improve the desorption kinetics, as already suggested in an other work **[5.15]**, and make the system more reversible. For this reason CaH_2+½MgB_2+½AlB_2 and CaH_2+AlB_2 mixtures have been prepared and tested. For these two samples the following reactions have been considered, respectively:

$$CaH_2 + ½\,MgB_2 + ½\,AlB_2 + {}^{7}/_{2}H_2 \rightarrow Ca(BH_4)_2 + ½\,MgH_2 + ½\,Al \quad 7.32\ wt\% \quad (5.2)$$

$$CaH_2 + AlB_2 + 3\,H_2 \rightarrow Ca(BH_4)_2 + Al \quad 6.25\ wt\% \quad (5.3)$$

in which is assumed that a) both borides take part to the formation of borohydride, b) all Mg of the MgB_2 reacts to form MgH_2 and c) Al does not absorb hydrogen, due to its kinetic limitations (as reported in **subsection 2.3.4**). Both samples were prepared by 90 min ball milling following the same procedure used for the CaH_2+MgB_2 mixture. Hydrogenation at 360 °C with an initial hydrogen pressure of 120 bar was performed for 3000 min on these two samples, as well as on the CaH_2+MgB_2 90 min milled sample for comparison. **Figure 5.6** shows the XRPD patterns obtained for the CaH_2+AlB_2 sample after absorption. The *Rietveld* analysis suggested the presence of borohydride and aluminum together with some unreacted calcium hydride, thus indicating that the assumed reaction **(5.3)** occurred, even though full hydrogenation was not achieved also in this case.

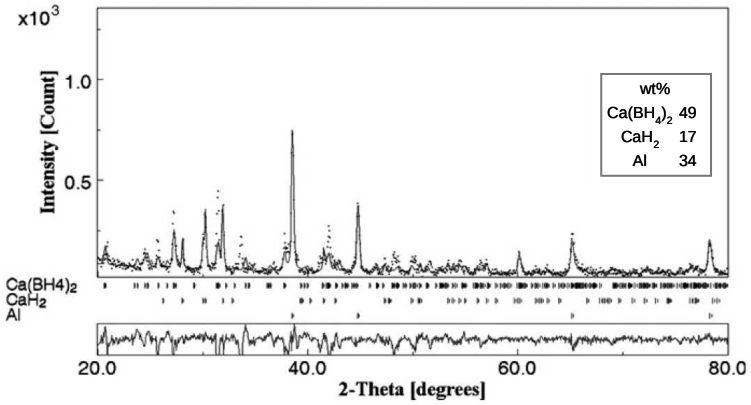

Figure 5.6 *XRPD pattern for CaH_2+AlB_2 milled for 90 min and hydrogenated. The inset shows calculated weight content of the constituent phases, as obtained from the Rietveld refinement.*

In **figure 5.7** the coupled manometric – calorimetric measurements performed on the two samples containing AlB_2 are shown. If we consider the theoretical capacity referring to reactions **(5.1)**, **(5.2)**, and **(5.3)**, it can be stated that there is a strong increase of the absorption

relative percentage for the CaH_2+AlB_2 sample, as it releases the 96% of the full theoretical hydrogen capacity, while there is no improvement when both borides are present. What is more, the absolute value of 5.9 wt% denotes an interesting hydrogen capacity for the system CaH_2+AlB_2. A summary of the results obtained on the three different studied systems is given in **table 5.2**. Interestingly, a reduction of the specific enthalpy of the desorption process confirms the better behaviour of the CaH_2+AlB_2 system, differently from what calculated by Wolverton et al. **[5.16]**.

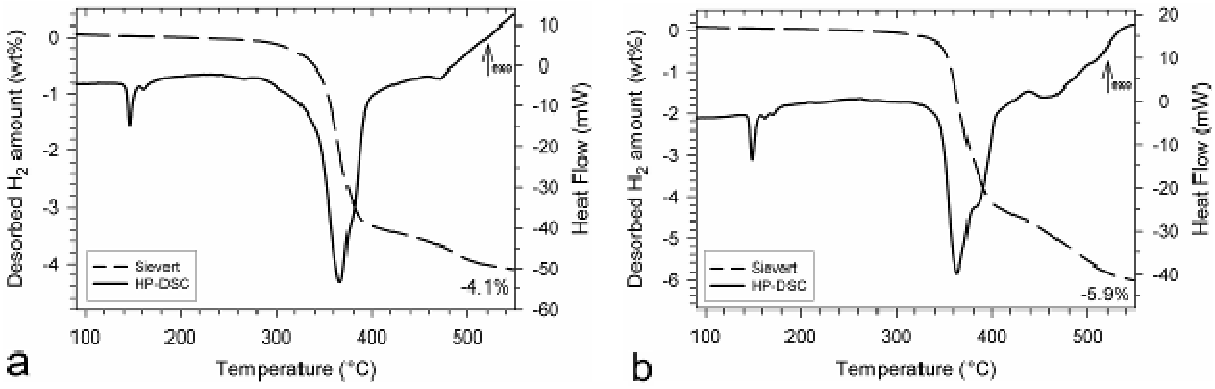

Figure 5.7 *Coupled calorimetric-volumetric measurements during a temperature programmed desorption (TPD) for two systems where MgB_2 has been, respectively, partially and totally substituted by AlB_2: a) CaH_2+½MgB_2+½AlB_2 ; b) CaH_2+AlB_2. The samples where ball milled for 90 min and then absorbed at 360 °C under 120 bar of hydrogen pressure.*

Desorption runs were also performed at 390 °C and under static vacuum on both the systems containing AlB_2. Also in this case the best result was obtained for the binary mixture containing aluminum boride, which released all the previously absorbed hydrogen amount in just 100 min, while the system with the two borides desorbed in thrice this time, which is still better than the desorption time needed by the CaH_2+MgB_2 system (**figure 5.8**).

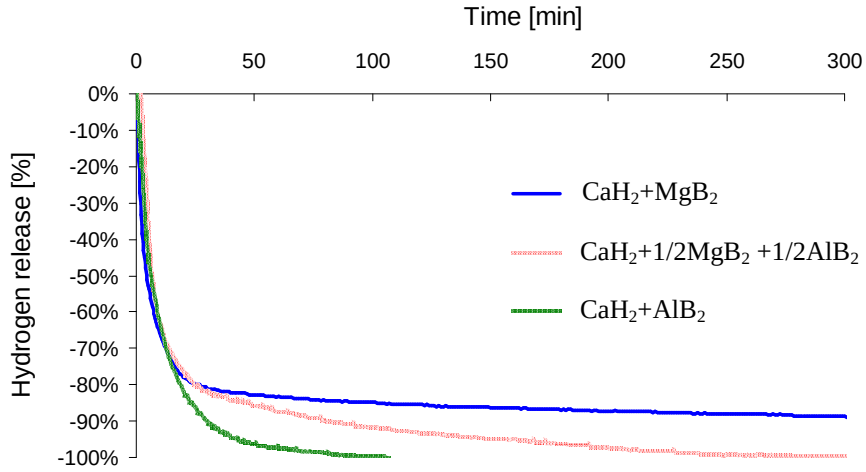

Figure 5.8 *Comparison among the hydrogen desorption curves of the three studied systems, after the first hydrogenation.*

In addition, a second hydrogenation test showed the better behaviour of the CaH_2+AlB_2 binary system, which was able to restore the highest hydrogen capacity percentage if referred to the theoretical capacities of each system, as reported in **table 5.2**.

Table 5.2 *Comparison among binary and ternary samples containing MgB_2 and/or AlB_2. The best behaviour is shown by the binary system containing aluminum boride.*

sample	theoretical hydrogen capacity [wt%]	H_2 released amount after hydrogenation for 3000 min [wt%]	H_2 released amount referred to theoretical capacity	H_2 release onset [°C]	ΔH double-peak [kJ/molH_2]	H_2 re-absorbed amount referred to theoretical capacity
(CaH_2 + MgB_2) 90 min milled	8.34	5.8	70 %	343	51.4	16 %
(CaH_2 + ½ MgB_2 + ½ AlB_2) 90 min milled	7.32	4.1	56 %	346	58.0	18 %
(CaH_2 + AlB_2) 90 min milled	6.25	5.9	94 %	341	45.3	21 %

At the MCX beam line of the Elettra synchrotron in Trieste (Italy) *in situ* synchrotron radiation X-ray powder diffraction (SR-XRPD) measurements have been performed in order to follow the dehydrogenation process of the system CaH_2+AlB_2 after its hydrogenation. A brief introduction to the SR-XRPD is reported in **subsection 3.7.3**, along with additional details on the performed measurements. **Figure 5.9** reports the evolution of the diffraction patterns obtained at various temperatures. As expected, below 200 °C the low temperature α-phase changes to the β- and γ- phases **[5.17]**, stable at high temperature.

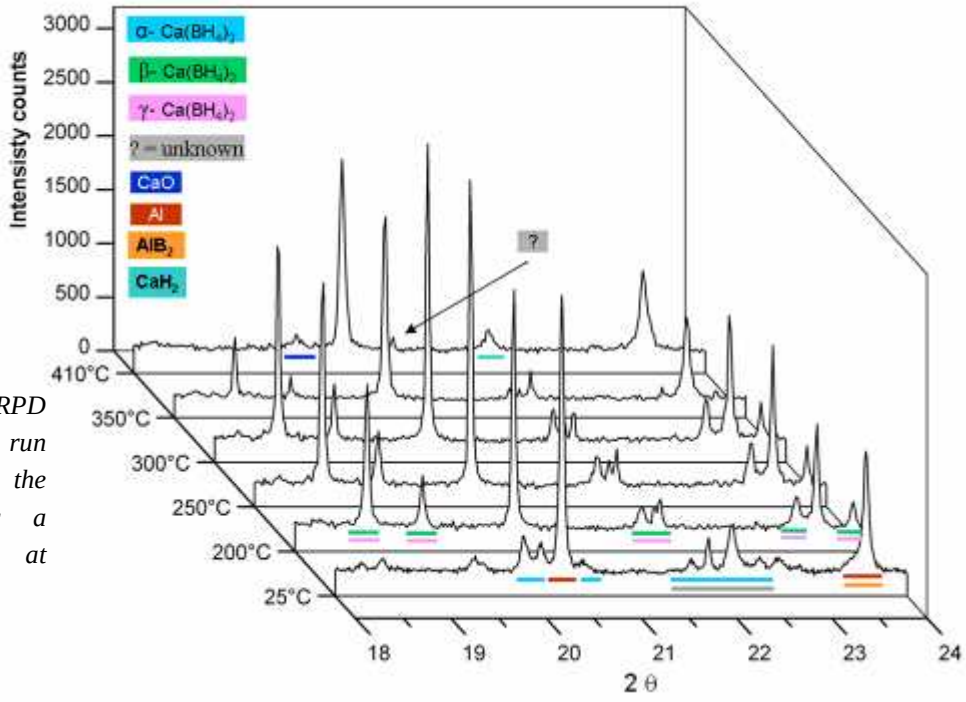

Figure 5.9 *In situ SR-XRPD measurements during a TPD run under Ar atmosphere for the sample CaH_2+AlB_2 after a previous hydrogenation at 360 °C and 10 bar of H_2.*

Above 300 °C the borohydride releases hydrogen and CaH_2 forms again. However, as reported in **table 5.2**, the system shows poor reversibility, with only the 21% of the theoretical capacity during the second hydrogenation. As mentioned, this value is anyway higher than the one obtained for the system with MgB_2 in place of AlB_2. By The enhanced reversibility of the system with the latter can be explained simply on the base of the relative absorption yield of the two systems. In other words, the second hydrogenation shows reduced hydrogen capacity for the two systems, but interestingly the ratio of the two values is rather the same for first and second hydrogenation (or, equally, it is always the same the ratio of the achieved capacity for the two systems).

As reported by Barkhordarian et al. **[5.10]**, the positive effect of MgB_2, with respect to amorphous boron, on the synthesis of calcium borohydride, seems to be due to the particular layered structure of the former. In this structure, with spatial group P6/mmm, boron atoms are located between layers of magnesium. Each boron atom is connected to a maximum of three other boron atoms by covalent sp^2 bonds, while the bonds with the magnesium atoms of the layers are of metallic type. Instead, in α- and β- polymorphs, pure born is connected to five other atoms in icosahedral units. The enhanced calcium borohydride formation, by using MgB_2 as reactant, instead of boron, seems to be due to the lower energy needed to detach the boron atoms from the reactant structure. Moreover, the magnesium of the layers could have a catalytic effect, by forming intermediate species with Mg-B-H bonds, such as $MgB_{12}H_{12}$. As mentioned above, AlB_2 was chosen to be tested in order to improve the system performances, because of its similarity with MgB_2. Similarly to magnesium boride, aluminum boride has the same spatial group P6/mmm and layered structure **[5.18]**. Thus, similar positive effects are provided by the AlB_2 structure toward the borohydride formation, with respect to other boron compounds. In addition, the enhanced yields in borohydride could be ascribed to the catalytic action of more reactive Al-B-H intermediates, or to the lower (even high) stability of the aluminum diboride with respect to magnesium boride (also confirmed by a lower, even very high, melting temperature). However no such a type of phases were identified by the XRPD measurements performed.

Nuclear magnetic resonance (NMR) spectroscopy is a technique providing information on the molecular structure of the analyzed samples. Solid-state NMR spectroscopy is a useful technique to detect solid phases that do not present a long range order, thus being hardly detected by diffraction techniques **[5.19]**. NMR is based on the analysis of the radiation emitted by an atom nucleus, when its spin comes back to the original state, under a strong applied magnetic field. Initially, the magnetization vector, due to the distribution of the atoms spin, performs a precession around the direction of the applied magnetic field. The precession angle can be changed by irradiating the system in resonance conditions with radio frequency (RF) waves. Once the RF perturbation ends, the magnetization relaxes to the initial equilibrium value, thus producing the NMR signal. This signal is typical of the element, but it is also affected by its chemical surrounding, which produces a shift of the signal obtained for that atomic species (e.g. ^{1}H, ^{13}C, ^{19}F, ^{23}Na, ^{31}P) in a reference compound.

Some preliminary measurements were performed by a research group at *University of Aarhus* (Sweden), on our CaH_2+MgB_2 and CaH_2+AlB_2 samples, by using ^{11}B magic angle spinning (MAS)[(a)] NMR spectroscopy. The used instrument is *Varian INOVA-400 (9.39 T)* spectrometer with a home-built CP/MAS probe for 5 mm outside diameter rotors. The spectra were obtained at room temperature using airtight end-capped zirconia (PSZ) rotors packed in an argon filled glovebox. In these preliminary measurements, the chemical shifts, referenced to neat $F_3B{\cdot}O(CH_2CH_3)_2$, showed presence of α-B for the hydrogenated and then dehydrogenated CaH_2+MgB_2. According to what reported above, the presence of pure boron, not detected by XRPD (see **figure 5.4**, right), reduce the absorption properties of the system, as confirmed by the low capacity registered during the re-hydrogenation test. The chemical shifts measured for the corresponding CaH_2+AlB_2 dehydrogenated sample could not detect pure boron, but revealed presence of CaB_6, not suggested by *in situ* SR-XRPD at high temperatures. In CaB_6 each boron atom is connected to at least four other boron atoms via covalent bonds. This means that, according to what reported above, the formation of the borohydride starting from CaB_6 requires more energy than that needed with a diboride with layered structure, such as MgB_2 or AlB_2. In fact, Rönnebro et Majzoub **[5.20]** showed that CaB_6 can be hydrogenated to calcium borohydride at high pressure (700 bar) and high temperature (400-440 °C), while Wang et al. **[5.21]** experienced even stronger kinetics barrier to the process. Bonatto Minella et al. **[5.22]** experienced the positive effect of fluorinated catalysts (TiF_4 and NbF_5) on the reversibility of calcium borohydride. In fact, while no re-hydrogenation occurred at 350 °C and 130 bar for 24h for calcium borohydride previously dehydrogenated at 450 °C and vacuum, for the doped system partial reversibility occurs with the same hydrogenation conditions. This was ascribed to the presence of CaB_6 and the intermediate $CaB_{12}H_{12}$ as dehydrogenation products of calcium borohydride, detected by ^{11}B MAS NMR measurements. In the analogous measurements on our samples, CaB_6 was revealed on the CaH_2+AlB_2 system, as mentioned above, while this no formation of this compound was detected for the CaH_2+MgB_2 system, differently from what reported by Kim et al. **[5.3]**. It is to note that recently Gosalawit-Utke et al. **[5.23]** could detect amorphous CaB_6 by *Raman* spectroscopy on the dehydrogenated system $Ca(BH4)_2$+MgF_2.

For the NMR measurements on our systems, no reference samples of $CaB_{12}H_{12}$ or other Ca-Al-H products could be measured, thus, the chemical shifts revealing the presence of this species could not be taken into account. However, on the base of what reported above, it is like the substitution of MgB_2 with AlB_2 facilitates the formation of CaB_6 (and possibly of $CaB_{12}H_{12}$ too), thus improving the system reversibility, similarly to what occurs by the addition of fluorinated catalysts to calcium borohydride. However, it must be noted that the enhancement of the system reversibility, with the used experimental conditions (350-360°C and 120-130 bar), due to the formation of CaH_6, is in contrast with the results of the previously cited works by Rönnebro's and Wang's groups.

[(a)] In a solid material, dipoles interactions, i.e. the nuclei reciprocal interactions, cause a significant broadening of the NMR signal (in liquids this problem is reduced by the brownian motion of the molecules). These dipoles interactions can be avoided by positioning the sample at the "magic" angle θ_m = 54.74° ($\cos^2\theta_m$=1/3) with the magnetic field and by rotating the sample at high speed.

This suggest that the enhance reversibility could be due to the presence of the ternary intermediates species, or to the presence of the fluorinated catalysts, rather than to CaB_6 formation. Another possibility which could be considered in order to investigate the second hydrogenation of the CaH_2+AlB_2 system is the formation of calcium alanate $Ca(AlH_4)_2$. As reported by Kabbour et al. **[5.24]** calcium alanate can be theoretically formed at temperatures below 300°C starting from CaH_2 and Al and in a two step reaction, through the formation of the intermediate compound $CaAlH_5$. However, up to now, along with the traditional synthesis form CaH_2 and $CaCl_2$ **[5.25]**, calcium alanate has been obtained by wet chemical **[5.26] [5.27]**, mechano- **[5.28]** or mechanochemical **[5.29]** synthesis, involving solvents (THF, DEE, ect.) and/or various starting compounds, such as $CaCl_2$, $AlCl_3$ and other alanats. Thus no synthesis from compounds containing only calcium, aluminum and hydrogen (or even magnesium) has been performed. Further investigation on the CaH_2+AlB_2 after first absorption/desorption cycle, as well as on the re-hydrogenated system are scheduled, in order to identify the constituting species and give more elements for the clarification of the absorption and desorption mechanism of the system. Looking again at the evolution of the *in situ* diffraction patterns during the temperature programmed desorption, small change in the formed Al and unracted AlB_2 peaks suggest that Al purely turns back to AlB_2. This is in line with the still poor reversibility of the system (21%) obtained with the second absorption run (**table 5.2**), as well as on the formation or amorphous boron contained species, as discussed above.

5.3.3 Tests with possible catalysts

In order to improve the performance of the CaH_2+AlB_2 system, the possible catalysing action of halides has been tested. The chosen catalysts were two fluorinated substances, TiF_3 and NbF_5 and a mixture of chlorides, $AlCl_3$+$TiCl_3$. The choice of the fluorinated dopants was suggested by the fact that the presence of fluorine containing substances in similar $Ca(BH_4)_2$ based systems seemed to improve the system performances, due to partial fluoride anion substitution, according to what reported in previous works **[5.22] [5.23] [5.30]**. The latter was chosen because of the presence of aluminum in the catalysts mixture as well as in one of the starting compounds (AlB_2), so that a potential affinity between the two species has been considered. **Figure 5.10** reports the comparison of the first absorption curves for samples of CaH_2+AlB_2 in which 5 wt% of dopant has been added. As can be noticed, the absorption tests do not indicate any improvement due to the use of the tested additives. Anyway, the systems in which niobium and titanium fluorides have been added, respectively, showed a better kinetics, if compared to the system with the two chlorides mixture as additive. For the NbF_5 this could be ascribed to its lower melting point (77 °C), that allowed a better dispersion of the catalyst in the system during milling because of the liquid state, as reported by *Rongeat* et al. **[5.31]** for desorption kinetics of $Ca(BH_4)_2$.

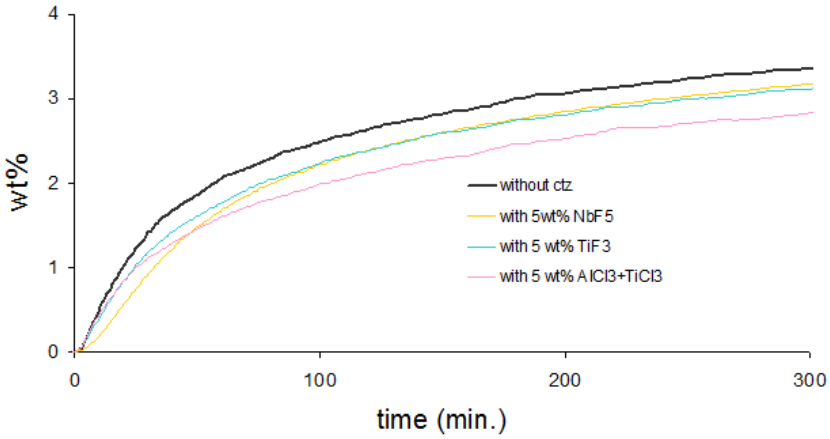

Figure 5.10 *Comparison of first absorption curves for the systems without and with the three different potential catalysts, respectively. No improvement, due the addition of 5 wt% of the each tested substance, is recognizable.*

Anyway, as evident in the figure, both the fluorides gave similar results (despite the high melting point of TiF_3, i.e. 1200 °C), thus suggesting that in general the presence of fluorine in the mixture, rather than the chlorine, gives better results. However, as already underlined, even the addition of the fluorides did not improve the performances of the undoped system, as regards the hydrogen uptake. Instead, the presence of the dopants improved the desorption kinetics, as reported in **figure 5.11**.

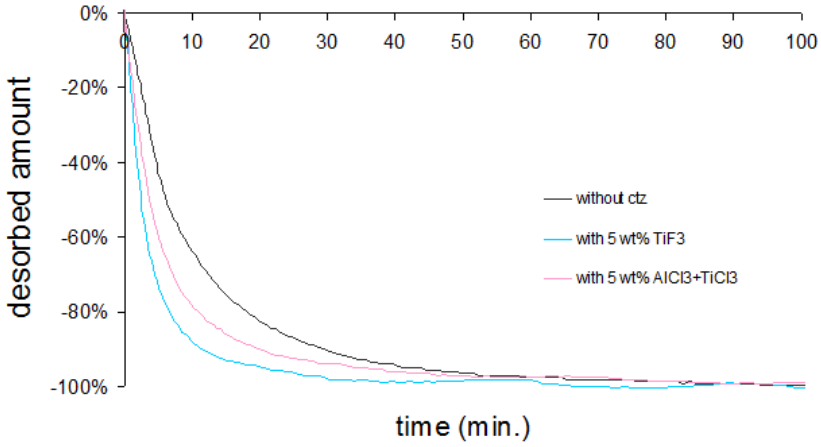

Figure 5.11 *Hydrogen release curves for the undoped system and the system with two different catalysts, respectively. The catalysts improve the desorption kinetics of the system. The desorbed hydrogen amount is referred to the value achieved in the previous absorption test.*

It is interesting to note that, once again, a fluorinated specie has a better influence than the chlorides mixture. Coupled manometric – calorimetric measurements, were also performed on the systems with the additives, as well as on the undoped CaH_2+AlB_2 mixture. The measurements are performed under static vacuum and with a heating ramp of 2°C/min up to a final temperature of 550 °C. In **table 5.3** the results obtained with the coupled measurements are compared and summarized. The lower desorbed amount shown for the doped systems comes from the lower absorbed amount during the previous absorption tests, lasted 3000 min. As a general positive effect, the tested dopants lower the specific energies for the hydrogen release at least by 200 J/g. In particular, NbF_5 causes an even more appreciable enthalpy reduction, with a difference of about 100 J/g, with respect to the other tested dopants. However, only the use of NbF_5 caused an increase of the hydrogen release onset temperature.

Table 5.3 *Summary of the results obtained by the addition of catalysts to the CaH_2+ AlB_2 system.*

samples ball milled for 90 min and absorbed for 3000 min	final released H_2 amount [wt%]	H_2 release onset [°C]	ΔH main peak [J/g]
CaH_2 + AlB_2	5.9	347	887
CaH_2 + AlB_2 + 5wt% NbF_5	5.4	386	584
CaH_2 + AlB_2 + 5wt% TiF_3	5.1	339	675
CaH_2 + AlB_2 + 5wt% ($AlCl_3$+$TiCl_3$)	4.2	338	671

Interestingly, although the effect of the tested dopants is positive for hydrogen release, and not for the absorption kinetics, a similarity can be suggested for the behaviour of the NbF_5 dopant. In both cases, NbF_5 seems to be the best additive substance among the tested ones, Moreover, both absorption and desorption tests revealed a delayed effect of this substance: in fact, during the first minutes of absorption runs, NbF_5 shows the worse behaviour and only after 50 min revealed its final effect. Similarly, during the desorption test with the programmed temperature ramp, it causes a higher hydrogen release onset temperature (i.e. a delay in the hydrogen release start) of the system, but as a good effect, it accelerates the release reaction (more narrow and intense peak in **figure 5.12**) and reduces the reaction energy.

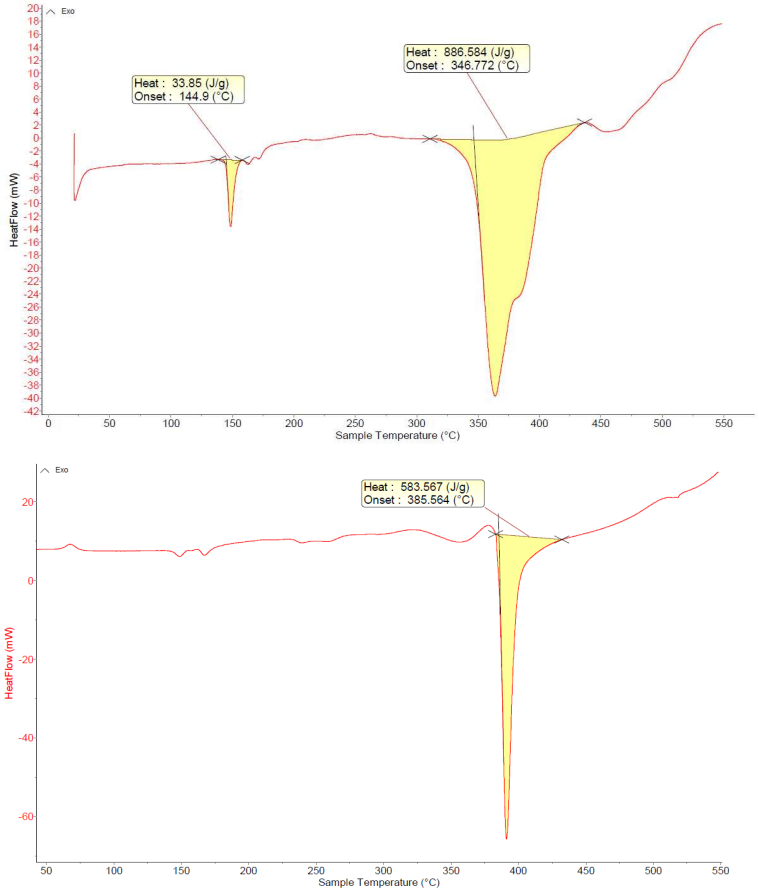

Figure 5.12 *DSC profiles for the temperature programmed desorption (TPD) runs for undoped CaH_2+AlB_2 system (above) and the one with NbF_5 catalyst (below). The addition of the niobium pentafluoride delays the desorption reaction start, but makes it faster and with a lower energy.*

As discussed, among the tested dopants, NbF_5 showed the best effect for hydrogen release for the CaH_2+AlB_2 system. Due to the presence of the fluorinated catalyst, some fluorine containing volatile compounds can be formed and their gas could be present in the released mixture, together with hydrogen. This is a very important aspect, which should be taking into account for material for hydrogen storage, which are supposed to be used in hydrogen storage systems for fuel cells feeding. Compounds such as hydrofluoric acid (HF) and diborane (B_2H_6) can cause corrosion in various components of the fuel cells and, at the same time, cause loss of fluorine or boron from the system. In order to check the presence of such compounds, an analysis of the gas released by the system CaH_2+AlB_2+5wt%NbF_5, ball milled for 90 min and hydrogenated as described above, was performed by mass spectroscopy (MS). As known, with this technique it is possible to identify molecular species, even when in traces amount. The technique is based on the separation of ions on the base of their mass/charge ratio. In a mass spectrometer, the sample's molecules are ionized because of the interaction with a striking electron beam with know energy. The excited molecules are unstable and divide into ions, according to typical known schemes, depending on their chemical structure. Usually a positive polarization is used for the ions to be analyzed, so that anions and electrons are collected by a positive electrode, while cations are driven toward the detector. As the ions must be free to move inside the spectrometer, high vacuum must be ensured. On the basis of the mass/charge ratio the cations are then selected by the detector and the primitive molecular species are identified. Various types of detector can be used, quadrupole being the most common one. The analysis on our sample was performed by coupling the *PCT-Pro2000 Sievert*'s type apparatus to a residual gas analyzer (*RGAPro*, by *Setaram*) for real-time compositional analysis on the gas released fro the *Sievert*'s apparatus chamber. The quadrupole detector of the *RGAPro* is able to discriminate chemical species up to 200 a.m.u.

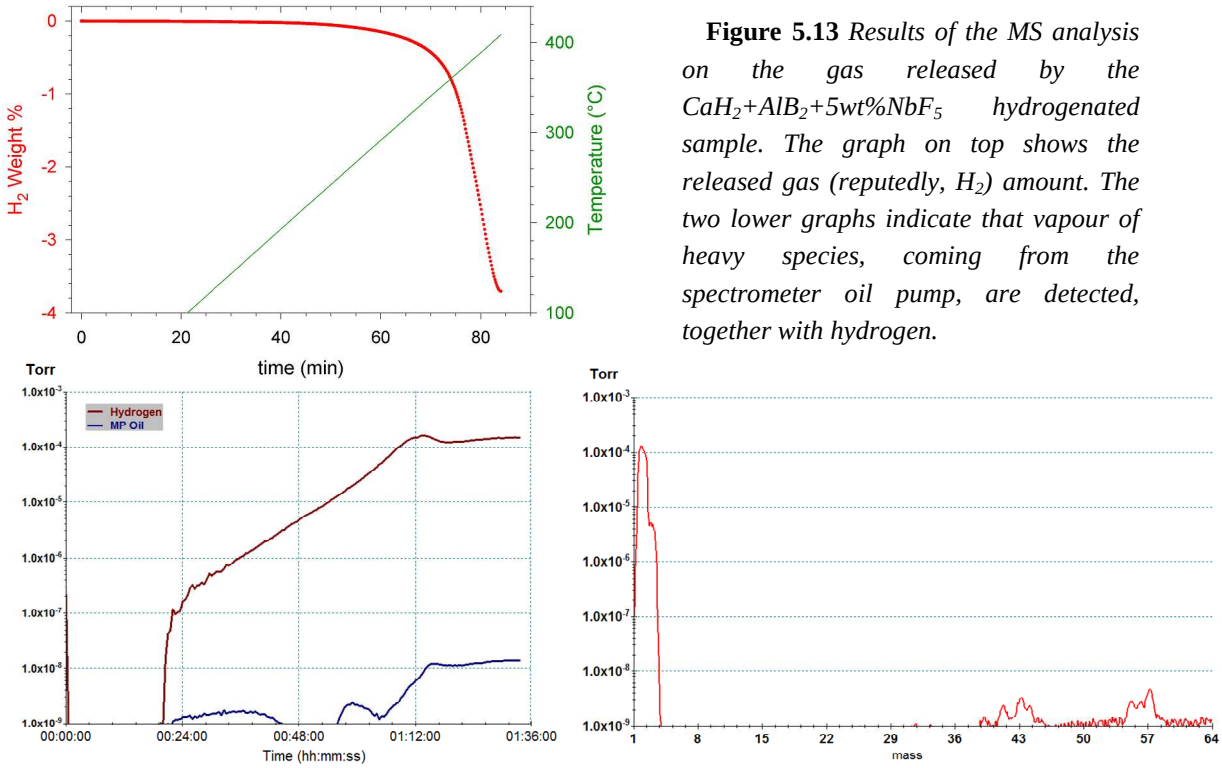

Figure 5.13 *Results of the MS analysis on the gas released by the CaH_2+AlB_2+5wt%NbF_5 hydrogenated sample. The graph on top shows the released gas (reputedly, H_2) amount. The two lower graphs indicate that vapour of heavy species, coming from the spectrometer oil pump, are detected, together with hydrogen.*

The three graphs in **figure 5.13** show the results of the analysis. The graph on top reports the hydrogen release amount up to the temperature of 410 °C, reached with a heating ramp of 2 °C/min. Below, the graph on the left shows the spectrometer signal, indicating the partial pressure of hydrogen and another component, which is identified with the vacuum pump oil. This is also confirmed by the mass spectrum on the right, were the main peak represents the hydrogen. The vacuum pump oil is constituted by species, with molecular mass higher than 38 a.m.u., while no other peaks belonging neither to HF (20) or B_2H_6 (28) are revealed, thus indicating that the gas released from the sample does not contain any poison or corroding agent for fuel cells. The mass spectrum shown above was acquired 24 min after the test start in an acquisition time of 30 sec. Subsequently, other spectra were acquired at regular intervals form the released gas, in order to register potential change of the gas mixture composition, which however did not occur.

5.4 Summary

In this chapter, a study on a calcium-based reactive hydride (RHC) composite is reported. The experiment activity started with the investigation of the hydrogen sorption properties of the system CaH_2+MgB_2, from which the RHC $Ca(BH_4)_2$+MgH_2 can be obtained upon hydrogenation. The used operative conditions lead to the formation of the desired products, together with an intermediate species, which hinders full hydrogenation of the system. The increase in ball milling time, tested up to 900 min, enhances the system kinetics and this is connected to the reduction of the particles size. Dehydrogenation and second hydrogenation of the system showed only partial reversibility of the system, due to the formation of amorphous boron. In order to improve the hydrogen sorption properties of the system, partial and total substitution of the magnesium diboride with the similar species aluminum boride was tested. The results of the first absorption/desorption cycle on the new systems indicated that partial (half) substitution did not cause any improvement on the first hydrogenation, while total substitution leads to better performances. In particular, even with a lower theoretical hydrogen absorption capacity, the system CaH_2+AlB_2 showed the same amount of absorbed hydrogen, thus considerably increasing the reaction yield. In addition, it was found that the presence of AlB_2 in the initial mixture improves the reversibility of the system. A comparison of the experimental evidences with the results present in the literature on calcium borohydride-based systems, suggest that the presence of AlB_2 has positive effect on the formation of boron containing intermediate phases, which improve the system reversibility. Actually, this is and effect which was found in literature to be provided also by the use of fluorinated catalysts. Some additives have been tested as potential catalysts for the CaH_2+AlB_2 system. While no positive effect was found on absorption kinetics, the tested substances were found to improve the hydrogen release process. In particular, NbF_5 can be indicated as the best additives, similarly to what reported in the literature for other calcium-

based systems. The analysis of the gas released during hydrogen desorption in the NbF_5 doped system did not show any evidence of species that can potentially damage a fuel cell. Finally, with the study reported in this chapter, some information is given on the system CaH_2+AlB_2, never reported before in the literature as a potential hydrogen storage medium. More investigations on the hydrogenated, dehydrogenated and rehydrogenated systems are needed in order to clarify the reactions path and thus assess the actual potential of the system for hydrogen storage.

[5.1] S. Orimo, Y. Nakamori, J.R. Eliseo, A. Züttel, C.M. Jensen, *Complex Hydrides for Hydrogen Storage*, Chem. Rev. 107 (2007) 4111-4132.

[5.2] F. Schüth, B. Bogdanović, M. Felderhoff, *Light metal hydrides and complex hydrides for hydrogen* storage, Chem Commun. 20 (2004) 2249-2258.

[5.3] Y. Kim, D. Reed, Y.S. Lee, J.Y. Lee, J.H. Shim, D. Book, Y.W. Cho, *Identification of the Dehydrogenated Product of $Ca(BH_4)_2$* , J. Phys. Chem. C 113 (2009) 5865-5871.

[5.4] M. Verga, F. Armanasco, C. Guardamagna, C. Valli, A. Bianchin, F. Agresti, S. Lo Russo, A. Maddalena, G. Principi, *Scaling up effects of Mg hydride in a temperature and pressure-controlled hydrogen storage device*, Int. J. Hydrogen Energy 34 (2009) 4602-10.

[5.5] P. De Rango A. Chaise, J. Charbonnier, D. Fruchart, M. Jehan, P. Marty, S. Miraglia, S. Rivoirard, N. Skryabina., *Nanostructured magnesium hydride for pilot tank development*, J. Alloys Compd. 446–447 (2007) 52–57.

[5.6] A. Khandelwal, F. Agresti, G. Capurso, S. Lo Russo, A. Maddalena, S. Gialanella, G. Principi, *Pellets of MgH_2-based composites as practical material for solid state hydrogen storage*, Int. J. Hydrogen Energy 35 (2010) 3565-3571.

[5.7] G. Barkhordarian et al., International patent application, Publ. n° WO2006063627.

[5.8] Vajo J. et al., Patent pending, Int. Pub. N° WO2005/097671 A2 2005.

[5.9] L. Lutterotti, *Maud version 2.0: Materials Analysis Using Diffraction* (2005) http://www.ing.unitn.it/~maud/

[5.10] G. Barkhordarian, T.R. Jensen, S. Doppiu, U. Bösemberg, A. Borgshulte, R. Gremaud, Y. Cerenius, M. Dornheim, T. Klassen, R. Bormann et al., *Formation of $Ca(BH_4)_2$ from Hydrogenation of CaH_2+MgB_2 Composite*, J. Phys. Chem. C 112 (2008) 2743-2749.

[5.11] T. Noritake, M. Aoki, M. Matsumoto, K. Miwa, S. Towata, H.-W. Li, S. Orimo, *Crystal structure and charge density analysis of $Ca(BH_4)_2$*, J. Alloys Compd. 491 (2010) 52-67.

[5.12] A.M. Russell, B.A. Cook, J.L. Harringa, T.L. Lewis, *Coefficient of thermal expansion of $AlMgB_{14}$*, Script. Mater.. 46 (2002) 629-633.

[5.13] C. Suryanarayana, *Mechanical Alloying and Milling*, Progr. Mater. Sci. 46 (2001) 1-184.

[5.14] D. R. Lide, *Handbook of Chemistry and Physics 84th edn*, Boca Raton, FL: CRC Press.

[5.15] G. Barkhordarian, T. Klassen, M. Dornheim, R. Bormann, *Unexpected kinetic effect of MgB_2 in reactive hydride composites containing complex borohydrides*, J. Alloys Compd. 440 (2007) L18-21.

[5.16] C. Wolverton, D.J.Siegel, A.R.Akbarzadeh, V.Ozoliņš, *Discovery of novel hydrogen storage materials: an atomic scale computational approach*, J. Phys.: Condens. Matter 290 (2008) 64228.

[5.17] Y. Filinchuck, E. Ronnebro, D. Chandra, *Crystal structure and phase transformation in $Ca(BH_4)_2$*, Acta Mater. 57 (2009), 732-738.

[5.18] B. Post, *Refractory Binary Borides, Metallo-Boron Compounds and Boranes*, Wiley - New York (1964).

[5.19] V.I. Bakhmutov, *Solid-State NMR in Materials Science: Principle and Applications*, CRC Press (2011).

[5.20] E. Rönnebro, E. Majzoub, *Calcium Borohydride for Hydrogen Storage*: Catalysis and Reversibility, J. Phys. Chem. B (Lett.) 111 (2007) 12045-12047.

[5.21] L.-L. Wang, D. Graham, I.M. Robertson, D.D. Johnson, *On the reversibility of Hydrogen-Storage Reactions, in $Ca(BH_4)_2$: Characterization via Experiment and Theory*, J. Phys. Chem. C 113 (2009), 20088-20096.

[5.22] C. Bonatto Minella, S. Garroni, C. Pistidda, R. Gosalawit-Utke, G. Barkhordatian, C. Rongeat, I. Lindemann, O. Gutfleisch, T. R. Jensen, Y. Cerenius, J. Christensen, M. D. Barò, R. Bormann, T. Klassen, M. Dornheim, *Effect of Transition Metal Fluorides on the Sorption Properties and Reversible Formation of $Ca(BH_4)_2$*, J. Phys,. Chem C (2011) 115, 2497-2504.

[5.23] R. Gosalawit-Utke, K. Suarez, j.M. Bellosta von Colbe, U. Bösemberg, T.R. Jensen, Y. Cerenius, C. Bonatto Minella, C. Pistidda, G. Barkhordarian, M. Schulze, T. Klassen, R. Bormann, M. Dornheim, *$Ca(BH_4)_2$-MgF_2 Reversible hydrogen Storage: reaction Mechanisms and Kinetic Properties*, J. Phys. Chem. C 115 (2011) 3762-3768.

[5.24] H. Kabbour, C.C. Ahn, S.-J. Hwang, R.C. Bowman Jr., J. Graetz, *Direct synthesis and NMR characterization of calcium alanate*, J. Alloys Compd. 446-447 (2007) 264-266.

[5.25] A.E. Finholt, *Method for producing diborane*, U.S. Patent 2550985 (1951).

[5.26] M. Fichtner, C. Frommen, O. Fuhr, *Synthesis and Properties of Calcium Alanate and Two Solvent Adducts*, Inorg. Chem. 44 (2005) 3479-3484.

[5.27] M. Schwarz, A. Haiduc, H. Still, P. Paulus, H. Geerlings, *The use of complex metal hydrides as hydrogen storage materials: Synthesis and XRD-studies of $Ca(AlH_4)_2$ and $Mg(AlH_4)_2$*, J. Alloys Compd. 404-406 (2005), 762-765.

[5.28] C. Li, X. Xiao, L. Chen, K. Jiang, S. Li, Q. Wang, *Synthesis of calcium alanate and its dehydriding performance enhanced by FeF_3 doping*, J. Alloys Compd. 509, 3 (2011) 590-595.

[5.29] M. Mamatha, B. Bogdanović, M. Feldererhoff, A. Pommerin, W. Schmidt, F. Schüth, C. Weidenthaler, *Mechanochemical preparation and investigation of properies of magnesium, calcium and lithium-magnesium alanates*, J. Alloys Compd. 407, 1-2 (2006) 78-86.

[5.30] J.-H. Kim, J.-H. S., Y.W. Cho, *On the reversibility of hydrogen storage in Ti- and Nb-catalyzed $Ca(BH_4)_2$*, J. Power Sources 181 (2008) 140-143.

[5.31] C. Rongeat, V. D'Anna, H. Hagemann, A . Borgschulte, A. Züttel, L. Schultz, O. Gutfleisch, *Effect of additives on the synthesis and reversibility of $Ca(BH_4)_2$*, J. Alloys Compd. (2010) 493, 281-287.

Appendix to chapter 5

The table below report additional results of the *Rietveld* refinement performed with the *MAUD* **[5.9]** software package on the experimental XRPD patterns shown in **Chapter 5**.

sample: CaH_2+MgB_2 90 min milled (**figure 5.1**) [R_{wp}% = 14.2]						
phases	wt%	structure	space group	cell parameters [Å]		
				a	b	c
CaH_2	48	orthorombic	Pnma	5.957(4)	3.603(8)	6.821(9)
MgB_2	52	hexagonal	P6/mmm	3.086(9)		3.524 (7)

sample: CaH_2+MgB_2 90 min milled and hydrogenated (**figure 5.3**) [R_{wp}% = 8.4]						
phases	wt%	structure	space group	cell parameters [Å]		
				a	b	c
β-$Ca(BH_4)_2$	23	tetragonal	P-4	6.916(0)		4.478 (8)
γ-$Ca(BH_4)_2$	13	orthorombic	Pbca	13.579(3)	8.149(8)	7.506(9)
$Ca_4Mg_3H_{14}$	39	hexagonal	P-62m	6.300(1)		6.877(6)
MgH_2	6	tetragonal	P42/mnm	4.514(1)		3.006(7)
MgB_2	19	hexagonal	P6/mmm	3.080(0)		3.529(3)

sample: CaH_2+MgB_2 90 min milled, hydrogenated and dehydrogenated (**figure 5.4**, left) [R_{wp}% = 16.6]						
phases	wt%	structure	space group	cell parameters [Å]		
				a	b	c
CaH_2	49	orthorombic	Pnma	5.996(2)	3.604(8)	6.819(6)
Mg	36	hexagonal	P63/mmc	3.213(3)		5.217(2)
MgB_2	52	hexagonal	P6/mmm	3.040(3)		3.528(0)

sample: CaH_2+AlB_2 90 min milled and hydrogenated (**figure 5.6**) [R_{wp}% = 23.8]						
phases	wt%	structure	space group	cell parameters [Å]		
				a	b	c
γ-$Ca(BH_4)_2$	52	orthorombic	Pbca	13.016(0)	8.782(7)	7.558(0)
CaH_2	14	orthorombic	Pnma	5.965(8)	3.605(2)	6.824(9)
Al	30	cubic	Fm-3m	4.053(9)		
AlB_2	4	hexagonal	P6/mmm	3.009		3.262

Chapter 6

Hydrogen storage in a polymer-based system

6.1 Polymeric materials for hydrogen storage

As reported in **chapter 2**, together with metal hydrides, high surface area materials are studied as potential candidates to store hydrogen. For this kind of materials, such as carbon nanostructures (carbon nanotubes, nanohorns, fibres, aerogel, fullerenes, graphite), metal-organic frameworks (MOFs) and zeolites, the sorption mechanism is typically a physisorption of the molecular hydrogen, which deposits on the surface material as a mono-layer or multi-layers. However, in some cases, chemisorption can occur and interface interactions are stronger, even for a process still limited to the surface (adsorption). For this reason, the main feature that affects the hydrogen capacity in these materials is the extent of the surface area and the size of the pores, while the bulk does not play any role in hosting the hydrogen. Actually, this is the main issue that hampers the use of these high surface area materials as hydrogen storage system. Moreover, the interaction of these materials with hydrogen is regulated by low energies forces (*Van Der Waals*, H-bonding); this implies that the maximum hydrogen amount is stored at cryogenic temperatures and high hydrogen pressure, where these types of bonds can exist and hydrogen release from the surface does not occur. For this reason, these materials are preferred to be used as scaffolds for other hydrogen storage materials (hydrides), rather than alone for hydrogen storage. The scaffolds would have the role to host the active material and maintain it in the nanometer range: the nanometer size particles of the material would offer high surface area for hydrogen dissociation/recombination mechanisms, and reduced diffusion paths for the growing phases. In this way, the hydrogen sorption kinetics and the thermodynamics of the system can be

theoretically improved. Unfortunately, the hydrogen sorption cycles in critical conditions can cause high mechanical stress on the porous material and the collapse of its structure.

Also polymeric materials can be used as scaffolds or matrices to host hydrogen storage materials. In fact, up to now, no polymer can be indicated as a material with high hydrogen storage capacity. For example, some results **[6.1]** **[6.2]** on conducting polymers such as polyaniline and polypyrrole with claimed high capacity could not be confirmed by other groups **[6.3]**, even when the material was prepared as a nanoporous polymer **[6.4]**.

In composite systems, the elasticity of polymers can be used to damp down the mechanical stress that the embedded hydrogen storage material (e.g. a metal hydride) can undergo during sorption cycles. What is more, at this time there is still the open question whether the hosting polymer plays a role in modifying the hydrogen storage capacity of a metal hydride. For example, depending on the charge of the hydrogen species, a combination of covalent, ionic, metallic, H-bonds and *Van Der Waals* interactions could exist within and between the polymer chains and/or with the metal hydride. Free radicals present within the polymer structure could further participate in hydrogen movement through the polymer network **[6.5]**. Other important aspects that make polymer-based systems attractive for hydrogen storage are the low density and costs of the materials and the relatively easiness in synthesizing, functionalizing and loading the polymer matrix.

Some transition metal oxides, such as TiO_2 and MnO_2, have been tested as dopants to improve the hydrogen sorption properties of light metals **[6.6]** **[6.7]** and complex **[6.8]** **[6.9]** hydrides.

This chapter reports the results of the investigation on the hydrogen sorption on functionalized PolyEhterEtherKetone (PEEK) in which MnO_2 has been incorporated. The samples were prepared and characterized with various techniques by a research group of the *Institute for Advanced Energy Technologies* (ITAE), Messina (Italy). The author contributed with the characterization of the hydrogen sorption properties of the synthesised powders. Both preparation and various characterizations of the system are reported in the present chapter.

6.2 Samples description

High performance *Victrex*® PEEK™ *450 PF* (**figure 6.1**) has been chosen due to its mechanical and chemical resistance **[6.10],** and purchased in form of powder. The material has been functionalized by chlorosulfonation reaction with the procedures reported in **[6.11]** and here described. At first, the commercial polymer has been dried under vacuum in an oven, at 80 °C for 4 h. The dry polymer has been functionalised via an electrophilic aromatic substitution with chlorosulfonic acid (*Aldrich*) at 30 °C under stirring for 24 h, in order to obtain a highly sulfonated PEEK with a sulfonation degree of roughly 100% **[6.12]**. The material obtained by chlorosulfonation is the precursor of the final target product, and is hereafter indicated also with the acronym SPCl (chlorosulfonated PEEK).

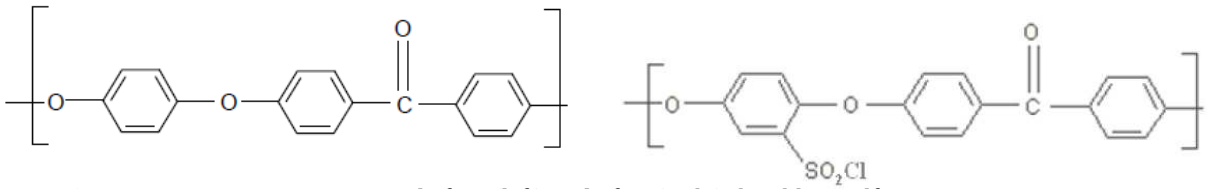

Figure 6.1 *PEEK monomer unit: before (left) and after (right) the chlorosulfonation.*

The SPCl has been precipitated in cold water and completely dried in an oven at 70 and 120 °C. Subsequently, with the addition of the polymer to an acid solution of $KMnO_4$ with different concentrations, the reaction has been carried out. The $KMnO_4$ solution has been added to the precursor, under stirring at room temperature for 2.5 h, and then the temperature has been increased to 50 °C and maintained for different reaction times. The acid environment determines the reduction reaction of MnO_4- to MnO_2, as reported below:

$$MnO_4^- + 4\,H^+ + 3\,e^- \rightarrow MnO_2 + 2\,H_2O \quad (6.1)$$

During the reaction time, the initially yellow polymer changed its colour until it became a dark brown, meaning that the formation of manganese oxide occurred. After the reaction at 50 °C, the obtained sample has been washed several times until obtaining a neutral pH. On the liquid filtered during the first rinse of the material, a chloride test has been performed with $AgNO_3$ 1M: in all the cases the filtered liquid turned to cloudy because of AgCl precipitation, thus indicating that Cl^-/MnO_4^- anionic exchange occurred. After the rinses, the sample has been stirred in water at 50 °C for 15 h, subsequently dried in an oven at 80 °C for 2 h and then finally ground. The acronym that is adopted here to indicate the so prepared material is $SPMnO_2$ (sulfonated PEEK with incorporated manganese oxide). As mentioned, samples have been prepared in different conditions, varying both $KMnO_4$ solution concentration and the duration at T = 50 °C of the $Cl^-/MnO4^-$ anionic exchange reaction. The three used combinations of these two parameters and the related obtained samples are reported **table 6.1**. The third column shows the ratio between the $KMnO_4$ amount and the chlorosulfonated polymer amount, used for the anionic exchange reaction. The fifth column shows the manganese oxide concentration calculated after keeping part of the sample inside an oven while heating from room temperature to 1100 °C and then at 1100° °C for 1h. After this treatment all the polymer is decomposed and the oxide remains, the initial oxide percentage is then calculated referred to the initial weight. As it is noticeable, both reaction time at 50 °C and permanganate percentage for the anionic exchange reaction strongly affects the final manganese oxide concentration (last column).

Table 6.1 *Samples synthesis conditions.*

sample	$[KMnO_4]$	mmol $KMnO_4$ / gr SPCl	Cl^-/MnO_4^- exchange reaction at 50 °C	manganese oxide %
$SPMnO_2$-A	0.02 M	2	1 h	15
$SPMnO_2$-B	0.02 M	2	3 h	20
$SPMnO_2$-C	0.1 M	10	3 h	78

In order to ascertain whether the formation of the functionalizing manganese oxide occurred, as it was supposed, the precursor (i.e. the chlorosulfonated polymer, SPCl) and the obtained powders have been dispersed in water and the pH has been monitored. The highly chlorosulfonated precursor decreased the pH from 5.5 to 3.8; this indicated that besides chlorosulfonation also simple sulfonation (SO_3H) is present, which is responsible of the presence of acid groups. For the water with dispersed polymer, the measured pH moved from 3.8 to higher values, with the increasing (supposed) oxide value. For $SPMnO_2$-A, B, C the pH was 4.5, 5.1 and more than 6, respectively. This results actually confirm the formation of manganese oxide, according to what reported by Malloy et al. **[6.13]**. In fact, metal oxides in an aqueous suspension tend to form hydroxyl groups on their surfaces. Chemisorption can occur, with the water molecules becoming singly coordinated on the surface; after coordination, dissociative chemisorption by the movement of protons to form hydroxyl groups can occur. Also Tamura et al. **[6.14]** examined hydroxyl groups specifically on the surface of manganese dioxide by a titration technique. The basicity of the hydroxyl groups would cause the deviation of the suspension pH toward values higher than 3.8.
In order to corroborate the results of the pH tests, on the actual presence of manganese oxide inside the prepared sample, other techniques were used and the qualitative analyses are reported in the next section. Subsequently, the results of the hydrogen absorption tests on the prepared samples, performed with a volumetric-manometric method, are reported.

6.3 Samples characterization

The polymer functionalization and the different oxide concentrations determine differences on the appearance of the samples, at both macro and micro scales. The pictures in **figure 6.2** show a progressive “hardening” of the system, mostly due to the increase of the manganese oxide percentage: the spongy consistency of the PEEK vanishes and totally disappears in sample $SPMnO_2$-C with the highest oxide content.

Figure 6.2 *Top line: PEEK before (left) and after(right) the chlorosulfonation treatment. Bottom line: the three samples $SPMnO_2$-A (left), $SPMnO_2$-B (centre) $SPMnO_2$-C (right).*

6.3.1 XRPD measurements

Figure 6.3 shows the X-ray powder diffraction patterns obtained by using a Philips X-ray automated diffractometer (model *PW3710*) with Cu Kα radiation source. The 2θ Bragg angles were scanned between 5° and 100°. The results of the XRPD analysis confirm the trend discussed on the basis of the pictures shown above. In fact, the semi-crystalline PEEK (azure curve) changes to amorphous after the chlorosulfonation treatment (SPCl, blue curve). Then, as the oxide content increases, the diffraction patterns of the samples show a bigger intensity of the crystalline MnO_2 peaks, compared to the intensity of the amorphous peak. The inset shows in a zoomed scale the diffraction pattern of the sample with the highest oxide percentage (**table 6.1**): the oxide peaks at 12°, 38° and 67° correspond to the barnesite-type manganese oxide **[6.15]**, with a lamellar structure, potentially suitable for molecular hydrogen intercalation.

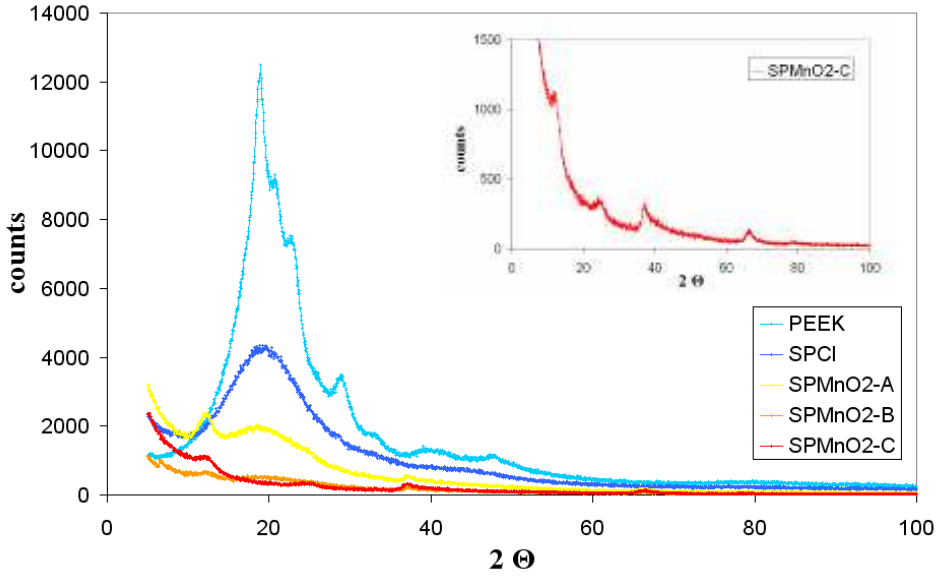

Figure 6.3 *XRD patterns for the polymer before and after chlorosulfonation treatment, and for the three samples with incorporated manganese oxide.*

6.3.2 Electron microscopy analysis

In order to deeper investigate the morphology of the prepared samples, an analysis with scanning electron microscope (SEM) and transmission electron microscope (TEM) has been performed. In general an electron microscope uses an electron beam (generated by a filament and a high voltage), differently from the optical microscope, for which radiation is used. The resolution of a microscope is in general inversely proportional to the wavelength of the used radiation. The photons of the light have a higher wavelength with respect to the electron beam, and thus, the electron microscopes achieve much higher resolution than the optical ones. In a SEM several particles are emitted from the sample struck by the electron beam, among which electrons. The emitted electrons are detected and converted into electrical pulses. The primary electron beam performs a scan on a rectangular part of the sample, in sequence of rows. Typically, the magnification provided by a SEM can reach 300000x and

the resolution can achieve 1 nm for some advanced models. In **figure 6.4** images of the prepared samples, obtained with a field emission scanning electron microscope *Philips XL30 S FEG*, are reported. In the SEM images the PEEK particles are clearly visible, with a diameter up to 50 μm (image a), while the chlorosulfonated polymer already shows a filament-like consistency (image b). The comparison of the three samples with the incorporated manganese oxide, at 5000x magnification (images c, d, e), shows the increase of the oxide crystals distribution inside the polymer matrix, as the oxide content increases (see **table 6.1**). A 30000x magnification image of the sample $SPMnO_2$-A, already shows the formation of white oxide agglomerates with size around 200 nm (image c').

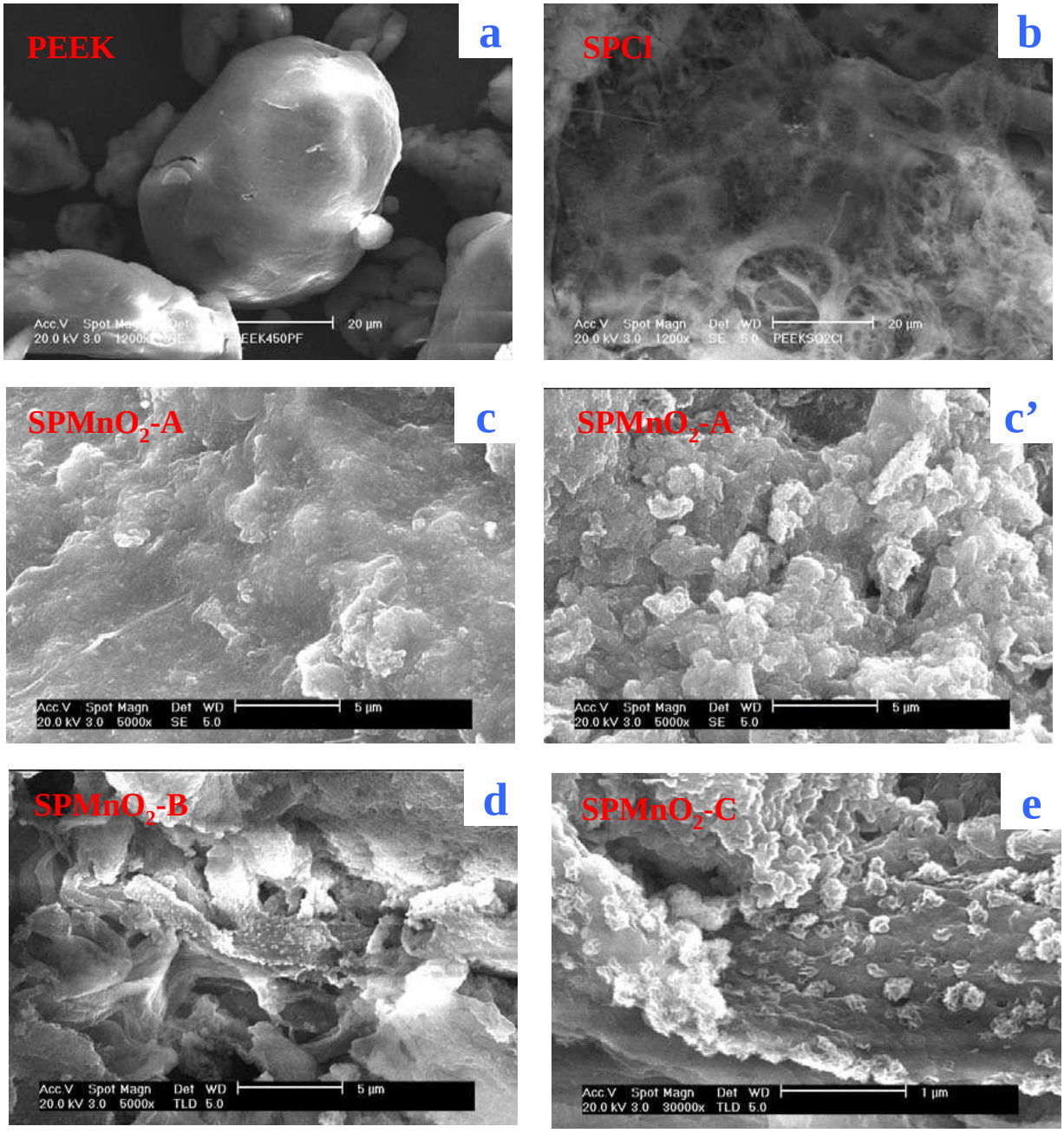

Figure 6.4 *SEM images. Top row: PEEK (left) and, SPCl (right); central row: $SPMnO_2$-A and $SpMnO_2$-A with higher magnification; bottom row: $SPMnO_2$-B (left), $SPMnO_2$-C (right).*

The method proposed by *Brunauer*, *Emmet* and *Teller* (BET method **[6.16]**) is nowadays the most used method for the evaluation of the specific surface area for a microporous material. As the method earlier proposed by *Langmuir* **[6.17]**, it is based on the evaluation of the volume of a gas (usually N_2) adsorbed on the sample surface. From the evaluation of the volume of the first layer of the adsorbate on the material's surface, the surface area amount can be obtained. Differently from *Langmuir*'s theory, the BET method takes into account the possible formation of further adsorbate layers, not only the first one, covering the material's surface. In general, the measurements are performed by isotherms (at this regard, see also introductions to **sections 2.2** and **2.4** of this thesis) at low temperature (77 K) and variable pressures, but below the saturation pressure (i.e. the pressure at which the adsorbate is saturated with its gas, at the temperature of the experiment).

BET measurements at 77 K under N_2 were performed on the sample SPMnO$_2$-A as well as on the PEEK before functionalization. Results indicate that the surface area remained in the range 10-23 m^2/g also after the manganese oxide insertion. Typically oxides have a surface area above 200 m^2/g, thus the BET measurements for the system suggest that the formed oxides have been incorporated in the polymeric matrix.

However, as already noticed with SEM images, oxide agglomerates form and increase in the polymeric matrix, as the oxide contents increases. A confirmation of this trend is also deducible from TEM analysis, which has been performed in order to deeper investigate the samples morphology. Differently from what occurs in a SEM, in a transmission electron microscope, the electron beam pass through the sample, which must be very thin, i.e. 50-500 nm. The beam, which already crossed the sample, is enlarged by special lenses in order to provide high magnification of the crossed sample image. Typically, the resolution of a TEM is about 0.2 nm (i.e. 500000 times the resolution of a human eye). **Figure 6.5** shows the images of the samples, obtained by using a *Philips CM12* transmission electron microscope with a LaB_6 filament and accelerating voltage of 120 kV. The typical needle-type morphology of the oxide, reported in literature, is clearly visible already for the sample SPMnO$_2$-A. A further magnification of this sample shows regions with reticular planes with similar inter-distances. In sample SPMnO$_2$-B the region where the oxide is present shows a higher concentration of needles, according to the higher oxide concentration (**table 6.1**). A more significant difference is visible in sample SPMnO$_2$-C where, together with an increased number and concentration of needles, the image at higher magnification shows reticular planes with different inter-distances. This suggests the presence of other oxides, with different manganese/oxygen ratio respect to MnO_2, such as Mn_2O_3, or other mixed K-Mn oxides, whose diffraction peaks overlap with those of MnO_2.

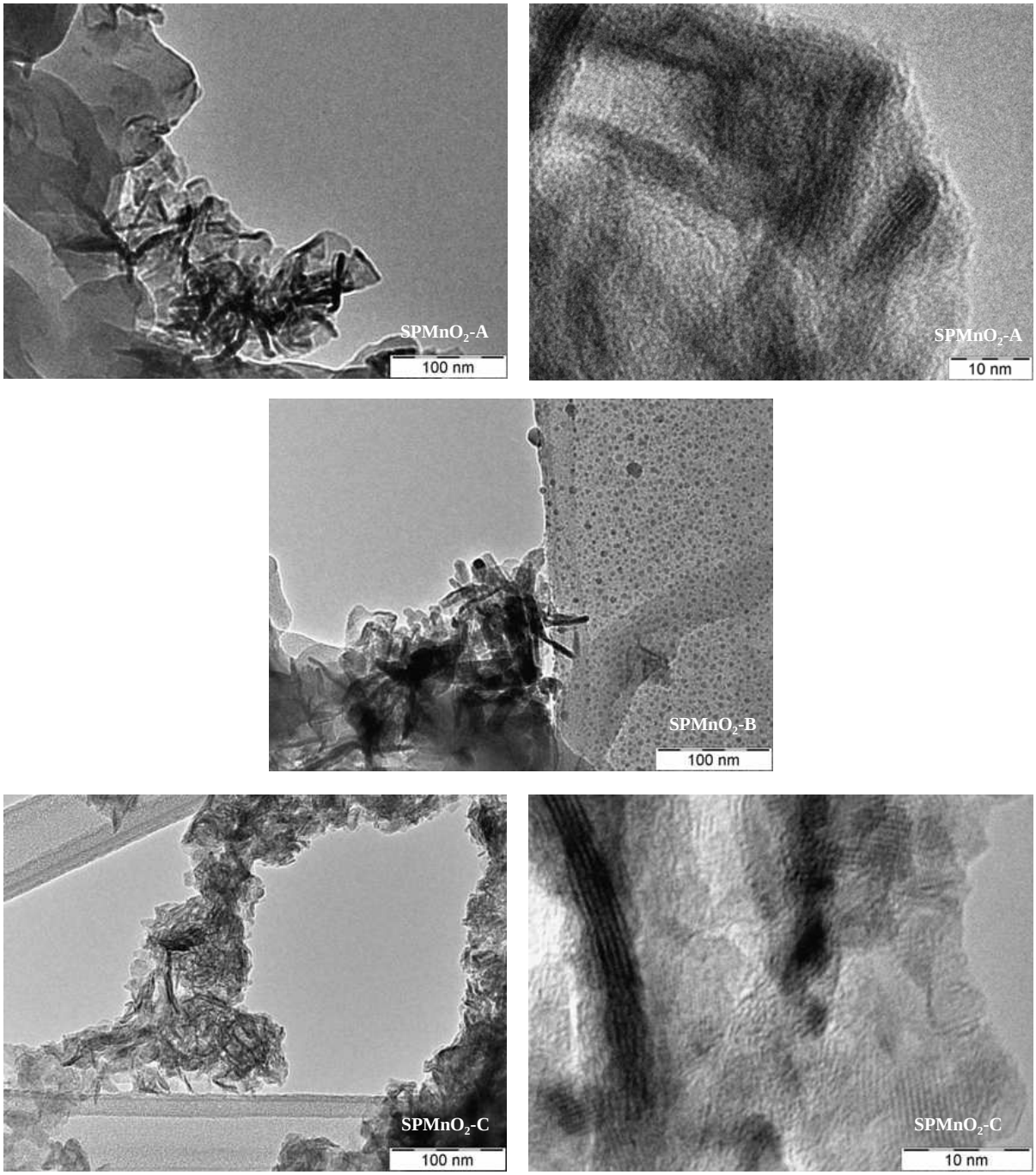

Figure 6.5 *Five TEM images of the three samples with incorporated oxide.*

By using the suitable microprobe of the SEM, an energy dispersive X-ray spectroscopy (EDX) analysis was performed on the samples. This elemental microanalysis is based on the measurement of the energy and the distribution of the intensity of the X-ray generated on the sample by the striking electron beam. In fact, once the beam strikes the material, some K or M electrons of the material are ejected and the atom gets excited. The X-rays produced by the atom relaxation can be emitted or cause an inner photoelectric effect, thus emitting Auger electrons. In the first case, X-ray photons are detected by an energy dispersion (ED) detector,

which take into account the electron-hole couples generated by X-ray passing through the detector material. By the interpretation of the induced electric signals, the nature of the element producing the X-rays can be revealed. The results of the EDX analysis are reported in **figure 6.6** and confirm the increase of the trend indicated by **table 6.1**, as regards the oxide amount inside the polymer. Nevertheless, presence of species from parent compounds, such as Cl and K, is also revealed, thus suggesting that the anionic exchange reaction did not go to completion (sample $SPMnO_2$-A), or that some mixed K-Mn oxides have been formed (sample $SPMnO_2$-C), as already suggested by TEM images.

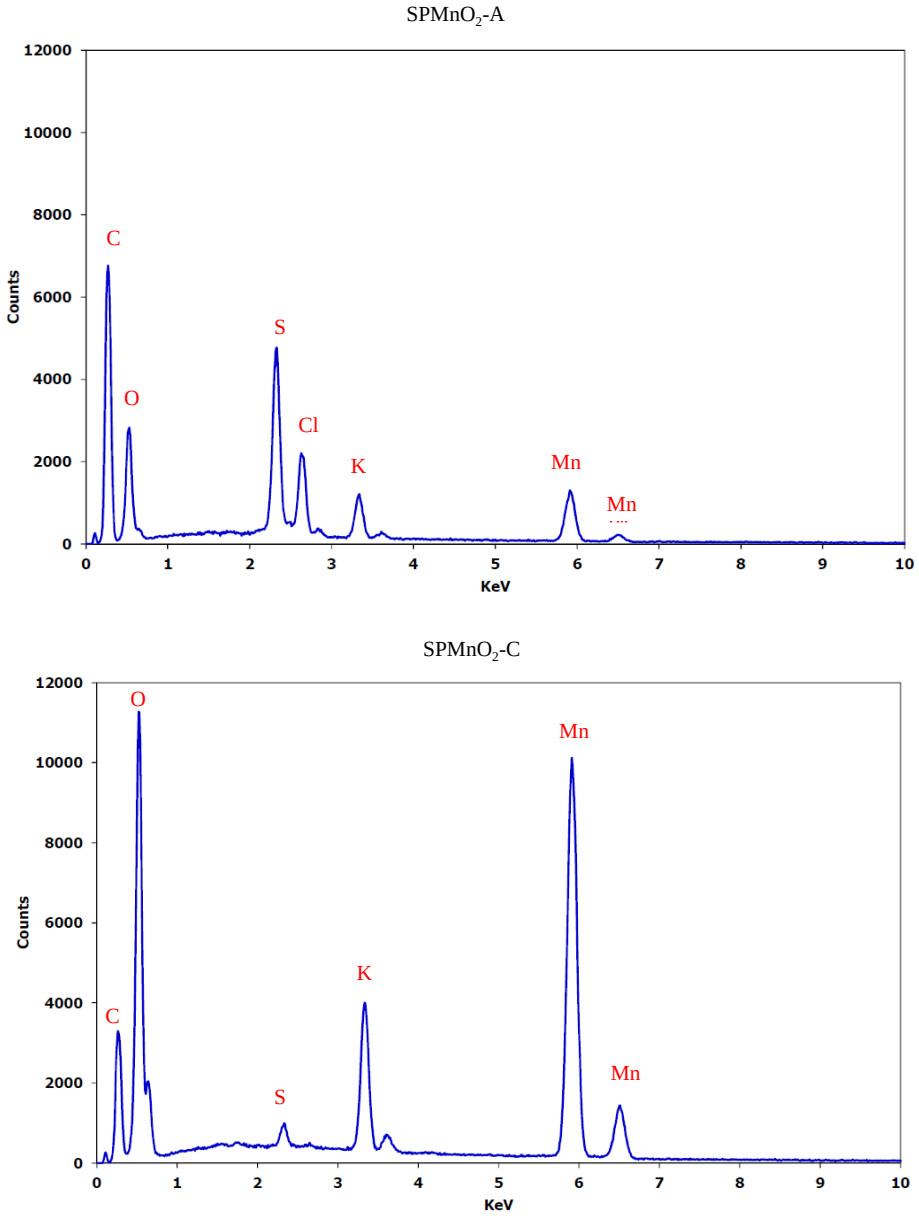

Figure 6.6 EDX analysis on *SPMnO2-A (upper) and SPMnO2-C (lower)* samples.

6.4 Hydrogenation

The synthesized composites $SPMnO_2$-A, $SPMnO_2$-B, $SPMnO_2$-C (**table 6.1**) have been tested with regard to their hydrogen sorption properties. By using a *PCT-Pro2000* (*Setaram*) *Sievert*'s type gas sorption analyzer (see **section 3.3**), kinetic hydrogenation curves have been obtained. The tests have been performed at 50 °C and 110 °C, which are temperatures compatible with PEM fuel cell operative conditions. For each test, a sequence of different steps of hydrogen pressure was used to charge the samples: in particular, in all the tests, 10, 20, 40, 60 bar of hydrogen pressure have been charged subsequently once the system reached the saturation each time with the current conditions. The tests lasted 1200 min in total. **Figure 6.7** shows the hydrogenation curves obtained for the three samples at 110 °C. The maximum hydrogen uptake increases as the manganese oxide content inside the sample increases. Interestingly, for sample $SPMnO_2$-A the hydrogen saturation (0.10 wt%) is reached with a hydrogen pressure (i.e. 40 bar) lower than that needed for sample $SPMnO_2$-B (60 bar). It must be observed that for the test on $SPMnO_2$-B the curve was affected by fluctuation of the hydrogen reservoir temperature, which caused the oscillation visible in the graph; however, this mishap seemed not to affect the average estimation of the hydrogen absorbed amount at saturation, which is around 0.18 wt%.

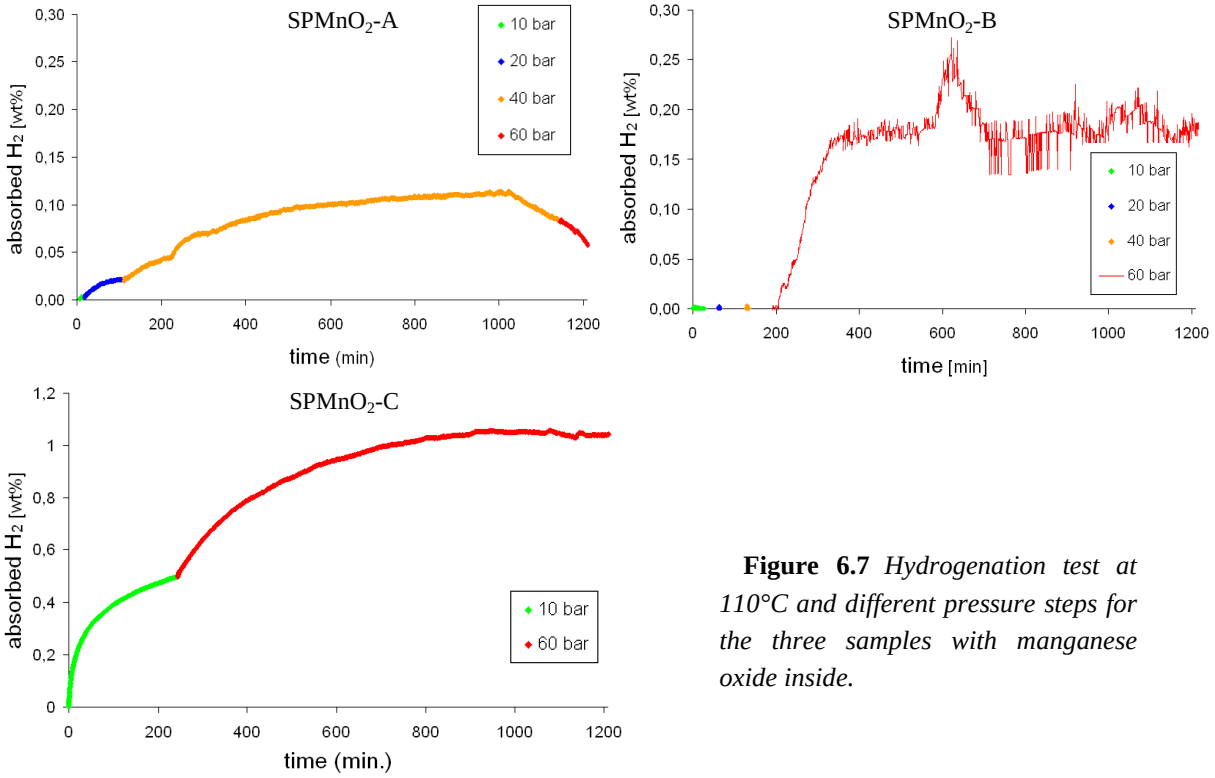

Figure 6.7 *Hydrogenation test at 110°C and different pressure steps for the three samples with manganese oxide inside.*

A remarkable result was obtained for the sample $SPMnO_2$-C, with the highest oxide content (**table 6.1**): the sample showed a high hydrogen capacity, compared to the other samples, already at 10 bar of hydrogen pressure. Once the system was approaching the saturation at 10 bar, a following step directly at 60 bar was used in order to reach the maximum hydrogen amount before 1200 min. Surprisingly, the sample was able to reach more than 1 wt% of

hydrogen capacity, which is, at the best of the author's knowledge, a value never reached up to now for polymer-based systems at room or higher temperature. Actually, this is a hydrogen storage capacity comparable to that of transition metals and/or rare earth alloys powders, commonly used for hydrogen storage applications at temperature below 150 °C. However, differently from polymer-based systems, these alloys are in general expensive, often pyrophoric, and must be reduced in size with mechanical process (e.g. high energy ball milling) before being used. Unfortunately, it was not possible to test the most interesting sample SPMnO_2-C for desorption. This is one of the tests that have been scheduled and that will be performed, once other amount of material will be synthesized with the procedure described in this chapter. All the samples were evacuated after performing the first hydrogenation at 110 °C. Only for a further SPMnO_2-A sample a desorption test was performed at 110 °C and 2 bar of hydrogen pressure, after the first hydrogenation. However, the desorption test could not give reliable data due two main reasons connected each other. As described in **section 3.3** of the thesis, when a manometric-volumetric measurement, performed with a *Sievert*'s type apparatus, starts, the sample holder and the reservoir volumes are instantly put in communication each other. The absorbed/desorbed hydrogen amount is then calculated on the basis of the change of the system global pressure. For desorption tests, usually a high reservoir volume (about 1 dm^3) must be used in order to keep the system pressure at low values for sample previously hydrogenated at high pressure. This means that even small variations of the big reservoir temperature can affect the calculation, especially whit low desorbed amounts. Referring to the hydrogenated sample SPMnO_2-A, this was just the case, because of the low hydrogen capacity value (< 0.1 wt%) achieved at the end of the first hydrogenation test at 80 bar. Surely, more reliable desorption data can be obtained with sample SPMnO_2-C, whose measurement are already scheduled, as mentioned.

It is worth to underline that, as visible in **figure 6.7**, for sample SPMnO_2-A a decrease of the stored hydrogen occurred after the system reached the saturation value and this trend continued even during the following and higher pressure step. This behaviour was registered also for other samples tested at 110 °C, where, after 2500 min and even with 80 bar of hydrogen pressure, the system showed a decrease of its hydrogen capacity (data not shown). As the decrease of the hydrogen absorbed amount occurs some time after the sample reached saturation, it could be hypothesized that the phenomenon is due to the effect of the temperature on the system kept for a long time at 110 °C. This seems not to be the case, as the samples were previously evacuated in a high vacuum (10^{-6} mbar) furnace at 100 °C, before the hydrogenation test. This thermal treatment was performed in order to remove the moisture potentially present in such hygroscopic materials. The results of the hydrogenation tests show a hydrogen capacity that seems to be in line with the manganese oxide inside the samples, as reported in **table 6.1**. The sample with almost the 80% of MnO_2 achieved the highest hydrogen capacity with operative conditions not usual for hydrogen adsorption process, even for materials with very high surface area (3000 m^2/g) **[6.18][6.19]**. This suggests at least a chemisorption effect of the material surface, or even a chemical interaction of the hydrogen

with the bulk of the material. The evident increase in the hydrogen uptake at 60 bar, for both sample SPMnO_2-B and -C suggest the presence of a clear thermodynamic behaviour of the system, similarly to what happens in metal hydrides. Together with desorption tests, further investigation on the structure and nature of the hydrogenated system will help to interpret the nature of the interaction of the material with the hydrogen and to clarify the cause of such encouraging results. Investigations are in progress also to clarify the cause of the hydrogen capacity reduction during the long time hydrogenation run.

6.5 Summary

This chapter reports the preliminary study on the hydrogen sorption properties of a high surface area functionalized polymer, PolyEhterEtherKetone (PEEK), in which MnO_2 should have been incorporated. The work reported in this thesis refers to a collaboration recently started off by the author with a research group of the *Institute for Advanced Energy Technologies* (*ITAE*), Messina (Italy). The samples were prepared and characterized morphologically, as well as by XRD, by the latter partner. The preliminary tests on hydrogen storage properties of the prepared samples were performed by the author. In order to give more information on the tested materials, preparation details and the results of the various characterizations are reported.

Commercial *PEEK™* was at first functionalized by chlorosulfonation reaction, thus preparing the precursor (here indicated by the acronym SPCl). Then, by an exchange reaction of chloride with permanganate, this chemical species, in which manganese is bound to the oxygen, is inserted in the material. The results of a pH test, performed on a water suspension of the prepared powders, suggest that actually manganese oxide formed and was incorporated in the polymer matrix. By varying permanganate concentration and the anionic exchange reaction time at 50 °C, three different systems have been prepared with respective oxide concentrations. The change of the powder appearance, as the hypothetical oxide content increases, is investigated also by electron microscopy. SEM and TEM images confirm the presence of (crystalline) species dispersed in the polymer matrix, as evidenced also by XRD measurements and suggested by BET measurements of the surface area extent. However, TEM images suggest, the presence of other species, in addition to manganese oxide, and this is also confirmed by elemental EDX analysis. Volumetric-manometric measurements have been performed in order to evaluate the hydrogen capacity of the prepared samples. Hydrogenation curves have been obtained at 110 °C and with consecutive steps of increasing pressures up to 80 bar. While poor hydrogen capacity was measured for the sample with lower oxide content, the interesting value of 1 wt% was found for the sample with almost the 80 wt% of oxide. This actually constitutes a surprisingly result for a system for which surface sorption mechanism was expected. In particular, the pressure values at which the maximum hydrogen capacity was reached is well below the 100 bar used at room temperature for tests

on other potential hydrogen adsorption candidate materials with high surface area up to 3000 m^2/g. Even more surprisingly, the value of about 1 wt% of stored hydrogen was reached at the temperature of 110 °C. These results seem to suggest a chemical interaction between hydrogen and the material, also possibly extended to the bulk, rather than the presence solely of weak forces, typical of physisorption. Unfortunately, reliable desorption measurements could not be performed during the period dedicated to the experimental activity reported in this chapter, and the synthesis of new powder is in progress in order to repeat the experiments here presented and to perform other tests, including desorption. In addition, further investigation on the structure and nature of the hydrogenated system are scheduled as a proceeding work for this seemingly promising low cost system.

[6.1] S.J. Cho, S.S. Kwang, T.H. Kim, K. Choo, Hydrogen Sorption in HCl-Treated Polyaniline and Polypyrrole; new Potential Hydrogen Storage Media, Prep. Paper Fuel Chem. Div. 47, 2 (2002) 790.

[6.2] S.J. Cho, K. Choo, D.P.Kim, J.W. Kim, *H_2 sorption in HCl-trated polyaniline and polypyrrole*, Catal. Today 120 (2007) 336-340

[6.3] B. Panella, L. Kossykh, U. Dettlaff-Weglikowska, M. Harsher, G. Zerbi, S. Roth, Volumetric measurement of hydrogen storage in HCl-treated polyaniline and polypyrrole, Synthetic Met. 151(2005) 208-210.

[6.4] J. Germain, J.M. Frèchet, F Svec, *Hypercrosslinked polyanilines with nanoporous structure and high surface area: potential adsorbents for hydrogen storage*, J. Mater. Chem. 17 (2007) 4989-4997.

[6.5] W.R. Schmidt, *Hydrogen storage in polymer-dispersed metal hydrides (PDMH)*, Activity report of the United Technologies Research Center for the Polymer Dispersed Metal Hydride program, DOE contract DEFC36-00G010535.

[6.6] W.Oerlich, T. Klassen, R. Bormann, *Metal oxides as catalysts for improved hydrogen sorption in nanocrystalline Mg-based materials*, J. Alloys Compd. 315, 1-2 (2001), 237-242.

[6.7] Z. Liu, Z. Lei, *Cyclic hydrogen storage properties of Mg milled with nickel nano-powders and MnO_2*, J. Alloys Compd. 443, 1-2 (2007) 121-124.

[6.8] B. Bogdanovic, M. Schwickardi, *Ti-doped alkali metal aluminium hydrides as potential novel reversible hydrogen storage materials*, J. Alloys Compounds 253-254 (1997) 1–9.

[6.9] Y. Suttisawat, P. Rangsunvigit, B. Kitiyanan, S. Kulprathipanja, *Effect of co-dopants on hydrogen desorption/absorption of $HfCl_4$- and TiO_2-doped $NaAlH_4$*, Int. J. Hydrogen Energy 33, 21 (2008) 6195-6200.

[6.10] http://www.victrex.com/it/victrex-library/datasheets/datasheets.php

[6.11] R. Pedicini, A. Saccà, a. Carbone, E. Passalacqua, *Hydrogen storage based on polymeric material, Int. J. Hydrogen Energy*, 36, 15 (2011) 9062-9068.

[6.12] S. Shane, J. Steven, A. David, *Crosslinked ion conductive membranes*, Int. Patent No. WO99/61141; 1999.

[6.13] A.P. Malloy, G.J. Browning, S.W. Donne, *Surface characterization of heat-treated electrolytic manganese dioxide*, J. Colloid Interface Sci. 285 (2005) 653-664.

[6.14] H. Tamura, T. Oda, M. Nagayama, R. Furuichi, *Acid-base dissociation of surface hydroxyl groups on manganese dioxide in aqueous solution*, J. Electrochem. Soc. 136 (1989) 2782-6.

[6.15] G. Zhu, H. Li, L. Deng, Z.-H. Liu, *Low-temperature synthesis of δ-MnO_2 with large surface area and its capacitance*, Mater. Lett. 64 (2010) 1763-1765.

[6.16] S. Brunauer, P.H. Emmett, E. Teller, *Adsorption of Gases in Multimolecular Layers*, J. Am. Chem. Soc. 60, 2 (1938) 309-319.

[6.17] I. Langmuir, *The constitution and fundamental properties of solids and liquids. part i. solids,*J. Am. Chem. Soc. 38 (1916) 2221-95.

[6.18] M. Hircher, B. Panella, *Nanostructure with high surface area for hydrogen storage*, J. Alloys Compd. 404-406 (2005) 399-401.

[6.19] G.P. Meisner, Q. Hu, *High surface area microporous carbon materials for cryogenic hydrogen storage synthesized using new template-based and activation-based approaches*, Nanotechnology 20, (2009) 204023.

Chapter 7

Design and building of a solid state hydrogen storage tank

7.1 The task

Together with the research on suitable materials for solid state hydrogen storage, another big issue for the development of alternative fuel tanks is the technological progress and know how in the storage vessel, as well as in the assembly of the whole storage system, which must be interfaced with the immediately following sections of the power train, typically fuel cells, internal combustion engines (ICEs), and burners.

In this view, a stage period of three and a half months at *Helmholtz Zentrum Geesthacht* (*HZG*) – Nanotechnology Department – Germany, has been devote to research activity on the design and building of a solid state hydrogen storage tank, as the main task. This activity was carried out in the frame of the "*Nios*" project in collaboration among automotive supplier *Strahle and Hess*, the universities of Merseberg and Giebichenstein, and *Fortis Saxonia* **[7.1]**. The project had as aim the development of a vehicle to be constructed with eco friendly and sustainable materials, and which could credibly take part in the *Shell Eco-marathon*[(a)]. In addition, the vehicle should be capable of carrying a driver and passengers in regular day-to-day traffic conditions. The task assigned to *HZG* is the design and the construction of a suitable hydrogen storage tank for the *Nios* car, according to the requirements in terms of occupied space and hydrogen supply.

(a) *Shell Eco-marathon* is a periodical international competition in which students energy efficient vehicle, designed and built by students, compete in a demonstrative race. More information at: http://www.shell.com/home/content/ecomarathon/.

The total requested amount of hydrogen to be provided with the storage system is at least 400 Nl, which is equivalent to 33.4 g (the density of hydrogen at 1 atm and 21°C is 0.08347 kg/m^3 **[7.2]**). 25 Nl/min are requested as an initial boost for at least 1 min, then the average gas supply should be of 400 Nl/h (= 6.7 Nl/min) to be hold up to the requested amount of total released hydrogen, or more. In **table 7.1** a summary of the hydrogen supply requirements from *Fortis Saxonia* are reported and **figure 7.1** shows the space available for the tank inside the car.

Table 7.1 *Base requirements for Nios concept car tank.*

Hydrogen flowrate [Nl/h]		Total hydrogen amount
Initial	Average	
25 Nl/min for 1 min	6.7 Nl/min (440 Nl/h)	400 Nl

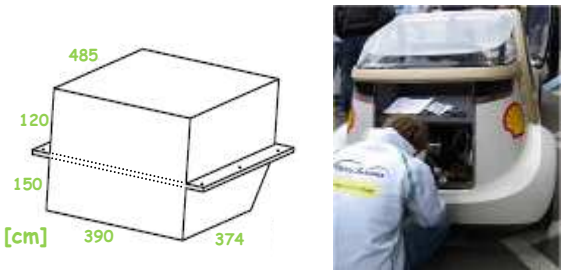

Figure 7.1 *Usable space for the tank inside the Nios car: schematic drawing (left) and location inside (right)*

With this values, the project focuses on a hydrogen supply system, which is intermediate between the laboratory scale, where typically few grams of materials (and much less than 1g of stored hydrogen) are used for the measurements, and the fully scale for vehicular applications, where 4-6 kg of hydrogen are requested for a 500 km driving range, with the ability to refuel in times comparable to conventional ICE vehicles **[7.3]**.

The car is not supposed to be equipped with elaborated system for the heat exchange with liquids and no particular requirements concerning the weight of the hydrogen tank were stated from the customer. For this reason, it was chosen as active storage medium a material able to work at room temperature, despite the consequent reduction in specific hydrogen capacity of the system. The results of the work are discussed in this chapter.

7.2 Preliminary tests

The material chosen for the preliminary test in order to design the *Nios* tank is the commercial product *HydralloyC5*® from GfE Company (Germany). This material has been chosen among some type of commercial "room temperature" alloys already present at the *HZG* Institute as stock (see **table 7.2** for a comparison among these materials). For the design of the system, a maximum hydrogen pressure of 30 bar inside the tank has been considered, while a value of 2 bar for the released hydrogen was assumed as sufficient for the fuel supply to the PEM-hydrogen-air fuel cell designed for the car. According to the values reported in **table 7.2**, the commercial product *HydralloyC5*® was chosen, since it shows a fair difference of the pressure values at equilibrium (values at half capacity) with respect to the values chosen for the hydrogen absorption and release for the application ($\leq$ 30 bar and $\geq$ 2 bar,

respectively), thus assuring a good driving for both processes. Actually, the values reported for this alloy are not the ones at room temperature, but at around 44°C, so the validity of the just reported assumption had to be born out with some preliminary experiments.

Table 7.2 *Base comparison of the types of room temperature alloys, already present as stock.*

Commercial Name	**Supplier**	**Composition**	**Plateau pressure**	**H_2 capacity**
HydralloyC5	*GfE*	**Mn**51,31% **Ti** 27,13% **V** 13,95% **Fe** 2,98% **Zr** 2,97% **Al** 0,27%	Abs: **20 bar** (T=44,4°C) Des: **12,6 bar** (T=44°C)	Abs: 1,81 wt% Des: 1,77 wt%
HydralloyE60/0	*GfE*	**La**18,4% **Ce**8,2% **Pr**1,6% **Nd**3,2% **Ni**64,2% **Sn**3,6%	Abs: **4,56 bar** (T=21,8 °C) Des: **2,11 bar** (T=18,7°C)	Abs: 1,42 wt% Des: 1,38 wt%
Hy– Stor	*MPD* Technology Corporation	**$LaNi_5$**	**1,35 bar** (T=21,8°C)	1,37 wt%
Ecka	*Eckart - Weeke*	(**Ti**, **V**, **Fe**, **Mn**) + 5 wt%Al	N.A.	N.A.

In order to obtain the necessary information for the design of the tank, some tests have been performed on a 500 cm^3 internal volume cylinder charged with about 1 kg of *HydralloyC5*® previously milled for 10 min on an high efficiency attritor mill. This simple tank was prepared to be used for another prototype car from *Fortis Saxonia*, called *Sax3* **[7.4]**.

The cylinder was connected to a testing system, named from now onward "Test Station": this apparatus was developed at *HZG* in the recent years **[7.5]** to perform tests of hydrogen tanks inside the operative range of 0.1 – 100 Nl/min of flow rate and up to 100 bar of pressure. The gas flow rate can be measured and managed by the use of two flow control units (FCUs) with two different operative ranges: 0.1-10 Nl/min and 10-200 Nl/min, respectively. Thus, one of the information used by the software of the Test Station to evaluate the absorbed or desorbed amount of hydrogen is the amount of flowed hydrogen measured from the FCUs. The other input data for the calculations are the temperature and the pressure, used to estimate the amount of hydrogen in the free volume gas phase, using the Van Der Waals equation of state. The Test Station is configured in a way that during hydrogen absorption or release tests, the set pressure value can be maintained until the hydrogen flow rate, toward the tank in case of adsorption, or from the tank in case of desorption, does not reach the limit value of 0.2 Nl/min. This is because beyond this value the accuracy of the low range flow control diminishes significantly. The set pressure value of the experiment can be achieved after a transient time needed to bring the tank at the desired pressure; this could be considered as the time needed to fill/discharge the hydrogen in/from the tank up to the final set pressure of the experiment. However, it must be taken into account that absorption/release in/from the

material already starts during this initial period. After the initial transient time the system proceeds in isobaric conditions up to the conclusion of the test.

This fact implies that, if also the temperature of the tank is controlled (using a thermal insulation for the tank and a heat exchanger), as well as the pressure, the system would operate in a way similar to the instruments used for the basic research on the sorption properties of hydrogen storage materials (manometric/volumetric *Sievert*'s type apparatus or others based on flowmeters).

Thus, the Test Station was initially designed with the idea of a scale-up process from the point of view of the study on hydrogen storage materials. Later on the implications of this fact on the test from an applicative point of view will be discussed.

The first results obtained with the Test Station on the *Sax3* tank are reported in **figure 7.2**, where absorption and release curves of the first 3 cycles are shown. The curves were obtained without any forced heat exchange on the system, with a constant room temperature set at 21°C, and with a pressure of 30 bar and 2 bar inside the tank, respectively for absorption and desorption. Only the small range FCU was used, so that the maximum achievable flow rate is 10 Nl/min.

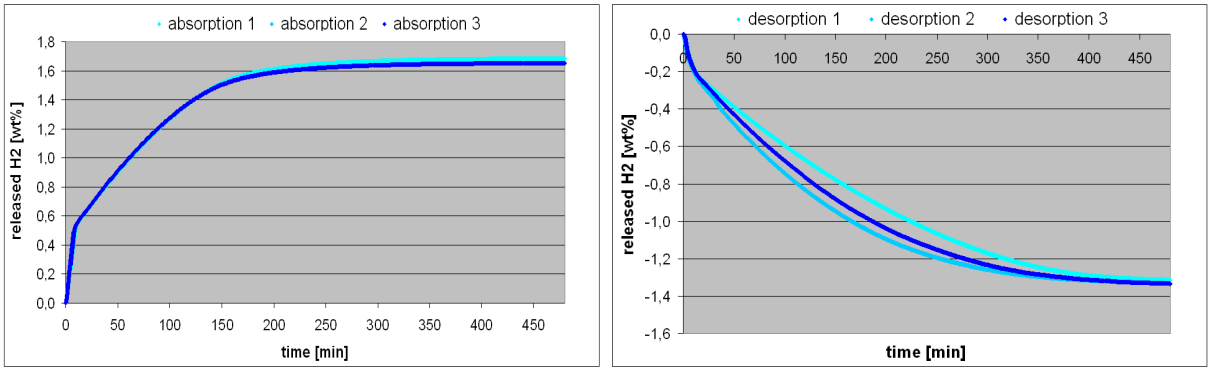

Figure 7.2 *First 3 sorption cycles on the Sax3 tank: absorption (left) and desorption (right) curves.*

The powder immediately showed its absorption performances already in the first cycle, while an improvement for the desorption is visible in the runs following the first one. Every absorption test was conducted on the system after a long evacuation period (at least 5h) under continuous vacuum: the powder showed a reproducible total absorbed amount of 1.65 wt%, which is not far from the one declared by the commercial supplier (**table 7.2**). The desorption curves indicate that the reversible cycling capacity, working within the selected pressure values of 30 bar and 2 bar for a cycle, is 1.35 wt%. For both absorption and release processes there is a discontinuity in the first part of the curves, after which the kinetics decreases in a continuous way up to the plateau. This is because, as mentioned above, there is a transient time used to let the system reach the desired working pressure as soon as possible. The sharp change in the slope is due to the sudden reduction of the flow rate, which was manually operated once the system reached the desired pressure value; from that moment onward each test proceeded in isobaric conditions.

Four thermocouples uniformly distributed along the cylinder on its external surface registered the temperature during each test. With the conditions reported above the local limit temperatures of the cylinder's external surface were 61 °C during the hydrogen absorption and 2 °C during the desorption, due to the exothermic and endothermic effects of the two processes, respectively. This limit temperatures could represent a problem for the environment in which the tank will be placed and for the surrounding surfaces and parts: in addition, the limit temperatures would be even more critical as the environment temperature inside the car will move away from the room temperatures (21°C) used for the tests. Moreover, a strong deviation from the reference temperature of 44 °C for good performance (see **table 7.2**) could stop or slow down the gas-solid reaction.

For this reason, other three cycles have been performed using two small fans, with the configuration showed in **figure 7.4**, to force and enhance the heat exchange between the cylinder and the surrounding air of the room. Surprisingly, the use of the two fans improved the absorption and desorption kinetics in a significant way, as shown in **figure 7.3**.

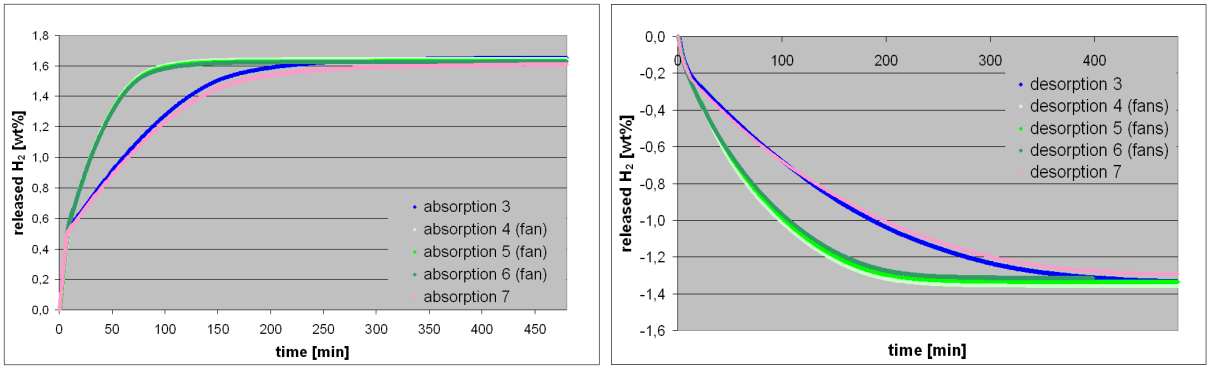

Figure 7.3 *Effect of the use of the fans (green curves) on the hydrogen absorption (left) and desorption (right) kinetics. For comparison two curves obtained without the use of fans (3rd and 7th cycles, blue and pink curves, respectively.*

The effect of the forced heat exchange on the kinetics is less powerful in the initial part, where the absorption and release processes are mainly driven by the fast change in the pressure of the system, before reaching the final desired pressure of the test (2 bar). The local limit temperatures registered with this new configuration were 57 °C and 6 °C, less critical than those obtained without the use of the fans.

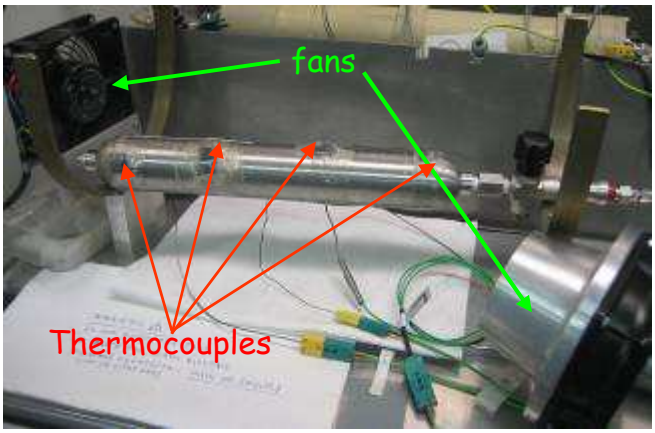

Figure 7.4 *The Sax3 hydrogen tank, consisting in a SS 500 ml internal volume cylinder. The thermocouples on the cylinder surface and the positions of the two fans are visible.*

After the three cycles with the use of the fans (runs 4,5,6), a further cycle (run 7) was performed with the initial configuration (run 1,2,3) without any forced heat exchange, in order to check whether the better results during the previous three cycles where due to a sort of powder activation, rather than to the effect of the fans. As can be easily noticed, the 7th cycle's curves (pink coloured) overlap to the last curve before using the fans (3th cycle, blue coloured curves), confirming that the better behaviour is due to the presence of the fans. The powder reaches its performances since the 2nd cycle and maintains the reversibility and kinetics of the sorption processes in the following cycles.

In order to obtain useful information for the design of the *Nios* car tank, referring to the requirements reported on **table 7.1**, two average hydrogen desorption rates have been considered in two regions of the graphs in **figure 7.3**, respectively: a) initial range 0.00-0.25 wt% , b) medium range 0.35-1.00 wt%. The linear fittings of the curves obtained without the use of the fans give 0.0145 wt%/min for the initial range and 0.0044 wt%/min for the medium range. In terms of available hydrogen volumetric flow rate, the average values in the two ranges were: 2 Nl/min and 0.6 Nl/min, respectively, the initial flow rate being enhanced by the discharge of the high pressure gas phase inside the tank from 30 bar to 2 bar. As expected, the corresponding values for the experiments with the fans are higher: 2.6 Nl/min and 1.1 Nl/min, for the initial and medium range, respectively. It is worth to underline that the use of the fans redouble the performances of the system in the middle range, where the process speed corresponds to the desorption kinetics of the powder in isobaric (2 bar) and isothermal (room temperature) conditions. One should refer this range as the average hydrogen supply to the car's fuel cell.

An indication of the opportunity of the use of the two fans can be obtained by comparing the net output power from the tank in the two cases: with and without fans. The power consumption of the two fans is between 20-25 W for each fan. As reported above, the output power from the tank in the medium range is 0.6 Nl/min and 1.1 Nl/min, without and with fans, respectively. This is equivalent to 101 W and 185 W, considering the lower heating value (LHV) of the hydrogen = 121 MJ/kg. If an efficiency of 70% is assumed for the fuel cell and if the power needed for the two fans is supplied by the fuel cell itself, the net final available power for the car in the medium range would be 70.7 W and 84.6 W in the two cases, respectively. Thus the use of the fans will increase by 20% the available power in the medium range, but will use the 35% of the total power generated by the fuel cell. This result would recommend the use of the fans only when the hydrogen rate rather than the total amount of supplied hydrogen is the critical aspect; furthermore, in this case the advantage for the use of the fan would be higher as higher the fuel cell efficiency is.

In **table 7.3** a summary of the results of the tests on the *Sax3* prototype hydrogen tank is reported.

Table 7.3 *Summary of the results obtained on the Sax3 tank with the test station. A schematic comparison of the results with the two different configurations, without fans and with two fans, is reported.*

Forced heat exchange (air)	Absorption			Desorption				Medium range	
	total H_2 amount		max local temper. [°C]	total H_2 amount		min local temper. [°C]	H_2 desorption rate		Fuel Cell output power (efficiency = 0.7)
	[Nl]	[g]		[Nl]	[g]		Initial range (0,0 - 0,25 wt%) [Nl/min]	Medium range (0,35 - 1,00 wt%) [Nl/min]	Total [W] / Net two fans [W]
none	226.1	18.9	61.4	180.7	15.1	2.1	2.0	0.6 (= 0.0044 wt%/min)	70.7 / 70.7
with 2 fans	222.1	18.5	56.7	182.3	15.2	5.8	2.6	1.1 (= 0.0079 wt%/min)	129.6 / 84.6

7.3 Tank design

The data obtained on the *Sax3* tank were used to design the *Nios* car hydrogen reservoir, according to the base requirements from *Fortis Saxonia* (**table 7.1**). The main requirements we focussed on were the hydrogen average flow rate of 400 Nl/h and the total amount of hydrogen of 400 Nl. As a first approximation for the initial flow rate of 25 Nl/min for 1 minute, it was assumed that this rate would be supplied from the hydrogen gas phase inside the tank during the transient from 30 bar to 2 bar. The following conservative assumptions were made in order to have some safety margin on the final performances of the designed tank; they are reported here below:

a) for the average hydrogen rate, calculations were done using the medium range average rate obtained on the *Sax3* tank without the use of the two fans: 0.0044 wt%/min;
b) the cycle capacity was considered reduced to 1.2 wt%, while the measured one was 1.35 wt%;
c) the *HydralloyC5*® density was calculated in first approximation as the average value between the weighted mean based on the alloy's composition (6343 kg/m^3) and the apparent density of the as received material, in form of flakes (3868 kg/m^3). This assumption is conservative because the free space between the flakes is high and thus the contribution of the as received material apparent density to the calculated average density makes it smaller;
d) the powder expansion inside the tank, during the hydrogenation process was supposed to be 20%: this is in general an high value also for this kind of material **[7.6]**;
e) the expanded powder would occupy only the 80% of the cylinder internal volume; thus even more free space is considered.

It is to be noted that each hypothesis reported above will have effect on the calculation of the suitable tank volume, which would be compared with the physical space available inside the car. In particular, the first assumption is related to the hydrogen desorption kinetics of the alloy and will have effect on the calculation of the total amount of powder necessary to fulfil the average hydrogen supply rate of 400 Nl/h (= 6.7 Nl/min). The second hypothesis is connected to the estimation of the total amount of material needed to release at least 400 Nl of hydrogen. Finally, all the other assumptions will lead to the calculation of the tank volume to host the previously estimated amount of powder.

The calculations gave:

- total amount of alloy to reach 400 Nl/h = 12.6 kg;
- total available hydrogen amount = 1818 Nl;
- total volume of the tank = 3.7 l

The second result states that the limiting factor to fulfil the customer's base requirements is the hydrogen release kinetics of the alloy, rather than its hydrogen capacity: in fact, the calculated amount of alloy necessary to reach the desired hydrogen rate will supply more than 4.5 times the minimum amount of requested hydrogen (400 Nl).

As said, the calculated tank volume should be compatible with the available space inside the car. In order to optimize the use of the available space a series of commercial cylinders and fittings from Swagelok® have been selected and 13 stainless steel cylinders with a 300 ml internal volume were chosen to host the material. Anyway, since the available space inside the car is able to host 15 cylinders of the selected type, the final designed layout of the tank is the one reported in **figure 7.5**. Three rows, named from now onwards "racks", of five cylinders each can be locate inside the car: two in the above part of the box and the third in the bottom part, below a sustain plate.

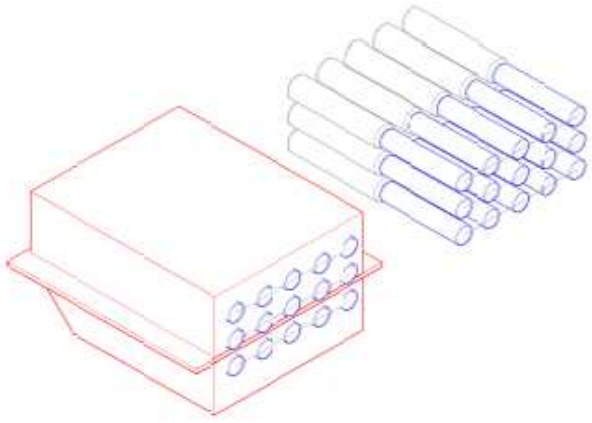

Figure 7.5 *Schematic designed layout of the Nios car's hydrogen storage tank: the blue cylinders indicate the volume occupied by the connections and fittings for each row of five cylinders; in grey colour the SS cylinders that will be filled with the HydralloyC5®.*

7.4 Alloy's preparation

The *HydralloyC5*® is received from the dealer in form of flakes, which are small stones with a distributed size around 1.5 cm. In order to reach the same conditions for the alloy used for the *Sax3* tank, ball milling process was supposed to be used to improve the hydrogen sorption kinetics of as received material. This technique, used for mechanosynthesis of the alloys, causes particle size reduction, thus increasing the active surface of the alloy and reducing the diffusion paths for the hydrogen inside the material **[7.7]**. However, the high efficiency attritor mill employed for the batch used for the *Sax3* was not available and thus another solution had to be found. Actually, this seemed to be an hard problem because of the huge total amount of powder needed for the system (at least 12.6 kg for 13 cylinders). The attritor mill is in fact able to process around 1kg of powder in one run and, just because of the high efficiency of this milling type, each run could have been only of ten minutes. This time is in fact sufficient to obtain loose powder, with a ball to powder ratio (BPR) of 10, and these were the conditions used for the *Sax3* alloy's powder. The high amount of powder necessary for the new tank could not be processed in a realistic time with a shaker mill, e.g., the Spex8000, due to the small amount of material that can be inserted in its vial: less than 20 g per run. For this reason, an attempt was done with a big planetary mill *Pulverisette 5*, equipped with four vials of 250 ml each. In order to compensate the lower efficiency of the planetary mill type **[7.8]** the milling time was initially set to 1h; using a BPR = 10 and a 50% filling percentage of the vials: in this way it was possible to charge around 300 g of *HydralloyC5*® flakes for the first test run.

Figure 7.6 *The three types of equipment available for the ball milling process; from left to right: attritor mill, shaker mill and planetary mill.*

The result of the milling process performed is shown in **figure 7.7**. Unfortunately, the use of planetary mill was not able to create loose powder, but rather all the ground material got stuck to the internal walls of the vial, forming a hard layer of agglomerated powder, which grows as the milling time increases, and that cannot be removed away easily. This hard agglomerate is located at a certain high of the internal wall of the vial and is identical for all the four vials charged in the planetary mill. Other attempts with lower milling time were performed in order to reduce the heating up of the powder and thus to prevent the sticking effect. Nevertheless, even using a milling time of 5 min, all the produced powder remained stuck to the internal walls of the vial, while not all the flakes were fragmented to fine powder but some of them just broken in smaller size particles. Similarly, the change in the rotation speed of the milling

(from 300 to 400 rpm) did not show any improvement. The formation of the hard stuck layer is a not rare phenomenon during the milling process of intermetallic alloys **[7.9]**, **[7.10]** and can be originated by specific features, like e.g. roughness on the internal surface of the vial, which would act as a centre of nucleation. In general, the presence of a hard layer stuck to the inner wall of the vial and on the balls surface is connected to the high temperature that the powder particles reach when they are involved in the crashes of the balls each other and of the balls to the vial's walls. This is anyway not directly connected to the milling efficiency, as it was demonstrated by Takacs and Henry **[7.11]**. Consequently, whenever the temperature may be high enough to influence a mechanochemical reaction or alloying process, it has to be considered as an independent parameter. The ball temperature is found to be lower in the *SPEX 8000* shaker mill and it is cooler when flat-ended rather than round-ended vial is used, although the milling intensity follows the opposite trend. Vibratory and shaker mills, such as the *SPEX 8000 Mixer Mill*, run at relatively low temperature (< 100 °C), while temperatures over 200 °C are typical in planetary mills operating at similar milling intensities. The same authors suggest that the higher ball temperatures result from more oblique collisions and friction, while the lower temperature but higher intensity of the shaker mill with flat-ended vial is due to the larger proportion of frontal collisions.

Figure 7.7 *The internal view of a planetary mill vial, before (left) and after (right) the milling process: the red lines mark off the region where the hard agglomerated formed on the wall, as well as in the bottom ring.*

High temperatures are achieved also in the high efficiency attritor mill, and this is confirmed by the lack of material in the input/output mass balance that occurred during the previous milling process of the alloy used to fill the *Sax3* tank.

Thus, because there was no way to obtain milled powder from the as received *HydralloyC5*® flakes, it was decided to investigate the possibility to fill the cylinders of the *Nios* car tank directly with the original flakes and to perform some preliminary hydrogen sorption cycles of the material in order to cause the so-called hydrogen "decrepitation". In fact, during absorption and desorption cycles hydrogen diffuses inside the material causing internal stress and subsequent cracks that determines particle size reduction and specific surface area increase. Thus the first hydrogen sorption cycles can have effects similar to the ball milling operated for a short time **[7.12]**, and improve the hydrogen sorption kinetics. Actually, the hydrogen decrepitation is an alternative route, respect to other mechanosynthesis, to prepare high surface area alloys **[4.11]**.

Before starting the cylinders filling operations, some preliminary tests have been performed on the *HydralloyC5*® flakes to check the validity of the new hypothesis. 2.5 g of flakes were introduced in the sample holder of the *Sievert*'s apparatus *PCT-Pro2000*, and 8 hydrogen absorption/desorption cycles were performed at constant temperature of 25°C and pressure of 30 bar and 2 bar, respectively. A continuous vacuum stage was used at the end of each cycle and before starting the following one, in order to totally evacuate the sample before each absorption run. The cycle-kinetics test behaviour is shown in **figure 7.8**, which is a snapshot of the equipment software window, during the final part of the test.

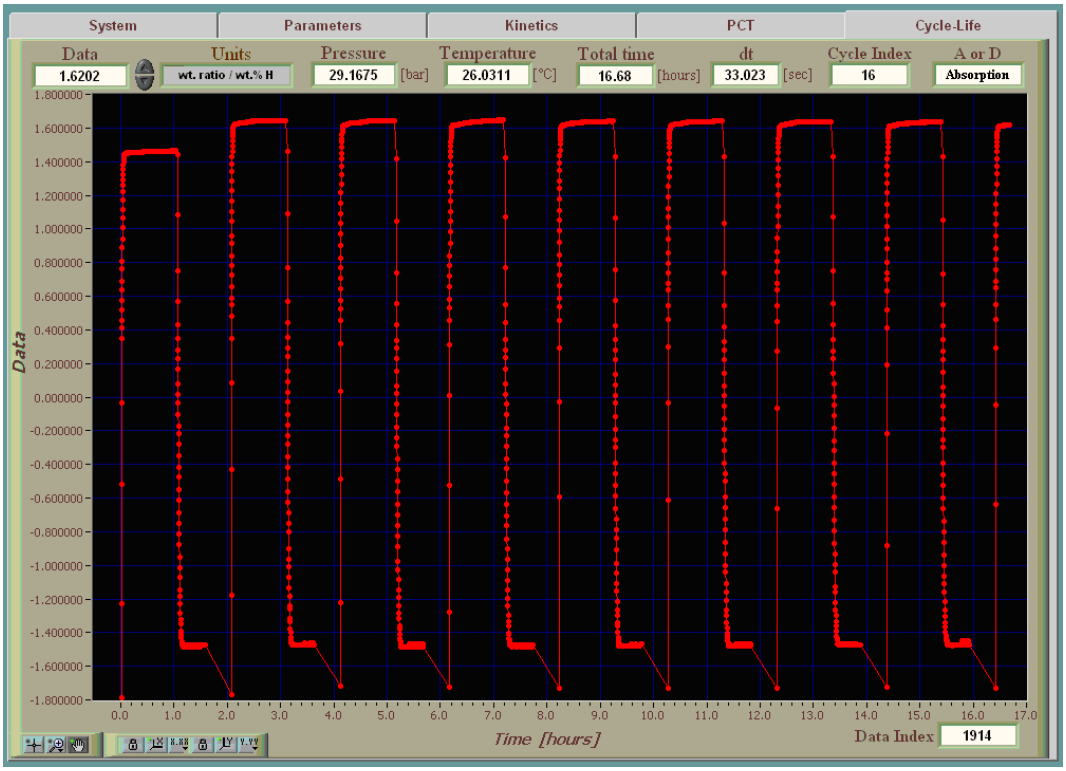

Figure 7.8 *Cycle-kinetics test on new HydralloyC5 flakes: the material shows reproducible behaviour and a constant cycle capacity of 1.5 wt% (desorption at 2 bar). Also the intermediate evacuation stages are clearly visible at the end of the desorption runs plateau: the released amount during the evacuation reaches the same absorbed amount during the previous absorption run (single points at -1.7 wt%).*

As shown in the graph, the material cycled in reproducible way up to the end of the test. It absorbed the 1.65 wt% of hydrogen at 30 bar, which is a capacity value not far from the one reported by the dealer (**table 7.2**). The released hydrogen amount is 1.5 wt% at 2 bar, so this can be indicated as the reversible capacity for the material in the chosen operative conditions. It is important to mention that the tested material was taken from a batch supplied by the dealer in a plastic bag inside a not air-proof metal can; this means that the flakes were potentially exposed to atmosphere for many days. Anyway, for a better practice, the material was kept inside a glove box (with oxygen and moisture concentration below 20 ppm), once the can was open and the plastic bag with the flakes inside was taken out. Nevertheless, the results of the cycle-kinetics test showed that the potential contact with air did not affect the

material performances. Moreover, the material showed good and reproducible behaviour just after the second cycle. After cycling, the material discharged from the sample holder was in form of loose powder (**figure 7.9**), definitively confirming that decrepitation occurred in an effective way and thus endorsing the possibility to fill the cylinders of the designed *Nios* car tank directly with the as received *HydralloyC5*® flakes.

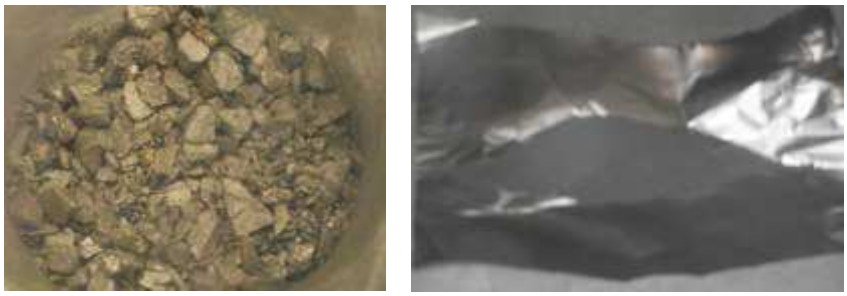

Figure 7.9 As received *HydralloyC5 flakes (left) and the powder obtained by cycling with the PCT-Pro2000 equipment(right).*

7.5 Tank building and testing

The apparent density of the as received *HydralloyC5*® in form of flakes was previously estimated as 3868 kg/m^3. As previously mentioned in **section 7.3**, this value was considered, together with the one obtained as weighted average based on the material composition and the molecular weight of the species (i.e. 6343 kg/m^3), in order to calculate an indicative average density of the material, that resulted of 5100 kg/m^3.

Thus, the density of the material in flakes is lower than the value used for calculations. Each cylinder of the *Nios* tank was filled as much as possible almost up to the entrance edge, but only about 950 g of material could go inside, while the design calculations suggested 1.3 kg of loose powder for each cylinder. This difference could have different implications on the system performances. For example, if the original designed number of 13 cylinders was used, the powder could not be enough to ensure the average rate of hydrogen supply. On the other side, the higher free volume inside the tank would increase the amount of hydrogen in the gas phase available for the initial boost (25 Nl/min) required for the car. Nevertheless, as reported before, some conservative assumptions during the design of the tank were done, so that there was a reasonable confidence in the suitability of the tank performances, even with less powder inside each cylinder.

The tank building has been performed by different steps, with the addition of other components, to build a larger unit, after the test of the previous smaller one; in this way a sort of small range scale-up process was performed, checking each time the particular occurring issues and comparing the results to the desired ones.

7.5.1 Tests with one cylinder

At first, only one cylinder of 300 ml internal volume (**figure 7.10**) and with 961 g of *HydralloyC5*® flakes inside was tested.

Figure 7.10 *The first cylinder of the Nios car's tank: internal volume = 300 ml, amount of material inside = 961 g.*

Figure 7.11 shows the behaviour of the system in the first four hydrogen absorption/release cycles. Desorption curves show similar results if compared to the *Sax3* tank: the material reaches reproducible performances starting from the second cycle. Looking at the absorption runs, the first one is characterized by an apparently strange curve: this is because the experiment was performed at pressure higher than that used for the following absorption tests (80 bar instead than 30 bar). This experiment at higher pressure was performed to test the absence of leaks in the system and acts as a first absorption run for the tank itself. Anyway, just because of the higher pressure inside the tank, the initial part of the graph, corresponding to the pressure decrease up to the desired pressure of 2 bar, is more consistent, while the higher final capacity value (1.9 wt%) is probably due to a lower accuracy in the calculation of the software at higher hydrogen pressures. Moreover, interestingly, the curve clearly shows once again the effect of the two fans' use. In fact, the fans have been activated after an initial part, during which the system warmed up to 53 °C and did not cooled down: once the fans were turned on, the temperature quickly drp down (red scattered curve) and this caused a strong increase of the absorption kinetics.

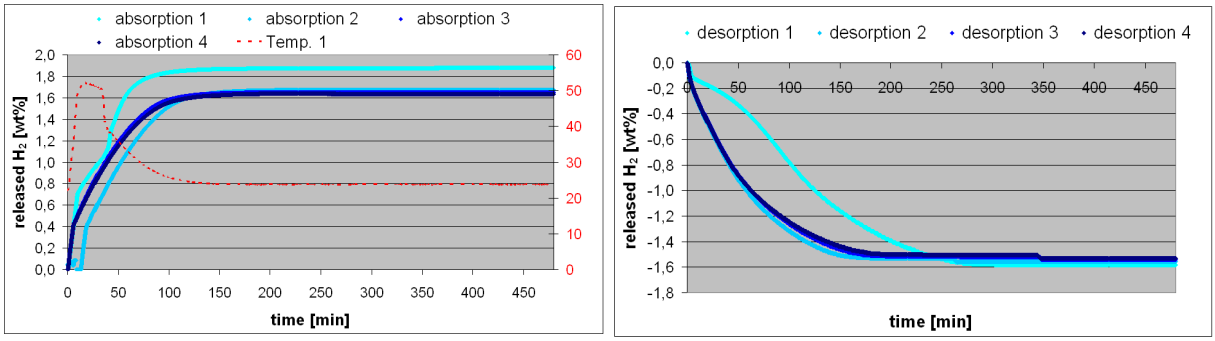

Figure 7.11 *Four hydrogen absorption (left) and desorption (right) curves for the first cylinder of the Nios car's tank. The mean temperature profile(red curve) of the tank surface during the first absorption run is also shown.*

From the second cycle onwards, the system shows a final hydrogen absorbed amount of 1.65 wt% and, , with the desorption at 2 bar, a reversible capacity of 1.5 wt%: these are exactly the values obtained with the measurements performed in the *Sievert*'s apparatus.

However, as shown in **figure 7.12**, the kinetics measured by the *Sievert*'s apparatus is much faster than the one measured with the Test Station. One of the factor that generate this difference is the temperature profile during the test: the temperature controller of the *Sievert*'s apparatus guarantees a constant value temperature of 25 °C, while the environment around the Test Station and the forced air exchange maintained the temperature in the range 17-23 °C. However, the difference in the kinetics is more likely to be ascribed to the difference in the phenomena that change with the scale-up process, such as diffusion of the hydrogen gas in the powder bulk, heat transfer, hydrogenated/ dehydrogenated phases nucleation and growing. The comparison clearly shows how these phenomena are enhanced when only few grams of material are used, while they become more and more critical when systems in bigger scale are considered.

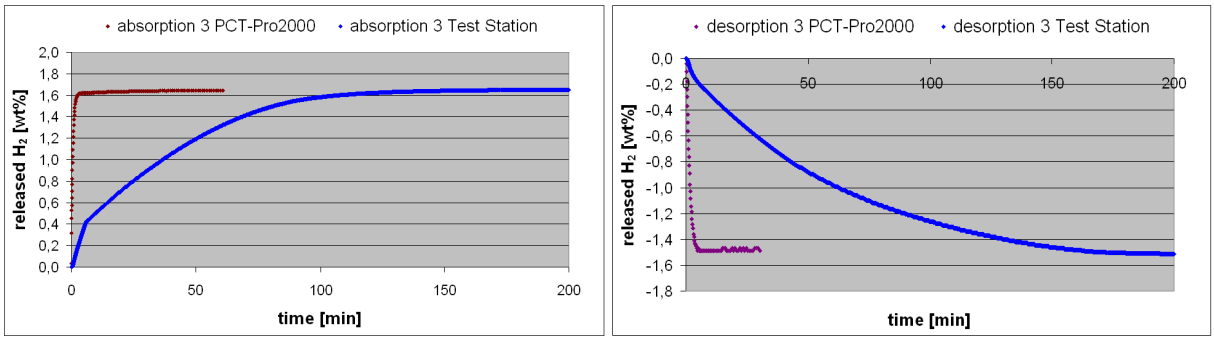

Figure 7.12 *Comparison of the third cycle absorption and desorption curves, obtained with the PCT-Pro2000 Sieverts' type apparatus (red) and the Test Station (blue).*

The reversible capacity (1.5wt%) is even higher than the one measured for the *Sax3* tank (1.35 wt%) with the powder previously milled in the attritor mill. These results combined with the conservative assumptions made during the tank design, when a lower cycle capacity of 1.2 wt% was considered to estimate the minimum amount of powder needed for the tank, contributes to improve the effective tank performance. Referring to these first results obtained with the new and not milled powder, it is important to underline that the material was exposed to air for some hours, before the connection of the cylinder (which was filled inside the glovebox) to the valve and then to the Test Station. This fact highlights two important aspects: a) the low or none effect that normal atmosphere has on the material when it is in form of flakes (as received), b) the powerful role of the decrepitation process for the activation of the material.

7.5.2 First rack testing

After the test on only one cylinder, a set of 5 cylinders was tested. The cylinders were arranged in a row, called "rack" (**Figure 7.13**). The rack is provided with a main ball valve and a safety relief valve to protect it against overpressure. Four thermocouples have been positioned on 4 of the 5 cylinders to record the temperatures during the tests. The same two fans used for the previous tests were put above the rack to force heat exchange with the

surrounding air in order to countervail the thermal effects of the hydrogen sorption processes. Almost 5 kg (4718 g) of *HydralloyC5*® were charged inside the five cylinders.

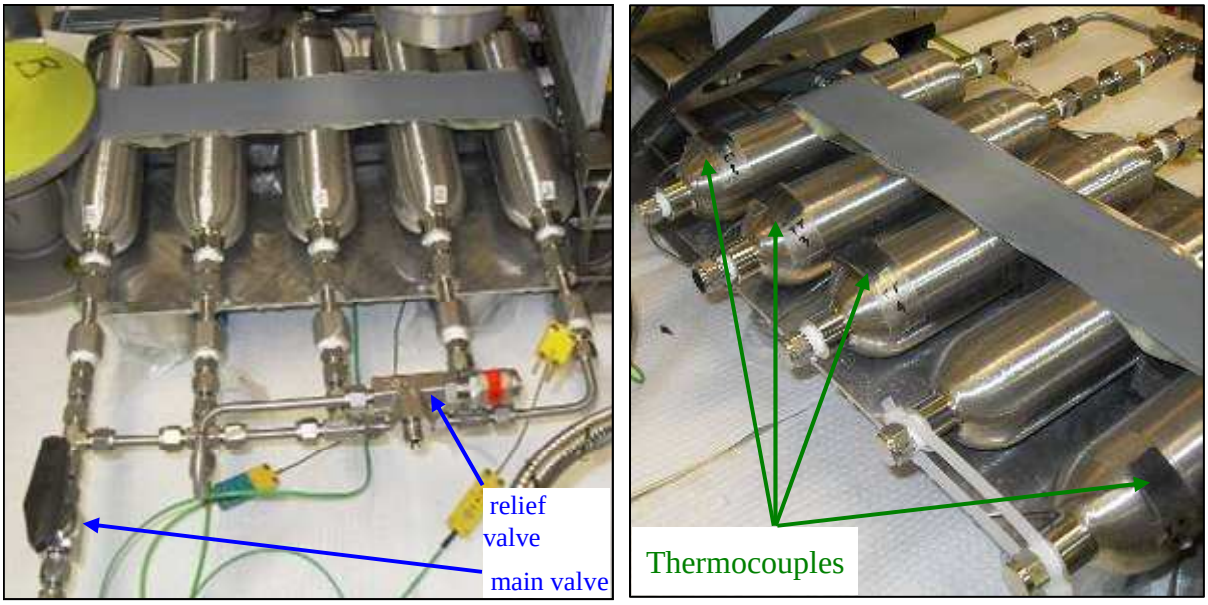

Figure 7.13 *The Rack I of the Nios car's tank: 5 cylinders with internal volume of 300 ml each. The total amount of HydralloyC5 inside is 4718 g. On the front view (left) and on the rear view (right) the valves and the thermocouples, respectively, are indicated.*

In **Figure 7.14** the three first hydrogen sorption curves are shown. As expected from the results obtained by *Sievert*'s apparatus during the test of one cylinder, the total absorbed amount is around 1.65 wt% and the desorption curves indicate 1.5 wt% of reversible capacity, which corresponds to 840 Nl or 70 g of hydrogen. Moreover, and similarly to the previous tests, the system reached its steady behaviour already after the second cycle.

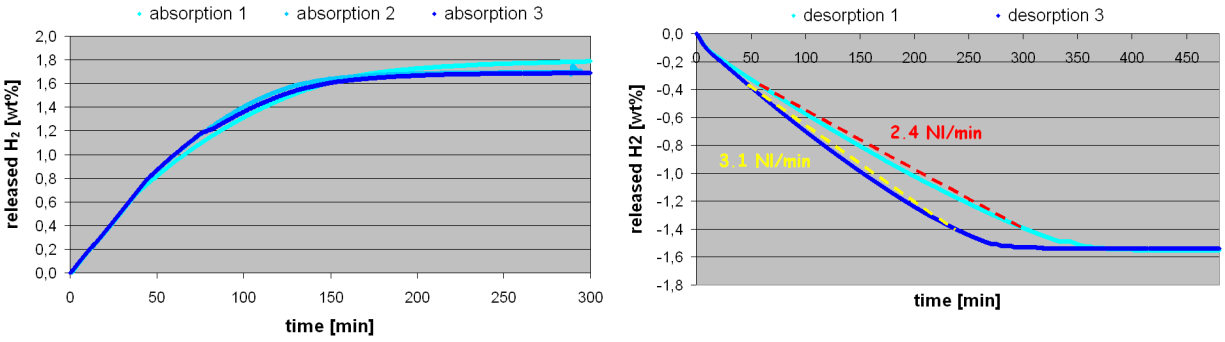

Figure 7.14 *Hydrogen absorption (left) and release (right) cycles for the Rack 1 of the Nios car's tank. Average rate of hydrogen desorption in the extended middle range (from 0.35 wt% to 1.40 wt%) are show for 1st and 3rd cycles curves.*

The average hydrogen desorption rate in the middle range of the desorption curves (0.35-1.00 wt%) was 3.4 Nl/min for the third cycle and, considering an extended middle range up to 1.40 wt%, the average value was 3.1 Nl/min. Thus, with this rack configuration, the power necessary to feed the two fans (45 W) is only the 12% of the total output power from the fuel cell (with efficiency of 0.7). The system already fulfils the customer's minimum requirement

as regards the total amount of hydrogen (400 Nl), while it is still far as regards the hydrogen supply to the fuel cell (6.7 Nl/min). However, going deeply with the results analysis, with a comparison between the average hydrogen desorption rates in the extended middle range for the cylinder 1 (0.97 Nl/min) and the rack I (3.1 Nl/min) configurations, it can be easily noticed that there was no proportional correlation to the powder amount used in the two cases, respectively. In particular, the rack I configuration showed a desorption rate lower than the expected one: it was likely there was somehow a hindrance to the hydrogen release in this bigger system. Actually, this is also recognizable from the shape of the desorption curves of **figure 7.15**, compared to those in **figure 7.14**: the previous one showed a linear behaviour, not a progressive approach to the plateau, indicating that there was a limiting phenomenon acting on the system and affecting its kinetics. The cause cannot be ascribed to a too small size of the line and tube fittings of the system, as they were opportunely chosen with a 6 mm internal diameter size, which allows high gas flow rate.

In order to deeper investigate the system behaviour, a desorption run was performed using the large range flow control unit, FCU-2, instead of the FCU-1. Here below the schematic layout of the Test Station is reported.

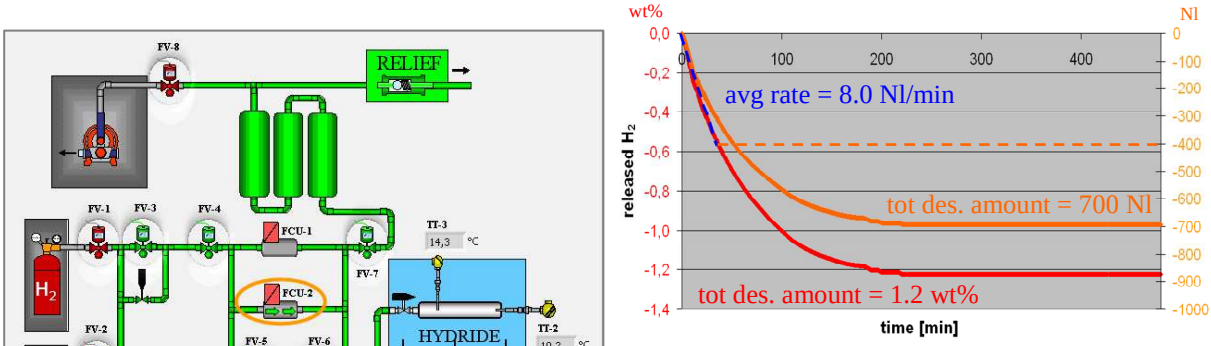

Figure 7.15 *Desorption run with the use of the wide range (10-200 Nl/min) flow controller FCU-2 (see the Test Station scheme on the left). The total amount of released hydrogen is higher than the minimum requirement (400 Nl), even though the showed values are underestimated (see the text for the explanation). Also the achieved average hydrogen flow rate (8.0 Nl/min) is higher than the customer requirement (6.7 Nl/min). For the schematic layout of the Test Station (see also **section 3.5**).*

In this case the initial set point of the FCU-2 was 13.4 Nl/min; this value was chosen because it is the double of the minimum flow requirement indicated by the customer (400 Nl/h = 6.7 Nl/min). Once the system reached the desired pressure of 2 bar, after the transient time and similarly to the other previous tests, the FCU-2 set point was regulated in order to keep this constant pressure in the system. The use of the large range flow controller caused a strong increase in the hydrogen release rate, thus demonstrating that the limiting effect in the previous test with the rack I configuration was due to the flow controller unit. Considering the range from the beginning up to 400 Nl (which is the minimum amount requested from the customer) of released hydrogen, the average hydrogen desorption rate was 8.0 Nl/min (**figure 7.15**), while the previous test with the FCU-1 gave 3.9 Nl/min (value derivable from **figure**

7.14). This confirms how the small range flow controller strongly limits the system potentiality. The measured average value indicated that the system is already able to fulfil two of the requirements from the customer: more than 400 Nl of hydrogen can be supplied with an average rate (8.0 Nl/min) higher than the requested one (6.7 Nl/min). Despite the fact that the test of the rack I set-up with the FCU-2 showed a higher potentiality of the system, it must be underlined that, as a result of the test, only the 1.2 wt% of released hydrogen was measured. This discrepancy, if compared to the 1.5 wt% obtained with the previous tests, must be ascribed to the use of the FCU-2 itself. In fact, the range in which this flow controller has a good reliability is 10-200 Nl/min, thus once the current flow goes below 10 Nl/min, as it happened after the transient time to reach and then keep 2 bar, the equipment underestimates the amount of hydrogen flown.

7.5.3 Two racks (I+II) configuration testing

The subsequent step of the tank scaling up process is the test of the system with two rows of five cylinders each. The total amount of powder used with this configuration is 9481 g. The two improving of the previous stages, i.e. a) the use of the two cooling fans and b) the use of the FCU-2, were both used since the beginning during the test with the configuration with two racks.

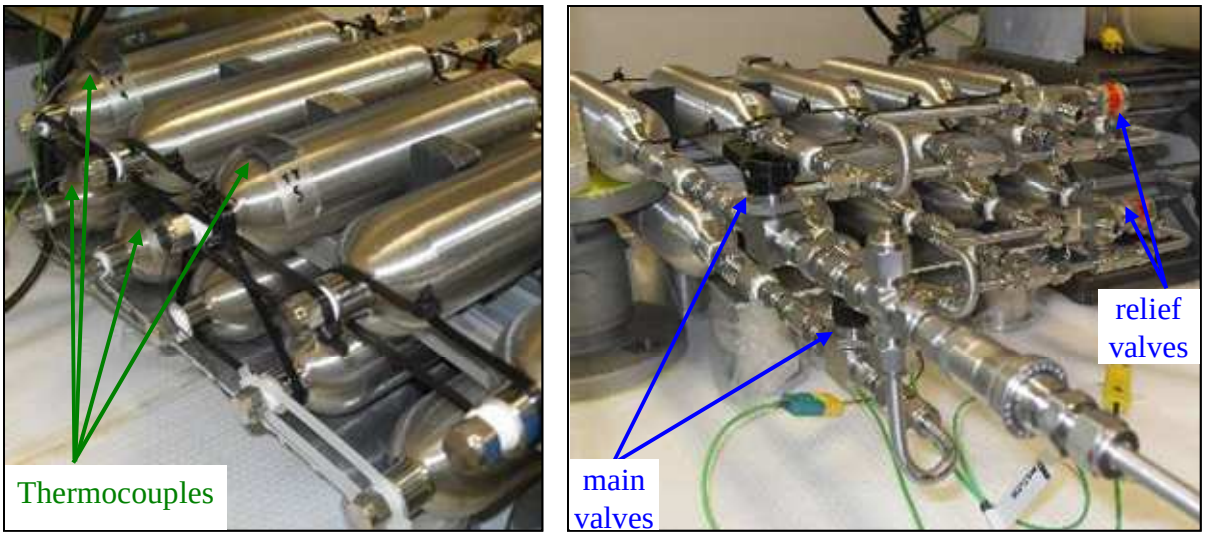

Figure 7.16 *The hydrogen storage tank: 10 cylinders of 300ml internal volume each, are assembled in two rows (Racks I+II). Four thermocouples used to register the temperature on the cylinders surface, are visible in the rear view (left), while the main valve and the relief valve to protect the system against overpressure, are indicated for both the rows in the front view (right)*

The so assembled hydrogen tank is suitable as regards the space that the customer indicates available inside the *Nios* car (**figure 7.1**). Actually, the described scale-up steps configurations are following the designed layout previously proposed as a solution for the space optimization. Thus, taking into account all the other requested performances of the tank, it can be noticed that the only one fulfilment still missing is the initial high hydrogen flow: the tank should in fact be able to ensure a hydrogen supply of 25 Nl/min during the first minute of

run. In order to check whether the racks I+II system (**figure 7.16**) is able to satisfy this issue, a test with the starting high flow rate of 25 Nl/min was performed. This set point was kept for the whole transient time up to the system achieved 2 bar, then the flow was regulated to keep the pressure at 2 bar. The results of the test are reported in **figure 7.17**: the system supplied 25 Nl/min not only for 1 min, but rather for about 9 min (540 s); after this time the final pressure of 2 bar is reached. In order to keep a constant pressure of 2 bar the flow was manually decreased step by step to 10 Nl/min; after that, once the necessary flow rate to keep 2 bar inside the tank went below 10 Nl/min (limit value to have a good reliability of the FCU-2), the test was interrupted. After a while needed for flow and pressure stabilization, the isobaric region lasted about 40 min (pink ovale) and the hydrogen flow rate remained in the range 10-13 Nl/min, which is almost the double of the average flow requested from the customer.

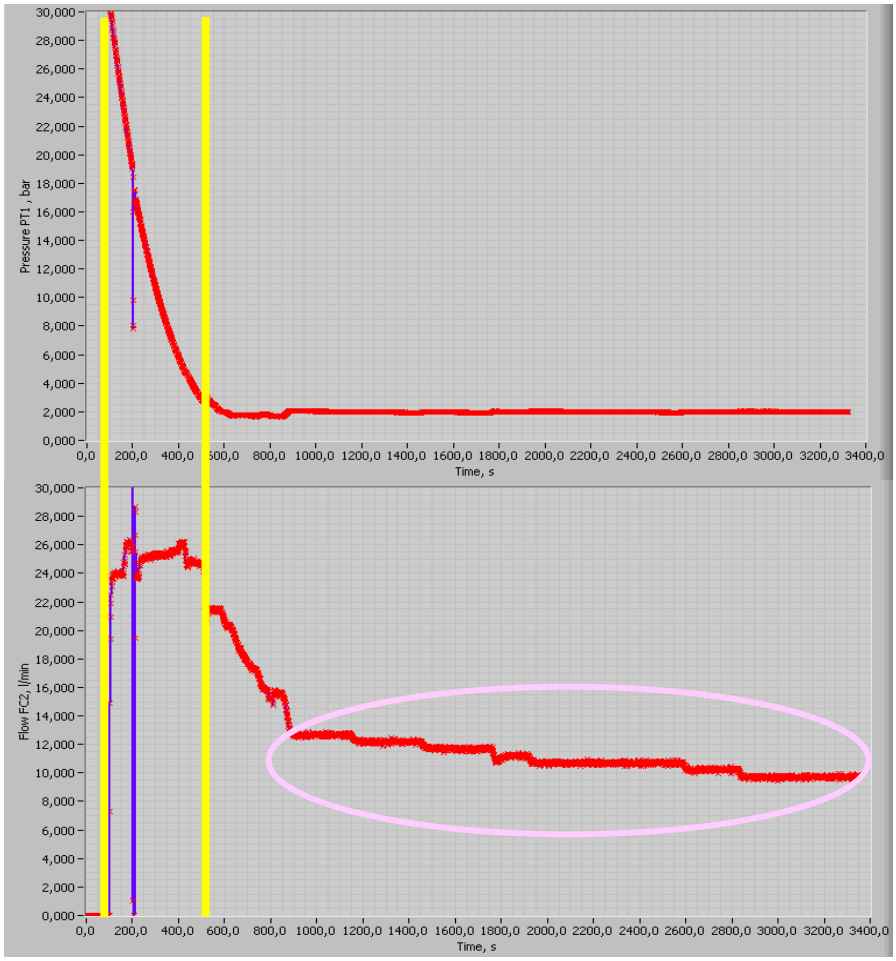

Figure 7.17 *Hydrogen release test on the tank with 10 cylinders arranged in two rows (Racks). The hydrogen flow rate of 25 Nl/min is ensured for about 9 min up to the system reaches 2 bar; then the isobaric part corresponds hydrogen supply rate above 10 Nl/min, with a quasi-stationary part lasting about 40 min (pink circle).*

Thus, in the end, the tank already with 10 cylinders of the configuration racks I+II is able to largely overcome the minimum requirements, with a total amount of released hydrogen equal to 140 g (around 1680 Nl), which is the 1,5 wt% of the powder total weight. Referring to the

available space inside the tank and to the designed layout of **figure 7.5**, there is still the opportunity to add a third rack with five cylinders in order to further increase the car performances in terms of power and total driving range. For this reason, the frame with fittings and connecting parts of the rack III was already prepared and other cylinders already filled.

Regarding the use of the two flow controller units, it has already been underlined how much critical is their reliability during the measurements and how these instruments can affect themselves the system efficiency. For example, the test performed with the FCU-2 in the rack I configuration demonstrated how the feed of the hydrogen from the tank was strongly limited by the FCU-1, even far away from its working limit (which is 10 Nl/min).

It is important to underline once again that the *HydralloyC5*®, charged in form of flakes inside the cylinders, remained in contact with air for some hours before connecting the system to the Test Station. This fact, together with the evidence of the performances of the material, close to the ones declared by the supplier and reproducible, already after the second-third cycle and for all the scaled tested configurations, constitutes a strong evidence of the versatility of the tanks based on this room temperature alloy. An additional powerful feature is the possibility to reduce the size of the material's particle to loose powder simply by decrepitation, which occurs already in the first hydrogen sorption cycles, thus suggesting that the onerous process of ball milling can be avoided for such a system. As demonstrated, the tank developed for the *Nios* car successfully fulfils the customer requirements as regards the PEM fuel cell hydrogen supply and occupies only part of the provided space inside the car.

[7.1] http://www.fortis-saxonia.de/sax/nios/nios-10/

[7.2] On-line calculator from NIST - National Institute of Standards and Technology, Thermophysical Properties of Hydrogen: http://webbook.nist.gov/cgi/fluid.cgi?ID=C1333740&Action=Page%20

[7.3] A. Burke, M. Gardiner, Hydrogen Storage Options: *Technologies and Comparison for Light-Duty vehicle Applications*, Institute of Transportation Studies, University of California, Davis, Research Report UCD-ITS-RR-05-01 (2005).

[7.4] http://www.fortis-saxonia.de/sax/sax3-08/

[7.5] G.A. Lozano Martinez, *Development of Hydrogen Storage Systems using Sodium Alanate*, PhD Thesis, *Helmholtz-Zentrum Geesthacht* (*HZG*), Zentrum für Material- und Küstenforschung GmbH (2010).

[7.6] W. Pyle, *Hydrogen Storage*, Home Power, 59, June/July (1997).

[7.7] C. Suryanarayana, *Mechanical alloying and milling*, Prog. Mater. Sci. 46 (2001) 1–184.

[7.8] L. Takacs, V. Šepelák, *Quantitative comparison of the efficiency of mechanochemical reactors*, J. Mater. Sci. 39 (2004) 5487-5489.

[7.9] S.-H. Hong, B.-K. Kim, *Fabrication of W-20 wt% Cu composite nanopowder and sintered alloy with high thermal conductivity*, Mater. Lett. 57, 18 (2003) 2761-2767.

[7.10] F.M.F. Rhen and M. Venkatesan, *Effect of ZrB_2 addition on SmCo-1:7 high temperature magnets*, J. Appl. Phys. 93, 10 (2003) 8683-8685.

[7.11] L. Takacs and J.S. McHenry, *Temperature of the milling balls in shaker and planetary mills*, J. Mater. Sci. 41 (2006) 5246-5249.

[7.12] B. Joseph, B. Schiavo, *Effect of ball-milling on the hydrogen sorption properties of $LaNi_5$*, J. Alloys Compd. 480 (2009) 912-916.

[7.13] A. Kianvash, I.R. Harris, *Hydrogen decrepitation as a method of powder preparation of a 2:17-type, Sm(Co, Cu, Fe, Zr)8.92 magnetic alloy*, J. Mater. Sci. 20, 2 (1985) 2, 682-688.

Chapter 8

Concluding remarks

As described in **chapter 1**, hydrogen storage is a key issue for the development of a hydrogen-based economy and, for this reason, research efforts are currently in progress in order to achieve efficient and safe hydrogen storage systems. In this frame, an experimental work on different systems for solid state hydrogen storage has been carried out. According to the purposes of the PhD course in Applied Physics, and to the strong applicative character of this research topic, the experimental activity has been performed taking into account the potentiality of the studied systems for applications and technological development. Rather than focusing on a single type material, different systems have been considered and investigated. Their different nature allowed an overview on the various options for solid state hydrogen storage and, at the current state of art, on their actual perspectives as suitable candidates for this purpose. Following the applicative mission, in addition to the study on candidate materials, a real-world prototype system of hydrogen storage for automotive application has been developed. This has provided some cues on the concrete issues in designing, building and testing a solid state hydrogen storage tank, in the view of interfacing it with a fuel cell.

As regards the study carried out on materials, compounds representative of each main class of hydrides, such as intermetallic alloys, binary hydrides, complex hydrides, have been considered in the reported research activity.

The first presented experimental work (**chapter 4**) concerns the investigation on the intermetallic alloy $LaNi_5$. As this is a well know and studied compound, it has been considered, at the beginning of the experimental activity, as a standard reference compound, in order to calibrate and test some new acquired instrumentation, used for characterizing hydrogen sorption properties of the materials. It has been found that long time ball milling has a negative effect on the hydrogen sorption properties of this material, differently from what

occurs in other cases (e.g. MgH_2). The causes of such an effect have been investigated both with long range and short range structural analysis. Local crystal structure (EXAFS) measurements revealed that long time ball milling causes a decrease of interatomic distances and an increase of local structural disorder, which hinder the hydrogen uptake and hydrogen release from the material. Annealing treatments have been found to be useful for the regain of the sorption properties of the material for powders milled up to 20 h, but not for samples milled for very long time (100 h). $LaNi_5$, as well as other intermetallic alloys, is already being used as room temperature material for solid state hydrogen storage in prototype or already commercial tanks for both vehicular and stationary applications. Thus, the results obtained on the long time ball milled $LaNi_5$ can give a contribution to the preparation procedures on this material. In general, especially for large scale processes, the opportunity of the ball milling technique should always be compared with the effect of a number of hydrogen absorption/desorption cycles. For example, as shown in **chapter 7**, the decrepitation of the material due to few hydrogen sorption cycles can give results similar to ball milling.

According to the promising destabilization approach of the reactive hydride composites (see **subsection 2.3.1** of this thesis), the second reported study concerns a two compounds system, CaH_2+MgB_2, from which the reactive hydride composite (RHC) $Ca(BH_4)_2$+MgH_2 can be synthesised upon hydrogenation. Thus, in this system, magnesium hydride, i.e. the binary hydride with the higher performances obtained up to now, and calcium borohydride, a complex hydride with high theoretical hydrogen density, have been considered. The effect of ball milling time on the hydrogen absorption properties of the system has been studied, and it was found that, differently from $LaNi_5$, the hydrogen absorption and desorption kinetics for this system improves as milling time increases. The partial and total substitution of MgB_2 with AlB_2 has been tested in order to improve the system performances. The total substitution has been found to increase the experimental gravimetric capacity and to show a higher reversibility. The reason for this has been discussed, also referring to the existing literature. Different dopants have been tested to further improve the properties of the CaH_2+AlB_2 composite. Among the tested additives, the fluorinated ones have been found to increase hydrogen desorption kinetics, while no positive effect has been noted on the absorption. In particular, NbF_5 has given the best results on the desorption process, although with a delayed effect on the system. The gas mixture released by the 5wt%NbF_5-doped system has been analyzed and no fuel cell corroding or damaging agents have been detected. While this studied RHC system is not yet ready for the application, due to the still limited reversibility, low kinetics and high working temperatures, however, the introduction of AlB_2 shows some interesting effect on improving the properties of the material. This could give useful elements for enhancing the performances of high hydrogen capacity materials, such as borohydrides and borohydrides-based RHC.

The third studied material system is a low cost polymer-based compound, constituted by manganese oxide, incorporated in a sulfonated-polyetheretherketone (S-PEEK) matrix. The characterization of the samples has shown that oxide encapsulation occurred at different

levels, depending on the preparation procedures. The measurements on the hydrogen absorption properties have shown a capacity of 1 wt% at temperature of 110 °C, which is interesting for this type of systems. This value has been obtained for the sample with the highest oxide content, and, in general, the hydrogen capacity has been found to increase as the oxide content increases. The interesting preliminary results obtained on this system, at not common conditions for hydrogen physisorption materials, suggest also the possibility of a chemical nature of the hydrogen-material interactions. This still makes interesting such a low cost and versatile system, for which more investigations are in progress. If a reversible hydrogen uptake will be proved, this material could offer a powerful alternative to the room temperature intermetallic alloys, currently used for some applications.

As mentioned, as a further contribution to the applicative nature of the scientific work carried out, a storage system for vehicular purposes has been developed. It consists of a hydride-based hydrogen storage tank developed to equip a city-car prototype. The chosen hydrogen storage material is a commercial room temperature intermetallic alloy, analogous to the studied $LaNi_5$ material, with storage capacity of 1.8 wt%. The design has been carried out, taking into account the issues related to the use of the solid state hydrogen storage material tank for its coupling with the customer's fuel cell in an integrated system. The tests on the designed and assembled tank have shown the fulfilment of all the customer's requirements, and the optimization of the provided space inside the car still allows enlarging the designed modular tank. During this applicative work, many critical practical aspects had to be faced, such as the material preparation in larger scale, the thermal effects of the hydrogen absorption/desorption reactions, as well as the suitability of the testing system from the applicative point of view, rather than from that concerning only the characterization of the hydrogen storage material at larger scales.

Hence, the experimental work carried out during the PhD course and reported in this thesis shows a heterogeneous study on new potential options for hydrogen storage, a current key issue for the spread use of the hydrogen based clean technologies. Solid state hydrogen storage systems have been investigated, with both materials science and base research aspects, but in a view of potential applications, an example of which has been already developed and reported.

Curriculum Vitae

Benedetto Schiavo, born in Palermo (Italy), 1978 February 8th. In 2004, Chemical Engineering Master's Degree (110/110 cum laude) at University of Palermo, with graduation work entitled "Set-up of a continuous reaction system for the synthesis of macromolecules in supercritical CO_2 as solvent". From May 2005 to Feb. 2007, process and production engineer in a Linear Low Density Polyethylene (LLDPE) production plant – ENI, Polimeri Europa – Priolo Gargallo, Siracusa (Italy). Since Mar. 2007, scientific researcher at Institute for Advanced Technologies, in Trapani (Italy). Since Jan. 2009, PhD student of the International PhD Course in Applied Physics at University of Palermo, Department of Physics.

List of publications

- **B. Schiavo**, A. Girella, F. Agresti, G. Capurso, C. Milanese, *Ball milling and AlB_2 addition effects on the hydrogen sorption properties of the CaH_2 + MgB_2 system*, Journal of Alloys and Compounds 509, S2 (2011) S714-S718.

- B. Joseph, **B. Schiavo**, G. D'Alì Staiti, B.R. Sekhar, *Effect of ball milling induced nanostructuring on the hydrogen sorption properties of $LaNi_5$*, International Journal of Hydrogen Energy 36, 13 (2011), 7914-7919.

- B. Joseph, A. Iadecola, **B. Schiavo**, A. Cognigni, L.Olivi, N.L. Saini, *Large atomic disorder in nanostructured $LaNi_5$ alloys: A La L3-edge extended X-ray absorption fine structure study*, Journal of Physics and Chemistry of Solids, 71 (2010) 1069-1072.

- B. Joseph, A. Iadecola, **B. Schiavo**, A. Cognini, L. Olivi, G. D'Alì Staiti, *Local structure of ball-milled $LaNi_5$ hydrogen storage material by Ni K-edge EXAFS*, Journal of Solid State Chemistry, 183 (2010) 1550-1554.

- B. Joseph, **B. Schiavo**, *Effect of ball milling on the hydrogen absorption of $LaNi_5$*, Journal of Alloys and Compounds 480 (2009) 912–916.

Presentations at scientific meetings

- G. Capurso, F. Agresti, L. Crociani, G. Rosseto, **B. Schiavo**, A. Maddalena, S. Lo Russo, G. Principi, *Nanoconfined mixed Li and Mg borohydrides as materials for solid state hydrogen storage*, 4th World Hydrogen Technologies Convention, Glasgow (UK), 14-16 September 2011.

- M. Dornheim, J.M. Bellosta von Colbe, G.A Lozano, C. Pistidda, R. Gosalawit-Utke, K. Suarez, J. Jepsen, O. Metz, **B. Schiavo**, U. Bösenberg, J. Puszkiel, C. Bonatto Minella, F. Karimi, N. Herbst, K. Taube, T. Klassen, *Nanostructured Materials and Systems for Hydrogen Technology*, Gordon Research Conference: Hydrogen- Metal Systems, Stonehill College - Easton, MA (USA), 17-22 July 2011.

- C. Milanese, A. Girella, S. Garroni, G. Mulas, R. Campesi, **B. Schiavo**, E. Pellicer, M.D. Barò, A. Marini, *Preparation and characterization of borohydrides-based reactive hydride composites (RHCs)*, Gordon Research Conference: Hydrogen- Metal Systems, Stonehill College - Easton, MA (USA), 17-22 July 2011.

- G. Capurso, F. Agresti, L. Crociani, G. Rosseto, **B. Schiavo**, A. Maddalena, S. Lo Russo, G. Principi, *Dehydrogenation behaviour of mixed borohydrides dispersed on high specific surface area carbons*, Farady Discussion 151: Hydrogen Storage Materials, STFC Rutherford Appleton Laboratory - Oxon (UK), 18-20 April 2011.

- **B. Schiavo**, A. Girella, B. Joseph and C. Milanese, *Hydrogen sorption properties of the CaH_2-MgB_2-AlB_2 system*, Farady Discussion 151: Hydrogen Storage Materials, STFC Rutherford Appleton Laboratory - Oxon (UK), 18-20 April 2011.

- **B. Schiavo**, A. Girella, F.Agresti, G. Capurso, C. Milanese, *Ball milling and AlB_2 addition effects on the hydrogen sorption properties of the CaH_2 + MgB_2 system*, "MH-2010 International Symposium on Metal – Hydrogen Systems", Mosca (Russia), 19-23 Luglio 2010.
- **B. Schiavo**, G. D'Alì Staiti, C. Milanese, F. Agresti, G. Principi, *Hydrogen sorption properties of the composite system calcium hydride – magnesium boride*, "European Energy Conference 2010", Barcelona (Spain), 20-23 Aprile 2010.

- **B. Schiavo**, B. Joseph, G. D'Alì Staiti, N. L. Saini, *Effect of nano-structuring on hydrogen sorption properties of $LaNi_5$ systems*, 4th International Symposium Hydrogen & Energy, Wildhaus (Switzerland), 24 - 29 January 2010.

- B. Joseph, **B. Schiavo**, G. D'Alì Staiti, B.R. Sekhar, *Effect of ball milling induced nanostructuring on the hydrogen sorption properties of $LaNi_5$*, "Hysydays 2009 3rd World Congress of Young Scientist on Hydrogen Energy Systems", Torino Esposizioni – Torino (Italia) 07-09 Ottobre 2009.

- B. Joseph, **B. Schiavo**, A. Paolone, O. Palumbo, P. Rispoli, R. Cantelli, *Nanostructuring – a possible way to enhance the hydrogen sorption properties of materials*, "Cochin Nano-2009 International conference on frontiers of nanoscience and technology", Cochin University of Science and Tecnology – Cochin, Kerala (India) 03-06 Gennaio 2009.

- B. Joseph, **B. Schiavo**, A. Paolone, O. Palumbo, P. Rispoli, R. Cantelli, Effect of nano-structuring on hydrogen sorption properties of materials, Joint ICTP- KFAS Workshop on Nanoscience for Solar Energy Conversion, International Centre for Theoretical Physics (ICTP) – Miramare, Trieste – Italy, 27-29 October 2008.

Acknowledgements

Many people contributed to make the PhD course a so useful and formative experience. Here I would like to give thanks to them for their contribution throughout this path.

Prof. Bernardo Spagnolo, Coordinator of the PhD course in Applied Physics, for his helpfulness and encouragement in submitting for the Doctor Europaeus title.

Prof. Giacomo D'Alì Staiti, Supervisor of the thesis and Vice-Chairman of the ITA research institute (Trapani, Italy), for his useful suggestions and his engagement in reinforcing and developing the Institute.

Prof. Giovanni Principi, Co-Supervisor of the thesis, who gave me support since the beginning of my research activity on hydrogen storage, by receiving me in his research group at University of Padua (Italy) and introducing to me the first elements of this research topic.

Colleagues at ITA, who are also friends. *Patrizia*, for her work at administration and her kindness. *Lucia*, for her key role in the initial design and building of the nanotechnology laboratory and her practical help everyday. *Alfonso*, for the interesting discussions and useful suggestions on physics matter. *Antonino*, for the help in the laboratory daily maintenance and problem solving. *Eng. Biagio Di Via*, Our local Coordinator, for his understanding in the organization of my work at ITA Institute and University of Palermo.

Colleagues at University of Palermo: *Anna*, *Francesca* and *Rosita*, they have been wonderful fellows in this adventure.

The group of the Hydrogen Lab - University of Pavia (Italy), for the collaboration on the RHC system. Thanks to *Alessandro* for the performed measurements and to *Prof. Amedeo Marin*i for the possibility to closely collaborate as a single research group.

Filippo Agresti and *Giovanni Capurso* of University of Padua, for the help in the XRPD acquisitions.

Rolando Pedicini of the CNR-ITAE institute (Messina, Italy), for the collaboration recently started on the polymer-based materials.

People at HZG institute (Geesthacht, Germany). *Prof. Thomas Klassen* and *Dr. Martin Dornheim*, who gave me the possibility to spend a research period at the Institute. *Dr. Josè Bellosta von Colbe*, for the supervision on the hydrogen tank work. Other colleagues: *Fahim*, *Nina*, *Gustavo*, *Juliàn*, for their cordiality and their help on the measurements at synchrotron facilities. Hearty thanks to *Claudio* and *Christian*, for their friendship, the useful suggestions on research topics, and to Claudio for the NMR preliminary measurements at *University of Aarhus* (Denmark). A special thanks to *Julian*, for the accuracy and care in all the bureaucratic and practical aspects during my period at HZG institute, as well as for the introduction to the use of the Test Station.

I want to reserve a very special thanks to two research colleagues, who are now my friends. *Dr. Chiara Milanese*, for the work on the RHC system at Hydrogen Lab - University of Pavia. Through her, the option for the research period abroad, became a reality at HZG institute, as well as to the possibility of submitting for the Doctor Europaeus title. *Dr. Boby Joseph*, for the EXAFS measurements and data analysis on $LaNi_5$ samples, and for the basic work at ITA in the first months of the research activity at the Institute in the field of hydrogen storage. Along with the supervisors' contribution, they also have a merit in the current aspect of this thesis.

Thanks to *My Family*, for always encouraging and supporting me in everything. Thanks to *My Wife*, *Maria Chiara*, an invaluable treasure, for bearing with me in a so lovely way. Thanks to *God*, for his infinite Grace.